Sintered Porous Silicon

—

Physical Properties and Applications for Layer-Tranfer Silicon Thin-Film Solar Cells

Von der Fakultät für Mathematik und Physik
der Gottfried Wilhelm Leibniz Universität Hannover
zur Erlangung des Grades
Doktor der Naturwissenschaften
Dr. rer. nat.
genehmigte Dissertation

von

Dipl.-Phys. Andreas Wolf

geboren am 19.03.1977 in Dortmund

2007

Referent: Prof. Dr. Rolf Brendel
Korreferentin: Prof. Dr. Karina Morgenstern
Tag der Promotion: 16.07.2007

Abstract

This work focusses on the characterisation of sintered porous silicon and on the development of monocrystalline silicon thin-film solar cells from the Porous Silicon Process (PSI process). For the fabrication of these solar cells, a thin silicon film is epitaxially grown on a monocrystalline silicon growth substrate, that features a layer of porous silicon (PS) at the surface. Due to the thermal activation during the epitaxial growth process, the PS layer reconfigurates and mechanically weakens, which later permits the transfer of the thin-film device to a second carrier substrate. When separating the epitaxial film from the growth substrate, a residual layer of *sintered* porous silicon (SPS) remains attached to the rear side of the device. So far, the physical properties of this layer and its impact on the performance of PSI solar cells have been poorly investigated. This thesis aims at a comprehensive determination of the physical properties of sintered porous silicon, in particular, its thermal, optical and electrical properties.

For the thermal characterisation of the fragile free standing SPS films, a contactless measurement technique based on lock-in thermography is developed and experimentally verified. This analysis identifies a third order power law dependence of the thermal conductivity of SPS on the porosity, in agreement with the predictions of the Looyenga model. Phonon scattering at the pore walls, which is known to drastically reduce the thermal conductivity of as-prepared PS, is also present in the sintered state. The obtained results reveal that, in the case of SPS, this effect is less pronounced, due to the increased structure size of the sintered material compared to the as-prepared state.

The effective refractive index of SPS complies with the predictions of effective medium models, whereas Mie's theory successfully describes light scattering by the spherical pores in SPS. An analysis of the measured scattering coefficient shows that the close spacing of the pores reduces the scattering efficiency of the individual voids. Accounting for adjacent pores by applying the afore measured effective refractive index for the calculation of the Mie scattering efficiency results in an agreement between measured and calculated curves. An optical model, that is developed in this work, allows the calculation of the reflection, transmission and depth-resolved absorption of planar multilayer structures, thereby accounting for both, coherent specular light as well as incoherent diffusely scattered radiation. The model is verified by reproducing the spectra measured for a free standing SPS sample.

Electrical conductance measurements on SPS films yield a resistivity that is slightly higher than the bulk conductance of the substrate , however, still much lower compared to the as-etched state, which is again explained by the larger structure size of SPS compared to as-etched PS. Quantum efficiency analyses of pn-diodes made from SPS reveal how the minority carrier diffusion length in SPS tends to decrease if the internal surface area increases. Dangling bonds and other defects located at the large internal surface of the pore walls act as recombination centres and reduce the carrier diffusion length.

In addition to the characterisation of SPS, this work presents a novel approach for the formation of an emitter in PSI solar cells and describes its successful technological implementation. This "autodiffusion" process utilises dopant out-diffusion from porous silicon to form a highly doped region in the epitaxial film of a PSI solar cell. An independently confirmed energy conversion efficiency of 14.5 % is achieved with a solar cell that features an emitter formed by autodiffusion.

Finally, one-dimensional device simulations of planar non-textured PSI solar cells indicate that the enhanced optical confinement due to light scattering by the pores in the residual SPS layer surpasses the recombination losses in the SPS region yielding an increased efficiency for PSI cells with an appropriate SPS rear reflector.

Kurzzusammenfassung

Das Thema dieser Arbeit ist die Charakterisierung von gesintertem porösem Silizium sowie die Fortentwicklung von monokristallinen Silizium Dünnschicht-Solarzellen aus dem Porösen Silizium Prozess (PSI Prozess). Die Herstellung solcher Solarzellen erfolgt durch das epitaktische Wachsen einer Siliziumschicht auf einem monokristallinen Silizium-Wachstumssubstrat, welches an seiner Oberfläche eine Schicht aus porösem Silizium (PS) aufweist. Die thermische Aktivierung während des epitaktischen Wachsens bewirkt eine Umformung der porösen Schicht, die mit einer mechanischen Schwächung einhergeht. Die sich so ausbildende Sollbruchstelle ermöglicht anschließend den Transfer der Dünnschicht-Solarzelle auf ein zweites Trägersubstrat. Beim Ablösen der Epitaxieschicht vom Wachstumssubstrat verbleibt ein Rest *gesinterten* porösen Siliziums (SPS) an der Rückseite der Solarzelle. Bisher wurden die physikalischen Eigenschaften dieser verbleibenden Schicht und ihr Einfluss auf die PSI Solarzelle wenig untersucht. Diese Arbeit hat eine umfassende Bestimmung der physikalischen Eigenschaften von SPS, speziell seiner thermischen, optischen und elektrischen Eigenschaften zum Ziel.

Aufgrund der Fragilität der analysierten freitragenden SPS Schichten sollte ein berührungsloses Messverfahren zur Bestimmung der thermischen Eigenschaften verwendet werden. Eine solche thermische Charakterisierungsmethode wird auf der Basis von lock-in Thermographie entwickelt und ihre Funktionsweise experimentell bestätigt. Die Anwendung des Verfahrens auf SPS Schichten zeigt, dass die Abhängigkeit der Wärmeleitfähigkeit von der Porosität einem Potenzgesetz dritter Ordnung folgt, in Übereinstimmung mit dem Looyenga Modell. Im Ausgangs- wie im gesinterten Zustand von PS wird die Wärmeleitfähigkeit durch Phononenstreuung an den Porenwänden reduziert. Allerdings ist aufgrund der größeren Strukturgröße nach dem Sintern dieser Effekt im gesinterten Material schwächer ausgeprägt als im Ausgangszustand.

Der effektive Brechungsindex von SPS stimmt mit Vorhersagen von Modellen für effektive Medien überein, während Lichtstreuung an den sphärischen Poren in SPS durch Mie's Streutheorie beschrieben wird. Eine Analyse des gemessenen Streukoeffizienten zeigt, dass der geringe Abstand der Poren in SPS die Streueffizienz der einzelnen Streuer reduziert. Die hohe Porendichte wird berücksichtigt, indem für die Berechnung des Streukoeffizienten der zuvor gemessene effektive Brechungsindex von SPS verwendet wird. Dies führt zu einer Übereinstimmung von gemessenem und berechnetem Streukoeffizienten. Im Rahmen dieser Arbeit wird ein optisches Modell entwickelt, welches die Reflektion, Transmission und die tiefen-aufgelöste Absorption von planaren Mehrschicht-Strukturen berechnet. Dieses Modell berücksichtigt sowohl die parallel zur Einfallsrichtung propagierende kohärente Strahlung als auch inkohärentes diffus gestreutes Licht. Optische Messungen an freitragenden SPS Schichten bestätigen die Vorhersagen des Modells.

Messungen der elektrischen Leitfähigkeit von SPS Schichten zeigen, dass der spezifische Widerstand von SPS gegenüber dem des Ausgangssubstrats leicht erhöht ist. Im Vergleich zum ungesinterten Zustand von PS nach der Herstellung, weisst SPS jedoch einen sehr geringen spezifischen Widerstand auf, was der gröberen Mikrostruktur zuzuschreiben ist. Quanteneffizienz-Analysen von pn-Dioden aus SPS zeigen, wie Rekombination über unabgesättigte Bindungen und andere Defekte, die sich an der großen inneren Oberfläche der Porenwände befinden, die Diffusionslänge der Minoritätsladungsträger in SPS reduziert.

Über die Charakterisierung von SPS hinaus wird in dieser Arbeit ein neues Verfahren zur Emitter-Diffusion in PSI Solarzellen vorgestellt und technologisch umgesetzt. Dieser ,,Autodiffusions"-Prozess nutzt die Ausdiffusion von Dotierstoffen aus dem porösen Silizium zur Bildung eines hochdotierten Bereichs in der Epitaxieschicht einer PSI Solarzelle. Eine mittels Autodiffusion hergestellte PSI Solarzelle erreicht einen unabhängig bestätigten Wirkungsgrad von 14.5 %.

Abschließend zeigen eindimensionale Simulationsrechnungen, dass für planare PSI Solarzellen ohne Oberflächentextur die erhöhte Absorption aufgrund von Lichtstreuung an den Poren in der verbleibenden SPS Schicht die Rekombinationsverluste in selbiger Schicht übersteigt, was zu einem erhöhten Wirkungsgrad von PSI Solarzellen mit einem angepassten SPS Rückseitenreflektor führt.

Keywords: sintered porous silicon, layer-transfer, silicon thin-film solar cells
Schlagwörter: gesintertes poröses Silizium, Schichttransfer, Silizium-Dünnschicht-Solarzellen

Contents

List of symbols

Symbol	Unit	Description
a	$\mathrm{m^2\,s^{-1}}$	thermal diffusivity
$A(x)$	$\mathrm{m^{-1}}$	absorption profile
$A_{\mathrm{diff}}(x)$	$\mathrm{m^{-1}}$	diffuse absorption profile
A_{etch}	$\mathrm{m^2}$	etched area
A_{int}	$\mathrm{m^{-1}}$	internal surface to volume ratio
A_{pore}	$\mathrm{m^2}$	cross sectional area of a pore
$A_{\mathrm{spec}}(x)$	$\mathrm{m^{-1}}$	specular absorption profile
B	m	distance, width
c	m/s	speed of light in vacuum
c_{p}	$\mathrm{J\,Kg^{-1}\,K^{-1}}$	specific heat
d	m	pore diameter
d_{avg}	m	average pore diameter
d_{med}	m	median diameter of lognormal distribution
d_{res}	m	resolution threshold diameter
D	$\mathrm{m^2\,s^{-1}}$	diffusion constant
$\hat{D}$		re-distribution operator
E		reduced electric field strength
f		fraction
$f(r)$	$\mathrm{m^{-1}}$	pore size distribution function
$F(x)$		exponential integral function
g_{sca}		Mie scattering asymmetry parameter
$g(\chi)$		spectral density function
g_0		percolation strength
G	$\mathrm{m^{-3}\,s^{-1}}$	photogeneration rate
G_{epi}	$\mathrm{m^{-2}\,s^{-1}}$	cumulated photogeneration within epitaxial layer
h	$\mathrm{J\,s}$	Planck's constant
$H_j^{(2)}$		Bessel functions of the third kind (Hankel functions)
I	A	electric current
I		reduced light intensity
$I(x)$	$\mathrm{m^{-1}}$	reduced light intensity profile
J	$\mathrm{A\,m^{-2}}$	electric current density
$J_{0,\mathrm{f}}$	$\mathrm{A\,m^{-2}}$	front surface recombination current density
$J_{0,\mathrm{r}}$	$\mathrm{A\,m^{-2}}$	rear surface recombination current density
J_{etch}	$\mathrm{A\,m^{-2}}$	etching current density

Symbol	Unit	Description
J_{SC}	$\mathrm{A\,m^{-2}}$	short-circuit current density
J_j		Bessel functions of the first kind
k_{B}	$\mathrm{J\,K^{-1}}$	Boltzmann constant
L	m	length, carrier diffusion length
L_{bulk}	m	bulk carrier diffusion length
L_{eff}	m	effective carrier diffusion length
L_{α}	m	absorption length
$L_{\alpha,\mathrm{eff}}$	m	effective absorption length
L_{γ}	m	scattering length
m		integer, ordinal number
m	Kg	mass
$\hat{M}$		transfer matrix
n		real part of refractive index
$\tilde{n}$		complex refractive index
n_{e}	$\mathrm{m^{-3}}$	electron concentration
n_{i}	$\mathrm{m^{-3}}$	intrinsic carrier concentration
N		number of layers in multilayer stack
N_{A}	$\mathrm{m^{-3}}$	acceptor dopant concentration
N_{D}	$\mathrm{m^{-3}}$	donor dopant concentration
N_{eff}	$\mathrm{m^{-3}}$	effective dopant concentration
N_{pore}	$\mathrm{m^{-3}}$	pore density (number of pores per unit volume)
N_{surf}	$\mathrm{m^{-3}}$	dopant concentration at surface
p	$\mathrm{m^{-3}}$	hole concentration
P		porosity
P_{Φ}	W	spectral power
q	C	elementary charge
Q	$\mathrm{W\,m^{-1}}$	heating power per unit length
Q_{sca}		Mie scattering efficiency
r	m	pore radius
r_{etch}	$\mathrm{m\,s^{-1}}$	etching rate for PS formation
R		reflection
R_{diff}		diffuse reflection
R_{sheet}	Ω	sheet resistance
R_{spec}		specular reflection

Symbol	Unit	Description
R_{F}		Fresnel interface reflection
$\hat{R}_{\mathrm{int}}$	m^{-1}	internal reflection operator
S		signal
S_{0°		IR camera in-phase signal
S_{-90°		IR camera -90°-phase shifted signal
S_{f}	$\mathrm{m\,s}^{-1}$	front surface recombination velocity
S_{r}	$\mathrm{m\,s}^{-1}$	rear surface recombination velocity
S_{tot}	$\mathrm{m\,s}^{-1}$	sum of front and rear surface recombination velocity
$\hat{S}$	m^{-1}	re-scattering operator
t	s	time
T	K	temperature
T		transmission
$\hat{T}$		transfer matrix
T_0	K	temperature amplitude
T_{diff}		diffuse transmission
T_{spec}		specular transmission
T_{tot}	K	sum of oscillating and static temperature
T_{F}		Fresnel interface transmission
V	V	voltage
V_{OC}	V	open-circuit voltage
V_{pore}	m^3	pore volume
w		refractive index ratio in Mie's theory
W	m	thickness, width
W_{opt}	m	optical thickness
x	m	depth, spatial coordinate
y	m	spatial coordinate
z	m	spatial coordinate
z		Mie size parameter

Symbol	Unit	Description
α	$\mathrm{m^{-1}}$	absorption coefficient
β	$\mathrm{W\,m^{-2}\,K^{-1}}$	heat transfer coefficient
β_0	$\mathrm{m^{-1}}$	Fourier coefficient for the fundamental mode
χ		integration variable
ϵ		relative dielectric function
ϕ		phase angle
ϕ_k		phase factor
Φ	$\mathrm{s^{-1}}$	photon flux
$\Phi(\lambda)$	$\mathrm{m^{-3}\,s^{-1}}$	spectral photon flux density
γ	$\mathrm{m^{-1}}$	scattering coefficient
η		solar cell energy conversion efficiency
κ		extinction coefficient
λ	m	wavelength
Λ_a	m	thermal diffusion length for the amplitude
Λ_p	m	thermal diffusion length for the phase
μ	$\mathrm{W\,m^{-1}\,K^{-1}}$	thermal conductivity
μ_e	$\mathrm{m^2\,V^{-1}\,s^{-1}}$	electron mobility
μ_h	$\mathrm{m^2\,V^{-1}\,s^{-1}}$	hole mobility
μ_s	$\mathrm{W\,m^{-1}\,K^{-1}}$	thermal conductivity of the solid phase
ν_0	$\mathrm{s^{-1}}$	infrared camera frame rate
ν_li	$\mathrm{s^{-1}}$	lock-in frequency
θ		angular coordinate
ρ	$\Omega\,\mathrm{m}$	resistivity
ρ_m	$\mathrm{Kg\,m^{-3}}$	mass density
$\rho_\mathrm{s},\ \rho_\mathrm{p}$		Fresnel amplitude reflection coefficients
ρ_{jk}		interface amplitude reflection coefficient
σ		width of lognormal distribution
σ_avg		averaged deviation
σ_sheet	Ω^{-1}	sheet conductance
τ_bulk	s	bulk carrier lifetime
τ_eff	s	effective carrier lifetime
τ_{jk}		interface amplitude transmission coefficient
ω	$\mathrm{s^{-1}}$	angular frequency
ξ_j, ψ_j		Mie scattering functions

List of abbreviations

Abbreviation	Description
a-Si	amorphous silicon
AC	alternating current
AM1.5G	Air Mass 1.5 Global (spectrum)
ARC	anti-reflection coating
BSF	back surface field
CZ	Czochralski (silicon)
CVD	chemical vapour deposition
DC	direct current
DR	depletion region
EQE	external quantum efficiency
FC	free-carrier
FF	fill factor
FSF	front surface field
H_2	hydrogen gas
HF	hydrofluoric acid
IQE	internal quantum efficiency
IR	infrared
KOH	potassium hydroxide
MIS	metal-insulator semiconductor
MW-PCD	microwave-detected photoconductance decay
PC1D	semiconductor device simulation program
PECVD	plasma-enhanced chemical vapour deposition
PEEK	polyetheretherketone
$POCl_3$	phosphorus oxychloride
PP	polypropylene
PS	porous silicon
PSI	Porous Silicon Process (layer-transfer technique)
PTFE	polytetrafluoroethylene
RF	radio-frequency
SCR	space charge region
SEM	scanning electron microscope
SiN_x	amorphous silicon nitride
SPS	sintered porous silicon
TEM	transmission electron microscope

1 Introduction

In 1956 Uhlir accidentally discovered porous silicon (PS) while performing electropolishing experiments of silicon in hydrofluoric acid [1]. Since he looked for a means to smoothen the surface of the silicon substrates, the observed formation of a brownish film was an unwanted effect and he published the results in a brief technical note [1]. Uhlir's colleague Turner then further investigated this phenomenon in more detail [2, 3] and a few years later, Archer obtained similar films by electroless chemical etching of silicon in a mixture of hydrofluoric acid and nitric acid [4]. However, it took almost twenty years until Watanabe et al. revealed the porous morphology of these films in the seventies [5]. In 1990 Canham reported on visible photolumiescence from PS at room temperature [6] and suddenly, the interest in this material increased drastically, since it seemed to be a promising candidate for silicon-based optoelectronic devices [7, 8].

Besides applications in optoelectronics and other fields, PS has been successfully applied as a sacrificial layer for the fabrication of silicon thin-film devices [9–11]. These layer-transfer processes and related technologies from the microelectronic field utilise high temperature processing for the device fabrication. When PS is exposed to high temperatures, the thermal activation induces a drastic change in the microstructure of this material. In fact, structural changes in PS emerge at temperatures as low as 350 °C [12]. Due to the described morphological alteration, the thermally annealed or sintered state of PS exhibits completely different physical properties compared to the as-prepared material. However, almost all investigations on PS deal with the as-prepared state and only a few articles focus on sintered porous silicon (SPS).

The application studied in this work are silicon thin-film solar cells from the Porous Silicon Process (PSI process) [11, 13, 14]. For this layer-transfer process, a silicon film is epitaxially deposited onto a monocrystalline silicon growth substrate. The growth substrate exhibits a porous surface layer that realises a predetermined breaking point, which enables the subsequent transfer of the thin-film device to a second low-cost carrier substrate, as illustrated in Fig. 1.1. After the separation of the solar cell from the growth substrate, a residual layer of SPS remains appended to the rear side of the epitaxial film.

Sintered porous silicon constitutes a key tool for the described process. Firstly, it plays two important roles during the device fabrication. On the one hand, the sintered porous layer serves as a seed layer for the epitaxial growth of the monocrystalline silicon film. On the other hand, its mechanical properties control the subsequent transfer of the film to a device carrier. Secondly, the optical and electrical properties of the residual SPS layer affect the performance of the finished thin-film solar cell. Thus, a detailed characterisation of SPS is essential for both, the development of the PSI fabrication process as well as for the enhancement of the conversion efficiency of PSI solar cells.

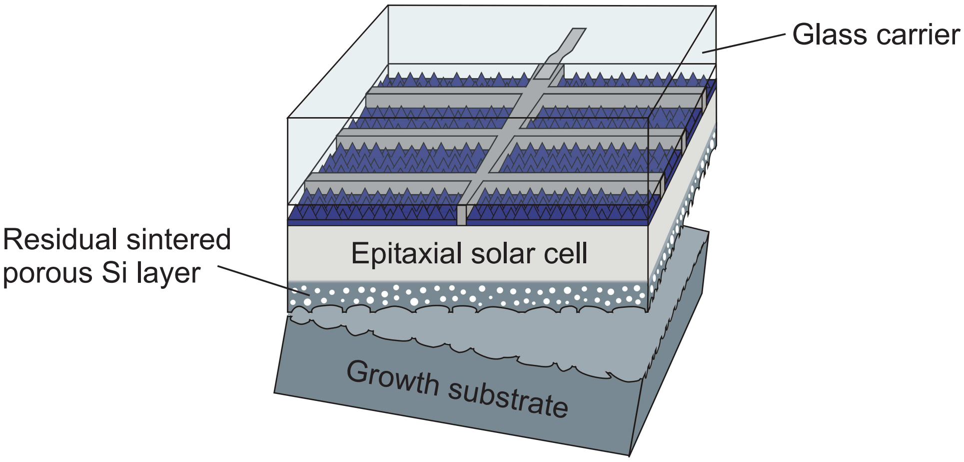

Figure 1.1. Fabrication of silicon thin-film solar cells by means of the Porous Silicon Process (PSI process). The epitaxially grown solar cell is attached to a glass carrier and separated from the growth substrate. Thereby, a residual layer of sintered porous silicon remains attached to the rear side of the cell.

This thesis analyses the sintered state of PS and focusses on its thermal, optical and electrical properties. Moreover, the present work deals with the fabrication of PSI solar cells and investigates the impact of the residual SPS layer on the efficiency of these devices.

Chapter 2 provides the physical and technological background for the electrochemical formation of porous silicon and its rearrangement during sintering. Moreover, a detailed description of the PSI process is given.

Chapter 3 analyses the thermal properties of SPS, which are important for PS-based sensors and thermoelectric devices. This analysis requires the development of a non-contact thermal characterisation technique. Effective medium theory describes the dependence of the thermophysical properties on the porosity.

In Chapter 4, the refractive index and the scattering coefficient of SPS are deduced from optical measurements and compared with the predictions of effective medium models and Mie's scattering theory. Moreover, an optical model is developed that describes the propagation of the specular light as well as the distribution of diffuse scattered radiation within the sample.

Chapter 5 investigates the effect of the porosity and the microstructure of SPS films on their electrical conductivity and the carrier diffusion length in this material.

Chapter 6 presents a novel method for emitter formation in PSI solar cells. This "autodiffusion" approach utilises the out-diffusion of dopant atoms from the growth substrate into the epitaxial layer of a PSI solar cell, thereby forming a highly doped region.

Finally, in Chapter 7 one-dimensional device simulations reveal the impact of two competing phenomena in the residual SPS layer on the cell efficiency. These two effects are light scattering on the one hand and carrier recombination on the other hand.

2 Review on the formation and sintering of porous silicon

The present thesis focusses on the properties of sintered porous silicon and on the PSI process [11], which is a layer-transfer technique based on sintered porous silicon, as outlined in the previous chapter. Therefore, the following sections review what is known in the literature on the formation of porous silicon by electrochemical etching and its reorganisation during high temperature annealing, as well as some technological details of the PSI process.

2.1 Formation by electrochemical etching

Porous silicon forms during the electrochemical anodisation of silicon substrates in hydrofluoric acid (HF) containing solutions when silicon atoms from the surface of the substrate dissolve in the electrolyte. Under certain conditions, not all atoms of the macroscopic surface are removed and a porous layer with a sponge-like microstructure remains while the etching front proceeds deeper into the substrate. This layer consists of two phases, a network of branched pores filled with the electrolyte and the remaining network of silicon bridges. This porous matrix still exhibits the same crystalline lattice structure as the substrate, since the etching process only removes a certain fraction of the atoms. An important quantity is the porosity which denotes the volume fraction of the removed material, that is, the volume of the pores divided by the total considered volume. Depending on the anodisation conditions, different porosities, pore sizes and morphologies are obtained. Porous materials are classified according to the characteristic size of the pores: A structure is referred to as *microporous* if the pore diameter is below 2 nm, *mesoporous* for diameters between 2 nm and 50 nm and *macroporous* for pore diameters larger than 50 nm. Lehmann provides a detailed overview on the formation of porous silicon and its physical properties [15]. The following sections briefly describe the current-voltage characteristics of the semiconductor-electrolyte junction, the chemistry and reaction mechanisms of the PS formation process, as well as the etching cell that is used in this work.

2.1.1 Current-voltage characteristics

Figure 2.1 qualitatively illustrates the current-voltage curve for moderately doped p-type and n-type silicon (doping level below $10^{18}\,\mathrm{cm}^{-3}$) in HF containing electrolytes after Föll [16]. The exact shape of the curve depends on the anodisation conditions as for example the doping level of the silicon electrode, the electrolyte composition and, if the electrode

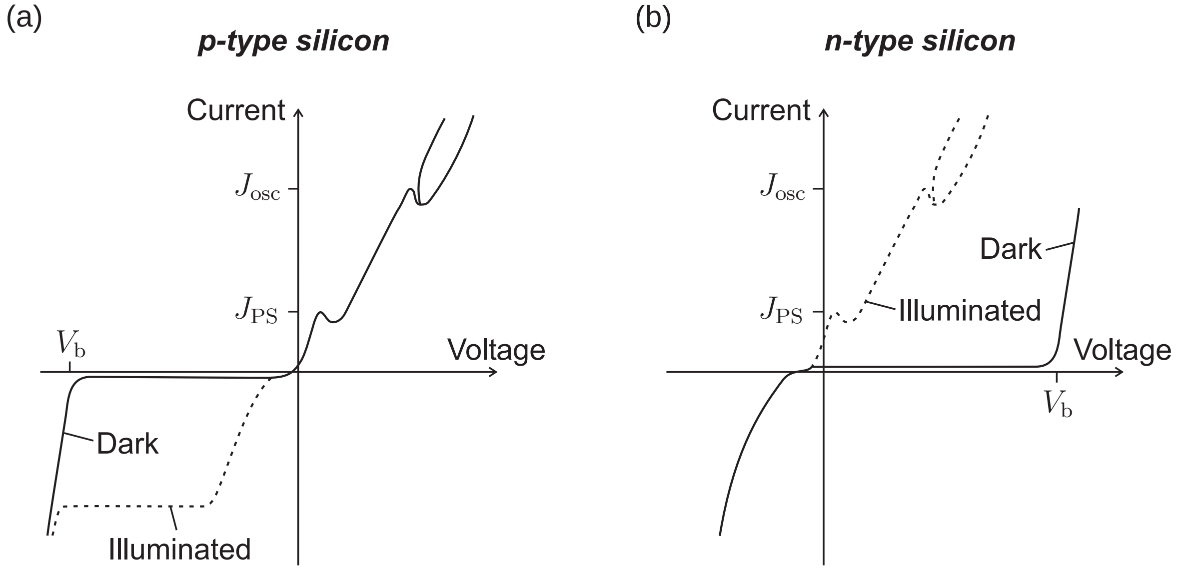

Figure 2.1. Qualitative current-voltage characteristics for moderately doped p-type and n-type silicon electrodes in HF solutions after Ref. 16, 17.

is illuminated, the illumination intensity. Apparently, if the charge transfer is limited by the silicon electrode, the semiconductor-electrolyte junction behaves similar to a rectifying semiconductor-metal junction (Schottky diode). For example under reverse bias (negative bias for p-type and positive bias for n-type silicon) and in the dark, only a small leakage current is observed and breakthrough occurs at a certain voltage V_{b}.

In contrast, the chemical reactions at the surface are independent of the doping type. Silicon is stable in the cathodic regime (negative bias) and hydrogen is formed due to the reduction of water. Under anodic conditions (positive bias) silicon dissolves. In this regime, the characteristics of p-type electrodes in the dark and illuminated n-type electrodes are similar. In both cases the current-voltage curve features two current maxima at J_{PS} and J_{osc} and branches out beyond J_{osc}, where the system shows oscillations.

The formation of porous silicon occurs in the anodic regime at current densities below the critical current density J_{PS} of the first current maximum. The details of the formation mechanism are discussed in Sections 2.1.2 and 2.1.3 below. For $J < J_{\mathrm{PS}}$, the current-voltage curve for p-type electrodes resembles the exponential characteristics of a Schottky diode [18, 19], whereas n-type electrodes are under reverse bias and only a small dark current density is observed [20, 21]. Thus, for moderately doped n-type substrates and an anodic bias below the break through voltage V_{b}, illumination is required to establish a significant anodic current [16, 22–24]. However, for highly doped n-type substrates with $N_{\mathrm{D}} > 10^{18}\,\mathrm{cm}^{-3}$, the width of the space charge region is sufficiently reduced to enable the charge carriers to tunnel through the reverse-biased Schottky barrier. This effect permits the formation of meso PS films on highly doped n-type substrates without the application of illumination [21, 25–28].

Current densities between J_{PS} and the second maximum at J_{osc} yield a polished mirror-like surface instead of a porous layer. This so-called electropolishing process is the result of the formation of an intermediate anodic oxide film and its subsequent chemical dissolution in HF [2, 29].

If the current density exceeds J_{osc} oscillations emerge for both potentostatic and galvanostatic conditions [2, 30, 31]. This is illustrated by the splitting of the current-voltage curve in Fig. 2.1. The origin of these oscillations is still under discussion, however, it seems to be related to the formation of two kinds of oxides, a dense and a soft one, where the latter is periodically formed and dissolved [31–36].

2.1.2 Dissolution reaction

Two reaction pathways for the electrochemical dissolution of silicon in HF are discussed in the literature [3, 37–41]. The divalent reaction

$$\mathrm{Si} + 4\mathrm{HF}_2^- + \mathrm{h}^+ \rightarrow \mathrm{SiF}_6^{2-} + 2\mathrm{HF} + \mathrm{H}_2 + \mathrm{e}^- \tag{2.1}$$

is proposed for anodic currents below the critical current density J_{PS}. In this regime PS formation takes place and gaseous hydrogen evolves. For anodic currents exceeding J_{PS}, the tetravalent mechanism

$$\mathrm{Si} + 2\mathrm{HF}_2^- + 2\mathrm{HF} + 4\mathrm{h}^+ \rightarrow \mathrm{SiF}_6^{2-} + 4\mathrm{H}^+ \tag{2.2}$$

dominates leading to electropolishing instead of pore formation. Reaction (2.2) summarises the above mentioned two step process consisting of the formation of a thin oxide layer which is subsequently dissolved in HF. No hydrogen evolution is observed in this case.

Figure 2.2 schematically illustrates the proposed reaction mechanism for the divalent reaction (2.1). Starting with a hydrogen-terminated surface [42], a hole from the bulk of the electrode approaches the surface where HF_2^- ions are present, which enables the nucleophilic substitution of a hydrogen atom by a fluorine atom (step 1 in Fig. 2.2). This is the rate-limiting step of the reaction chain and responsible for the formation of the porous structure, which is discussed in more detail in the next section. The reaction rate scales with the applied current, since the dissolution is accomplished by charge transfer through the interface.

In steps 2 and 3, the second hydrogen atom is substituted under injection of an electron and a volatile H_2 molecule is formed. The Si−F bonds polarise the two remaining silicon back bonds which are then attacked by HF_2^- ions (steps 4 and 5). Finally, in step 6 a SiF_4 molecule dissolves and the silicon surface is saturated with hydrogen. By binding two F^- ions, the dissolved SiF_4 molecule reacts to SiF_6^{2-}.

Besides electrochemical anodisation, another way of forming PS are so-called stain etching or chemical etching processes [3, 4, 43, 44]. In this case, no external currents are applied during etching. Instead, the etching solution contains an oxidising agent, as for example

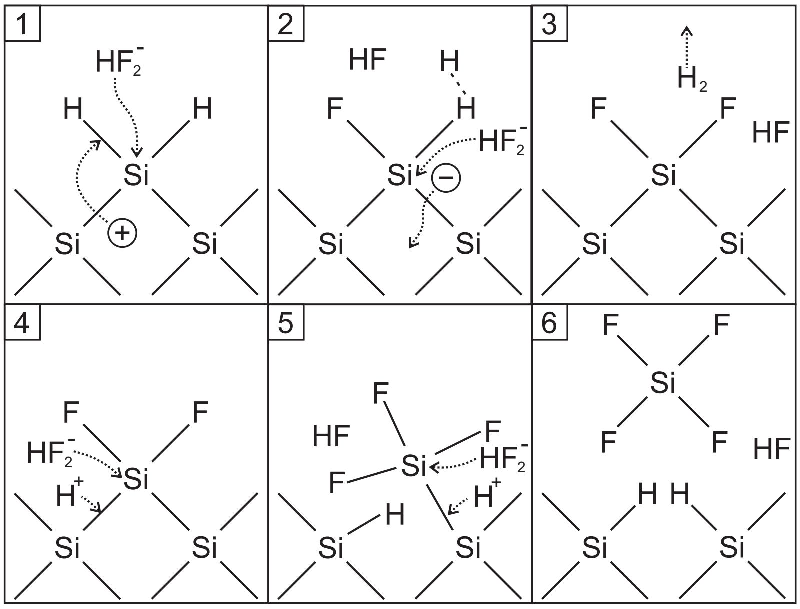

Figure 2.2. Reaction mechanism for the divalent dissolution of silicon in HF after Eq. (2.2) as proposed by Lehmann and Gösele [39].

nitric acid, which provides the holes that are required for the dissolution reactions (2.1) and (2.2). However, electrochemical etching is more frequently used, since the anodisation technique allows a better process control and reproducibility compared to chemical etching.

2.1.3 Pore wall passivation mechanisms

The formation of a porous structure requires a mechanism that locally stops the dissolution reaction at the pore walls, whereas the etching process continues at the pore tips. Due to this mechanism, the silicon bridges of the porous skeleton remain undissolved, while the active etching front moves deeper into the substrate. This phenomenon is referred to as a *passivation* of the pore walls. As outlined above, holes from the bulk of the semiconductor are consumed during the anodic dissolution of silicon. Thus, most models attribute the described active-passive transition of the pore walls to the depletion of holes in the porous skeleton. The two most promising candidates for the passivation mechanism are quantum confinement and the formation of a space charge region.

The energy of charge carriers increases if they are confined to a small volume. In the case of a semiconductor, this quantum confinement widens the band gap since the energy of both electrons and holes is increased [45–48]. The higher band gap hinders the charge carriers from entering the porous structure, which causes the depletion of holes in the porous region. The porous structure is not further dissolved, whereas the reaction continues at the pore tips where holes still are available. The confinement effect emerges for structure sizes of a few nm and is thus proposed to cause the fine structure observed in microporous silicon [39].

Another mechanism that could stop the dissolution reaction is the presence of a space charge region (SCR). Such a carrier-depleted layer could still exist, although a p-type silicon electrode is under forward bias in the anodic regime, as described in Section 2.1.1. In fact, capacity-voltage measurements indicated the presence of a depletion region during PS formation, independent of doping type and density of the silicon substrate [19]. Moreover, several experiments showed that the doping density of the substrate, and thus the width of the SCR, correlates with the size of the remaining silicon bridges in mesoporous silicon [27] and with the distance of macropores in the macroporous case [49]. However, in contrast to quantum confinement, a SCR covers the whole surface and is thus also present at the bottom of the pores. Therefore some mechanism has to break the passivation at the pore tips. Several effects are qualified for this so-called passivity breakdown.

Tunneling of charge carriers through the SCR is the proposed mechanism for the formation of mesoporous silicon on p^+-type and n^+-type substrates with doping densities above $10^{18}\,\mathrm{cm}^{-3}$. Depending on the radius of curvature at the pore tip, a bias of a few volts is sufficient to induce a significant tunnel current through the tip [27, 50]. Other suggested mechanisms are diffusion and thermoionic emission leading to macropore formation on p-type silicon with doping densities below $10^{16}\,\mathrm{cm}^{-3}$ [49], avalanche breakdown causing etch pits in moderately doped n-type silicon ($N_\mathrm{D} < 10^{18}\,\mathrm{cm}^{-3}$) [27] and the formation of macropores due to minority carrier collection generated by illumination or injection from p-type regions in moderately doped n-type substrates [23, 24].

2.1.4 Effect of the anodisation conditions

The anodisation conditions not only determine the porosity and the morphology of the fabricated PS films, they also affect the dynamics of the etching process, that is, the etching rate r_etch that denotes the speed at which the etching front proceeds into the bulk of the substrate. Basic process parameters are the applied current density, the crystal orientation and the doping type and density of the silicon substrate, the temperature and composition of the used electrolyte and the illumination intensity.

This work focusses on the formation of mesoporous silicon on p^+-type and n^+-type substrates in the dark. In this case, the most important parameters that affect the porosity and etching rate are the etching current density, the doping level of the substrate and the HF concentration of the applied electrolyte. The following relations were found for these three parameters [27, 37, 51–54].

Etching current density: With increasing current density both the etching rate and the porosity increase. The higher etching rate is a consequence of the enhanced current, since every charge transfer through the semiconductor-electrolyte interface is accompanied by the dissolution of silicon atoms. Moreover, the enhanced dissolution rate results in an increased porosity.

Substrate doping level: In the case of n^+-type silicon, the porosity increases with the doping density, whereas the etching rate reduces. A higher doping level reduces the width of the SCR and, in turn, the size of the residual silicon bridges yielding an increased porosity. Due to the higher porosity, more material has to be removed when the etching front proceeds a certain distance into the bulk. Thus, assuming a constant dissolution rate, the speed of the etching front reduces. Similar results are obtained for the anodisation of p^+-type silicon with doping densities in excess of $10^{18}\,\mathrm{cm}^{-3}$.

HF concentration: Increasing the HF concentration in the electrolyte results in a higher etching rate and a reduced porosity. The higher HF concentration enables a faster dissolution at the pore tips and, since dissolution is accomplished by charge transfer, a locally increased current density. Thus, for maintaining the macroscopic current density, the area of the pore tips reduces, yielding narrower pores and thus a lower porosity.

2.1.5 Etching setup and procedure

The electrochemical formation of porous silicon needs an etching cell that has to fulfil a number of different requirements. Since hydrofluoric acid is a hazardous substance, safe handling has a high priority. Moreover, the setup should allow to pass high currents through the sample and, eventually, feature adjustable illumination. To obtain PS films with a homogeneous thickness and porosity, the cell design has to assure a uniform distribution of the electric field over the whole sample surface. Reference 15 provides an overview on the most frequently used configurations.

The anodisation setup used in this work is a so-called double cell reactor, as illustrated in Fig. 2.3. The reactor consists of two chambers separated by a wall that features a circular opening. The etching cell is made from highly acid resistant material, such as polypropylene (PP), polyetheretherketone (PEEK) or polytetrafluoroethylene (PTFE). Each chamber contains a flat electrode that consists of platinum or other HF resistant conducting material. The substrate is placed in the anode chamber (left hand side in Fig. 2.3) in front of the opening. A seal covers the wafer rim and eliminates leakage currents around the wafer edge. When a current is applied, a porous layer forms on the side of the substrate that is facing the cathode. A tunnel, which is an extension of the circular opening into the cathode chamber, homogenises the electric field and allows the formation of uniform PS layers. An external power supply, that is controlled by a personal computer, forces a user-defined current through the cell (galvanostatic anodisation) and allows to apply a predefined current-time profile. All etching processes are performed in the dark, no illumination is applied.

The electrolyte usually contains HF in high concentrations and a wetting agent, as for example ethanol. The wetting agent not only increases the wettability of the substrate surface, it also provides the removal of the hydrogen bubbles that evolve during the dissolution process. Moreover, in contrast to aqueous solutions, ethanoic solutions infiltrate the pores, which increases the depth-uniformity of the PS layers.

In the described configuration, the anodised substrate is not in direct contact with the anode. Instead, the current flows from the anode via the electrolyte into the sample. For the shown polarity, the semiconductor electrolyte junction at the rear side of the substrate is reverse-biased for p-type substrates. Thus, only for highly doped substrates the charge

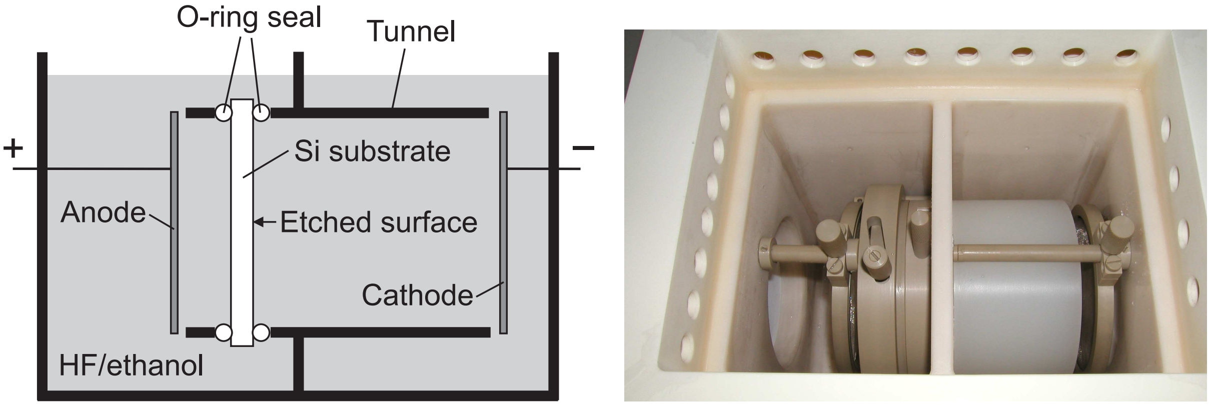

Figure 2.3. Schematic (left hand side) and photograph (right hand side) of the double cell reactor used for the anodisation of 4 inch-large silicon substrates in an HF/ethanol electrolyte.

carriers can tunnel through the Schottky barrier allowing a high current flow through the system. Lower doped substrates require an ohmic back contact or illumination and thus a different etching configuration, as for example described in Ref. 15.

The etching procedure starts with the mounting of the substrate in the etching cell, which is already filled with the electrolyte. The HF solution rapidly dissolves any native oxide and subsequently, the predefined current-time profile is applied. After dismounting the sample, rinsing in deionised water removes the residual electrolyte from pores. Finally, the sample is dried in a nitrogen flow.

2.1.6 Determination of the porosity and the etching rate

The porosity P and the etching rate r_{etch} are important parameters for the characterisation of the fabricated PS films and for the process control. These quantities are most frequently obtained by gravimetrical measurements, however, other techniques, as for example ellipsometry [55–58], might be used as well.

In this work, the gravimetric method is applied for the determination of the porosity and the etching rate. The porosity follows from weighing the sample before (m_1) and after (m_2) the etching process to determine the amount of Si removed during etching. Then a potassium hydroxide (KOH) solution bath selectively dissolves the PS layer and weighing the sample a third time yields the mass m_3 of the remaining substrate. The porosity then follows as

$$P = \frac{m_1 - m_2}{m_1 - m_3} \tag{2.3}$$

and the etching rate is

$$r_{\mathrm{etch}} = \frac{m_1 - m_3}{\rho_{\mathrm{m,Si}} \cdot A_{\mathrm{etch}} \cdot t}, \tag{2.4}$$

where $\rho_{\mathrm{m,Si}}$ denotes the mass density of silicon, A_{etch} the etched macroscopic area and t the etching time. It has to be mentioned that the described method yields an average porosity for the PS layer. In most cases, the analysed mesoporous films are homogeneous in depth, however, thick films might exhibit a porosity gradient. Hence, it is advisable to control the morphology of the etched films, for example by means of a scanning electron microscope (SEM).

2.2 Sintering of porous silicon

In a number of applications, the fabrication of PS devices requires processing at high temperatures. For example, when PS is used for layer-transfer processes, it is exposed to temperatures of up to 1100 °C during the epitaxial deposition of the silicon film. Although these temperatures are well below the melting point of 1412 °C [59], the increased thermal activation enables the silicon atoms to reconfigurate, which changes the morphology of the porous matrix. In fact, morphological changes in PS were observed already at temperatures as low as 350 °C [12].

In general, sintering denotes the thermal treatment of porous materials or powders below the melting point which is accompanied by structural changes. In the case of a crystalline solid, such as silicon, the crystal structure is preserved and the atoms solely exchange their positions within the crystal lattice. The described reorganisation leads to a reduction of the internal surface area and thus fewer but larger voids. The driving force for this rearrangement is the minimisation of the surface energy, which is linked to the internal surface area [12, 54, 60–63]. The thermal activation permits the atoms to diffuse to energetically more favourable positions, thereby reducing the surface to volume ratio.

2.2.1 Sintering mechanisms and phenomena

Three basic diffusion mechanisms are described in the literature for the reconfiguration during sintering of monocrystalline solids. Figure 2.4 illustrates these three mechanisms that are referred to as gas phase diffusion, solid-state diffusion and surface diffusion [64]. In the first case, atoms located at the internal surface evaporate, diffuse through the gaseous volume of the pore and precipitate again somewhere else at the pore walls. In the case of volume diffusion, vacancies that originate from the pore surfaces diffuse through the solid phase of the porous matrix. Finally, surface diffusion denotes the movement of atoms along the pore walls. All three processes are qualified to change the morphology of porous materials. However, for the reorganisation of PS, surface diffusion seems to be the dominant mechanism, as shown by experimental studies and simulations of Müller [54, 61].

Figure 2.5 presents cross sectional SEM images of a mesoporous sample after the anodisation (left hand side) and after H_2-annealing (right hand side). Starting from the

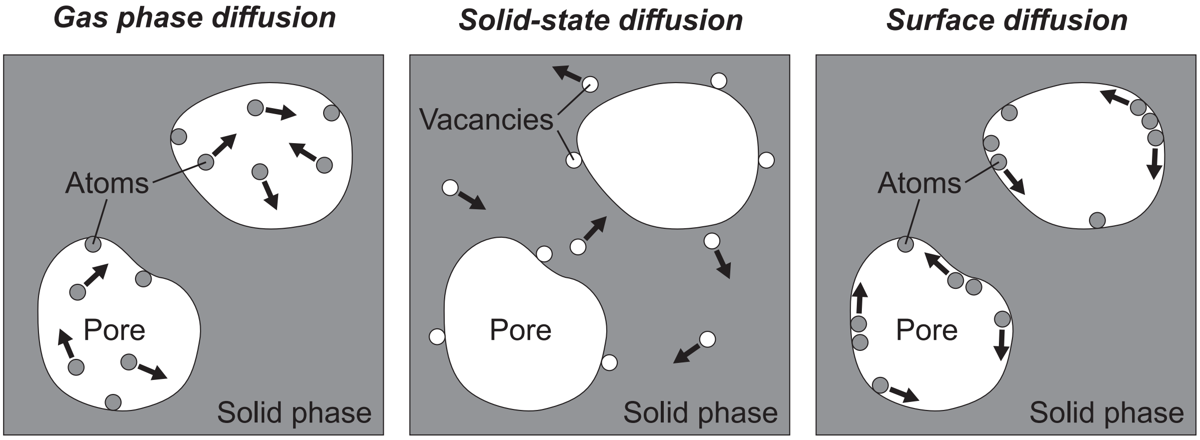

Figure 2.4. Illustration of the basic diffusion mechanisms responsible for the reconfiguration during sintering of monocrystalline solids (after Ref. 54).

open sponge-like configuration of the as-etched state, the sintering process proceeds in two phases [54, 64]. In the first step, the open dendritical structure closes to form isolated pores. During this transformation, adjacent pores merge into larger closed voids, the pore size increases from a few nm to several 10 nm and, consequently, the internal surface area reduces by one order of magnitude. The second phase describes the evolution of the frequency, size and shape of the closed pores. In this regime, the voids contract to a spherical shape and the average size increases only moderately with the sintering time [61, 63]. The size distribution of the ensemble of closed pores resembles the characteristics of a lognormal function [54, 61–63].

Besides a drastic increase of the pore size, the minimisation of the surface energy also induces facetting of the pores, as observable for some pores in Fig. 2.5 (right hand side). This effect emerges at high temperatures above 900 °C and increases with the annealing time [61–63]. The pore walls of a facetted pore predominantly constitute $\{111\}$ and $\{100\}$ planes, since these surfaces exhibit the lowest surface energy [65].

Another observed phenomenon is the closure of the macroscopic surface, as first reported by Labunov et al. [60, 66]. This closed surface layer forms during sintering, since the macroscopic surface acts as a sink for vacancies. Pores initially located close to the surface dissolve into the gas phase, leaving behind a several 10 nm thick monocrystalline layer free of pores [54, 62, 63]. The same effect is observed at interfaces between adjacent layers of different porosity. In this case, vacancies diffuse from the lowly into the highly porous region resulting in an increased porosity of the highly porous region and the formation of a thin pore-free layer at the interface. Both effects are important for the PSI layer-transfer technology, as described in Section 2.3 below. However, in the bulk of a homogeneous sample, no vacancy sink is available and the number of vacancies per volume is preserved. Therefore, the porosity of the sintered sample is equivalent to the initial porosity of the as-etched state.

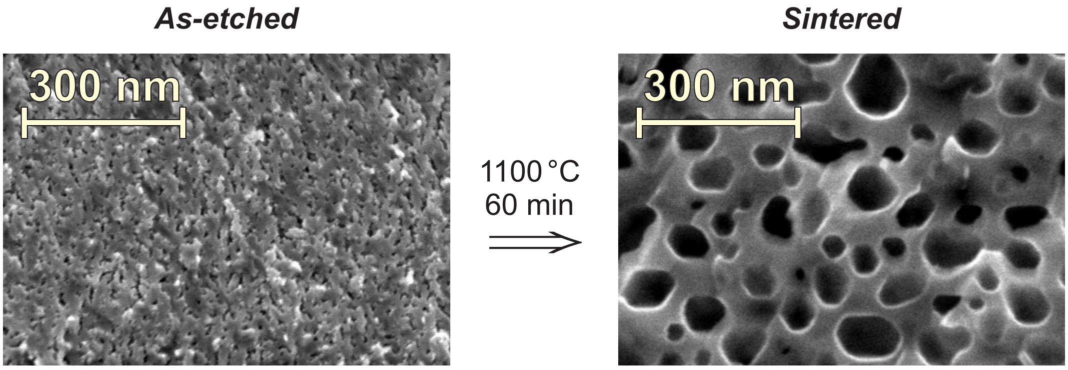

Figure 2.5. Cross sectional SEM images of a 21 % mesoporous silicon sample after the etching process (left hand side) and after annealing (right hand side) at 1100 °C for 60 minutes in a 1 bar H_2 atmosphere. The etching direction is from top to bottom. The substrate is (100)-oriented and highly boron-doped.

2.2.2 Sintering furnace and process

For the reorganisation of PS, the internal surface must be free of native oxide, since the presence of an oxide layer drastically reduces the mobility of the silicon atoms [67]. However, if the PS sample is exposed to air, the internal surface is rapidly oxidised. One way to remove this native oxide is to perform the sintering process in the reducing ambience of a hydrogen atmosphere. Such an atmosphere is also used for preconditioning in silicon epitaxy, since it prevents the formation of an oxide during the process.

In this work, a commercial bench top furnace (PEO 601 by ATV) is used for the sintering of PS samples. The system consists of a quartz tube that is heated by six externally mounted resistor wires. The process chamber is sufficiently large for up to 25 substrates of 4 inch diameter and reaches a maximum temperature of 1150 °C. A vacuum system permits the evacuation of the chamber which enables a fast exchange of the atmosphere. Two gas lines, one for pure nitrogen and the other one for pure hydrogen, allow to control the composition of the atmosphere in the chamber. All annealing processes are performed under atmospheric pressure.

After loading the samples into the tube, the standard sintering process starts with preheating to 100 °C. Meanwhile, the chamber is evacuated and subsequently filled with nitrogen. This process is repeated a second time to minimise the oxygen content in the chamber. After switching from nitrogen to hydrogen supply, the temperature is raised to the desired value, which takes approximately 15 minutes for a temperature of 1000 °C. When reaching the set-point, the heat control unit stabilises the temperature for a predefined duration, usually 30 to 120 minutes. For the cooling down, the system uses active cooling. At a temperature of 200 °C, the control unit initiates the nitrogen purge of the chamber and, subsequently, the samples are unloaded.

2.2.3 Determination of the pore size distribution

An analysis of the cross sectional SEM image of a sintered PS sample enables the determination of the pore size distribution function $f(r)$, where r is the pore radius. For this purpose, the image is first contrast-enhanced using conventional image processing software. Then an image evaluation program, as for example *ImageTool* [68], reads the modified images and identifies the pores as individual objects. The program calculates the equivalent diameter

$$d = \sqrt{\frac{4A_{\mathrm{pore}}}{\pi}} \tag{2.5}$$

that corresponds to the cross sectional area A_{pore} of each pore and classifies the resulting diameters. Figure 2.6 shows a typically measured size distribution for a 21 % porous sample (light grey bars).

The described image analysis systematically underestimates the pore diameter, since in the cross sectional view, most of the pores are not cut precisely through the centre. This stereological phenomenon was first described by Wicksell [69] and is sometimes denoted the “tomato salad problem” [70–73]. Several methods were developed for estimating the actual three-dimensional size distribution of spherical particles from the distribution of the circular profiles observed in a cross-sectional cut [74–77]. In this work, the Cruz-Orive algorithm [74] is used for reconstructing the three-dimensional distribution from the two-dimensional one that results from an analysis of the cross sectional SEM images. This correction procedure was already applied for analysing transmission electron microscope (TEM) images of SPS [62, 63].

The Cruz-Orive algorithm involves additional parameters, such as the thickness W of the analysed sample slide, the resolution threshold d_{res} and the capping angle θ_{c}, that quantifies the minimum observable fraction of a sliced sphere [74]. The thinner dark grey bars in Fig. 2.6 represent the corrected distribution. Due to the correction, the average pore diameter changes slightly from 41.2 nm to values between 41.1 nm to 41.6 nm assuming a slide thickness W between zero and 10 nm[1]. As apparent from Fig. 2.6, the stereological correction affects the appearance of the distribution by introducing oscillations around the maximum at $d \approx 30$ nm. However, as stated above, the average pore size increases only by a few percent. Furthermore, the parameters θ_{c} and W for the transformation are not precisely determined, which results in an uncertainty for the corrected distribution that is larger than the effect of the correction itself. Therefore, this work does not apply a stereological correction and the uncorrected distribution, as determined from the SEM images, is used instead.

After sintering, the distribution of the pore diameter d is of lognormal type, as mentioned in Section 2.2. Two parameters, the median d_{med} and the dimensionless width σ

---

[1] Usually, a slide thickness of zero is used for cross sectional images. But when collecting the SEM image, the electrons penetrate a few nm into the bulk of the sample. Consequently, higher values might be used as well.

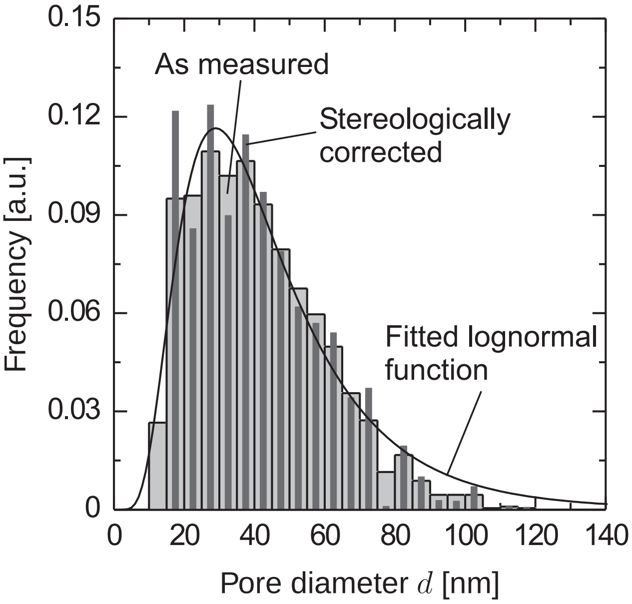

Figure 2.6. Pore size distribution in sintered PS as determined from the SEM image (light grey bars) and stereologically corrected (thinner dark grey bars). The correction algorithm assumes a slide thickness $W = 5\,\mathrm{nm}$, a resolution threshold of $d_{\mathrm{res}} = 15\,\mathrm{nm}$ and a capping angle of $\theta_{\mathrm{c}} = 0$. Negative frequencies are ignored. The solid line is a lognormal function fitted to the measured distribution.

characterise the normalised lognormal function

$$f_{\mathrm{lognorm}}(d) = \frac{1}{\sqrt{2\pi}\sigma d} \exp\left\{ - \left(\frac{\ln{(d/d_{\mathrm{med}})}}{\sqrt{2}\sigma} \right)^2 \right\}. \tag{2.6}$$

The average pore diameter of such a distribution follows from the median and the width as

$$d_{\mathrm{avg}} = d_{\mathrm{med}} \cdot \exp\left\{ \frac{\sigma^2}{2} \right\} \tag{2.7}$$

The solid line of Fig. 2.6 illustrates a lognormal function that is matched to the measured distribution (light grey bars). The curve complies with the measured distribution. Only for large diameters the lognormal function predicts higher frequencies. The median of the fitted distribution is $d_{\mathrm{med}} = 38.8\,\mathrm{nm}$ and the width $\sigma = 0.54$, corresponding to an average diameter of $d_{\mathrm{avg}} = 45.0\,\mathrm{nm}$. The latter lies above the average value of 41.2 nm for the measured distribution, due to the described overestimation of the frequency at large diameters.

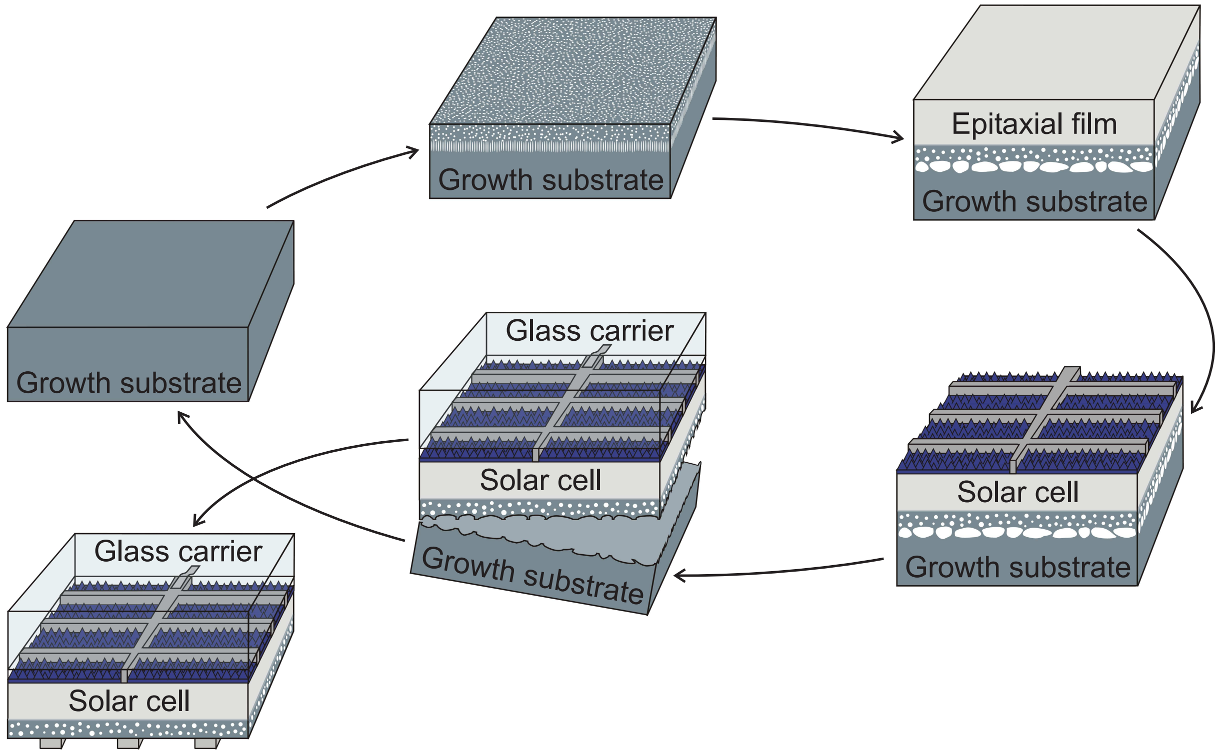

Figure 2.7. Illustration of the Porous Silicon Process (PSI process). The cycle starts with the porosification of the growth substrate followed by the epitaxial growth of the silicon thin-film, solar cell processing and the transfer of the fabricated thin-film device to a glass carrier. Finally, the growth substrate is cleaned and re-used for the next cycle.

2.3 Porous Silicon Process

The Porous Silicon Process (PSI process) [11, 13, 14] is a layer-transfer technique that allows the fabrication of monocrystalline silicon thin-films with a thickness varying from a few to several tens of micrometers. Figure 2.7 schematically illustrates the PSI process. Starting with a monocrystalline growth substrate (left hand side in Fig. 2.7), the first step consists of the formation of a porous double layer on the substrate surface by means of electrochemical etching. The upper layer of this double layer has a low porosity and is denoted the *starting layer*, whereas the second layer underneath is a highly porous *separation layer*. Section 2.3.1 below gives more information on the formation and the intent of this double layer structure. In the next step, the silicon thin-film is epitaxially deposited onto the porosified surface, for example by means of chemical vapour deposition (CVD). The crystal structure of the grown thin-film is monocrystalline as well, since the growth process uses a monocrystalline substrate. The high temperature during the growth of the silicon film induces the reconfiguration of the porous structure, as already discussed in Section 2.2.1. Due to this rearrangement, the highly porous separation layer mechanically weakens, which later enables the controlled lift-off of the epitaxial film. After the epitaxy, the front side of the solar cell device is processed, while the silicon film is still attached to the growth substrate. This allows the application of technologies commonly used for the fabrication of wafer-based solar cells, such as wet-chemical surface texturing and cleaning processes, diffusion for emitter formation and the deposition of metal contacts and dielectric coatings. Section 2.3.2 describes the solar cell fabrication process in more detail. In the next step, the device is fixed to a low-cost substrate, for example a glass carrier, and mechanical stress permits the separation of the epitaxial film from the growth substrate. Here, the mechanically weakened separation layer serves as a predetermined breaking point. The reorganised porous starting layer remains attached to the epitaxial film. After the transfer, the now accessible rear side of the device is processed which includes the formation of the rear contact. Finally, the growth substrate is cleaned and re-used for the next cycle.

The advantage of this process is the reduction of the silicon consumption per watt peak output power. From a physical point of view, solar cells from the PSI process have the potential to reach energy conversion efficiencies of 18.6 % with an epitaxial layer thickness of 25 µm [78], which is almost a factor of ten thinner than current wafer cells. Not only the thickness of the epitaxial layer, but also the number of cycles for the manifold use of the substrate determines the silicon consumption. Therefore, the re-use of the growth substrate is an important point of the PSI process. So far, the ten-fold application of the PSI cycle to the same substrate has been demonstrated [79] and, after an optimisation of the substrate cleaning procedure, only 12 µm of silicon were removed per cycle. However, in principle, there is no limit for the number of cycles, as long as the growth substrate is sufficiently thick to withstand the mechanical stress during the lift-off of the epitaxial film.

2.3.1 Porous double layer for layer-transfer

As outlined above, a porous double layer structure is used to enable the layer-transfer within the PSI process. This structure consists of the low porosity starting layer on top and the highly porous separation layer underneath the starting layer. The step in the porosity is realised by adjusting the etching current density during the anodisation process.

The PSI process commonly applies mesoporous double layers formed on p^+-type silicon substrates [11, 13, 14]. Figure 2.8 presents the dependence of the porosity P on the etching current density J_{etch} for (100)-oriented, boron-doped silicon wafers with a resistivity of 10 mΩcm. The electrolyte is an HF(50 %) : ethanol = 2:1 (by volume) mixture. For the formation of the starting layer, a low current density of 5 mA/cm^2 is applied resulting in a porosity of $P = 21\,\%$. An etching time of 100 seconds yields a homogeneous porous layer with a thickness of ∼1 µm. Abruptly increasing the current density to values between 150 and 250 mA/cm^2 creates the highly porous separation layer underneath the starting layer. This layer exhibits a thickness of several 100 nm and a porosity that exceeds 40 %. Table A.5 in Appendix A lists the etching parameters in detail. The porous starting layer is virtually not further dissolved during this current pulse, due to the above described pore wall passivation effect. Thus, the formation of the separation layer does hardly effect the porosity and morphology of the already etched starting layer. The left hand side of Fig. 2.9 shows an SEM image of such a double layer structure after the etching process.

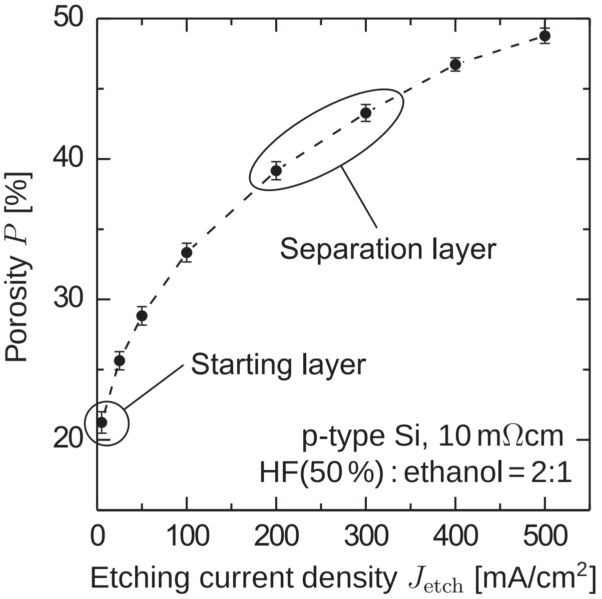

Figure 2.8. Dependence of the porosity P on the etching current density J_{etch} for the electrochemical etching of (100)-oriented 10 mΩcm p^+-type silicon substrates. An etching solution of HF(50 %) : ethanol = 2:1 (by volume) is applied. The two circles mark the parameter ranges for the formation of the starting and the separation layer. The dashed line serves to guide the eye.

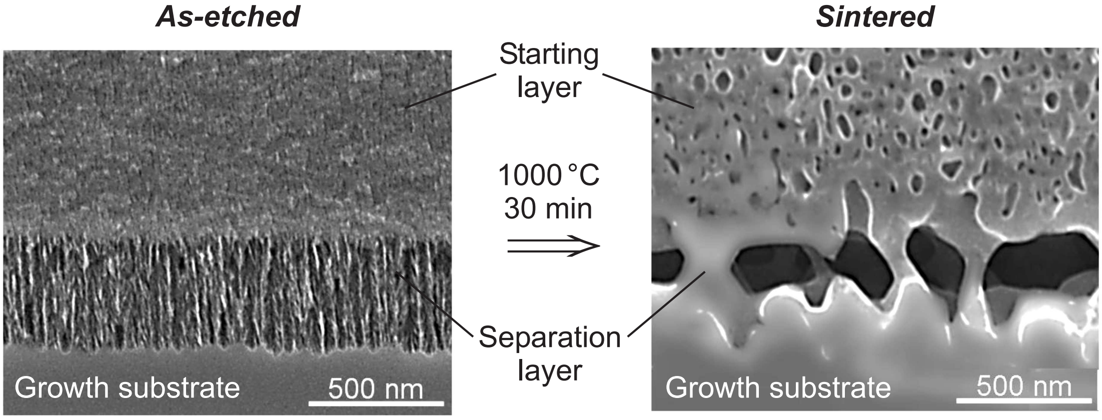

Figure 2.9. Cross sectional SEM images of a porous double layer in the as-etched state (left hand side) and after annealing (right hand side) at 1000 °C for 30 minutes in a 1 bar H_2 atmosphere. The images are taken from Ref. 54.

Subsequently to the porous layer formation, the silicon film is epitaxially grown by CVD at atmospheric pressure. The epitaxial growth process contains a 30 minute-long pre-annealing step (bake), which is performed at 1100 °C in a 1 bar H_2 atmosphere prior to the epitaxy [80]. During this annealing step, the porous layer reorganises and the outer surface closes to form an ideal seed layer for the subsequent epitaxy. This allows the growth of silicon films with a low defect density [81] and a carrier diffusion length that is large compared to the layer thickness [14].

Moreover, during sintering, the porosity of the separation layer increases due to the above described transport of material from the highly porous layer to the adjacent low porosity regions. Figure 2.9 presents an SEM image of the reorganised double layer (right hand side). The separation layer dissolves almost completely leaving only a few silicon bridges between the starting layer and the growth substrate. When applying mechanical forces, the silicon bridges break which allows to detach the starting layer and the epitaxial film from the growth substrate.

2.3.2 PSI thin-film solar cells

For the fabrication of silicon thin-film solar cells by the PSI process, the porous layer formation and the deposition of the silicon film are performed as described above. The epitaxially grown film usually consists of a 2 µm thick highly boron-doped p^+-type back surface field (BSF) layer and a several ten µm thick p-type base region on top. The BSF layer reduces the minority carrier concentration and thereby the recombination at the rear side of the device yielding a higher efficiency [82]. After the epitaxy, a wet chemical solution, for example a KOH/isopropyl mixture, textures the front side of the epitaxial film

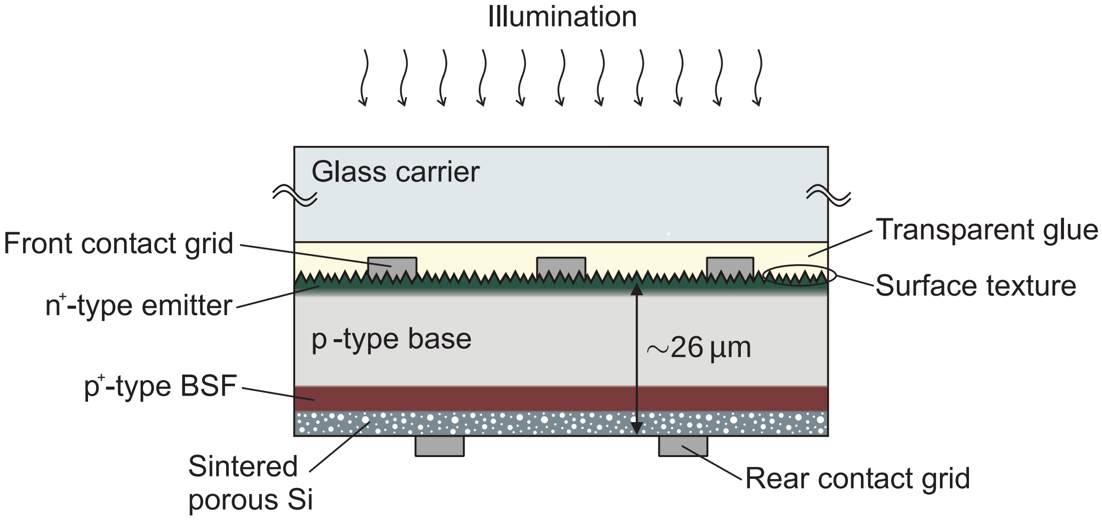

Figure 2.10. Schematics of a PSI thin-film solar cell with p-type base and a highly doped BSF for rear surface passivation. Here, the sintered porous silicon layer remains attached to the rear side of the cell.

by forming random pyramids on the surface. This surface texture reduces the reflection losses and increases the optical confinement of the cell. Subsequently, the n^+-type emitter is formed by means of solid source- or $POCl_3$-diffusion, followed by the evaporation of the front metal contacts through a shadow mask and the deposition of dielectric layers, such as amorphous silicon (a-Si) or amorphous silicon nitride (SiN_x) for surface passivation and anti-reflection purposes. In the next step, the device is glued to a glass carrier by means of transparent glue and separated from the growth substrate. Finally, the rear contact is applied either directly onto the residual porous starting layer, or onto the underlying BSF layer, if the sintered porous silicon has been removed prior to the deposition of the metal contact. Figure 2.10 illustrates the resulting device structure.

Silicon thin-film solar cells fabricated by the above described process reached efficiencies of 15.4 % on an area of $3.9\,cm^2$ [14] and 14.1 % on an area of $95.5\,cm^2$ [83]. The thickness of the device was 25.5 µm and 26 µm, respectively, including the BSF and the residual SPS layer. Using photolithographic technology and high temperature oxidation, an efficiency of 16.6 % was reported for a film thickness of 44.5 µm and a cell area of $4\,cm^2$ [84].

2.4 Summary of Chapter 2

Porous silicon forms when an anodic current passes through the surface of a silicon substrate that is immersed in an HF-containing electrolyte. The dissolution reaction involves a hole from the bulk of the semiconductor and the depletion of holes in the porous region preserves the latter from being further etched. This passivation mechanism gives rise to the formation of a network of branched pores with active pore tips that proceed into the bulk of substrate. The porosity P quantifies the volume fraction of the removed material.

When PS is exposed to high temperatures, the thermal activation allows the silicon atoms to reconfigurate. The system minimises the free energy by reducing the internal surface area leading to fewer but larger pores. During sintering, the open structure of mesoporous silicon closes and the pore diameter changes drastically from a few nm to several ten nm. In the sintered state, the size distribution of the spherical pores exhibits a lognormal characteristic.

The Porous Silicon Process (PSI process) utilises PS as a sacrificial layer for the fabrication of thin monocrystalline silicon films. A porous double layer formed at the surface of a monocrystalline growth substrate enables the lift-off of an epitaxially deposited silicon film from the substrate. This double layer structure consists of a low porosity starting layer for the epitaxy and a highly porous separation layer underneath the starting layer. The step in the porosity results from abruptly increasing the etching current density during the anodisation process. Due to the high temperature of the epitaxial growth process, the porous structure reorganises, which later permits the separation of the epitaxial film from the growth substrate. After the layer-transfer of the silicon film to a low-cost substrate, the growth substrate is cleaned and re-used for the next cycle. With a film thickness of ∼26 µm, silicon thin-film solar cells fabricated by the PSI process reach efficiencies of 15.4 % on $2\times2\,cm^2$ and 14.1 % on $10\times10\,cm^2$ (pseudo-square) area.

3 Thermal properties

For many applications that utilise PS, the knowledge of the thermal properties of this material is a major issue. Examples for such applications are PS-based sensors [85–87], or thermoelectric devices [88, 89]. In the as-etched state, meso- and microporous silicon exhibits a thermal conductivity that is up to two orders of magnitude smaller than the bulk value of silicon [90–94]. This reduction is mainly caused by the microstructure of as-etched PS that features structure sizes in the nm range. Phonon scattering at boundaries of the porous nanostructure limits the phonon mean free path resulting in a reduced thermal conductivity [95–97]. This phenomenon is commonly known as the *phonon size effect*. Reference 85 gives in-depth information on thermal transport in nano-scaled materials.

When meso- and microporous silicon is sintered, the porous structure reorganises and the microstructure changes from an open sponge-like configuration to larger closed pores, as described in Section 2.2. Thus, one expects that the thermophysical properties of sintered porous silicon should differ from the as-etched state.

3.1 Analysis by lock-in thermography

This section describes the measurement method developed in this work for the determination of the thermal diffusivity, thermal conductivity and heat capacity, of free standing SPS films. The analysis of free standing samples has the advantage of excluding the influence of the substrate thereby allowing a simplified data evaluation. The analysed SPS films are less than 30 µm thick and thus fragile. Therefore contactless measurement principles are preferred. Established non-contact techniques are the laser flash method [98] and the mirage technique [99, 100]. For the flash method, a millisecond radiation pulse hits the front side of the sample and the thermal diffusivity follows from the time dependent temperature rise at the sample rear surface. The mirage technique detects the change of the refractive index of a gas in contact with the periodically heated sample by the deflection of an optical beam. Both methods offer a fast and contact-free analysis but have certain disadvantages: For the application of the laser flash method, the knowledge of the sample thickness is necessary to obtain the diffusivity. The mirage technique does not permit the determination of the thermal conductivity, only the diffusivity is obtained.

The analysis of small-sized and thin film materials has to account for thermal losses, since the influence of thermal losses increases with decreasing sample size due to the enhanced surface to volume ratio. Special methods for analysing small samples were developed [101, 102]. In Ref. 102, the thermal conductivity is detetermined by locally heating the sample and analysing the stationary spatial temperature distribution by means of an infrared (IR) camera. The described setup permits the contact-free determination of the thermal conductivity under ambient conditions. However, the thermal losses were not measured, but estimated and thus a relatively low measurement accuracy of 30 % resulted. With a vacuum system, a higher accuracy of 10 % was obtained [103], but the use of a vacuum system is time consuming and costly.

In this work a non-contact non-vacuum method for the thermophysical analysis of thin-films with high accuracy is developed. This approach combines lock-in thermography [104] and a simple data evaluation procedure to permit a fast contactless measurement of the thermophysical properties of free standing thin films under ambient conditions. An accuracy of 10 % is reached. The approach described here is based on a periodically modulated thermal excitation, first introduced by Ångström [105]. The procedure permits the determination of not only the in-plane thermal diffusivity but also a damping factor that describes the thermal coupling of the sample to the surrounding. In addition, the in-plane thermal conductivity and the volumetric heat capacity are obtained by means of a temperature calibration.

3.1.1 Experimental setup

Figure 3.1 shows a schematic of the measurement setup used in this work. The thermophysical properties are deduced from the thermal diffusion length and the temperature amplitude of a thermal wave propagating in the sample excited by an oscillating laser heat source. An IR camera images the wave and the thermal diffusion length of the amplitude Λ_a and that of the phase Λ_p are measured. Thermal losses influence both, Λ_a and Λ_p. Their geometric mean $\sqrt{\Lambda_\mathrm{a}\Lambda_\mathrm{p}}$ is, however, not effected by thermal losses [106, 107]. Thus, the evaluation of $\sqrt{\Lambda_\mathrm{a}\Lambda_\mathrm{p}}$ allows to perform measurements under ambient conditions avoiding the use of a vacuum chamber. The in-plane thermal diffusivity of the sample directly follows from the geometric mean $\sqrt{\Lambda_\mathrm{a}\Lambda_\mathrm{p}}$, whereas a temperature calibration of the camera sample system is required for the determination of the in-plane thermal conductivity and the volumetric heat capacity.

The applied in-house-built measurement setup shown in Figure 3.1 resembles the experimental configurations of other authors [108, 109]. The samples are clamped as free standing films into the measurement setup. A diode laser module illuminates the backside of the free standing thin film sample. The optics attached to the laser generates a line-shaped focus. The width of the focus line is 0.5 mm and the intensity variation (standard deviation) along the line-shaped focus is 15 %. The output power of the laser (maximum 75 mW) is controlled by an externally applied voltage V. For the determination of the thermal conductivity μ and the volumetric specific heat $\rho_\mathrm{m}c_\mathrm{p}$, the power per unit length Q coupled into the sample must be known. For this purpose a solar cell of known spectral response is used to measure the photon flux $\Phi(V)$ of the laser and the total power output is calculated as

$$P_\Phi(V) = \frac{hc}{\lambda}\,\Phi(V), \tag{3.1}$$

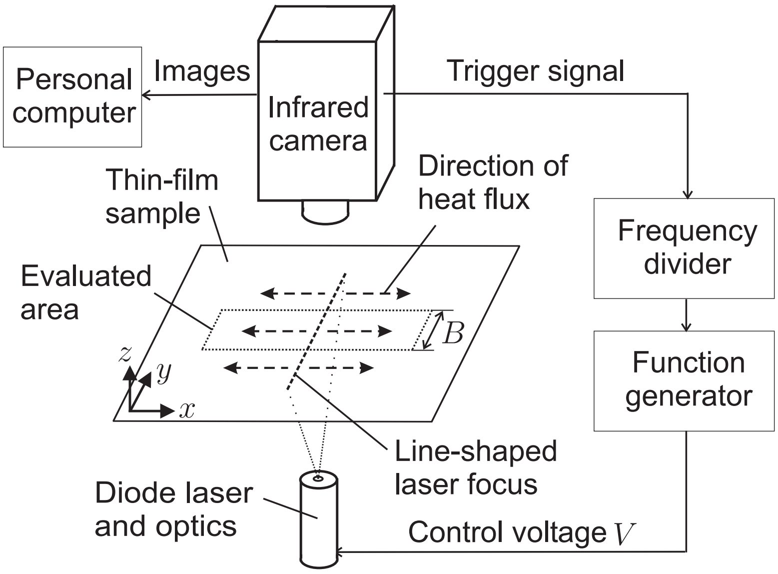

Figure 3.1. Experimental setup used for the thermal characterisation of thin-film samples. A sinusoidally modulated diode laser illuminates the backside of a thin film sample. The focus of the laser light is line-shaped. The induced thermal wave is visualised by a lock-in procedure using an IR camera. The dashed arrows symbolise the direction of the heat flux.

where h is Planck's constant, c the speed of light and $\lambda = 669\,\mathrm{nm}$ the laser wavelength. The evaluation procedure accounts for data taken from an area $\Delta y = B$ around the centre of the focus line, as shown in Fig. 3.1. Only a fraction f_{pow} of the laser power P_Φ is incident onto this area of the sample. Another source of power loss is the reflection of laser light at the back surface of the sample. Therefore the reflection R of the backside of the sample is measured with a spectrophotometer, as described in Section 4.1.2. The heating power per unit length

$$Q = \frac{f_{\mathrm{pow}}(1-R)P_\Phi}{B} \tag{3.2}$$

follows from f_{pow}, the reflectance R, the width B of the evaluated area, and the total incident power P_Φ from Eq. (3.1).

The surface temperature of the sample is detected by an IR camera system. The camera is equipped with a focal plane array that consists of 640×486 quantum well infrared photodetector pixels [110]. The spectral detection window ranges from 7.8 µm to 8.5 µm and the frame rate is $\nu_0 = 38.9\,\mathrm{Hz}$. The noise equivalent temperature difference of the camera system is 20 mK. With the applied optical setup, a spatial pixel resolution of 0.17 mm is reached. An image acquisition board and a personal computer are used for data acquisition and analysis.

The IR camera passes a trigger signal to a frequency divider after every image. The frequency divider counts the incoming pulses and generates another trigger signal after every

m images. This output has the lock-in frequency $\nu_{\mathrm{li}} = \nu_0/m$ and is passed to a function generator that generates a sine wave $V = V_{\mathrm{offs}} + V_{\mathrm{amp}} \sin(2\pi\nu_{\mathrm{li}})$ with amplitude V_{amp} and offset $V_{\mathrm{offs}} > V_{\mathrm{amp}}$. The control voltage V sinusoidally modulates the laser power P_Φ.

The applied lock-in frequencies range from 9.725 Hz down to 117 mHz. This corresponds to $m = 4$ to 332 images per period. In-house-written software evaluates the images online. The lock-in data analysis used in this work is described in detail by Breitenstein and Langenkamp [104]. This evaluation includes the calculation of the in-phase camera signal S_{0° and the quadrature signal S_{-90°, as well as the corresponding amplitude $|S| = \sqrt{S_{0^\circ}^2 + S_{-90^\circ}^2}$ and the phase angle $\phi = \arctan\left(-S_{-90^\circ}/S_{0^\circ}\right)$. Due to the finite time required for reading the focal plane array, a phase shift occurs. This phase shift is $< 0.1°$ for the evaluated image area, a correction is thus not necessary. To improve the signal to noise ratio, the camera records 2000 to 10000 images, which results in a temperature noise level of 0.9 mK to 0.4 mK [104].

3.1.2 Temperature calibration

A temperature calibration is required to determine the amplitude $|T|$ of the oscillating temperature field in units of Kelvin. For calibration the camera images the sample at a stationary temperature defined by a thermostatic heating plate. The temperature of the sample is measured with a thermocouple.

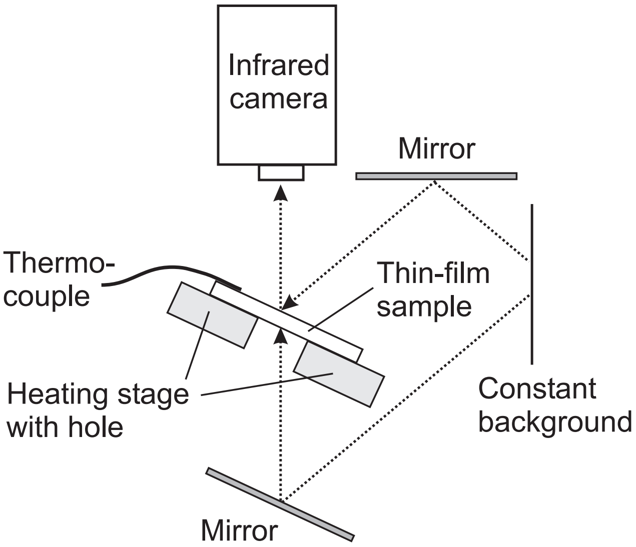

Figure 3.2. Temperature calibration setup for semitransparent thin-film samples. The camera images the sample mounted on a slightly tilted heating stage. The mirror assembly accounts for a constant reflection and transmission signal from the sample. Thus, when increasing the temperature of the heating stage, the change in the camera signal arises solely from an increased IR emission of the sample.

In a range of several ten degrees around room temperature, the camera signal S scales linearly with the sample temperature T. A linear fit yields a calibration factor $\partial S/\partial T$ for each sample. This calibration factor is used to calculate the amplitude $|T| = |S|/(\partial S/\partial T)$, the in-phase temperature $T_{0^\circ} = S_{0^\circ}/(\partial S/\partial T)$, and the quadrature temperature $T_{-90^\circ} = S_{-90^\circ}/(\partial S/\partial T)$ from the measured camera signals $|S|$, S_{0°, and S_{-90°, respectively.

When applying the calibration procedure to silicon thin-film samples, special care must be taken, because the surface of the thin-film sample has a high reflectivity and the sample is semitransparent in the infrared. To account for these optical properties of the samples, a special calibration configuration is used. Figure 3.2 shows a schematic of this calibration setup. The sample is mounted on a slightly tilted heating stage that features a hole. Mirrors focus a constant background signal to the front and rear side of the sample from where the signal is reflected and transmitted, respectively, to the camera. Thus, when heating the sample stage only the emission of the thin-film sample towards the camera increases.

3.1.3 Theory

Due to the low film thickness and the symmetry of the problem, a one dimensional treatment of the heat conduction is sufficient. Figure 3.1 on p. 23 illustrates the geometry and the definition of the coordinate system. The temperature field within the sample satisfies the one dimensional diffusion equation [106]

$$\left(\rho_\mathrm{m}\, c_\mathrm{p}\frac{\partial}{\partial t} - \mu\frac{\partial^2}{\partial x^2} + \frac{2\beta}{W}\right) T_\mathrm{tot}(x,t) = \frac{Q_\mathrm{offs} + Q\mathrm{e}^{\mathrm{i}\omega t}}{W}\,\delta(x), \tag{3.3}$$

where ρ_m is the mass density, c_p the specific heat, μ the thermal conductivity, and W the thickness of the sample, β the heat transfer coefficient, and T_tot the temperature of the sample with respect to the constant temperature of the surrounding. The heat transfer coefficient describes the thermal flux to the surrounding and includes both effects, radiation losses as well as convection. The symbols Q_offs and Q denote the offset and the amplitude of the oscillating heating power per unit length, respectively, and ω is the angular frequency of the periodic heating source. The δ-shaped source is located at $x = 0$. Inserting

$$T_\mathrm{tot}(x,t) = T_\mathrm{offs}(x) + T(x)\,\mathrm{e}^{\mathrm{i}\omega t} \tag{3.4}$$

in Eq. (3.3) yields the time dependent component of the differential equation

$$\left(k^2 - \frac{\partial^2}{\partial x^2}\right) T(x) = \frac{Q}{\mu W}\,\delta(x), \tag{3.5}$$

where

$$k = \sqrt{\frac{\mathrm{i}\omega\rho_{\mathrm{m}}c_{\mathrm{p}} + 2\beta/W}{\mu}} \tag{3.6}$$

is a complex number. The boundary condition of Eq. (3.5) for an infinitely long sample in the x-direction is

$$T\big|_{|x|\to\infty} = 0. \tag{3.7}$$

Half of the power Q flows in $+x$, half in $-x$ direction and thus one finds

$$-\mu\frac{\partial T}{\partial|x|}\bigg|_{|x|\to 0} = \frac{Q}{2W}. \tag{3.8}$$

Using Eqs. (3.5), (3.7) and (3.8), the temperature oscillation is

$$T(x) = \frac{Q}{2k\mu W}\,\mathrm{e}^{-k|x|}. \tag{3.9}$$

The amplitude of the thermal wave

$$|T(x)| = T_0\,\mathrm{e}^{-|x|/\Lambda_{\mathrm{a}}} \tag{3.10}$$

and its phase

$$\phi(x) = \arg\left(T(x)\right) = -|x|/\Lambda_{\mathrm{p}} + \phi_0 \tag{3.11}$$

with respect to the oscillating heat source follow from Eqs. (3.9) and (3.6). Here, the thermal diffusion length of the amplitude

$$\Lambda_{\mathrm{a}} = \left(\sqrt{\left(\frac{\beta}{\mu W}\right)^2 + \left(\frac{\omega}{2a}\right)^2} + \frac{\beta}{\mu W}\right)^{-\frac{1}{2}} \tag{3.12}$$

and the thermal diffusion length of the phase

$$\Lambda_{\mathrm{p}} = \left(\sqrt{\left(\frac{\beta}{\mu W}\right)^2 + \left(\frac{\omega}{2a}\right)^2} - \frac{\beta}{\mu W}\right)^{-\frac{1}{2}} \tag{3.13}$$

are given by the inverse real and inverse imaginary part of k (Eq. (3.6)), respectively.

$$a = \frac{\mu}{\rho_{\mathrm{m}}c_{\mathrm{p}}} \tag{3.14}$$

denotes the thermal diffusivity of the sample, while

$$T_0 = \frac{Q}{2\mu W}\,\Lambda_\mathrm{a} \cos\phi_0 \tag{3.15}$$

is the temperature amplitude, and

$$\phi_0 = -\arctan\left(\Lambda_\mathrm{a}/\Lambda_\mathrm{p}\right) \tag{3.16}$$

is the phase shift at the source position $x = 0$. The geometric mean

$$\sqrt{\Lambda_\mathrm{a}\Lambda_\mathrm{p}} = \sqrt{2a/\omega} \tag{3.17}$$

of Λ_a and Λ_p does not contain the heat transfer coefficient β [106, 107]. Instead, it only depends on the diffusivity a, while the difference of the inverse squares

$$\frac{1}{\Lambda_\mathrm{a}^2} - \frac{1}{\Lambda_\mathrm{p}^2} = \frac{2\beta}{\mu W} \tag{3.18}$$

yields twice the term $\beta/\mu W$, which quantifies the thermal losses from the sample to the surrounding and is referred to as the damping factor. By measuring Λ_a and Λ_p, the diffusivity a and the damping factor $\beta/\mu W$ can thus be obtained using Eqs. (3.17) and (3.18).

Equations (3.15) and (3.16) may be combined to calculate the temperature amplitude

$$T_0 = \frac{Q}{2\mu W}\,\Lambda_\mathrm{a} \cos\left(\arctan\left(\Lambda_\mathrm{a}/\Lambda_\mathrm{p}\right)\right) \tag{3.19}$$

at source position as a function of Λ_a, Λ_p, the heating power per unit length Q, and the thickness W of the specimen. Equation (3.19) is used to determine the thermal conductivity μ. Finally the volumetric heat capacity $\rho_\mathrm{m} c_\mathrm{p} = \mu/a$ follows from Eq. (3.14).

3.1.4 IR camera image evaluation

Figure 3.3 shows measured spatial temperature images that result from the numerical lock-in procedure and the associated amplitude and phase angle images. The analysed sample is a nickel silver strip covered with black paint to increase its emission in the IR. The camera signal S is converted to a temperature T by the above described calibration procedure.

In Fig. 3.4 temperature and phase profiles along a line in the x-direction (horizontal line through the middle of the images in Fig. 3.3) are shown. The measured amplitude profile $|T(x)|$ shows good agreement with Eq. (3.10), as seen in the semi-logarithmic plot of Fig. 3.4 (a). An exponential decay function is fitted to the amplitude data to determine

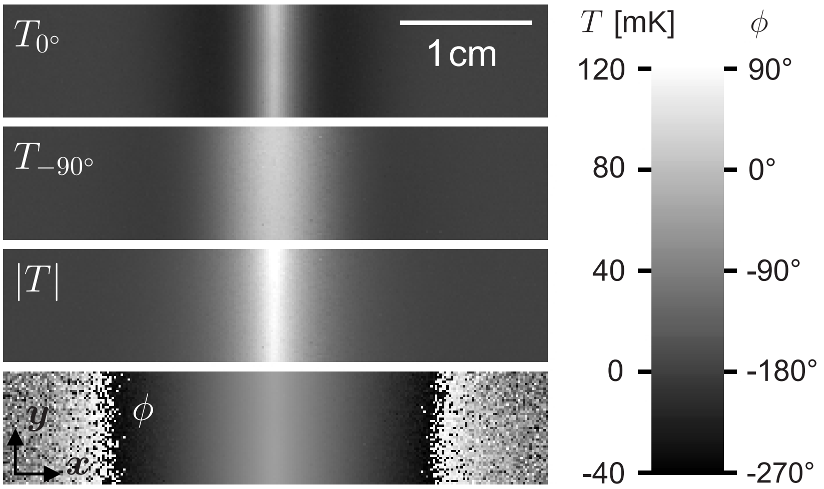

Figure 3.3. Images of the measured in-phase component $T_{0°}$ and quadrature component $T_{-90°}$ and the corresponding amplitude $|T|$ and the phase ϕ of a thermal wave propagating in a thin nickel silver strip. The sample is covered with black paint. The lock-in frequency is $\nu_{\mathrm{li}} = 0.27\,\mathrm{Hz}$. 10000 images are evaluated corresponding to 69 periods. The x-scale of the $T_{0°}$-image also applies to the other three images.

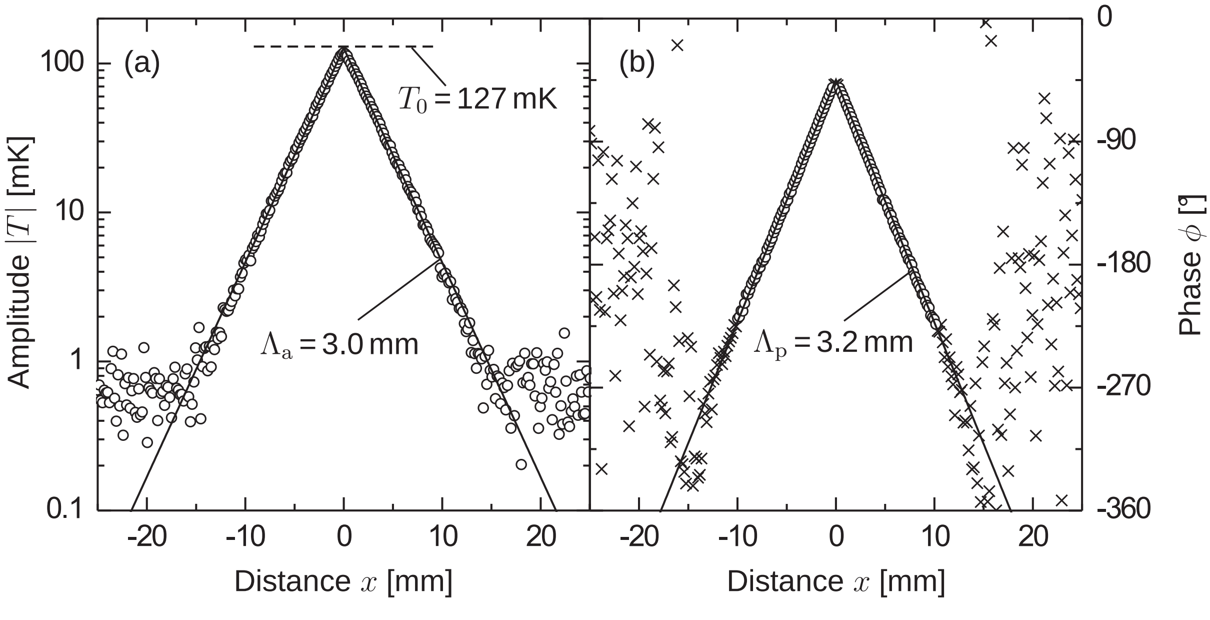

Figure 3.4. Temperature and phase profiles along a line scan in the x-direction (symbols) and fitted functions using Eqs. (3.10) and (3.11) (solid lines). The data are taken from the center of the images shown in Fig. 3.3 and averaged over three rows of pixels. The temperature noise level is 0.7 mK.

Λ_a. The temperature amplitude T_0 is given by the intersection of the two fitted lines in Fig. 3.4 (a). Figure 3.4 (b) shows the obtained phase profile $\phi(x)$. Again the measurement results comply well with the theoretical prediction of a linear decreasing phase from Eq. (3.11). A linear fit to the relevant phase data (circles in Fig. 3.4 (b)) yields Λ_p.

The finite width of the line source restricts the data usable for fitting to the region $|x| > 0.3\,\mathrm{mm}$. For the phase image in Fig. 3.4 (b), the evaluation range is additionally limited to $|x| < 10\,\mathrm{mm}$ by the noise. The line profiles of Fig. 3.4 result from averaging the temperature and phase images (Fig. 3.3) over an interval $\Delta y = 0.5\,\mathrm{mm}$ at every x-value. This corresponds to three rows of pixels.

3.1.5 Applicability of the one-dimensional model

The theoretical model presented in Section 3.1.3 assumes one-dimensional transport. The following points are important concerning the experimental implementation:

Due to the 15 % inhomogeneity of the line-shaped laser focus, a heat flux in the y-direction also occurs, which is not accounted for in the one dimensional model. This results in a variation of 5 % to 10 % of the obtained thermal diffusion lengths and the temperature amplitude along the line. The evaluation procedure accounts for the inhomogeneity by including these variations in the error calculation.

The temperature gradient and associated heat flux in the z-direction (see Fig. 3.1) is negligible for thermally thin samples. A sample is considered thermally thin if $\mathrm{W} \ll \Lambda_\mathrm{a}, \Lambda_\mathrm{p}$. This condition depends not only on the sample properties but also on the lock-in frequency. All the analysed samples are thermally thin at the applied lock-in frequencies.

When analysing highly diffusive samples at low lock-in frequencies (large Λ_a, Λ_p), it has to be assured that the thermal diffusion lengths Λ_a and Λ_p are still small compared to the length of the laser focus line. This allows a one dimensional treatment of the problem. In addition, care must be taken that the sample extension L in the x-direction is still much larger than Λ_a, Λ_p to fulfil the boundary condition of Eq. (3.7). Otherwise the finite length must be accounted for and Eq. (3.7) has to be replaced by

$$\mu \frac{\partial T}{\partial x}\bigg|_{x=\pm L/2} = 0. \tag{3.20}$$

3.1.6 Experimental verification of the measurement method

Three materials, copper, nickel silver and a polyimide film, are analysed for the experimental verification of the developed measurement method. The metal samples are covered with black paint on both sides to enhance their IR emission and to reduce the reflection of the heating laser. The thermal diffusivity a, thermal conductivity μ and volumetric heat capacity $\rho_\mathrm{m} c_\mathrm{p}$ of the test samples are determined from the frequency dependence of the thermal diffusion lengths Λ_a and Λ_p and the temperature amplitude T_0. This procedure is described in detail in Section 3.2.2 below. Table 3.1 lists the measurement results for the three different test samples.

Table 3.1. Measurement results and literature values for the thermal diffusivity a, the thermal conductivity μ, the volumetric specific heat $\rho_\mathrm{m}c_\mathrm{p}$ of the three analysed test samples.

Sample	Diffusivity a [$\mathrm{mm^2/s}$]	Thermal conductivity μ [W/(m K)]	Volumetric heat capacity $\rho_\mathrm{m}c_\mathrm{p}$ [$\mathrm{J/(cm^3K)}$]	Reference
Copper	105 ± 5	400 ± 42	3.79 ± 0.33	This work
	112.5	386	3.43	104
Nickel silver	8.18 ± 0.4 [a]	31.4 ± 3.3 [a]	3.84 ± 0.34 [a]	This work
	-	> 33 [a]	-	111
	7.3 [b]	24.9 [b]	3.40 [b]	104
Polyimide film	1.12 ± 0.13 [c]	2.21 ± 0.37 [c]	1.96 ± 0.24	This work
	-	-	2.02	112

[a] Composition is 62 % Cu, 18 % Ni, 20 % Zn
[b] Composition is 62 % Cu, 15 % Ni, 22 % Zn (rounded numbers)
[c] in-plane

Copper sample: The measurement results agree with literature values. The deviations are -7 % for the diffusivity, +4 % for the thermal conductivity, and +10 % for the heat capacity, approving the measurement accuracy of 10 %. The main source of uncertainty is the inhomogeneity of the laser focus, as outlined above.

Nickel silver sample: The results for this sample also comply well with literature values. The measured thermal conductivity is 5 % lower than the literature value. To the knowledge of the author, no information is available in the literature on the diffusivity and the heat capacity of a sample with precisely the composition as the sample analysed in this work. For a slightly different composition a heat capacity that agrees with the measurement to 13 % was published [104].

Polyimide film: Again, no literature values for the in-plane diffusivity and conductivity of the polyimide film are available. The value published for the heat capacity [112] lies within the uncertainty range of the measured heat capacity.

The heat capacities measured for the two metal samples are 10 % to 13 % higher than the literature values. This deviation is explained by the influence of the paint coating. When the coating is included in the thermal model as a non-conducting layer coupled to the sample via a negligible thermal resistance, a higher heat capacity than for an uncoated sample is expected [113]. From the thickness of one coating layer $W_\mathrm{c} \approx 15$ µm and an approximated heat capacity of the coating $\rho_\mathrm{m}c_\mathrm{p} \approx (2 \ldots 3)\ \mathrm{J/(cm^3\,K)}$ a deviation of 10 % to 15 % is predicted [113]. The measured deviations lie within this range.

3.2 Thermal characterisation of SPS films

3.2.1 Fabrication of free standing SPS films

The analysed samples are free standing SPS films that are separated from the silicon substrate by means of the PSI layer transfer technique, as described in Section 2.3. The PS layers are formed by electrochemical etching of p-type monocrystalline silicon substrates in a hydrofluoric acid/ethanol electrolyte and subsequent high temperature annealing. The substrates are (100)-oriented, boron doped Czochralski (CZ) wafers with a resistivity of 0.01 Ωcm and a diameter of 4 inch. For anodisation, the setup described in Section 2.1.5 is used with an electrolyte solution mixture of HF(50%) : ethanol = 3:2 (by volume). The current densities of anodic etching range from 5 mA/cm^2 to 350 mA/cm^2 and result in porosities between 27 % and 66 %. After the etching process the samples are annealed for 30 minutes at 1000 °C in a 1 bar hydrogen atmosphere.

Figure 3.5 (a) illustrates the preparation of free standing samples with a porosity below 50 %. In a two step process, a low porosity starting layer is etched in the first step, followed by a high current pulse creating a second several 100 nm thick highly porous separation layer underneath the first layer. This separation layer dissolves during sintering due to its high porosity. Subsequent to the sintering process, the sample is glued to a plastic frame and mechanical stress permits the separation of the sintered porous film from the substrate. Table A.1 in Appendix A lists the etching parameters used to form the starting

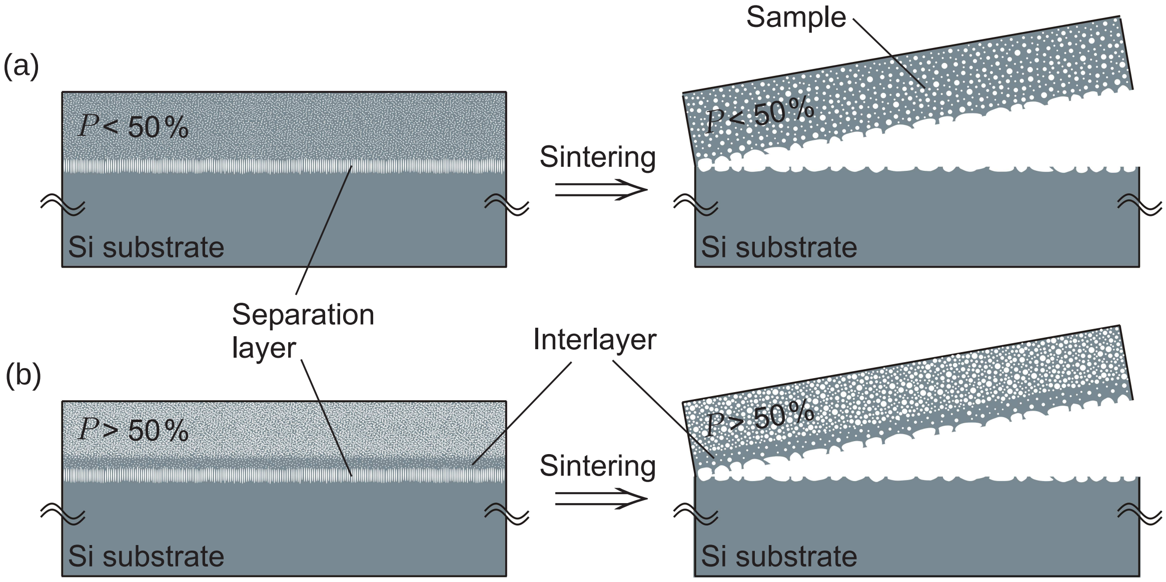

Figure 3.5. Preparation of free standing SPS samples. A highly porous separation layer, that dissolves during sintering, permits the separation of the sample from the substrate. The left hand side shows the fabrication of samples with a porosity $P < 50\,\%$, whereas the right hand side illustrates the case for $P > 50\,\%$. For the high porosity samples the introduction of a low porosity interlayer is necessary to permit the separation.

Table 3.2. Properties of the fabricated free standing SPS films. For the double layer Samples T5, T6 and T7, the average porosity and total sample thickness are given.

Sample	Porosity P [%]	Thickness W [µm]	Sample area [cm^2]
T1	27.5 ± 0.6	3.2 ± 0.5	2.8 ± 0.5
T2	37.2 ± 0.2	20.8 ± 0.3	15.4 ± 1.2
T3	44.2 ± 0.2	20.7 ± 0.4	10.2 ± 0.7
T4	48.4 ± 0.2	25.1 ± 0.5	12.7 ± 0.9
T5	51.7 ± 0.2	26.8 ± 0.2	9.8 ± 0.5
T6	58.8 ± 0.2	26.9 ± 0.2	9.7 ± 0.5
T7	66.2 ± 0.2	25.5 ± 0.2	19.1 ± 0.9

and the separation layer. This procedure allows the fabrication of 3 µm to 25 µm thick free standing SPS films with porosities between 27 % and 48 % (Samples T1, T2, T3 and T4, see Table 3.2). Figure 3.6 shows a photograph of such a free standing thin-film.

Figure 3.5 (b) exemplifies the preparation of the highly porous samples ($P > 50\,\%$). For these samples, the introduction of an interlayer is necessary to allow the separation of the starting layer from the substrate. This interlayer, characterised by a low porosity and a thickness well below 1 µm, is located between the starting layer and the separation layer. The mechanical weakening of the separation layer during sintering allows the removal of a double layer structure that consists of the starting layer and the interlayer (see Fig. 3.5 (b)).

Figure 3.6. Photograph of a ∼25 µm thick free standing SPS thin-film. A plastic frame mechanically stabilises the sample. The dissolving of a highly porous separation layer during sintering permits the separation of the porous film from the silicon substrate.

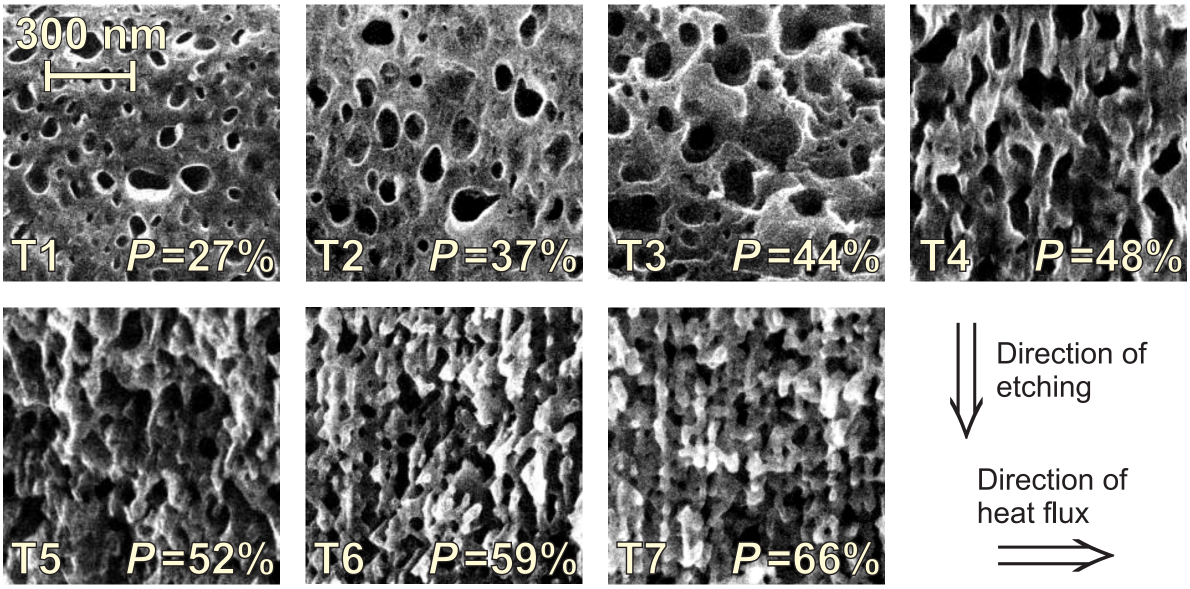

Figure 3.7. Cross section SEM images of the seven analysed samples. The etching direction is vertical, while the direction of heat flux during the measurements is horizontal. The porosity P is given in the the bottom right corner of the images. The scale bar in the upper left also applies to the other images.

Thus, each of the high porosity Samples T5, T6 and T7 consists of two layers, the 25 to 27 µm thick highly porous starting layer and the < 1 µm thick interlayer of low porosity. The etching current densities and times for the formation of the layers are listed in Table A.1 in the appendix. Table 3.2 gives an overview on all fabricated samples.

Figure 3.7 presents cross section images of the samples obtained with an SEM. The etching direction is from top to bottom. With increasing etching current density (increasing porosity) the pores become more elongated and aligned to the etching direction. This anisotropy is preserved during the annealing process [63]. The thermal diffusivity and conductivity is measured in the horizontal direction, perpendicular to the etching direction.

The porosity is determined by gravimetric measurements on equivalent samples, as described in Section 2.1.6. For the high porosity Samples T5, T6 and T7, this method only gives an average sample porosity, since these samples consist of a $\sim$25 µm thick starting and a < 1 µm thick interlayer. The thickness of the samples is determined using an SEM. Table 3.2 lists the measured sample porosities and thicknesses.

3.2.2 Determination of thermophysical properties

The diffusivity a and the damping factor $\beta/\mu W$ are determined from the frequency dependence of the measured diffusion lengths Λ_a and Λ_p. This analysis does not require a temperature calibration. In a second evaluation step, the thermal conductivity μ and the volumetric heat capacity $\rho_\mathrm{m} c_\mathrm{p}$ are deduced from the measured temperature amplitude

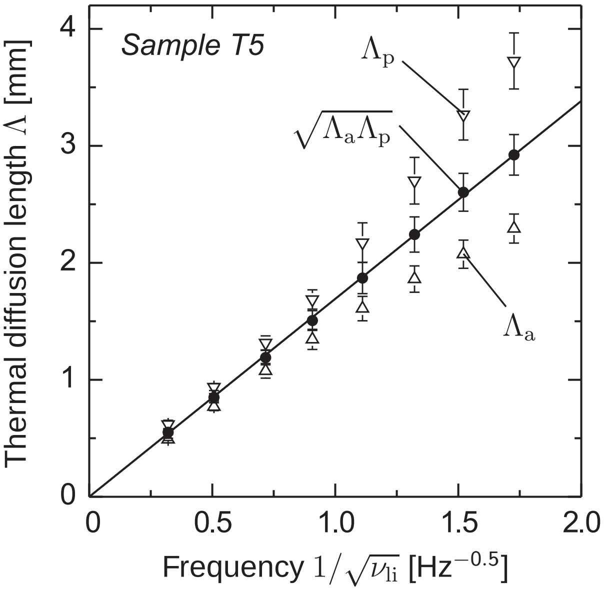

Figure 3.8. The thermal diffusion lengths for the amplitude Λ_a and for the phase Λ_p, and their geometric mean $\sqrt{\Lambda_a\Lambda_p}$ measured for Sample T5 (symbols). The geometric mean shows a linear dependence on $1/\sqrt{\nu_{li}}$ (see Eq. (3.17)). A linear fit (solid line) that is forced through the origin yields the thermal diffusivity a.

at source position T_0 by means of Eq. (3.19). A temperature calibration of the measurement system, as described in Section 3.1.2, is necessary for this second step of the analysis procedure.

Diffusivity: Figure 3.8 shows the diffusion lengths Λ_a and Λ_p of the amplitude and the phase as well as their geometric mean $\sqrt{\Lambda_a\Lambda_p}$. Apparent from Eq. (3.17), the diffusivity a follows from the slope of the geometric mean $\sqrt{\Lambda_a\Lambda_p}$ plotted versus $1/\sqrt{\nu_{li}}$. Table 3.3 on p. 36 lists the thermal diffusivities for the prepared samples that result from a linear fit to the experimental data.

Damping factor: Figure 3.9 shows the experimental values for $1/\Lambda_a^2 - 1/\Lambda_p^2$ that are used to determine the damping factor $\beta/\mu W$ by means of Eq. (3.18). Only the data points at lower lock-in frequencies are used for the evaluation, since with decreasing ν_{li}, the influence of the thermal losses on the diffusion lengths Λ_a and Λ_p increases, as indicated by Eqs. (3.12) and (3.13). For sufficiently low frequencies $1/\Lambda_a^2 - 1/\Lambda_p^2$ becomes independent of ν_{li}. The average value of the low frequency data points (filled circles in Fig. 3.9) yields $2\beta/\mu W$.

Thermal conductivity and heat capacity: Figure 3.10 shows the measured temperature amplitude T_0 at the source position. For the evaluation of the thermal conductivity μ, Eq. (3.19) is fitted to the experimental data (solid line in Fig. 3.10). For this purpose the above determined thermal parameters a and $\beta/\mu W$ are used to calculate the frequency dependence of Λ_a and Λ_p with Eqs. (3.12) and (3.13). Thus the thermal conductivity μ is

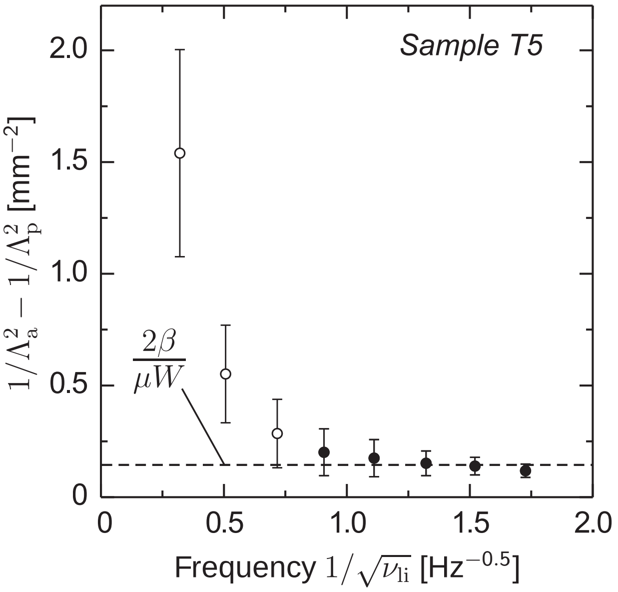

Figure 3.9. Determination of the damping factor $\beta/\mu W$ by means of Eq. (3.18). The dashed line marks the average value of the filled circles, weighted by the inverse length of the error bars.

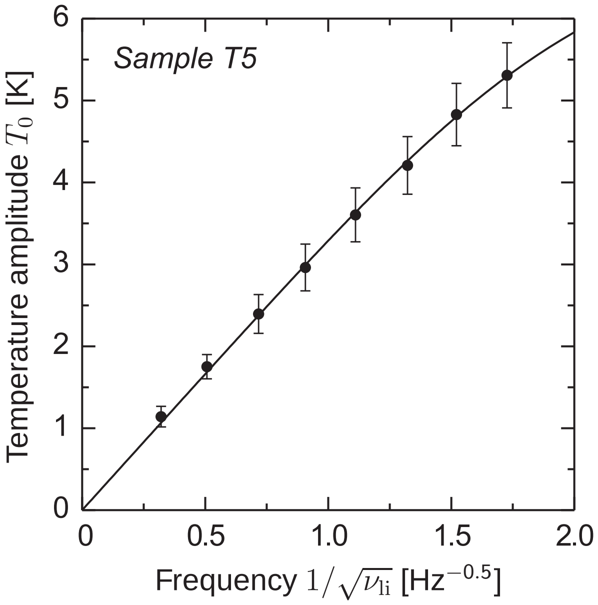

Figure 3.10. Measured temperature amplitude T_0 (dots) and fitted theoretical functions (solid line) using Eq. (3.19) and the values for a and $\beta/\mu W$ obtained from Figs. 3.8 and 3.9, respectively.

Table 3.3. Measurement results for the thermal properties of SPS films with different porosities.

Sample	Porosity P [%]	Diffusivity a [$\mathrm{mm^2/s}$]	Thermal conductivity μ [W/(m K)]	Volumetric heat capacity $\rho_\mathrm{m}c_\mathrm{p}$ [$\mathrm{J/(cm^3K)}$]
T1	27.5 ± 0.6	14.3 ± 1.2	20.8 ± 4.6	1.46 ± 0.30
T2	37.2 ± 0.2	13.9 ± 1.0	12.7 ± 2.0	0.91 ± 0.13
T3	44.2 ± 0.2	12.5 ± 0.7	11.3 ± 2.2	0.90 ± 0.17
T4	48.4 ± 0.2	9.1 ± 1.3	8.7 ± 2.4	0.96 ± 0.23
T5	51.7 ± 0.2	9.0 ± 1.1	6.1 ± 1.2	0.68 ± 0.12
T6	58.8 ± 0.2	6.8 ± 0.4	4.5 ± 0.7	0.67 ± 0.09
T7	66.2 ± 0.2	5.1 ± 0.4	2.3 ± 0.5	0.45 ± 0.09

the only free parameter in Eq. (3.19), once the heating power per unit length Q (Eq. (3.2)) and the sample thickness W are known. The volumetric heat capacity $\rho_\mathrm{m}c_\mathrm{p} = \mu/a$ is then calculated from the diffusivity a and the thermal conductivity μ. The results are given in Table 3.3 together with the porosity values.

3.3 Effect of the porosity and the microstructure

3.3.1 The Looyenga model

The effective medium expression that is used to describe the measurements on SPS was first introduced by Looyenga for modelling the dielectric function of heterogeneous mixtures [114]. Gesele et al. already applied this model in the analysis of the thermal conductivity of as-etched PS [93]. The model assumes a porous medium consisting of a solid phase with the thermal conductivity μ_s and voids with a vanishing thermal conductivity. The effective thermal conductivity

$$\mu_\mathrm{eff} = \mu_\mathrm{s}\, g_0\, (1-P) = \mu_\mathrm{s}\, (1-P)^3 \tag{3.21}$$

of the porous medium depends on the thermal conductivity of the solid phase μ_s and on the porosity P [93, 114]. Here

$$g_0 = (1-P)^2 \tag{3.22}$$

denotes the percolation strength, which quantifies the interconnection of the porous structure [93, 114]. The interconnection strongly affects the transport properties of the porous medium.

In this work effective medium theory is also applied to the volumetric heat capacity. A simple approach, already suggested by Lysenko et al. [115], predicts an effective volumetric heat capacity

$$(\rho_\mathrm{m} c_\mathrm{p})_\mathrm{eff} = (\rho_\mathrm{m} c_\mathrm{p})_\mathrm{s} \, (1 - P) \, , \tag{3.23}$$

with $(\rho_\mathrm{m} c_\mathrm{p})_\mathrm{s}$ being the volumetric heat capacity of the solid phase. The percolation factor g_0 is not included, since it is assumed that transport phenomena do not affect the heat capacity.

3.3.2 Thermal conductivity

Figure 3.11 shows the measured thermal conductivities (dots) ranging from 21 W/(m K) for $P = 27\,\%$ to 2.3 W/(m K) for $P = 66\,\%$. This is a factor of 7 to 64, respectively, lower than the thermal conductivity $\mu_\mathrm{Si} = 148$ W/(m K) of bulk Si [59]. However, the measured values are significantly higher than the thermal conductivity of as-etched PS, which is of the order of 1 W/(m K) [92, 93]. This is explained by the phonon size effect [85, 97, 116]. Size and distance of the pores in SPS are of the order of 100 nm (see Fig. 3.7), whereas the crystallite size of as-etched PS is of the order of 10 nm [92, 93]. The structure size of both, SPS and as-etched PS, is thus comparable to the phonon mean free path, which is 41 nm for bulk Si in the Debye model [117] and 260 nm in the more realistic dispersion model [117, 118], that accounts for the different phonon dispersion relations. Thus, in both materials, SPS and as-etched PS, phonons are scattered at the pore surfaces which reduces their effective mean free path and thereby the thermal conductivity. However, the increased thermal conductivity that is measured for SPS shows that this effect is weaker in the case of SPS compared to as-etched state due to the larger structure size of SPS.

In this work the Looyenga formula is applied in order to model the thermal conductivity of SPS as a function of the porosity P. For the determination of the solid phase thermal conductivity μ_s , which is the only parameter of the model besides the porosity, the equation

$$\mu = \mu_\mathrm{s} \, (1 - P)^3 \, , \tag{3.24}$$

is fitted to the experimentally determined data with μ_s as a free parameter. As seen in Fig. 3.11, the measured data and the model agree for

$$\mu_\mathrm{s} = (55.7 \pm 1.9) \, \mathrm{W/(m\,K)}. \tag{3.25}$$

In a first guess one could expect that the thermal conductivity μ_s of the porous skeleton is equivalent to the bulk thermal conductivity μ_Si of silicon. However, the value determined for μ_s is almost a factor of three lower than μ_Si. This reduction is explained by the phonon size effect, as outlined above. The Looyenga model assumes that the porous structure does

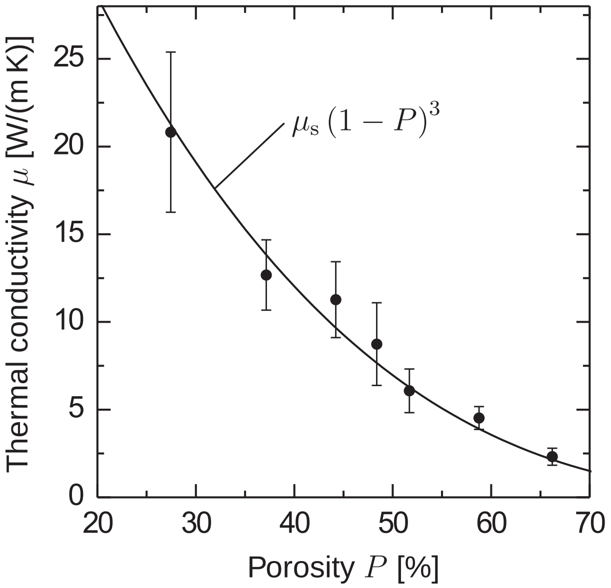

Figure 3.11. Measured in-plane thermal conductivity μ (dots) of free standing SPS films with porosities between 27 % and 66 %. The solid line is a fitted Looyenga model using Eq. (3.24).

not affect the thermal conductivity μ_s of the porous network. However, in SPS phonon scattering reduces the phonon mean free path within the remaining silicon bridges. The distance of the pores in SPS is significantly smaller than the phonon mean free path (260 nm in the dispersion model [117, 118]) giving rise to a reduced thermal conductivity of the porous network.

Figure 3.7 shows that the characteristic size of the porous structure varies from sample to sample. For the low porosity samples (T1 to T3) the size of the pores seems to increase, whereas for higher porosities (Sample T4 to T7) it decreases again. This variation of the structure size impairs the applicability of the Looyenga model, because the use of the Looyenga model requires a constant structure size and thus constant μ_s. However, the change in porosity seems to be the dominant effect compared to the variation of the characteristic size, because both, the measured effective thermal conductivity as well as the porosity, decrease monotonically from Sample T1 to Sample T7.

Moreover, due to the anisotropy of the microstructure, as outlined in Section 3.2.1, an anisotropic thermal conductivity is expected. For the high porosity samples (T4 to T7) one would expect a higher *cross-plane* than *in-plane* thermal conductivity, due to the higher interconnection in the direction of etching (see Fig. 3.7). The measured *in-plane* thermal conductivity is successfully described by the Looyenga model. However, the obtained results do not give any information on the *cross-plane* thermal conductivity.

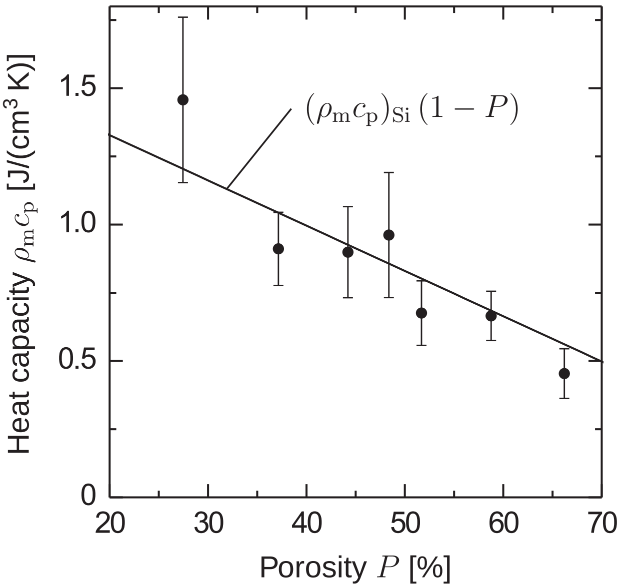

Figure 3.12. Measured volumetric heat capacity $\rho_\mathrm{m}c_\mathrm{p}$ (dots) of free standing SPS films with porosities between 27 % and 66 %. The straight line represents the volumetric heat capacity of bulk Si $(\rho_\mathrm{m}c_\mathrm{p})_\mathrm{Si}$ multiplied by $(1-P)$. No fitting is applied here.

3.3.3 Volumetric heat capacity

Figure 3.12 shows the measured volumetric heat capacity of the seven SPS samples together with the effective medium prediction according to Eq. (3.23) using the bulk value $(\rho_\mathrm{m}c_\mathrm{p})_\mathrm{Si} = 1.63\,\mathrm{J/(cm^3K)}$ of silicon [59]. The agreement of the calculated curve and the measured data yields the conclusion that the *mass-specific* heat capacity c_p of SPS is close to the bulk value. Thus, the decrease of the *volumetric* heat capacity $\rho_\mathrm{m}c_\mathrm{p}$ is directly related to the reduced mass density ρ_m of SPS that decreases as $(1-P)$.

3.4 Summary of Chapter 3

In this chapter the thermal properties of SPS are investigated. For this purpose a method for the thermophysical investigation of thin-film samples is developed. The procedure applies a non-contact thermal analysis that is based on IR lock-in thermography. The evaluation of both the phase and the amplitude of an excited thermal wave that propagates in the sample enables the quantification of the thermal losses to the surrounding. Thus, in contrast to a number of configurations described in the literature, the approach developed in this work allows to measure under ambient conditions, omitting the use of a vacuum system. The experimentally verified evaluation permits the determination of the in-plane thermal diffusivity, thermal conductivity and volumetric heat capacity with an accuracy of 10 %.

Applying the described method for the thermal characterisation of free standing SPS films yields a thermal conductivity ranging from 21 W/(m K) to 2.3 W/(m K) and a volumetric heat capacity between 1.46 J/(cm^3 K) and 0.45 J/(cm^3 K) for porosities of 27 % to 66 %, respectively. The Looyenga model successfully describes the thermal conductivity of SPS as functions of the porosity. This analysis shows that the thermal conductivity in the silicon network is a factor of three lower than the thermal conductivity of bulk silicon. Phonon scattering at the pore walls, an effect that is known to drastically reduce the thermal conductivity of as-etched PS, also reduces the mean free path of the phonons in SPS, resulting in a reduced thermal conductivity of the solid phase.

4 Optical properties

When separating the epitaxially grown silicon thin-film of a PSI solar cell from the growth substrate, the sintered porous starting layer is still attached to the rear side of the thin-film, as shown in Figs. 2.7 on p. 15 and 2.10 on p. 18. The pores in SPS scatter the incident light and could thus be used to enhance the optical confinement of the cell. But dangling bonds and other defects located at the large internal area of the pore walls give rise to enhanced recombination of the photogenerated charge carriers. Thus, for the optimisation of PSI solar cells, a comprehensive determination of both the optical and the electrical properties of SPS is essential. This chapter focusses on the optical characterisation of SPS, whereas the electronic properties are discussed in Chapter 5.

Modelling the optical constants of composite materials involves effective medium theory [119, 120]. Several authors successfully applied effective medium approximations to describe the refractive index of as-etched PS [121–124]. For example Theiss provides a detailed analysis of the dielectric function of PS by means of effective medium models [125]. During high temperature annealing, the microstructure of PS changes and larger pores with diameters of up to several 100 nm form. The larger pores give rise to light scattering which is not included by the effective medium models. Some authors applied Mie's theory [126] to model light scattering by the voids in SPS [127–130].

In this chapter both approaches, effective medium theory and Mie scattering, are combined. The refractive index and the scattering coefficient of SPS are derived from measurements on free standing SPS films. The results are compared with effective medium approximations and the predictions of Mie's theory, respectively. Finally a Lambertian model for the distribution of the scattered diffuse radiation within the sample is developed and verified by reproducing the measured spectra.

4.1 Sample preparation and optical measurements

The experimental work of this chapter is based on a more detailed analysis of the results of Seel [130], who measured the specular and diffuse component of the reflection and transmission of free standing SPS films. For completeness, the following sections briefly recapitulate the sample preparation as well as the optical characterisation that was done by Seel.

4.1.1 Fabrication of free standing SPS thin-films

The fabrication of free standing SPS films, as performed by Seel in Ref. 130, is similar to the process illustrated in Fig. 3.5 (a) on p. 31. As in this work, the substrates are

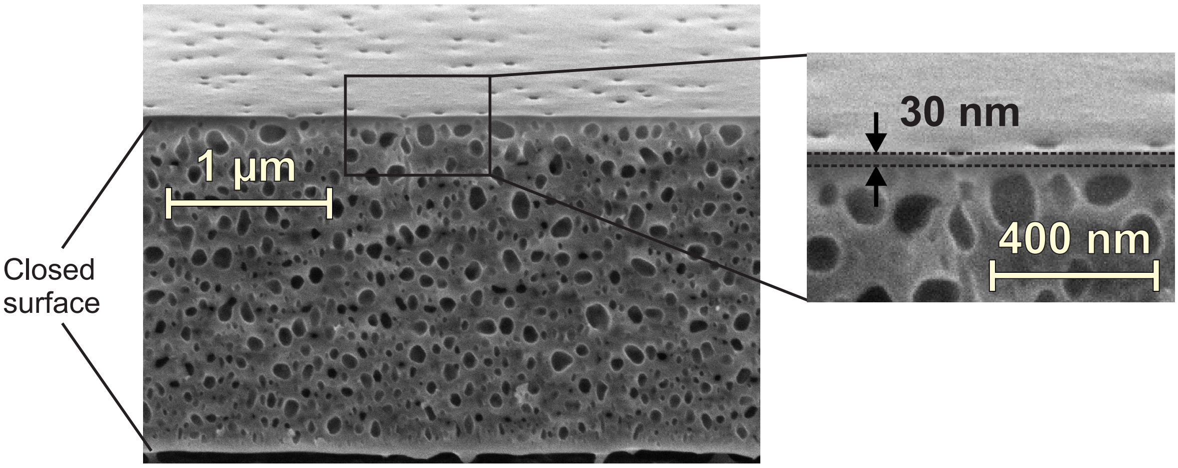

Figure 4.1. SEM image of a 2 µm thick SPS film (Sample S2). During annealing a several 10 nm thick pore-depleted surface layer forms on both sides of the sample. The micrograph is a composite of two images from the same sample. Two different contrast settings were necessary for the cross section and the layer surface.

(100)-oriented p-type CZ wafers with a resistivity of 0.01 Ωcm. The application of an HF(50%) : ethanol = 1:1 (by volume) electrolyte mixture results in a porosity of (30 ± 2) % for an etching current density of 5 mA/cm^2. A variation of the etching time yields nominal film thicknesses of 1 µm, 2 µm and 4 µm for Sample S1, S2 and S3, respectively. For the formation of the separation layer, a 3 second-long current pulse is applied. Table A.2 in Appendix A lists the complete fabrication parameters. During reorganisation of the porous layers at 1000 °C for 20 minutes, spherical pores form and the separation layer mechanically weakens. The use of plastic carriers with a hole of 1 cm in diameter enables the separation of free standing SPS thin-films from the growth substrate. Figure 4.1 presents an SEM image of Sample S2. The image also reveals the several 10 nm thick pore-depleted surface layer that forms during sintering, as explained in Section 2.2.1. An analysis of the cross

Table 4.1. Properties of the samples prepared by Seel (see Ref. 130) and results from a structural analysis by means of an SEM. A lognormal function is fitted to the measured pore size distribution.

	Sample properties			**Lognormal distr.**	
Sample	Porosity P [%]	Thickness W [µm]	Pore diam. d_{avg} [nm]	Median d_{med} [nm]	Width σ
S1	30 ± 2	1.05 ± 0.05	41.7 ± 1.3	34.7	0.47
S2	30 ± 2	2.07 ± 0.1	48.6 ± 0.9	42.7	0.56
S3	30 ± 2	3.92 ± 0.2	45.0 ± 0.8	40.6	0.48

section SEM images permits the determination of the pore size distribution, as described in Section 2.2.3. The average pore diameter is ∼45 nm and varies by ±4 nm for the three analysed samples. Temperature inhomogeneities during the H_2-anneal probably cause this variation. Table 4.1 gives the sample properties as well as the average pore diameter and the median and width of a lognormal function that is fitted to the measured distribution.

4.1.2 Measurement of the specular and diffuse reflection and transmission

A spectrophotometer, that is equipped with an integrating Ulbricht sphere, allows the determination of both the specular and the diffuse component of the reflection and the transmission. A set of lamps in combination with a double Littrow monochromator serves as a monochromatic light source. The typical spectral bandwidth is 1 nm to 20 nm. The system uses a double beam-mode with a primary beam and a monitor beam, as illustrated in Fig. 4.2. The beams originate from the same source and alternately enter the sphere, where the intensities I_{prim} and I_{mon} are detected. The ratio of the two intensities

$$\frac{I_{\mathrm{prim}}}{I_{\mathrm{mon}}} = S \tag{4.1}$$

yields the signal S, thereby eliminating the wavelength-dependence of the light source intensity and that of the detector sensitivity.

The first step of the measurement procedure consists of the collection of the baseline S_{base}. For this measurement, Reflectance Standard 1 with a known reflection R_{std} replaces the sample at the exit port of the primary beam. After measuring the baseline, a second measurement with the primary beam passing through the sphere (entrance and exit port opened) allows the determination of the background signal S_0. Finally, the third measurement S_{samp} is performed using the configuration illustrated on the left hand side of Fig. 4.2. The slightly tilted sample deflects the primary beam onto the diffuse reflecting Standard 2. For all configurations it is assured that no external or back-scattered light enters the sphere. The reflection

$$R = R_{\mathrm{spec}} + R_{\mathrm{diff}} = R_{\mathrm{std}} \cdot \frac{S_{\mathrm{samp}} - S_0}{S_{\mathrm{base}} - S_0} \tag{4.2}$$

follows from three measured signals and contains the specular and the diffuse component. In a second measurement, the removal of Reflectance Standard 2 enables the determination of the diffuse reflection R_{diff}, by allowing the specular component to leave the sphere. The specular reflection $R_{\mathrm{spec}} = R - R_{\mathrm{diff}}$ then follows from Eq. (4.2). In the reflection mode, the sample has to be slightly tilted to allow the separate measurement of R and R_{diff}. The tilt of $\theta = 7°$ results in a small deviation $\Delta R < 10^{-5}$ of the reflection of polished surfaces compared to normal incidence, which is negligible.

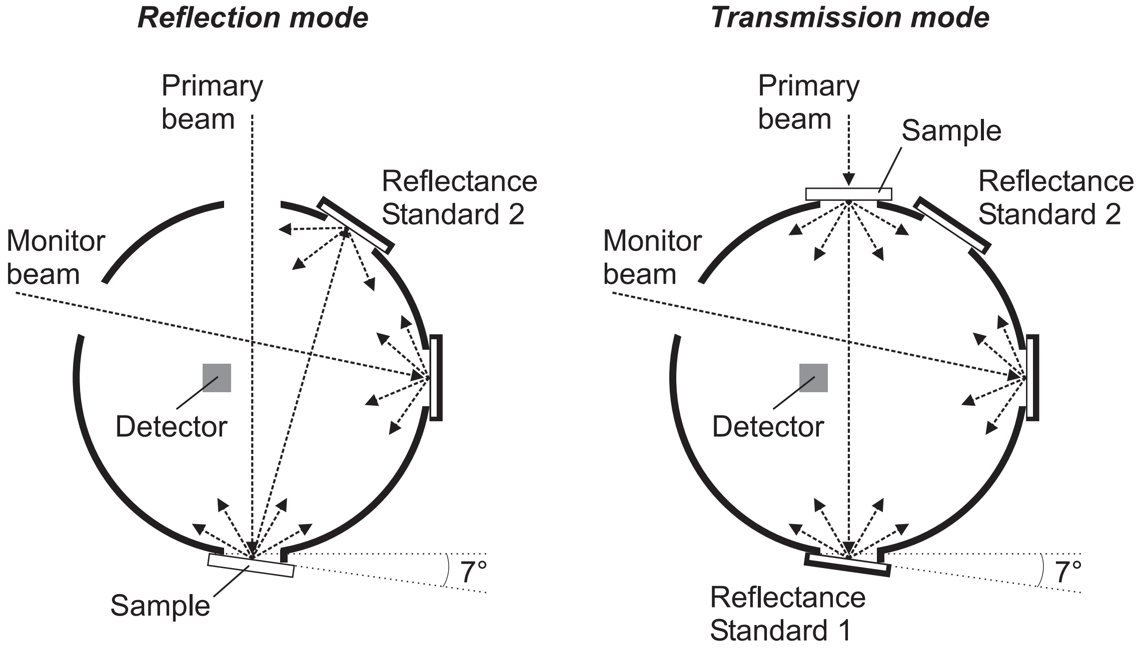

Figure 4.2. Measurement of the diffuse and specular component of the reflection and transmission by means of an integrating sphere. The removal of Reflectance Standard 2 and 1 permits the determination of the diffuse reflection and transmission, respectively, by allowing the specular component to leave the integrating sphere.

The measurements of the transmission mode are similar to those of the reflection mode, however, for the transmission, the unblocked entrance port serves as a 100 % transmission reference and blocking the port allows the measurement of the background signal S_0. The right hand side of Fig. 4.2 exemplifies the sample configuration for the determination of the transmission T. For determining the diffuse component T_{diff}, Reflectance Standard 1 is dismounted.

Figure 4.3 shows the spectra measured for the three Samples S1, S2 and S3 with a nominal thickness of $W = 1\,\mu\text{m}$, $2\,\mu\text{m}$ and $4\,\mu\text{m}$, respectively. The data are taken from Ref. 130. As expected, thicker samples exhibit a decreased transmission and narrower interferences, due to an increased optical thickness $W_{\text{opt}} = W \cdot n$, where n denotes the refractive index. The diffuse components R_{diff} and T_{diff} reach values up to 14 %, confirming light scattering by the sperical voids.

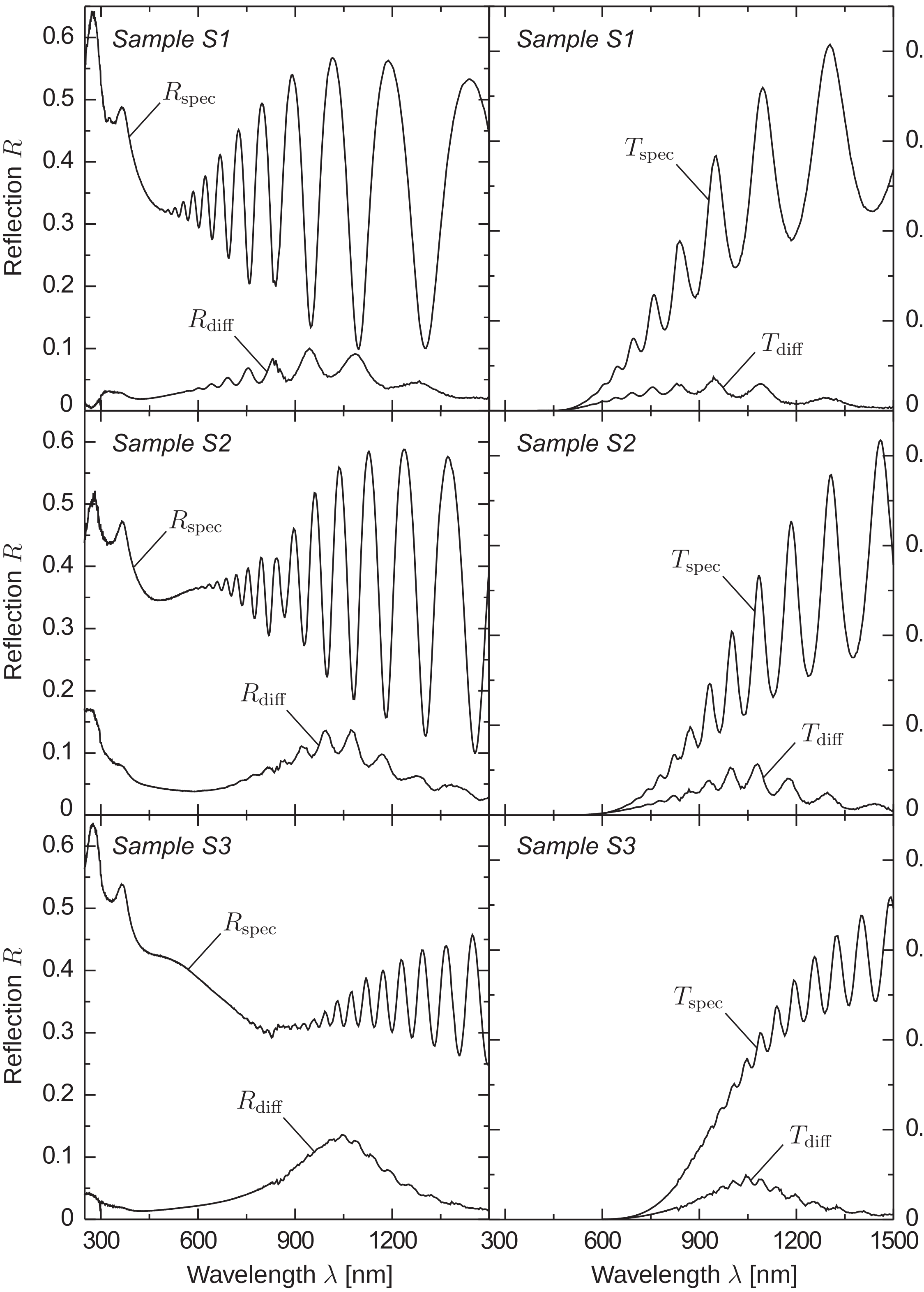

Figure 4.3. Specular and diffuse reflection and transmission of free standing SPS thin-films. The data are taken from Ref. 130. The nominal film thickness is $W = 1\,\mu\text{m}$, $2\,\mu\text{m}$ and $4\,\mu\text{m}$ for Sample S1, S2 and S3, respectively. Note the different y-scales for transmission and reflection.

4.2 Theoretical background

For an absorbing medium, the complex refractive index

$$\tilde{n} = n + \mathrm{i}\,\kappa \tag{4.3}$$

describes the interaction of light with the medium. The imaginary part of $\tilde{n}$, the extinction coefficient

$$\kappa = \frac{\lambda}{4\pi}\alpha, \tag{4.4}$$

accounts for the damping of the light intensity due to absorption. Here α denotes the absorption coefficient and λ is the vacuum wavelength.

4.2.1 Absorption in silicon

Several mechanisms contribute to the absorption of photons in silicon. In the visible range of the spectrum, the most dominant effect is the band-to-band absorption, which is the basic process for semiconductor-based photovoltaics. Photons with energies above the band gap generate excess carriers by shifting electrons from the valence to the conduction band. Silicon is an indirect band gap semiconductor. Thus, the band-to-band absorption process is phonon-assisted resulting in a low absorption coefficient compared to direct band gap semiconductors.

For photon energies below the band gap, the absorption by free carriers within the valence and conduction band dominates. If other effects, such as the absorption by impurities, defects, excitons or lattice vibrations are neglected, the absorption coefficient of silicon

$$\alpha_{\mathrm{Si}} = \alpha_{\mathrm{gen}} + \alpha_{\mathrm{FC}} \tag{4.5}$$

is the sum of the absorption by carrier generation α_{gen} and the free-carrier absorption α_{FC}. This work applies the literature values from Ref. 131 for both the absorption coefficient α_{gen} and the real part of the refractive index n_{Si}. Green's empirical model [132, 133] gives the absorption coefficient for free carriers as

$$\frac{\alpha_{\mathrm{FC}}}{[\mathrm{cm}^{-1}]} = 2.6 \times 10^{-18}\,\frac{n_{\mathrm{e}}}{[\mathrm{cm}^{-3}]}\,\frac{\lambda^3}{[\mathrm{\mu m}^3]} + 2.7 \times 10^{-18}\,\frac{p}{[\mathrm{cm}^{-3}]}\,\frac{\lambda^2}{[\mathrm{\mu m}^2]}. \tag{4.6}$$

Here n_{e} and p denote the concentration of electrons and holes, respectively, and λ is the vacuum wavelength. The classical theory predicts a free carrier absorption coefficient that scales as λ^2 [134]. The λ^3-dependence for absorption by the free electrons in Eq. (4.6) results from including excitations between different conduction bands, which is particularly important for photon energies slightly below the band gap [133]. Figure 4.6 on p. 51

shows a plot of both absorption coefficients, α_{gen} and α_{FC}. The latter is determined from Eq. (4.6) for p-type silicon with a hole concentration of $p = 8\times10^{18}\,\text{cm}^{-3}$, corresponding to a resistivity of $10\,\text{m}\Omega\text{cm}$. The contribution of free electrons is ignored, since $n_{\text{e}} = n_{\text{i}}^2/p \ll p$ for an intrinsic carrier concentration of $n_{\text{i}} \approx 1\times10^{10}\,\text{cm}^{-3}$ [135–137]. Moreover, other high doping effects, such as band gap narrowing, are neglected, due to their small impact on the absorption coefficient [132].

4.2.2 Effective medium models for the refractive index of PS

The optical properties of a non-magnetic material are represented in terms of the complex refractive index $\tilde{n} = \sqrt{\epsilon}$ or by the dielectric function ϵ. Most effective medium approximations are based on the dielectric function ϵ. However, using $\epsilon = \tilde{n}^2$ permits the application of effective medium theory to the complex refractive index $\tilde{n}$ [120].

In general, the effective refractive index of a porous material $\tilde{n}_{\text{eff}}$ depends on the complex refractive index of the host medium $\tilde{n}_{\text{host}} = \tilde{n}_{\text{Si}}$, which is silicon in the present case, and that of the embedded material with $\tilde{n}_{\text{emb}} = 1$ for vacuum. Furthermore the porosity P as well as the topology of the porous structure affect $\tilde{n}_{\text{eff}}$. The Bergman expression [119,123]

$$\tilde{n}_{\text{eff}}^2 = 1 - (1-P)\int_0^1 \frac{g(\chi, P)}{\left(1-\tilde{n}_{\text{Si}}^2\right)^{-1} - \chi}\,\text{d}\chi \tag{4.7}$$

is a general representation for the effective complex refractive index of such a mixture. Here the spectral density $g(\chi, P)$ is a normalised distribution function of so-called geometrical resonances. These resonances characterise the impact of the microstructure on $\tilde{n}_{\text{eff}}$ [120]. For example, the spectral density at $\chi = 0$ reflects the percolation strength $g_0 = g(0, P)$ of the porous structure [125]. The percolation strength quantifies the interconnection of the silicon bridges in the porous network. Generally, all effective medium approximations are representable by Eq. (4.7) using the appropriate $g(\chi, P)$. However, if the spectral density is not known, the first approach is to choose one of the established effective medium models, thereby defining the spectral density in advance.

Sintered porous silicon exhibits larger pores compared to the as-etched state. Empirical studies showed that for a large structure size an effective medium approach with a spectral density representing a high percolation strength should be considered [124,125]. Two of the three most frequently used effective medium models, the Bruggeman approximation [138] and the Looyenga formula [114], comply with this requirement. The third model, the Maxwell Garnett mixing rule [139], might be less suited for SPS, since, in the present case, it represents isolated silicon particles in a vacuum matrix resulting in a vanishing percolation strength for $P > 0$ [124].

The Bruggeman approximation [119, 138]

$$P\frac{1-\tilde{n}_{\text{eff}}^2}{1+2\tilde{n}_{\text{eff}}^2} + (1-P)\frac{\tilde{n}_{\text{Si}}^2 - \tilde{n}_{\text{eff}}^2}{\tilde{n}_{\text{Si}}^2 + 2\tilde{n}_{\text{eff}}^2} = 0 \tag{4.8}$$

with the solution

$$\tilde{n}_{\mathrm{eff}}^2 = \frac{1}{4}\left(\left(3P\left(1-\tilde{n}_{\mathrm{Si}}^2\right)+2\tilde{n}_{\mathrm{Si}}^2-1\right)+\sqrt{\left(3P\left(1-\tilde{n}_{\mathrm{Si}}^2\right)+2\tilde{n}_{\mathrm{Si}}^2-1\right)^2+8\tilde{n}_{\mathrm{Si}}^2}\right) \tag{4.9}$$

is adequate for irregularly shaped particles and low porosities and showed good agreement with experimental data for as-etched meso PS [121,122,125]. The Looyenga model

$$\tilde{n}_{\mathrm{eff}}^{2/3} = (1-P)\,\tilde{n}_{\mathrm{Si}}^{2/3} + P \tag{4.10}$$

is also suitable for high porosities and was already applied to SPS [140,141]. The Maxwell Garnett formula [139]

$$\frac{1-\tilde{n}_{\mathrm{eff}}^2}{2+\tilde{n}_{\mathrm{eff}}^2} + (1-P)\,\frac{\tilde{n}_{\mathrm{Si}}^2-1}{\tilde{n}_{\mathrm{Si}}^2+2} = 0 \tag{4.11}$$

with the solution

$$\tilde{n}_{\mathrm{eff}}^2 = \frac{(3-2P)\,\tilde{n}_{\mathrm{Si}}^2+2P}{P\,\tilde{n}_{\mathrm{Si}}^2+3-P}, \tag{4.12}$$

predicts lower values for $\tilde{n}_{\mathrm{eff}}$ than the other two mixing rules. For an in-depth discussion of effective medium theory and its application to PS see Ref. 120,123,125.

Figure 4.4 shows the predictions of the effective medium models for the real and the imaginary part of the refractive index of PS at $\lambda = 600\,\mathrm{nm}$. For comparison the simple linear interpolation

$$\tilde{n}_{\mathrm{eff}} = (1-P)\,\tilde{n}_{\mathrm{Si}} + P \tag{4.13}$$

that corresponds to

$$n_{\mathrm{eff}} = (1-P)\,n_{\mathrm{Si}} + P \qquad \text{and} \qquad \kappa_{\mathrm{eff}} = (1-P)\,\kappa_{\mathrm{Si}} \tag{4.14}$$

is plotted as well. Both the Bruggeman approximation and the Looyenga mixing rule lie close to the linear interpolation, in particular for low porosities. For porosities $P < 30\,\%$ and a wavelength between 300 nm and 1500 nm, the linear calculation of Eq. (4.13) deviates only 3 % from the Bruggeman formula and 10 % from the Looyenga model. Thus, when restricting to porosities below 30 %, the simple interpolation might be used instead of the more complicated Bruggeman or Looyenga expressions. The Maxwell Garnett mixing rule yields significantly lower values compared to the other models, due to a reduced percolation strength g_0.

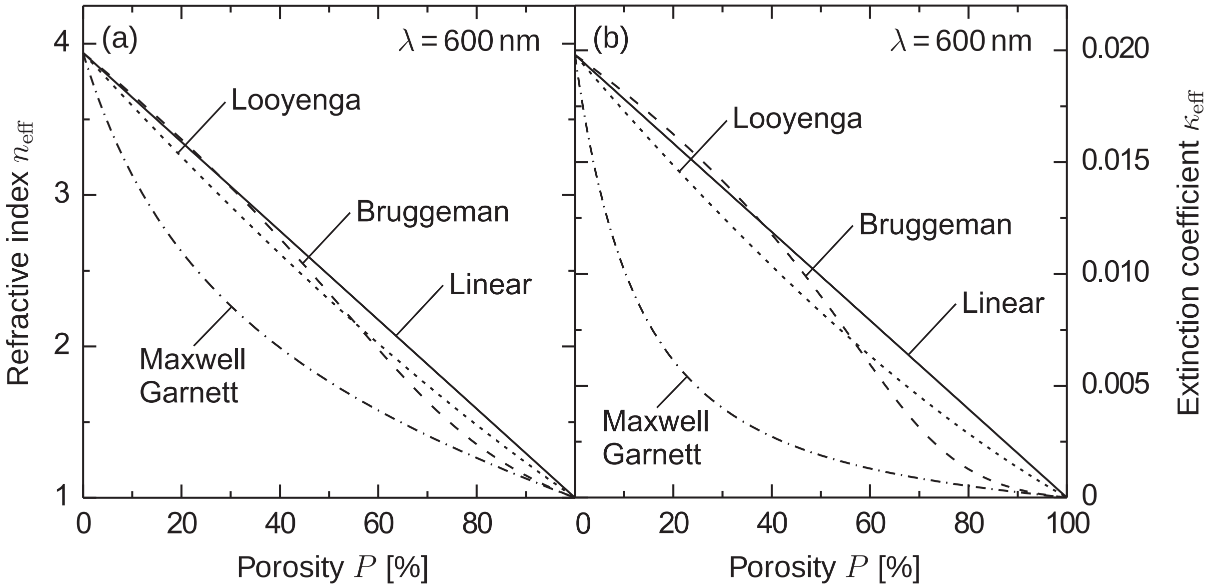

Figure 4.4. Effective medium predictions for the refractive index n_{eff} and extinction coefficient κ_{eff} of porous silicon at $\lambda = 600\,\text{nm}$. The straight solid lines represent the linear interpolation from Eq. (4.13).

4.2.3 Mie scattering

The effective medium models introduced above do not account for light scattering by the cavities of the microstructure. However, the SPS samples analysed in Section 4.1.2 show a significant level of diffuse reflection and transmission indicating scattering by the spherical voids. The increased pore size of SPS compared to as-etched PS requires the consideration of light scattering, since the pore diameter approaches the wavelength $\lambda' = \lambda/n_{\text{Si}}$ within the silicon bulk. The pores in SPS have a close to spherical shape, which suggests the application of Mie's theory [126].

The Mie theory is a complete analytical solution of the Maxwell equations and describes the scattering of a plane electromagnetic wave by an isotropic spherical particle embedded in a homogeneous non-absorbing medium. Kokhanovsky [142] provides a complete derivation of the solution to the Mie problem. The scattering efficiency Q_{sca} of a single particle is calculated in Appendix B.1. It is a dimensionless number that describes the scattering cross sectional area of a sphere with respect to its geometric cross sectional area πr^2, where r is the sphere radius. Two quantities determine Q_{sca}, the size parameter

$$z = \frac{\pi d}{\lambda'} = \frac{\pi d\, n_{\text{host}}}{\lambda}, \tag{4.15}$$

where d is the diameter of the sphere, λ' the wavelength in the host medium, λ the vacuum wavelength, and n_{host} the refractive index of the non-absorbing host medium, as well as

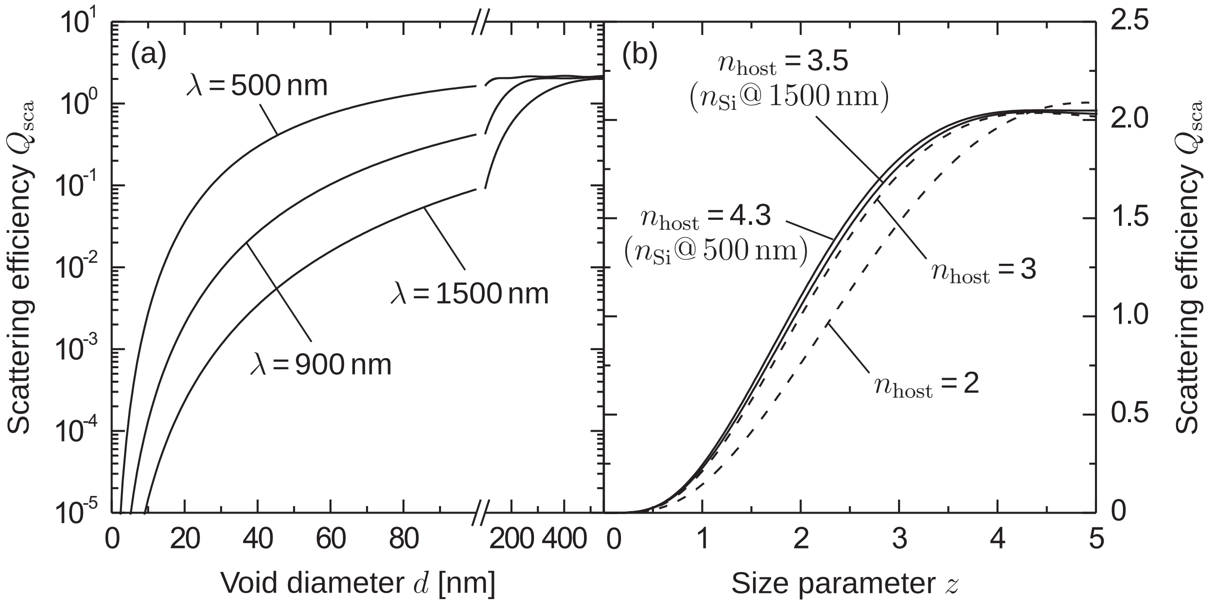

Figure 4.5. Scattering efficiency of spherical voids embedded in bulk silicon for different wavelengths after Eq. (B.1). The corresponding refractive index is 4.3, 3.6 and 3.5 for $\lambda = 500$ nm, 900 nm and 1500 nm, respectively. When plotted versus the size parameter $z = \pi d\, n_{\mathrm{host}}/\lambda$, the curves nearly coincide. Only for $n_{\mathrm{host}} < 3$, a reduction of the scattering efficiency due to an increased refractive index ratio $w = 1/n_{\mathrm{host}}$ emerges, as illustrated by the dashed lines.

the refractive index ratio

$$w = \frac{\tilde{n}_{\mathrm{emb}}}{n_{\mathrm{host}}} = \frac{n_{\mathrm{emb}} + \mathrm{i}\kappa_{\mathrm{emb}}}{n_{\mathrm{host}}} \tag{4.16}$$

with $\tilde{n}_{\mathrm{emb}}$ being the complex refractive index of the embedded spherical particle. In Fig. 4.5 (a) the scattering efficiency Q_{sca} of vacuum voids ($\tilde{n}_{\mathrm{emb}} = 1$) embedded in bulk silicon is plotted as a function of the void diameter d. This calculation ignores the imaginary part of $\tilde{n}_{\mathrm{Si}}$. For all considered wavelengths, the scattering efficiency strongly increases with the size of the voids. For example at $\lambda = 900$ nm the scattering efficiency rises from 8.4×10^{-6} to 5.7×10^{-2} when enlarging the voids from $d = 5$ nm to $d = 50$ nm. The strong dependence on the pore size reveals that scattering in porous silicon is important in the sintered state, whereas it might be negligible for the small pores of the as-etched material. The scattering efficiency saturates at $Q_{\mathrm{sca}} \approx 2$ if the diameter approximates the wavelength $\lambda' = \lambda/n_{\mathrm{Si}}$ in the host medium or, equivalently, if the size parameter z approaches π [143–147]. Figure 4.5 (b) shows the same curves plotted versus the size parameter. For comparison the scattering efficiencies for a host medium with $n_{\mathrm{host}} = 2$ and $n_{\mathrm{host}} = 3$ are also shown. The curves for bulk silicon almost coincide, showing that in the case of $n_{\mathrm{host}} > 3$, the size parameter z is the relevant wavelength-dependent quantity, whereas the wavelength-

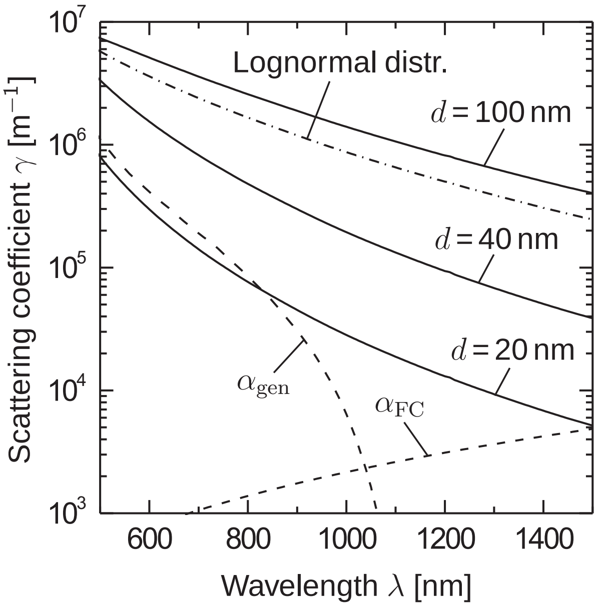

Figure 4.6. Scattering coefficient of vacuum voids embedded in bulk silicon for three different monodispersive distributions (solid lines) and for a lognormal distribution ($d_{\mathrm{med}} = 35$ nm, $\sigma = 0.5$, dash-dotted line) after Eq. (4.17). The porosity is $P = 30\,\%$. For comparison, the band-to-band absorption coefficient α_{gen} of bulk silicon from Ref. 131 as well as the free-carrier absorption coefficient α_{FC} for $p = 8\times10^{18}\,\mathrm{cm}^{-3}$ after Eq. (4.6) are plotted as dashed lines.

dependent refractive index ratio $w = 1/n_{\mathrm{host}}$ from Eq. (4.16) has only a small impact on Q_{sca}.

For a polydispersed medium containing spheres with the size distribution $f\,(r)$, the scattering coefficient [142]

$$\gamma = N_{\mathrm{pore}} \int_0^\infty \pi r^2 Q_{\mathrm{sca}}(r) f(r) \mathrm{d}r \tag{4.17}$$

results from weighting the scattering cross sectional area $\pi r^2 Q_{\mathrm{sca}}$ with the distribution function $f\,(r)$. Here N_{pore} denotes the number of pores per unit volume that follows from the porosity P as

$$N_{\mathrm{pore}} = \frac{P}{\langle V_{\mathrm{pore}} \rangle} \tag{4.18}$$

where

$$\langle V_{\mathrm{pore}} \rangle = \int_0^\infty \frac{4\pi}{3} r^3 f\,(r)\,\mathrm{d}r. \tag{4.19}$$

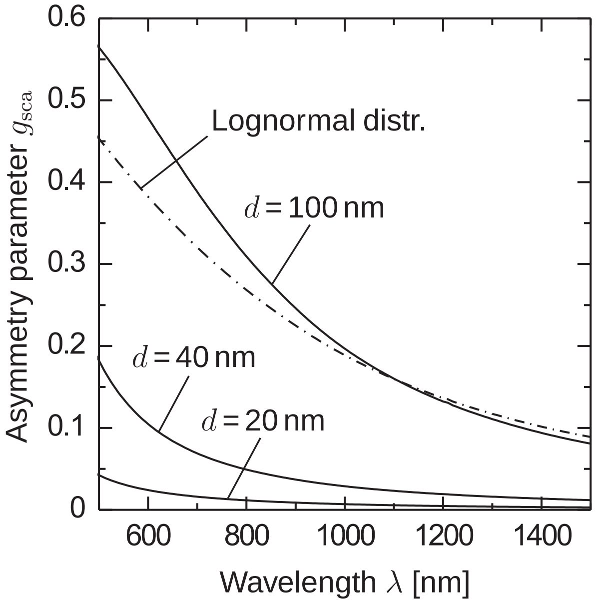

Figure 4.7. Asymmetry parameter for monodisperse vacuum voids embedded in bulk silicon for different void diameters d (solid lines) and for a lognormal distribution ($d_{\mathrm{med}} = 35\,\mathrm{nm}$, $\sigma = 0.5$, dash-dotted line) after Eq. (4.20).

is the average void volume. Figure 4.6 shows the scattering coefficient γ for monodisperse spheres $f(r) = \delta(2r - d)$ with different diameters d and for a lognormal size distribution with the median $d_{\mathrm{med}} = 35\,\mathrm{nm}$ and the width $\sigma = 0.5$, which is typical for pores in SPS. For void diameters $d \geq 40\,\mathrm{nm}$, the scattering coefficient γ clearly exceeds the absorption coefficient α_{Si} in the considered wavelength range. Thus, one expects scattering to dominate over absorption in SPS leading to multiple scattering processes.

A quantity that describes the directional distribution of the scattered radiation is the asymmetry parameter g_{sca}, that is derived in Section B.1. This parameter is unity for a non-deflected wave that propagates parallel to the impinging wave, whereas it is zero for isotropically scattered radiation. In Fig. 4.7 the asymmetry parameter for vacuum spheres embedded in bulk silicon is plotted as a function of the wavelength. The anisotropy is highest for large voids and short wavelengths. For void diameters $d < 40\,\mathrm{nm}$ and wavelengths above 600 nm the asymmetry parameter is $g_{\mathrm{sca}} \leq 0.1$ corresponding to nearly isotropic scattering. The asymmetry parameter of a polydispersed medium results from the convolution [142]

$$\langle g_{\mathrm{sca}} \rangle = \frac{\int_0^\infty \pi r^2 Q_{\mathrm{sca}}(r) g_{\mathrm{sca}}(r) f(r)\,\mathrm{d}r}{\int_0^\infty \pi r^2 Q_{\mathrm{sca}}(r) f(r)\,\mathrm{d}r}. \tag{4.20}$$

The dash-dotted line in Fig. 4.7 represents the asymmetry parameter for a representative lognormal distribution. Due to the inclusion of the scattering cross sectional area $\pi r^2 Q_{\mathrm{sca}}$

as a weighting factor in Eq. (4.20), larger pores give a larger contribution to $\langle g_{\mathrm{sca}} \rangle$. Thus, scattering by the large voids dominates resulting in a higher asymmetry of the scattered radiation, compared to the scattering by monodisperse voids with a diameter comparable to the average diameter $d_{\mathrm{avg}} = 39.7\,\mathrm{nm}$ of the distribution.

When applying Mie's theory to bulk silicon, care should be taken, since the Mie calculation assumes an undamped impinging wave, whereas silicon is an absorbing medium. Several authors extended the Mie problem to an absorbing host medium [148–151]. Their calculations showed that for an absorption length $L_\alpha = 1/\alpha$ that is much larger than the size of the sphere, the effect of absorption in the host medium on the scattering efficiency is negligible. Thus, for silicon as the host medium and voids with $d < 100\,\mathrm{nm}$, the classical Mie calculation, that uses only the real part of $\tilde{n}_{\mathrm{Si}}$, yields correct results, when restricting the spectral range to wavelengths above 500 nm, where $L_\alpha > 1\,\mu\mathrm{m}$.

4.2.4 Optical model for specular and diffuse radiation

The interaction of any device with incident light depends on the optical constants of the involved media and on the device geometry. For structures that exhibit light scattering, a model describing the distribution of the scattered light intensity within the device is required. Under some approximations, the radiative-transfer equation [142] provides a solution to this problem. However, radiative-transfer theory neglects interference effects of the non-scattered light that are particularly important for thin-film devices. A time-consuming ray-tracing analysis [152] does not consider interference effects either. Ghannam and Abouelsaood combined Mie scattering with a coherent random medium approach [127, 128]. But their model is limited to the case where the distance between the pores is significantly larger than their average size, an assumption that might be violated in the case of SPS. Seel and Brendel [129, 130] incorporated Mie scattering into a coherent model for planar films. Their concept is applied in this work, extended by a model that describes the distribution of the scattered diffuse radiation within the sample.

Figure 4.8 illustrates the structure of the optical model developed in this work. It consists of two parts, a specular calculation and a consideration of the scattered diffuse light intensity. The mathematical implementation is explained in detail in Sections B.3 and B.4 of Appendix B. Similar to the approach of Seel and Brendel [129, 130], the specular part of the present model uses the coherent transfer matrix technique [153] for the determination of the specular reflection R_{spec} and specular transmission T_{spec} of a planar multilayer stack that consists of N layers, each with the thickness W_j, the refractive index n_j, the absorption coefficient α_j and the scattering coefficient γ_j. The calculation assumes normal incidence and accounts for interference effects. In addition to R_{spec} and T_{spec}, the specular model calculates the depth-resolved absorption profile $A(x)$ for the whole stack. This calculation applies the scattering coefficient as an additional absorption coefficient and thus accounts for all processes that attenuate the specular intensity, that is, absorption as well as scattering. Therefore the absorption profile $A(x) = A_{\mathrm{spec}}(x) + I_{\mathrm{sca}}(x)$ consists of the initial or specular absorption $A_{\mathrm{spec}}(x)$ that includes the absorption processes, as for example photogeneration and free-carrier absorption in the case of silicon, as well as the

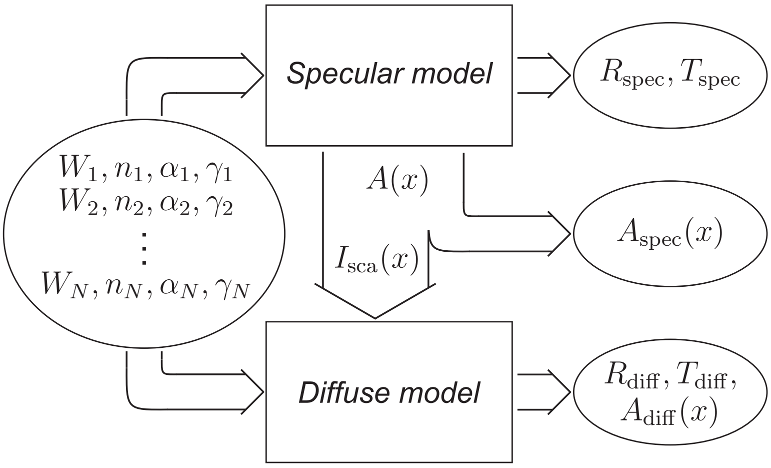

Figure 4.8. Structure of the developed optical model. The model is derived and explained in detail in Section B.4 of Appendix B.

scattered intensity $I_{\text{sca}}(x)$, that is similar to an absorption profile and describes the spatial distribution of the primarily scattered radiation. Since an incident photon is in the first place either reflected, transmitted, absorbed or scattered, it follows that

$$R_{\text{spec}} + T_{\text{spec}} + \int_0^W \left(A_{\text{spec}}(x) + I_{\text{sca}}(x)\right) \mathrm{d}x = 1, \tag{4.21}$$

where $W = \sum_j W_j$.

In a second step, the primarily scattered intensity $I_{\text{sca}}(x)$ is passed to a separate diffuse model that evaluates the distribution of the diffuse radiation propagating at oblique angles within the multilayer stack and apportions the initially scattered radiation among the diffuse absorption $A_{\text{diff}}(x)$, diffuse reflection R_{diff} and diffuse transmission T_{diff}. Unlike the model of Seel [130], that considers just one single scattering event and assumes a homogeneous distribution of the scattered intensity within the sample, the present model determines the depth-resolved distribution of the scattered radiation thereby accounting for multiple scattering processes and reflection at internal and external interfaces. For this purpose the model calculates the probability for a photon scattered at the position x' to be

- transmitted through the front or rear surface, thereby contributing to the diffuse reflection R_{diff} and transmission T_{diff}, respectively
- reflected back to the same position x' by reflection at internal or external interfaces
- absorbed at any position x within the multilayer stack, thereby contributing to the diffuse absorption $A_{\text{diff}}(x)$, or re-scattered at x.

The distribution $I_1(x)$ of the diffuse intensity after the first internal scattering or reflection event then follows from the initial diffuse intensity profile $I_{\text{sca}}(x)$ and the probabilities for internal reflection and re-scattering. The new distribution $I_1(x)$ is then in turn used to calculate the distribution after two events $I_2(x)$, and so forth. This iterative procedure converges for an infinite number of scattering or reflection events and permits the determination of the cumulated diffuse reflection R_{diff}, diffuse transmission T_{diff} and the diffuse absorption profile $A_{\mathrm{diff}}(x)$. Here,

$$R_{\mathrm{diff}} + T_{\mathrm{diff}} + \int_0^W A_{\mathrm{diff}}(x)\,\mathrm{d}x = \int_0^W I_{\mathrm{sca}}(x)\,\mathrm{d}x \tag{4.22}$$

is valid since an initially scattered photon is either absorbed or leaves the stack as diffuse reflection or transmission. In combination with Eq. (4.21)

$$R_{\mathrm{spec}} + R_{\mathrm{diff}} + T_{\mathrm{spec}} + T_{\mathrm{diff}} + \int_0^W \left(A_{\mathrm{spec}}(x) + A_{\mathrm{diff}}(x)\right)\mathrm{d}x = 1 \tag{4.23}$$

follows.

For the calculation of the above described probabilities, the model applies a Lambertian absorption scheme assuming totally randomised isotropic radiation. The reflection and transmission of the randomised light at internal and external interfaces follows from including the angle-dependent Fresnel transmission into the angle-averaging integral of the Lambertian transmission (see Eq. (B.77), Section B.4.3), as for example suggested by Green [154]. The applied Lambertian absorption scheme corresponds to totally isotropic diffuse radiation and implicates the following assumptions:

- complete randomisation of the initially scattered specular intensity as well as the subsequently scattered radiation
- complete randomisation of the diffuse intensity after reflection at an internal or external interface
- complete randomisation after transmission through such an interface.

In the case of Mie scattering, the scattering processes are not totally isotropic, as explained in Section 4.2.3 above. Thus, the assumption of isotropic scattering is not strictly fulfilled for the initial scattering event. However, since scattering is predominant in SPS, each photon is multiply scattered and after a few scattering events, the radiation is completely randomised.

The angular distribution of the diffuse radiation changes upon reflection or transmission at an interface between two adjacent layers, according to Snell's law and the Fresnel equations. As stated above, the model assumes isotropically distributed radiation *after* a reflection or transmission event. This assumption is justified if the reflected or transmitted photons are again randomised by a subsequent scattering event before they are absorbed or reach the next interface. This is the case if the scattering length $L_\gamma = 1/\gamma$ is not significantly larger than both L_α and the effective layer thickness $2W$, which is an acceptable approximation for the analysed samples, where $L_\gamma < 4$ µm for wavelength below 1000 nm.

4.3 Determination of the optical constants

In this section the optical constants of SPS are determined from the measured specular spectra R_{spec} and T_{spec}. For the use of SPS as a light diffuser and back reflector in PSI solar cells, the spectral range where the absorption length L_α in silicon approaches the thickness of the cell is most relevant. Therefore the analysis of this section focusses on wavelengths above 500 nm, where $L_\alpha > 1\,\mu\mathrm{m}$ and a significant fraction of the incident light reaches the back of the cell.

4.3.1 Envelope method

The envelope method [155] allows the determination of the refractive index n, the absorption coefficient α and the film thickness W solely from the fringe pattern of the transmission spectrum of a homogeneous, weakly absorbing, parallel-faced film surrounded by a non-absorbing medium. For the application of the procedure, the variation of the optical constants n and α of the film with the wavelength λ should be small and the contribution of the extinction coefficient $\kappa = \lambda/(4\pi\alpha)$ to the interface reflection negligible (see Eq. (B.14), Section B.2). The latter is an acceptable approximation if $\kappa < 0.1$ [155].

For air or vacuum as the surrounding medium, the refractive index [155]

$$n = \sqrt{K + \sqrt{K^2 - 1}} \tag{4.24}$$

with

$$K = 1 + 2\frac{T_{\mathrm{max}} - T_{\mathrm{min}}}{T_{\mathrm{max}} T_{\mathrm{min}}}, \tag{4.25}$$

follows from the upper and lower envelope T_{max} and T_{min}, respectively, of the oscillating specular transmission T_{spec}. Both T_{max} and T_{min} are continuous functions of the wavelength λ, as exemplified in Fig. 4.9. The determined refractive index n enables the calculation of the layer thickness [155]

$$W = \frac{1}{2} \frac{\Delta m \lambda_1 \lambda_2}{n(\lambda_1)\lambda_2 - n(\lambda_2)\lambda_1} \tag{4.26}$$

from the positions λ_1 and λ_2 of any two extrema as well as the corresponding refractive indices $n(\lambda_1)$ and $n(\lambda_2)$. Here, Δm is the step in the ordinal number between the maximum or minimum at λ_1 and that at λ_2, for example $\Delta m = \pm 0.5$ for a maximum and its adjacent minimum (or vice versa) and $\Delta m = \pm 1$ for two consecutive maxima or minima. Thus, for each pair of extrema, a value for the film thickness W is obtained.

The solid and partly dotted line in Fig. 4.10 represents the results for the refractive index n from Eq. (4.24) for Sample S1. The error bars result from the accuracy estimation given in Ref. 155 assuming an absolute uncertainty of ±2 % for the transmission measurement.

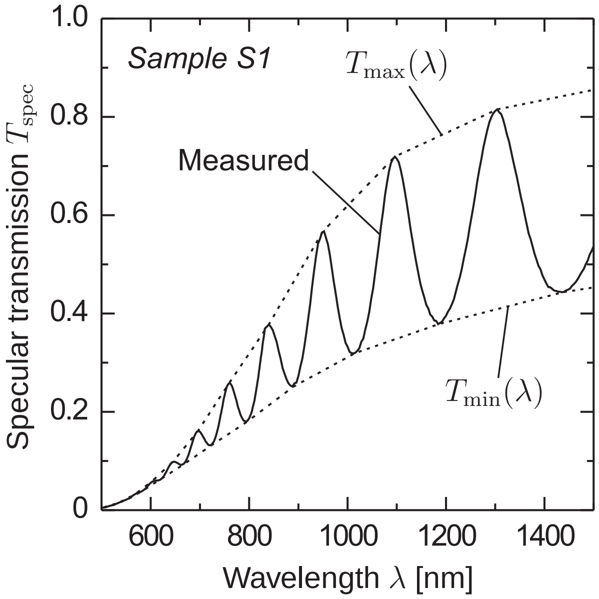

Figure 4.9. Transmission spectrum for Sample S1 (solid line) and envelopes $T_{\max}$ and $T_{\min}$ (dashed lines) that follow from a linear interpolation between the extrema and an estimation beyond the last maximum and minimum on the right hand side.

The known thickness of the samples enables a validation of the results obtained by the envelope method. For this purpose Eq. (4.26) is applied to determine the film thickness using two adjacent extrema at λ_1 and λ_2. The agreement of the obtained thickness with the value determined with the SEM (Table 4.1 on p. 42) is a measure for the correctness of the envelope procedure in the wavelength interval $\lambda_1 < \lambda < \lambda_2$. The solid part of the line in Fig. 4.10 corresponds to an agreement of the thickness values within $\pm\,20\,\%$, whereas for the dotted part of the line, the discrepancy is $> 20\,\%$. Thus, for Sample S1 the envelope method gives reliable results only for wavelengths $\lambda > 1000\,\mathrm{nm}$. In the case of Sample S2, a deviation between -40 % and +70 % is obtained for wavelengths $900\,\mathrm{nm} < \lambda < 1500\,\mathrm{nm}$, whereas for Sample S3, the envelope procedure overestimates the thickness by a factor of 2 to 3.

This overestimation is explained as follows. As apparent from Fig. 4.3 on p. 45, the interferences are weaker for Sample S3 compared to the other two samples. This reduces the distance between the envelopes $T_{\max}$ and $T_{\min}$ giving a lower value for the refractive index n from Eqs. (4.24) and (4.25). To reproduce the measured spacing of the interference extrema, a high value for W has to compensate for the low refractive index in Eq. (4.26).

There are several possible effects that could reduce the accentuation of the interference extrema, as observed in the measurements. Firstly, the samples are not perfectly planar and the measurement averages over sample areas with slightly different thicknesses. This averaging flattens the curve, since the thickness of the sample determines the position of the extrema. Secondly, the presence of the pores could disturb the phase of the non-scattered photons, that are reflected back and forth within the sample. The loss of phase

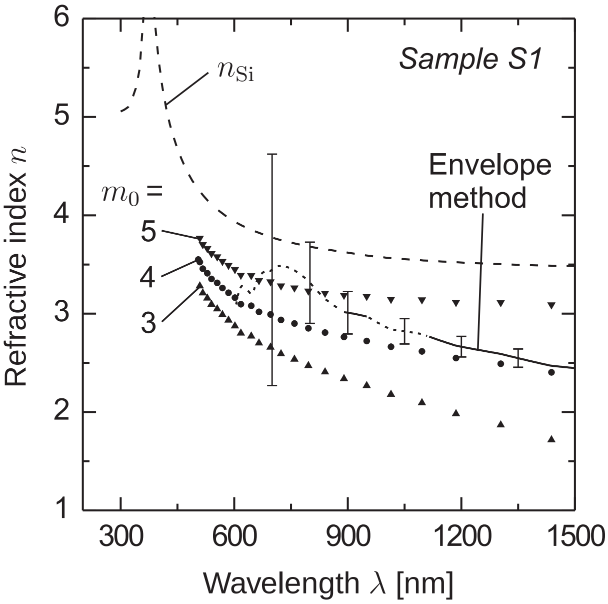

Figure 4.10. Refractive index of Sample S1 determined with the envelope method (solid line) and possible values that follow from the positions of the interference extrema assuming ordinal numbers with $m \geq m_0$ (symbols). The three symbol-curves correspond to different m_0-values. The bulk value n_{Si} is shown for comparison (dashed line).

information reduces the coherence length yielding weaker pronounced interferences. Both effects are stronger for thicker samples, which constricts the application of the envelope procedure to the thicker samples. Finally, the envelope method assumes a homogeneous film, whereas the samples feature a several 10 nm thick layer almost free of pores at the surface, as apparent from Fig. 4.1 on on p. 42. The refractive index of this surface layer is close to the bulk value of silicon, whereas for the porous bulk, a reduced refractive index is expected. The presence of this pore-depleted surface layer affects the internal reflection at the sample surface. But the envelope method determines the refractive index solely from the reflection at the sample surfaces. Therefore a more detailed analysis is required that, for example, includes the known thickness of the samples and accounts for the pore-depleted surface layer.

4.3.2 Advanced analysis of the measured spectra

The positions of the interference maxima and minima contain information on the optical thickness and thus on the refractive index n. Constructive interference for the transmitted light requires an optical thickness that is a multiple of the wavelength. Thus, the peak wavelength $\lambda_{\mathrm{T_{max}}}$ for maximum transmission (minimum reflection) fulfils

$$m \cdot \lambda_{\mathrm{T_{max}}} = n \cdot 2W, \tag{4.27}$$

where $m = 1, 2, 3, \ldots$ is the ordinal number. Consequently, for destructive interference and minimum transmission (maximum reflection)

$$\left(m - \frac{1}{2}\right) \cdot \lambda_{\mathrm{T_{min}}} = n \cdot 2W \tag{4.28}$$

is valid. Here, a film with homogeneous optical properties is assumed. This assumption is justified in the present case, since the pore-depleted surface layer does not significantly affect the optical thickness. Equations (4.27) and (4.28) enable the determination of the refractive index n from the positions $\lambda_{\mathrm{T_{max}}}$ and $\lambda_{\mathrm{T_{min}}}$ and the sample thickness W. However, the associated ordinal number m is not known in advance. Figure 4.10 shows the refractive index calculated from the peak positions of the specular transmission and reflection for Sample S1 together with the results from the envelope method. The three curves correspond to different m_0-values, where $m \geq m_0$. Each value for m_0 represents a particular refractive index curve. Higher values than $m_0 = 5$ yield a refractive index $n > n_{\mathrm{Si}}$ and are therefore not considered, whereas $m_0 < 3$ results in implausible values close to and below unity.

For the determination of the correct ordinal number m_0, a more detailed analysis of the measured spectra is necessary. For this purpose, the coherent transfer matrix model from Appendix B.3 is used to simulate the specular reflection and transmission. The reflection and transmission of a single homogeneous film depend on the film thickness W, the refractive index n and the absorption coefficient α. Thus, when choosing the value of m_0 (and thereby n) in advance, the remaining unknown parameter is the absorption coefficient α, since the film thickness follows from the SEM analysis. The thickness values from Table 4.1 on p. 42 and the refractive index data corresponding to a particular m_0 value (see Fig. 4.10) are used as input parameters for the model and, for each wavelength, the unknown absorption coefficient is varied until the best agreement with both the measured specular reflection and the transmission is achieved. Here, the best agreement is defined as the lowest value for $\sqrt{(\Delta R_{\mathrm{spec}})^2 + (\Delta T_{\mathrm{spec}})^2}$, where ΔR_{spec} and ΔT_{spec} denote the difference between the simulated and measured spectra. Section 4.3.4 below deals with the determined absorption coefficient. The deviation

$$\sigma_{\mathrm{avg}} = \frac{\int_{\lambda_{\mathrm{min}}}^{\lambda_{\mathrm{max}}} \sqrt{[\Delta R_{\mathrm{spec}}(\lambda)]^2 + [\Delta T_{\mathrm{spec}}(\lambda)]^2}\, \mathrm{d}\lambda}{\lambda_{\mathrm{max}} - \lambda_{\mathrm{min}}} \tag{4.29}$$

follows from averaging over the relevant wavelength range. The value for σ_{avg} reflects the compatibility of the applied optical constants with the measured spectra. Hence, the ordinal number m_0 that yields the lowest deviation σ_{avg} corresponds to the refractive index curve that gives the best agreement with the measured data.

So far, the evaluation described above does not account for the pore-depleted layer at the surface of the samples. However, this layer affects the internal reflection at the sample surface, as outlined in Section 4.3.1. Thus, a more advanced analysis is performed where

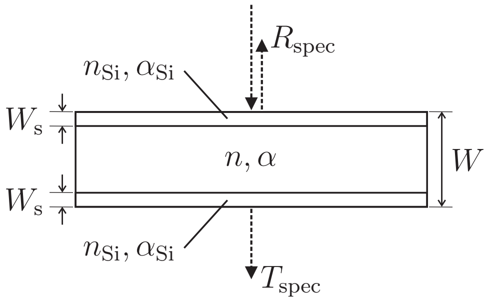

Figure 4.11. Sample structure for the optical model that is used to determine the optical constants. The simulation includes a thin layer of bulk silicon at both sample surfaces. The coherent transfer matrix algorithm from Section B.3 calculates the specular reflection and transmission of such a structure.

the optical model includes a thin pore-depleted surface layer of bulk silicon on both sides of the sample. Figure 4.11 illustrates the assumed sample structure. Here, the bulk values n_{Si} and α_{Si} are applied for the surface layer. The inclusion of the surface layer into the optical model requires a slight reduction of the effective refractive index n of the film to keep the interference maxima and minima at constant positions. In Fig. 4.12 the deviation σ_{avg} is plotted versus the thickness W_{s} of the surface layer assuming different values for m_0 and thus different refractive index curves. For sample S1, a 20 nm thick surface layer in combination with the refractive index that corresponds to $m_0 = 4$ yields the lowest value for σ_{avg}. This refractive index curve also complies with the results from the envelope method

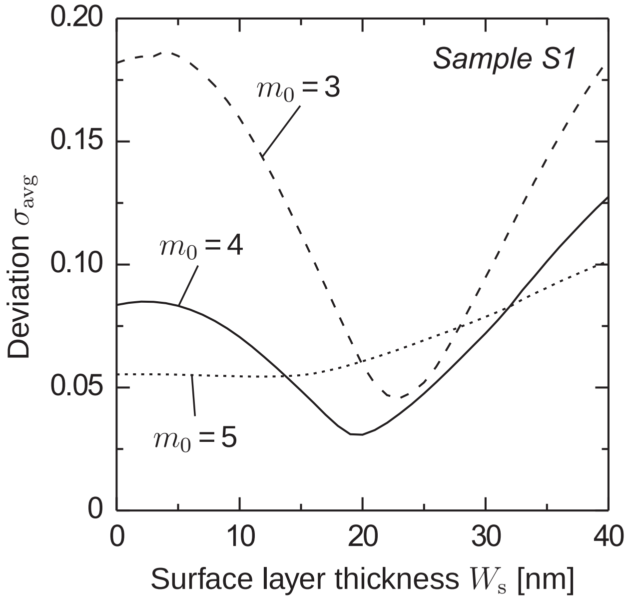

Figure 4.12. Deviation σ_{avg} between the measured and simulated specular reflection and transmission. The incorporation of the surface layer results in a lower deviation compared to a single homogeneous film ($W_{\text{s}} = 0$). Here, the refractive index curve corresponding to $m_0 = 4$ (see Fig. 4.10) in combination with $W_{\text{s}} = 20$ nm exhibits the lowest deviation.

(see Fig. 4.10). As apparent from Fig. 4.12, the incorporation of the surface layer results in a lower deviation compared to a single homogeneous film ($W_s = 0$) confirming the necessity of the inclusion of the surface layer into the optical model. A similar procedure gives the refractive index for the two remaining Samples S2 and S3. The values for W_s that yield the lowest deviation σ_{avg} range from 15 nm to 30 nm, which is of the same order as the thickness values of 30 nm (front surface) to 60 nm (rear surface) that are obtained from an analysis of the SEM images, as illustrated in Fig. 4.1 on p. 42. The model assumes identical thickness values for the front and the rear surface layer. The thickness of 15 nm to 30 nm obtained from the fit of the model are closer to the value of 30 nm measured for the front surface layer, since the front surface has a stronger impact on the specular reflection and transmission compared to the rear surface. Besides the value for m_0, that permits the determination of the refractive index, the applied evaluation method also yields a value for the absorption coefficient α, as explained above. These results are discussed in Section 4.3.4 below.

4.3.3 Refractive index

Figure 4.13 shows the effective medium predictions from Section 4.2.2 together with the refractive indices that result from the analysis of the three samples described in the previous section. The results for all samples are similar, as expected, since only the film thickness is varied from Sample S1 to S3. The agreement confirms the applicability of the evaluation method described above. In the wavelength range from 500 nm to 1500 nm, the refractive

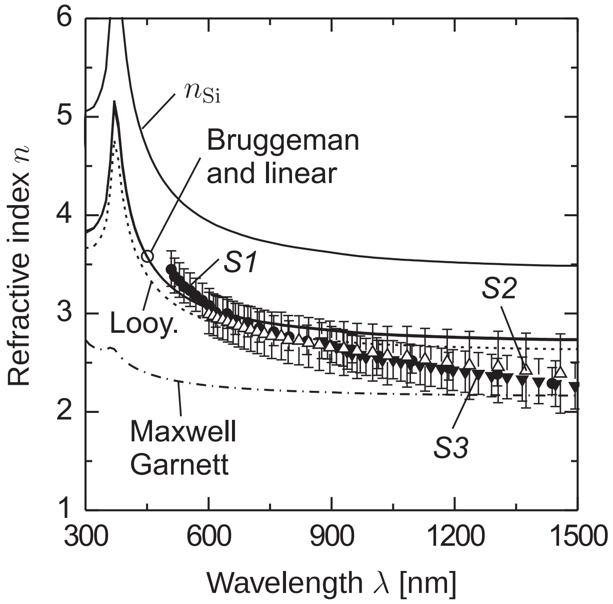

Figure 4.13. Refractive index for Samples S1, S2 and S3 (symbols) that result from the analysis described in Section 4.3.2 and effective medium predictions (lines) for a porosity of $P = 30\,\%$. The refractive index of bulk silicon is shown as well.

index of SPS lies 19 % to 35 % below the value for bulk silicon. Except for the Maxwell Garnett formula, the measured values agree with the predictions of the effective medium models for $\lambda < 1000$ nm. The difference between the three remaining models (Bruggeman, Looyenga and the linear interpolation) is too small to allow a validation of a particular model. For wavelengths above 1000 nm, these models overestimate the refractive index and the measured data are closer to the predictions of the Maxwell Garnett mixing rule, which represents a lower percolation strength compared to the other models.

4.3.4 Scattering coefficient

Besides the refractive index, the evaluation procedure performed in Section 4.3.2 also delivers the absorption coefficient α. This coefficient accounts for both the absorption of photons and the scattering by the voids, since both effects reduce the specular transmission and reflection of the sample. Thus

$$\alpha = \alpha_{\text{eff}} + \gamma \tag{4.30}$$

follows, where γ is the scattering coefficient and α_{eff} the effective absorption coefficient of the porous material. The latter is unknown, however, for wavelengths $\lambda > 600$ nm, scattering dominates over absorption, since the measured absorption coefficient α is large compared to the absorption coefficient of silicon, yielding $\alpha \approx \gamma$. The dots in Fig. 4.14 represent the scattering coefficient γ that follows from Eq. (4.30) using the afore determined absorption coefficient α. Here $\alpha_{\text{eff}} = (1-P)\alpha_{\text{Si}}$ is assumed, but a variation within $0 \leq \alpha_{\text{eff}} \leq \alpha_{\text{Si}}$ does hardly affect the resulting γ, as explained above. The measured scattering coefficient decreases from $2\times10^6\,\text{m}^{-1}$ for $\lambda = 600$ nm to $\sim5\times10^4\,\text{m}^{-1}$ at $\lambda = 1400$ nm. A decrease by more than one order of magnitude is also expected from Mie's theory (Fig. 4.6). The oscillations of γ, that are particularly present for Sample S3, reveal the incompleteness of the optical model, that does not consider any thickness inhomogeneities or the finite surface roughness. This issue is discussed in more detail in Section 4.4 at the end of this chapter. During the fitting procedure, the varied absorption coefficient compensates for the effects not included by the optical model resulting in oscillations that reflect those of the measured specular transmission and reflection.

The use of Mie's theory permits the calculation of the scattering coefficient from the measured pore size distribution $f(r)$ by means of Eq. (4.17). Due to the strong dependence of the scattering efficiency on the void diameter, as illustrated in Fig. 4.5 (a) on p. 50, an accurate determination of the size distribution $f(r)$ is necessary. An SEM image analysis, as described in Section 2.2.3, yields $f(r)$ for each individual sample. Figure 4.14 presents the calculated scattering coefficients assuming different refractive indices n_{host} for the host medium. For $n_{\text{host}} = n_{\text{Si}}$, Mie's theory overestimates the scattering coefficient. The agreement with the curve obtained by using effective medium theory $n_{\text{host}} = n_{\text{eff}}$ (linear model from Eq. (4.13)) is more satisfying and applying the measured values n_{meas} from Fig. 4.13 for the refractive index n_{host} gives the best match.

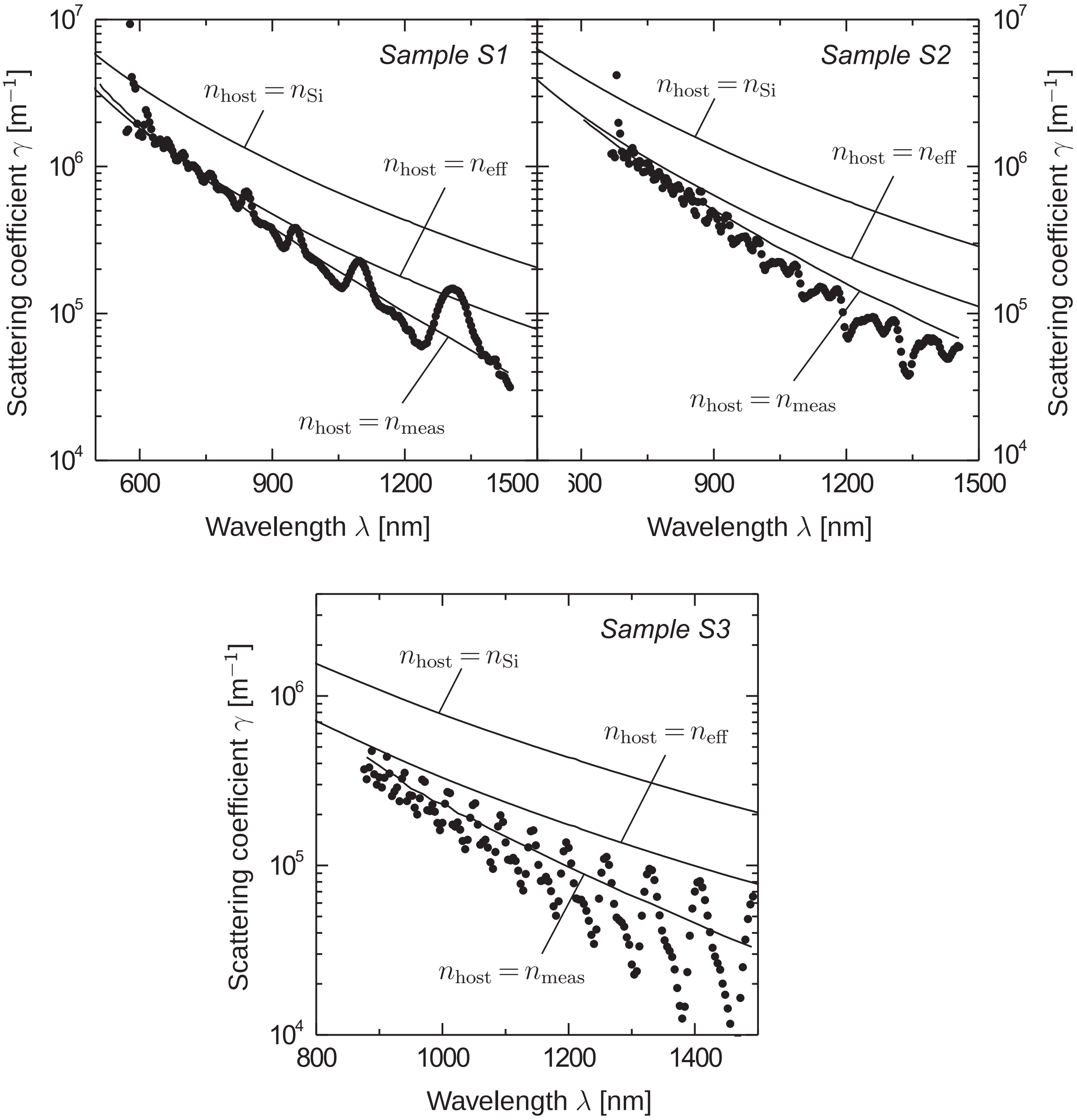

Figure 4.14. Measured scattering coefficient (dots) obtained from the fitting procedure described in Section 4.3.2. The lines are theoretical curves that follow from Mie's theory assuming different refractive indices n_{host} for the host medium. The linear model is used in the case of $n_{\mathrm{host}} = n_{\mathrm{eff}}$. Using the measured refractive index n_{meas} for the host medium accounts for the close spacing of the pores and gives the best match to the measured data.

Mie's theory describes the scattering by a single isolated particle embedded in a homogeneous host medium. However, the pores in SPS are densely packed and the spacing between the pores is comparable to the pore size (see Fig. 4.1 on p. 42). It seems that in this case the presence of the surrounding pores has to be taken into account by using a reduced effective refractive index for the calculation of the scattering efficiency Q_{sca} of the individual voids. The lower refractive index of the host medium results in a reduced size parameter $z = \pi d\, n_{\mathrm{host}}/\lambda$ which, in turn, yields a lower scattering efficiency, as apparent from Fig. 4.5 (b).

Not only the size parameter z but also the refractive index ratio $w = 1/n_{\mathrm{host}}$ depends on the refractive index n_{host} of the host medium. Since the parameter w describes the refractive index step between the sphere and the surrounding medium, one could argue that the neighbouring pores do not affect this parameter and, consequently, the bulk value n_{Si} should be used for w instead of the lower effective refractive index. The dashed line in Fig. 4.14 illustrates this case for $w = 1/n_{\mathrm{Si}}$ and $z = \pi d\, n_{\mathrm{meas}}/\lambda$. Using n_{Si} for the refractive index ratio yields a slightly higher scattering coefficient compared to n_{meas}. However, the calculated curves still comply well with the measured data. For $n_{\mathrm{host}} \geq 3$ the ratio w has a weaker impact on the scattering efficiency Q_{sca} compared to the effect of the size parameter z, as discussed in Section 4.2.3.

In conclusion, Mie's theory successfully describes the scattering by the spherical voids in SPS. However, due to the close spacing of the pores, the effective refractive index of the host medium n_{host} is reduced which results in an increased wavelength $\lambda' = \lambda/n_{\mathrm{host}}$ for the incident wave. This, in turn, reduces the size parameter and gives rise to a lower scattering efficiency compared to the scattering efficiency of an isolated sphere without neighbouring pores.

4.4 Verification of the optical model

The determined optical constants of the samples enable the verification of the optical model developed in Section 4.2.4. This model considers both the specular light and the scattered diffuse intensity. The specular calculation applies the coherent transfer matrix technique for the determination of the specular reflection, transmission and absorption. The same model is used to determine the optical constants from the measured specular spectra (see Section 4.3.2). For the verification of the complete model, both, the specular as well as the diffuse reflection and transmission of Sample S1, S2 and S3, are calculated and the results are compared with the measured data.

The input parameters for the simulation are the film thickness from Table 4.1 on p. 42, the measured refractive index n_{meas} from Section 4.3.3 and the linear model $\alpha_{\mathrm{eff}} = (1-P)\alpha_{\mathrm{Si}}$ with $P = 30\,\%$ for the unknown effective absorption coefficient.

The determined scattering coefficient from Fig. 4.14 on p. 63 shows oscillations, that correspond to the interferences of the measured spectra and reflect the incompleteness of the specular model, as described in Section 4.3.4 above. Thus, instead of using the measured scattering coefficient (dots in Fig. 4.14), the smooth curve that results from Mie's theory (solid line, $n_{\mathrm{host}} = n_{\mathrm{meas}}$) is applied. As explained above, this curve follows from Eqs. (4.17) and (4.18) with the pore size distribution $f(r)$ obtained from the SEM image evaluation and the use of the measured refractive index n_{meas} for both the size parameter $z = \pi d\, n_{\mathrm{meas}}/\lambda$ and the refractive index ratio $w = 1/n_{\mathrm{meas}}$. The simulation includes a thin surface layer of bulk silicon on both sides of the sample, as illustrated in Fig. 4.11 on p. 60. As apparent from Fig. 4.12 (solid line, $m_0 = 4$), a surface layer thickness of $W_{\mathrm{s}} = 20\,\mathrm{nm}$ yields the lowest deviation σ_{avg} for Sample S1 and thus gives the best match to the measured specular data R_{spec} and T_{spec}. For the same reason, a value of $W_{\mathrm{s}} = 28\,\mathrm{nm}$ and $W_{\mathrm{s}} = 12\,\mathrm{nm}$ is applied for Sample S2 and S3, respectively. The discretisation of the diffuse model uses an increment of 2 nm to 10 nm (see Section B.4.2).

Hence, besides the optical constants n_{Si} and α_{Si} for the surface layer, the applied parameters are the measured refractive index n_{meas}, the thickness W_{s} of the surface layer and that of the complete film W, the pore size distribution $f(r)$, the porosity P (Eq. (4.18)) and the estimated absorption coefficient $\alpha_{\mathrm{eff}} = (1-P)\alpha_{\mathrm{Si}}$. No fitting is used here.

Figures 4.15, 4.16 and 4.17 present the specular and diffuse reflection and transmission calculated by means of the optical model developed in this work (lines) together with the measured data (dots) for Sample S1, S2 and S3, respectively. For the measured data an uncertainty of ± 2 % (absolute) is assumed, as illustrated by the error bars. The use of the measured refractive index as an input parameter limits the spectral range of the simulations to $\lambda > 500\,\mathrm{nm}$ for sample S1, $\lambda > 600\,\mathrm{nm}$ for Sample S2 and $\lambda > 900\,\mathrm{nm}$ in the case of Sample S3. The agreement for the specular components R_{spec} and T_{spec} is good, as expected, since the specular component of the model is applied for the determination of the ordinal number m_0, which, in turn, yields the refractive index n_{meas} (see Section 4.3.2). The latter is determined from the positions of the interference maxima and minima. Therefore the interference oscillations of the simulation match those of the measured spectra.

For Sample S1, the simulation (dashed line) underestimates R_{spec} at the reflection minima and overestimates T_{spec} at the transmission maxima. The described disagreement results from a thickness inhomogeneity of the sample, that is not included by the simulations. To account for the thickness inhomogeneity, two additional simulations are performed, one with a 2 % higher and the other one with a 2 % lower thickness value. The solid line in Fig. 4.15 represents the average of all three simulations with $\Delta W = -2\,\%, 0\,\%$ and $+2\,\%$. The averaging procedure results in a weaker accentuation of the interferences, which is particularly visible at the sharp minima of R_{spec}. For the other two samples (S2 and S3), the thickness-averaged spectra using $\Delta W = \pm 1\,\%$ yield a better agreement with the measured data as well, which confirms that thickness inhomogeneities reduce the magnitude of the interference extrema. The same effect also causes the oscillations in the determined scattering coefficient γ (dots in Fig. 4.14), since in Section 4.3.4 γ is derived from fitting the specular model to the measured spectra R_{spec} and T_{spec}, without accounting for the thickness inhomogeneity.

In the case of Sample S1, the simulations comply well with the measured diffuse reflection R_{diff}, whereas they slightly overestimate the diffuse transmission T_{diff}. The deviation of a few per cent (absolute) is comparable to the measurement accuracy of ± 2 % (absolute). The simulated diffuse reflection and transmission are almost similar, representing the high level of randomisation assumed by the model. Solely for wavelength below 600 nm, the diffuse reflection exceeds the transmission, since a significant number of photons is absorbed before reaching the rear surface. This feature is also apparent in the measured spectra.

For wavelengths above 700 nm, the measured diffuse transmission is lower compared to the measured diffuse reflection, whereas the model predicts similar values for both quantities. This asymmetry might originate from an inhomogeneous spatial distribution of the pore size. A quantitative SEM image analysis reveals that, in the case of Sample S1, the average pore diameter in the top half of the sample is 8 % higher than in the bottom

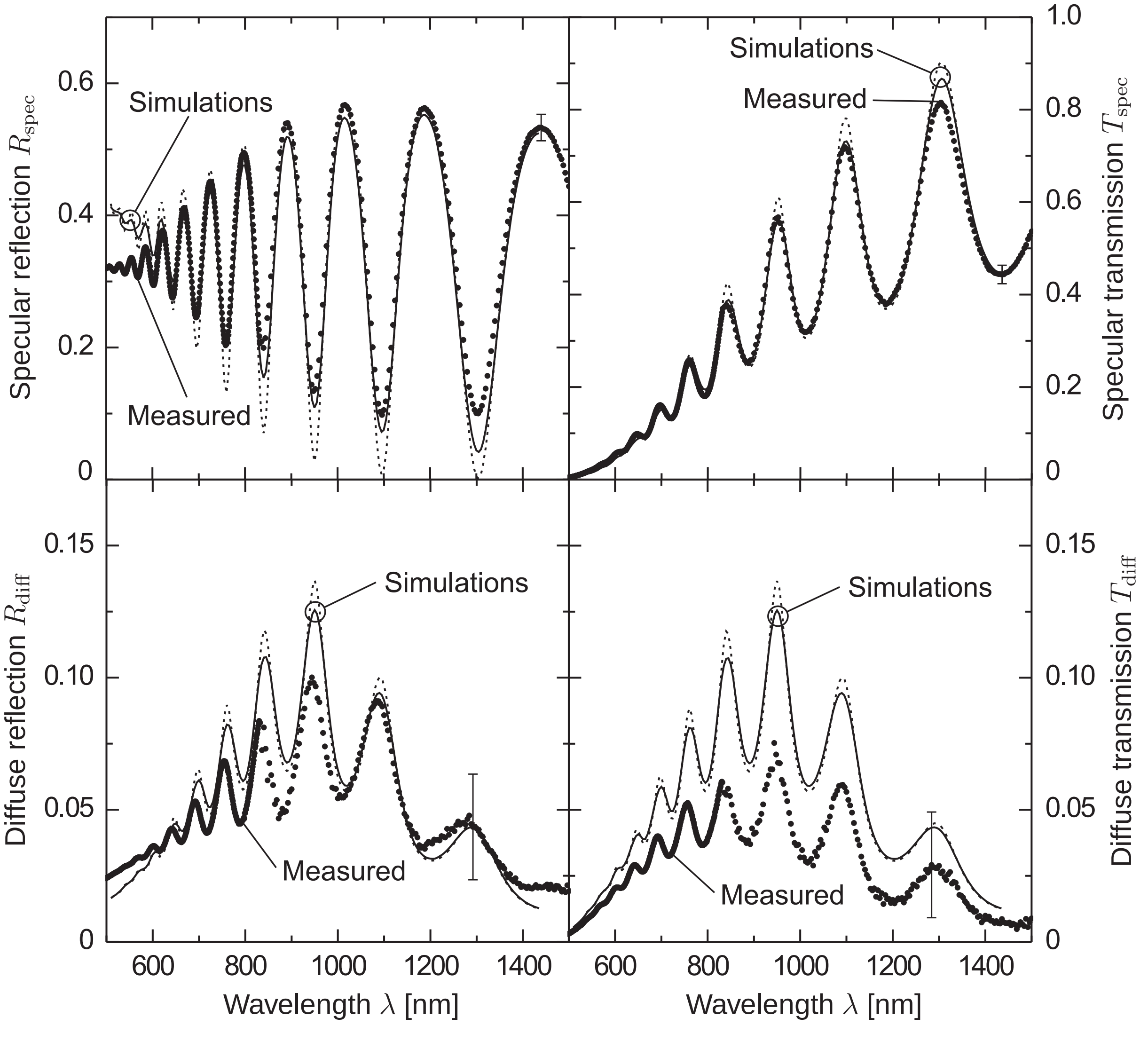

Figure 4.15. Comparison of simulated (lines) and measured spectra (dots) of a 1 µm thick free standing SPS film (Sample S1). The measurement data are taken from Ref. 130. The dashed line represents a simulation using $W = 1.05\,\mu\text{m}$ from Table 4.1, whereas the solid line is an average of three simulations using different film thickness values with $\Delta W = -2\,\%, 0\,\%$ and $+2\,\%$.

half corresponding to a ~30 % higher scattering efficiency (at $\lambda = 900\,\mathrm{nm}$). The described anisotropy of the scattering efficiency possibly causes the difference between the measured diffuse reflection and transmission.

For Sample S2, the measured specular reflection and transmission are a few per cent higher compared to the simulations, whereas the measured diffuse spectra lie below the simulated curves. Figure 4.14 on p. 63 reveals that, for Sample S2, the calculated scattering coefficient used for the simulation (solid line, $n_{\mathrm{host}} = n_{\mathrm{meas}}$) exceeds the measured values (dots in Fig. 4.14) by 30 % to 90 % for $1000\,\mathrm{nm} < \lambda < 1500\,\mathrm{nm}$. Consequently, the simulation overestimates the ammount of scattered photons yielding higher diffuse reflec-

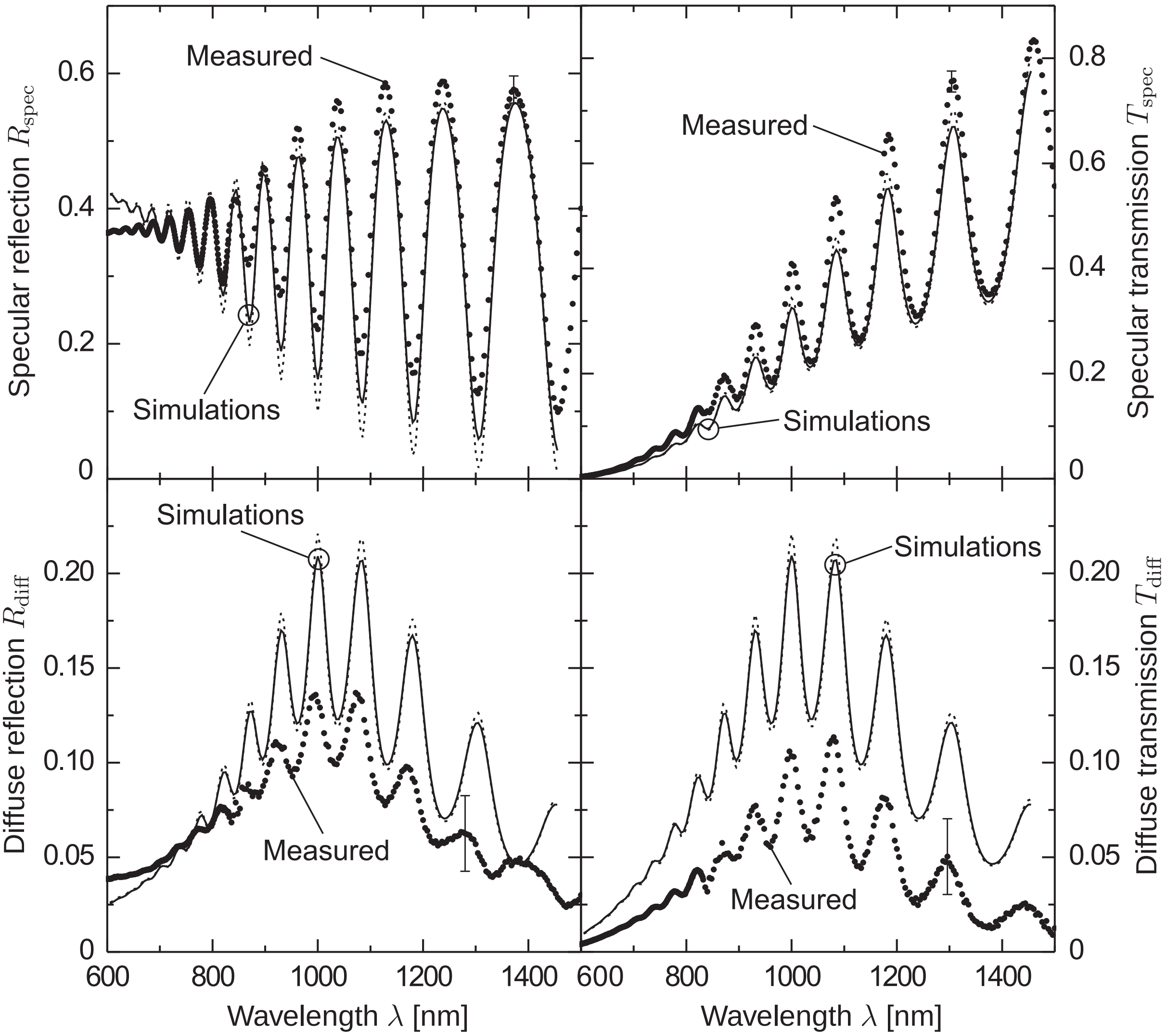

Figure 4.16. Simulated spectra (lines) and measured values (dots, from Ref. 130) for Sample S2. The dashed line follows for $W = 2.07\,\mu\mathrm{m}$ from Table 4.1, whereas the solid line results from an average over $\Delta W = \pm 1\,\%$.

tion and transmission and a lower specular reflection and transmission, compared to the measurement. In addition, Sample S2 features an inhomogeneously distributed pore size as well (see Fig. 4.1 on p. 42), which results in a lower diffuse transmission compared to the diffuse reflection.

The deviations between the measured and simulated spectra are similar for Sample S3. The simulation underestimates the specular transmission and, in particular, the specular reflection, whereas the diffuse components are overestimated. Again, too high values for the calculated scattering coefficient might cause this deviation. Moreover, the inhomogeneous distribution of the pores yields an increased diffuse reflection compared to the diffuse transmission, as discussed above.

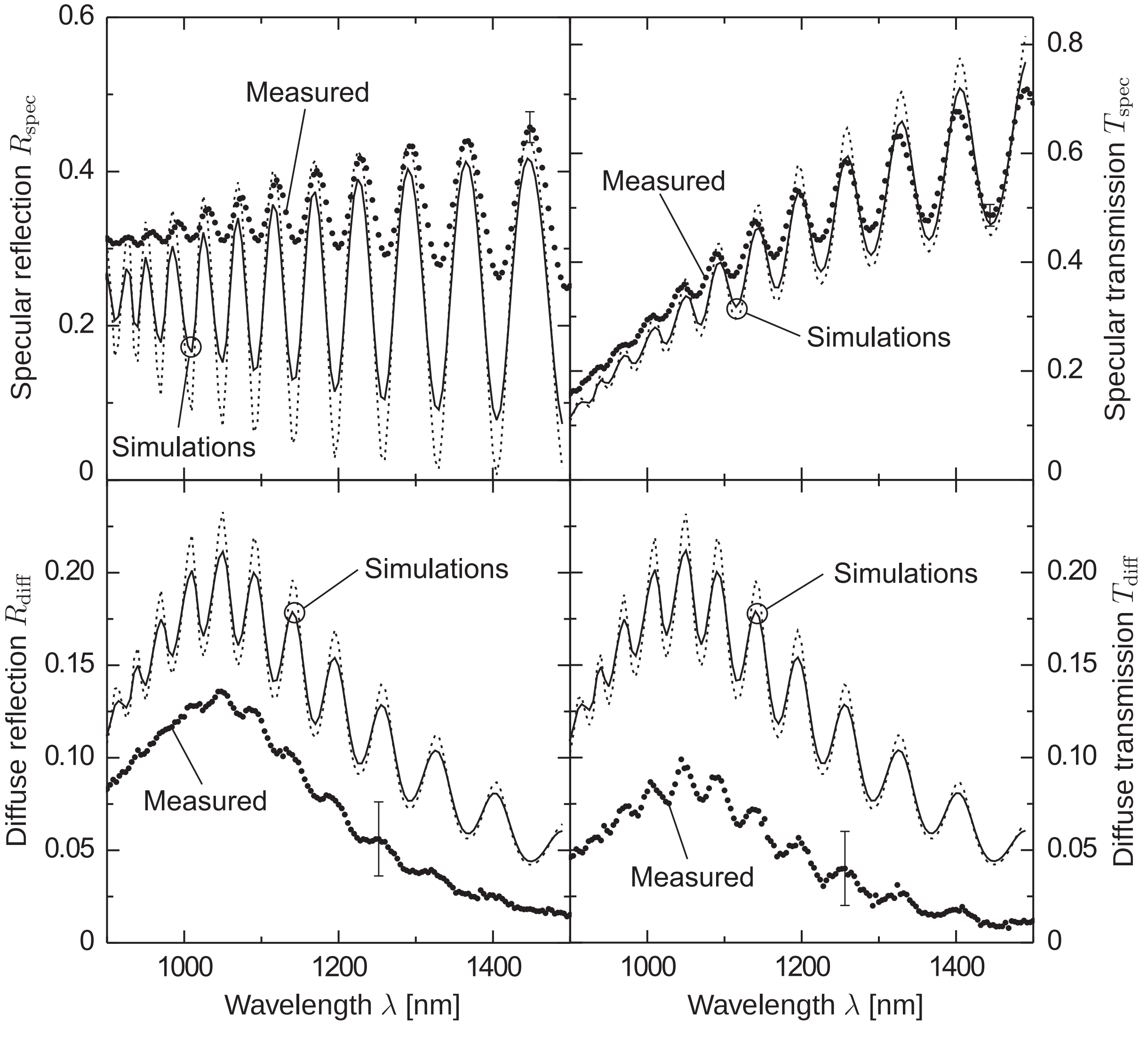

Figure 4.17. Simulation (lines) and measurement (dots, from Ref. 130) for Sample S3. A thickness of $W = 3.92\,\mu\mathrm{m}$ from Table 4.1 is applied for the dashed line and averaging over $\Delta W = \pm 1\,\%$ yields the solid line.

4.5 Summary of Chapter 4

An analysis of the specular transmission and reflection of free standing SPS films yields the refractive index n and the scattering coefficient γ of SPS. The obtained results reveal that effective medium models, which are frequently used to describe the optical constants of as-etched PS, also comply well with the refractive index of sintered PS. In the visible range, the refractive index of SPS agrees with predictions of the Looyenga, the Bruggeman or the linear model, whereas in the IR, the Maxwell Garnett formula gives a better match.

Mie's theory enables the quantitative description of light scattering by the spherical pores in SPS. The comparison of measured and calculated scattering coefficients reveals that in SPS, the close spacing of the pores reduces the scattering efficiency of the individual spheres. The performed analysis shows that, when accounting for adjacent pores by using a reduced refractive index for the host medium in Mie's theory, the measured and calculated scattering coefficients agree.

The optical model developed in this work calculates both, the specular radiation by means of a coherent model and the diffuse intensity using a Lambertian absorption scheme. Compared to previously published models, the approach developed here also accounts for multiple scattering events as well as reflection and transmission of diffuse radiation at internal and external interfaces. The validity of the developed optical model is confirmed by reproducing the measured specular and diffuse spectra.

5 Electrical properties

Thin-film solar cells from the PSI process feature a layer of SPS that remains at the rear side of the PSI cell, as outlined in Section 2.3. The most important issues for understanding the impact of this layer on the cell performance are its optical and electrical properties. The optical properties are discussed in the previous chapter. In this chapter the dependence of the resistivity and carrier diffusion length of SPS films on the porosity and microstructure are analysed.

5.1 Electrical conductivity

At room temperature the resistivity of as-etched PS ranges from $10^4\,\Omega\text{cm}$ to $10^7\,\Omega\text{cm}$ for meso PS and $10^7\,\Omega\text{cm}$ to $10^{14}\,\Omega\text{cm}$ in the microporous case [15, 37, 156–158]. Thus, in both cases the resistivity is several orders of magnitude higher compared to the silicon substrate on which the porous layers are formed. Early publications suggested that the low conductivity results from quantum confinement effects due to small size of the silicon bridges [159, 160]. However, Lehmann et al. also measured low conductivities for meso PS with structural dimensions of about 10 nm, which are too large to show quantum confinement [161]. To explain these results they proposed a new model accounting for carrier trapping at the large internal surface of as-etched PS. The porous skeleton of micro and meso PS consists of thin interconnected silicon wires. According to this model carriers are captured by dangling bonds located at the surface of such a wire. These fixed charges induce a carrier-depleted region that reduces the conducting cross-sectional area of the wire. This narrowing of the conductive pathway by charged surface traps limits the charge transport through the porous network. The detection of a reduced free-carrier absorption in meso PS [161], as well as the drastically increased conductivity that is observed if PS is exposed to polar substances [162–164], support this idea. The latter results from the adsorption of polar molecules, such as methanol, ammonia or nitrogen dioxide, at the internal surface of the porous network. This adsorption leads to de-charging of the surface states which results in a conductance recovery of the silicon wires [163, 165, 166].

The microstructure of as-etched PS also affects the carrier mobility, since the structure size is comparable to the mean free path of the carriers. Measurements of the Hall mobility in n-type meso PS indicated an electron mobility of $30\,\text{cm}^2/(\text{V s})$, which is one order of magnitude lower than the value of $310\,\text{cm}^2/(\text{V s})$ that was measured for the silicon substrate [167]. For micro PS a much lower effective mobility of $\sim 10^{-4}\,\text{cm}^2/(\text{V s})$ was reported [157]. For a more detailed discussion of the carrier mobility in as-etched PS see Ref. 168.

During annealing of PS, larger voids form and the internal area reduces from several

$100\,\mathrm{m^2/cm^{-3}}$ for meso PS [15] to $\sim 20\,\mathrm{m^2/cm^{-3}}$ (see Section 2.2). Thus, size and surface effects should be less dominant in SPS compared to the as-etched state and a higher conductivity and mobility is expected. Only a few publications report on the electrical properties of SPS [169–171]. Unfortunately, no information on the resistivity of SPS is available. However, in Ref. 171 the authors analyse the carrier mobility by Hall measurements. These measurements showed a hole mobility of $\mu_\mathrm{h} = 78\,\mathrm{cm^2/(V\,s)}$ which is close to the bulk value of $198\,\mathrm{cm^2/(V\,s)}$ for the applied $0.05\,\Omega\mathrm{cm}$ p-type substrate. Assuming the same carrier concentration, the higher mobility in SPS alone results in a much lower resistivity compared to as-etched PS. In addition, the reduction of the surface to volume ratio during sintering as well as the increased thickness of the silicon bridges should further reduce the resistivity. Thus, for SPS a resistivity close to the bulk value of the silicon substrate is expected.

5.1.1 Sample preparation

Electrochemical anodisation and subsequent annealing in a hydrogen atmosphere allow the fabrication of SPS films, as illustrated in Fig. 3.5 (a) on p. 31. Since the aim of this study is the optimisation of PSI solar cells, the parameters used for the fabrication of the SPS films are those commonly applied in the PSI process.

The substrates are (100)-oriented, boron doped CZ wafers with a resistivity of $0.01\,\Omega\mathrm{cm}$. The electrolyte is an HF(50%) : ethanol = 2:1 (by volume) mixture. The applied etching

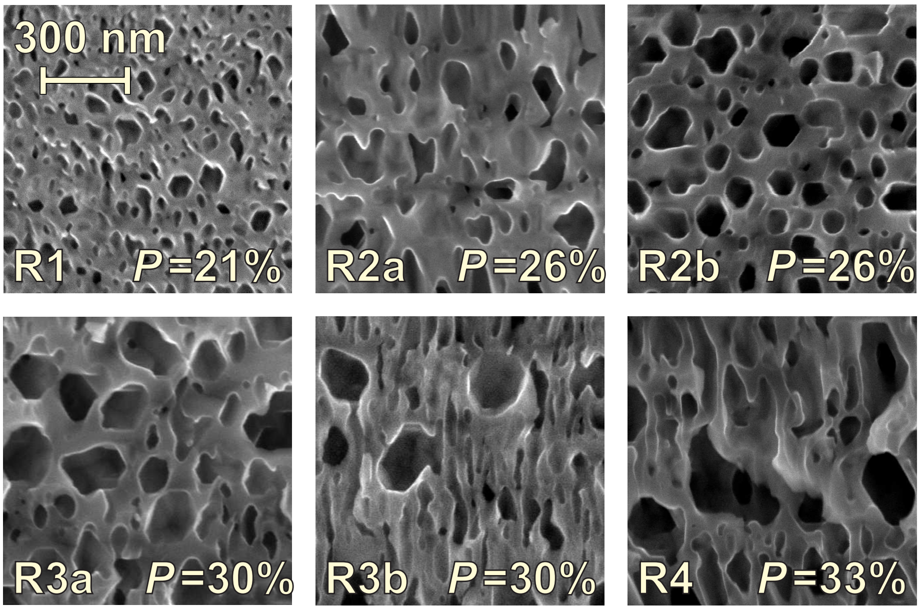

Figure 5.1. Cross sectional SEM images of the analysed samples. The porosity P is given in the the bottom right corner of the images. The scale bar in the upper left also applies to the other images. The etching direction is from top to bottom, whereas the current flow during the resistivity measurements is vertical.

current densities of 5, 30, 60 and 90 mA/cm^2 result in porosities between 21 % and 33 %. Higher porosities are not investigated, since the PSI process utilises SPS films with porosities of 20 % to 30 % (see Section 2.3). After etching the starting layer with a low current density, a current pulse forms the highly porous separation layer. Table A.3 in Appendix A lists the applied etching parameters. During sintering at 1100 °C in a H_2 ambience for 60 minutes the porous structure reorganises and the separation layer dissolves. In the next step the sample is glued to a 2.5×2.5 cm^2 glass carrier and separated from the substrate.

The preparation of equivalent samples allows the determination of the porosity of the etched PS layers, as already described in Section 2.1.6. An SEM is used to measure the thickness of the separated SPS films. Figure 5.1 presents cross sectional SEM images of the samples. It is apparent that the size of the pores increases from Sample R1 to R3a. These four samples also exhibit an isotropic pore geometry, whereas Samples R3b and R4 show just a few spherical pores that are embedded in a matrix of elongated pores aligned parallel to the direction of etching.

5.1.2 Resistivity measurement

For a sample that exhibits a homogeneous resistivity, the measurement of the sheet resistance R_{sheet} and the thickness W enables the calculation of the resistivity

$$\rho = R_{\mathrm{sheet}} \cdot W. \tag{5.1}$$

In this work two methods for the determination of the sheet resistance are applied, the four point probe technique and the measurement of the sheet conductance $\sigma_{\mathrm{sheet}} = 1/R_{\mathrm{sheet}}$ by a radio-frequency (RF) bridge circuit. The application of both methods allows a more detailed evaluation, since SPS might response differently to eddy currents induced by a RF bridge circuit compared to an applied voltage.

5.1.2.1 Four point probe measurement

The four point probe method [172, 173] is commonly used for determining sheet resistances. Figure 5.2 schematically presents the measurement principle. A constant current I is passed through the two outer probes and the voltage drop V over the two inner probes is measured. For thin samples with a thickness W well below the sample edge length L, the sheet resistance

$$R_{\mathrm{sheet}} = \frac{V}{I} \cdot f_{\mathrm{corr}} \tag{5.2}$$

follows from the current I, the voltage V and a correction factor f_{corr} that depends on the geometry of the setup. For samples that are large compared to the distance B of the equally spaced probes ($L \gg B$), the correction factor approaches $\pi/\ln(2) = 4.53$ [173]. Repeated

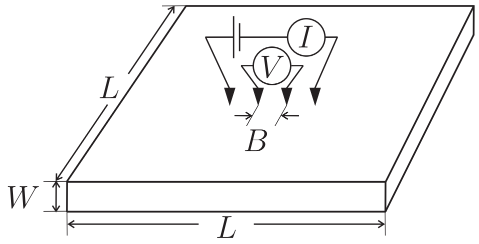

Figure 5.2. Four point probe measurement setup. A constant current I is passed through the two outer probes and the voltage drop V over the two inner probes is measured.

measurements using the same sample permit the determination of an average value and a standard deviation that serves as an estimate for the uncertainty of the measurement.

5.1.2.2 Radio-frequency bridge method

A second method for determining the sheet resistance is the use of a radio-frequency bridge circuit [173]. Figure 5.3 shows a sketch of the RF bridge setup. For the measurement, the sample is placed on top of a coil that is part of a resonant circuit. The circuit operates at a frequency of 10 MHz and causes eddy currents in the bulk of the sample. The power dissipation associated with the eddy currents damps the resonant circuit, thereby increasing the output voltage. This voltage V scales linearly with the sheet conductance $\sigma_{\text{sheet}} = 1/R_{\text{sheet}}$ of the sample. A set of silicon wafers with known conductance permits the conductance-voltage calibration of the circuit.

5.1.3 Effect of the porosity and the microstructure

Both measurement methods, four point probing and the RF bridge technique give similar results as apparent from Table 5.1 and Fig. 5.4 on p. 76. The deviations lie within the uncertainty of the measurements. Thus, SPS exhibits the same resistivity in both cases, when introducing a potential gradient by the four point probe technique, or when inducing eddy currents using a RF bridge circuit. The resistivities measured for the SPS films range from 21 mΩcm to 220 mΩcm which is a factor of 2 to 21 higher than the value of 10 mΩcm

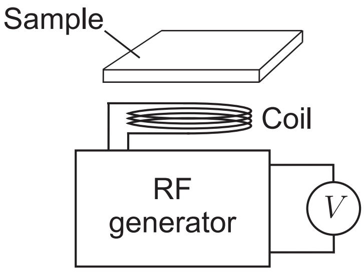

Figure 5.3. Schematic of the RF bridge circuit. The output voltage V scales linearly with the sheet conductance σ_{sheet} of the sample.

Table 5.1. Sample properties and measurement results. Two methods, the four point probe technique and RF bridge coupling are used for the determination of the resistivity.

	Sample properties		**Resistivity ρ**	
Sample	Porosity P [%]	Thickness W [µm]	Four point probe [mΩcm]	RF bridge [mΩcm]
R1	21.2 ± 0.4	1.7 ± 0.3	40 ± 12	42 ± 10
R2a	25.9 ± 0.5	22.8 ± 1.1	45 ± 14	49 ± 12
R2b		18.6 ± 0.9	40 ± 8	41 ± 11
R3a	29.8 ± 0.5	25.1 ± 1.3	22 ± 2	21 ± 5
R3b		20.8 ± 1.0	219 ± 74	201 ± 88
R4	32.8 ± 0.5	24.9 ± 1.2	148 ± 46	138 ± 58

that results for the silicon substrate. Thus, compared to the resistivity of as-etched PS, the measured resistivities are only slightly above the bulk value.

For a quantitative interpretation, the results are compared to effective medium calculations. The effective resistivity

$$\rho_{\text{eff}} = \rho_{\text{bulk}} \, (1 - P)^{-b} \tag{5.3}$$

of the porous structure is modelled as a function of the porosity P and the bulk resistivity $\rho_{\text{bulk}} = 0.01\,\Omega\text{cm}$. For $b = 3$ Eq. (5.3) is equivalent to the Looyenga model [114] which was already introduced in Section 3.3.1 for modeling the thermal conductivity of SPS. The higher resistivity that is observed for increasing porosity values agrees with the prediction of Eq. (5.3). However, as apparent from Fig. 5.4, the increase seems to be stronger than predicted by the Looyenga model, that is Eq. (5.3) using $b = 3$. The agreement is better for higher value of b, for example $b = 6$, as shown in Fig. 5.4.

Not only the value of the porosity but also the pore geometry has an impact on the resistivity of SPS. For example, for the identically prepared samples R3a and R3b, the measured resistivities differ by a factor of ten. This difference might be caused by the deviating microstructure of the two samples. Apparent from Fig. 5.1 on p. 72, Sample R3a has an isotropic structure that is quite similar to that of Sample R2b, which also shows a comparable low resistivity. In contrast, Sample R3b resembles the anisotropic structure of Sample R4. The resistivities of Sample R3b and R4 are comparable as well although they are both much higher compared to the rest of the samples. Both samples, R3b and R4, show a few larger spherical pores that are surrounded by elongated, vertically oriented pores. For both measurement methods the current flow occurs in the horizontal direction of the SEM images in Fig. 5.1. Thus, in the case of Sample R3b and R4, the walls of the vertical pores constrict the horizontal current flow and the carriers have to travel around the longish pores which gives rise to an increased resistivity.

In conclusion, an increase of the resistivity of SPS for a higher porosity is observed,

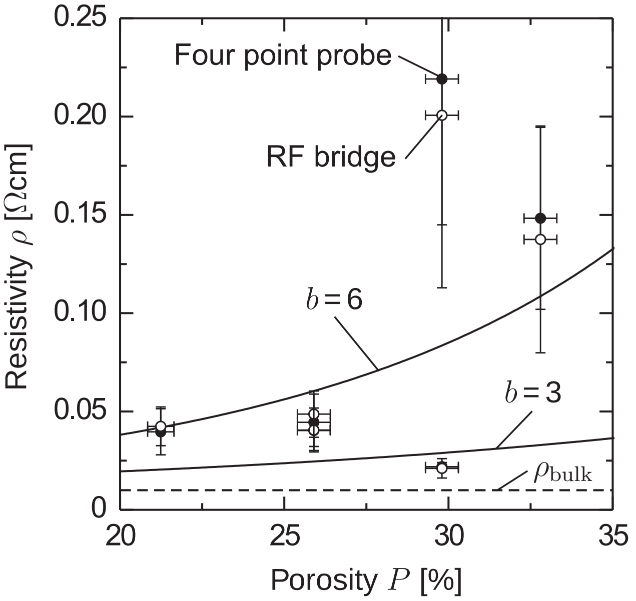

Figure 5.4. Measured electrical resistivity (dots) of SPS films with porosities between 21 % and 33 %. Two measurement mehods are applied, the four point probe technique (filled circles) and coubling via a RF bridge (open circles). The solid lines represent effective medium models using Eq. (5.3) with $b=3$ and $b=6$. The dashed line marks the bulk resistivity of the silicon substrates.

as predicted by effective medium theory. Nevertheless, the microstructure seems to have a predominant effect on the resistivity of SPS compared to the porosity. This limits the adaptability of effective medium models that only use porosity as an input parameter, such as the Looyenga model. A more precise model should include structural parameters, such as the pore size and the geometry and orientation of the pores, as well.

The resistivity of SPS is of importance for the design of PSI solar cells. For example, the low resistivity of SPS allows the deposition of the back contact directly onto the residual SPS layer as illustrates in Fig. 2.10 on p. 18. The contribution of the SPS layer to the series resistance of the device is negligible, since the resistivity of SPS is lower than that of the base of the cell, which is typically 0.5 Ωcm. Experiments of other authors yielded similar results [174].

5.2 Carrier diffusion length

Another property of SPS that is important for PSI solar cells is the minority carrier diffusion length. This parameter describes the probability of collecting carriers that are generated within the SPS layer.

In the as-etched state, recombination and trapping due to defects located at the large internal surface of PS limit the diffusion of photogenerated carriers. For meso PS, minority carrier diffusion lengths from a few tens of nanometers to 150 nm were measured [175,176]. However, during annealing the internal surface area of PS reduces by one order of magnitude (see Section 2.2). The lower surface to volume ratio in SPS yields a lower number of defects per unit volume and should thus result in an enhanced carrier diffusion length compared to as-etched PS. In Ref. 170 a diffusion length of 8 µm was estimated for electrons in p-type SPS by means of microwave photoconductance decay measurements. But this high value is contradictory to the low efficiency of 1.16 % that was achieved by the photovoltaic cells fabricated from this material [177].

In this work the carrier diffusion length is deduced from quantum efficiency measurements. The samples are pn-diodes made from SPS. The optical model developed in the previous chapter permits the extraction of the carrier diffusion length from the measured quantum efficiency.

5.2.1 Device fabrication

The starting substrates are (100)-oriented, boron-doped CZ wafers with a resistivity of 0.01 Ωcm and a thickness of 525 µm. Again, this material is chosen, since it is commonly used for the PSI process. The first step of the fabrication procedure consists of the formation of the porous layers by electrochemical etching in an HF(50%) : ethanol = 2:1 (by volume) solution. As for the resistivity samples from Section 5.1.1, etching current densities of 5, 30, 60 and 90 mA/cm^2 are used yielding porosities from 21 % to 33 % for Sample D1 to D4, respectively. In contrast, in the present case no separation layer is etched. Instead, the PS-layers remain attached to the substrate. The thickness of the etched layers is ∼13 µm. Table A.4 in Appendix A lists the fabrication parameters in detail. During H_2-annealing at 1100 °C for 60 minutes the porous network rearranges and the macroscopic surface closes. Figure 5.5 presents cross-sectional SEM images of the annealed samples. Apparently, not only the porosity but also the size of the pores increases from Sample D1 to D4.

In the next fabrication step, the formation of the phosphorus-doped n^+-type emitter is performed by means of a $POCl_3$-diffusion. The sheet resistance of this emitter is $(40 \pm 5)\,\Omega/\square$ and the junction depth $W_{\mathrm{em}} = (240 \pm 20)$ nm, both measured on a non-porous reference. The low junction depth originates from the high substrate doping level

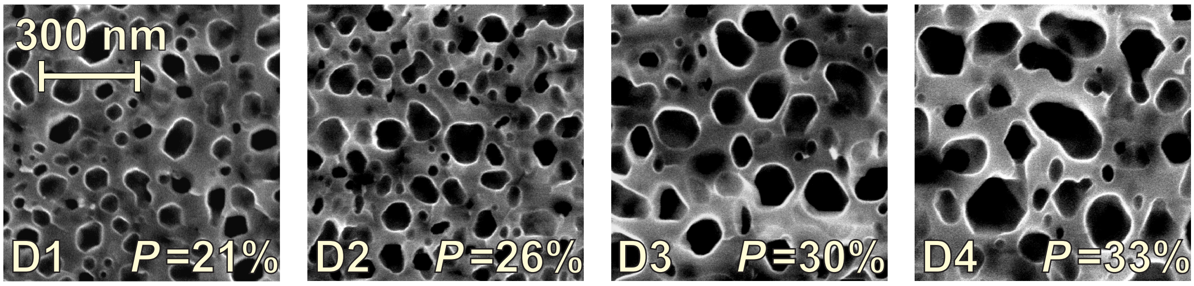

Figure 5.5. Cross sectional SEM images of the SPS devices. The porosity P is given in the bottom right corner of the images. The pore size increases from Sample D1 to D4.

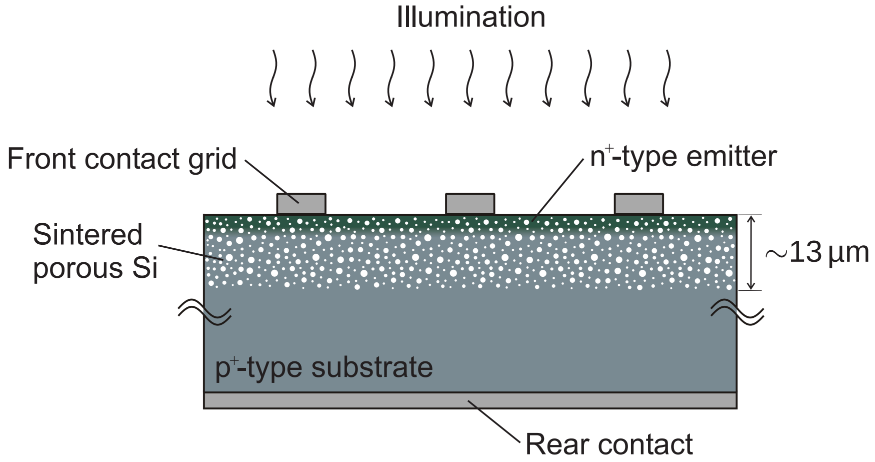

Figure 5.6. Schematics of the fabricated SPS pn-diodes. The active SPS layer remains attached to the substrate.

of $p = 8\times10^{18}\,\mathrm{cm}^{-3}$. Following the diffusion, the front contact grid, that consists of a Ti/Pd/Ag-stack, is deposited through a shadow mask. Finally, the full area aluminium rear contact is applied. Figure 5.6 illustrates the resulting device structure.

In addition to the SPS pn-diodes, a reference cell is fabricated from the same starting material. The processing sequence is identical, except for the omitted electrochemical etching and the subsequent annealing step. Furthermore, the $POCl_3$ diffusion is performed separately resulting in a higher sheet resistance of $\sim 240\,\Omega/\square$. A SiN layer deposited onto the front side passivates the front surface and serves as an anti-reflection coating. The four SPS devices do not feature such a coating.

5.2.2 Current-voltage characterisation

The dark and illuminated current-voltage curves of the fabricated devices are measured under standard testing conditions. Table 5.2 presents the obtained illuminated current-voltage parameters. Initially, the devices achieve open-circuit voltages of up to 436 mV (Sample D2) and efficiencies between 0.7 % and 1.9 %. The short-circuit currents range from $5.8\,\mathrm{mA/cm^2}$ to $14.5\,\mathrm{mA/cm^2}$ and the fill factors from 36.5 % to 41.1 %.

For a more detailed analysis, a simple single diode model, that includes a serial and a parallel resistance [178], is fitted to the measured dark current-voltage curves. The results show that a low parallel resistance of $\sim 100\,\Omega\mathrm{cm}^2$ and below reduces the fill factor of the SPS diodes. In addition, high ideality factors between 1.8 and 2.9 are obtained for the diode. The junction region of the fabricated SPS devices exhibits a high density of defects and strong electric fields due to the high base doping level. This combination is known to produce high ideality factors above 2 by tunneling enhanced recombination [179–182].

After a storage of several weeks under ambient conditions, the devices degrade. The open-circuit voltage and the fill factor drop significantly, whereas the parameters for the reference cell stay on the initial level. An analysis of the dark current-voltage curves of

Table 5.2. Current-voltage parameters of the SPS pn-devices and the non-porous reference. The measurements are performed under standard testing conditions.

Sample		Short-circuit current J_{SC} [mA/cm^2]	Open-circuit voltage V_{OC} [mV]	Fill factor FF [%]	Efficiency η [%]
D1	initial	5.8	355	37.4	0.77
	degraded	5.8	98	26.4	0.15
D2	initial	11.8	436	37.9	1.94
	degraded	10.6	138	30.8	0.45
D3	initial	11.8	393	36.5	1.69
	degraded	11.6	241	35.2	0.99
D4	initial	14.5	321	41.1	1.92
	degraded	12.9	290	30.8	1.15
Reference		15.3	593	75.1	6.81

the degraded devices reveals that a further reduced parallel resistance causes the degradation. Conducting channels at the pore walls possibly cause the observed shunting. Rinke observed comparable values with fill factors that did not exceed 38 % for SPS devices with a similar structure [177]. Using a metal-insulator-semiconductor (MIS) junction instead of a diffused emitter could possibly reduce the observed shunting, since the junction region is then located close to the surface within the pore-depleted surface layer [183].

The short-circuit current of both the SPS devices and the reference cell is limited by a low bulk diffusion length. For the reference cell, Auger recombination due to the high doping level dominates, whereas for the SPS devices, dangling bonds and other defects located at the large internal surface act as recombination centres and further reduce the diffusion length of the photogenerated carriers.

5.2.3 Quantum efficiency analysis

An evaluation of the quantum efficiency enables the determination of the effective diffusion length L_{eff} of the minority carriers generated within the base of the device [184, 185]. The external quantum efficiency

$$EQE = \frac{J_{\mathrm{SC}}}{q\Phi} \tag{5.4}$$

constitutes the number of extracted electron-hole-pairs per incident photon under monochromatic illumination. Here J_{SC} is the short-circuit current, Φ the incident photon flux and q the elementary charge. The internal quantum efficiency

$$IQE(\lambda) = \frac{EQE(\lambda)}{(1 - R(\lambda))\,(1 - f_{\text{met}})} \tag{5.5}$$

follows from the EQE when correcting for the reflection losses. Here R is the reflection of the area between the fingers of the front grid, and the metal grid shades a fraction f_{met} of the front surface. Equation (5.5) assumes zero transmission.

5.2.3.1 Measurement setup

The application of a lock-in technique, as for example described in Ref. 186, permits the determination of the differential EQE. Figure 5.7 schematically illustrates the experimental configuration. The sample and a monitor cell are illuminated with monochromatic intensity-modulated light. Both cells are held at a temperature of 25 °C. Additionally, constant white bias light of 0.33 suns illuminates the sample cell. Pre-amplifiers convert the photo current of the sample and the monitor cell into a voltage signal and remove the DC component. Two lock-in amplifiers, one for the sample and one for the monitor cell, read the AC signals V_{samp} and V_{mon}, respectively. A calibration cell with a known spectral response EQE_{cal} enables the determination of quantum efficiency for the measured cell. For this purpose, first a measurement with the calibration cell is performed yielding the signals $V_{\text{samp,cal}}$ and $V_{\text{mon,cal}}$. In a second step, the measured cell replaces the calibration cell resulting in $V_{\text{samp,meas}}$ and $V_{\text{mon,meas}}$. The quantum efficiency for the measured cell then

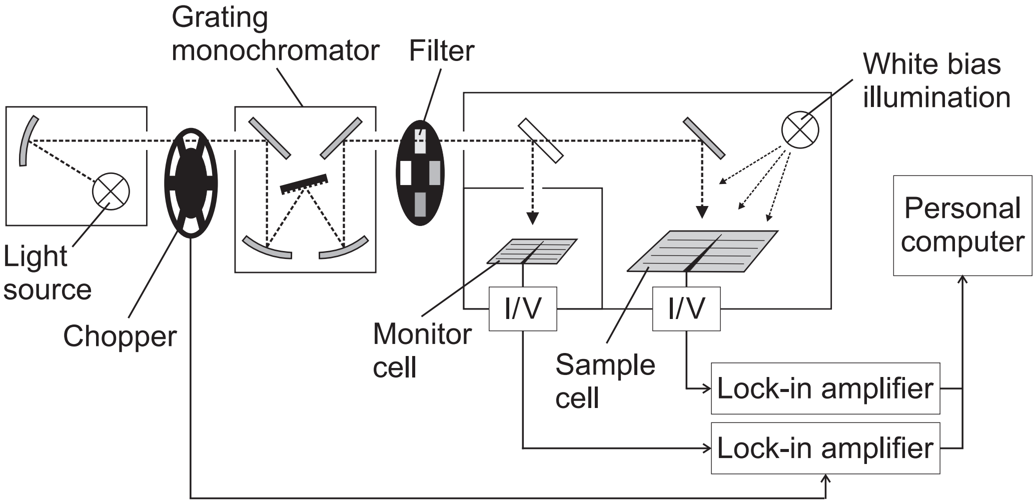

Figure 5.7. Measurement setup used for the determination of the external quantum efficiency. Periodically modulated monochromatic light illuminates both, the sample and the reference cell. Adjustable bias light allows to establish the working point of the sample cell.

follows from

$$EQE_{\mathrm{meas}} = EQE_{\mathrm{cal}} \frac{V_{\mathrm{samp,meas}}}{V_{\mathrm{samp,cal}}} \frac{V_{\mathrm{mon,cal}}}{V_{\mathrm{mon,meas}}}. \tag{5.6}$$

The described technique is a small signal method, hence the measured quantities are differential by nature, whereas the evaluation requires absolute values [187, 188]. However, the analysed devices exhibit a linear behaviour with a short-circuit current J_{SC} proportional to the photon flux Φ. Thus, in the present case, the differential signal equals absolute EQE.

The conversion of the external into an internal quantum efficiency by Eq. (5.5) requires the knowledge of the reflection R between the fingers of the front grid. The hemispherical reflection R_{meas} of the device is measured with a spectrophotometer using an integrating sphere, as described in Section 4.1.2. The reflection of the non-shaded area

$$R = \frac{R_{\mathrm{meas}} - f_{\mathrm{met}} R_{\mathrm{met}}}{1 - f_{\mathrm{met}}} \tag{5.7}$$

follows from the measured reflection corrected for the known contribution by the reflection R_{met} of the metal grid. Here, absorption losses within an optional front surface coating are neglected.

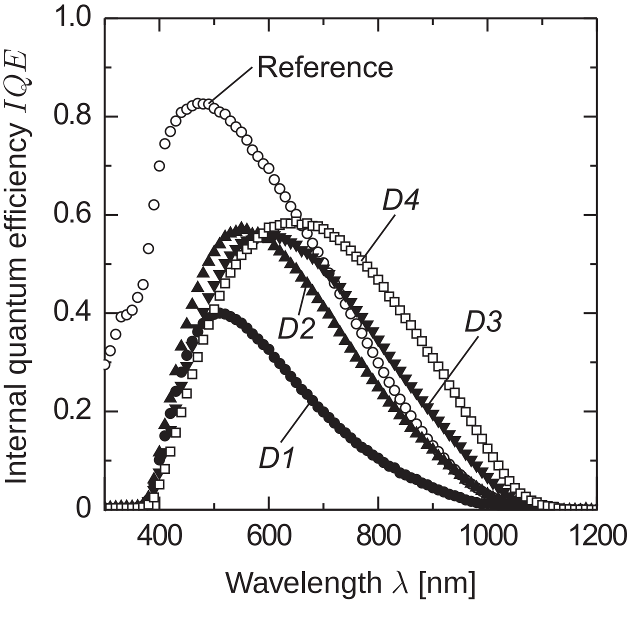

Figure 5.8. Internal quantum efficiencies measured for the four SPS devices and the non-porous reference.

5.2.3.2 Internal quantum efficiency of SPS devices

Figure 5.8 presents the measured IQEs for Sample D1 to D4 and the reference cell. The measurements are performed in a stable state after an initial degradation of the devices. Compared to the reference cell, all SPS devices exhibit a low blue response which drops below 1 % for $\lambda < 370\,\text{nm}$. The unpassivated front surface together with additional recombination at the pore walls within the emitter cause a lower short wavelength response of the SPS devices compared to the reference cell, that features a passivated pore-free emitter with a sheet resistance of $240\,\Omega/\square$.

The average pore size increases from Sample D1 to D4, as apparent from Fig. 5.5 on p. 77 and Table 5.3 on p. 85. The same holds for the red response of the devices and the IQE maximum shifts to longer wavelengths. For $\lambda > 700\,\text{nm}$, the IQEs of Sample D3 and D4 even exceed the reference. The SPS samples exhibit a shorter effective absorption length compared to the reference, due to light scattering by the pores. The larger pores give rise to enhanced light scattering which reduces the effective absorption length from Sample D1 to D4. Assuming a comparable diffusion length for the SPS devices, the reduced effective absorption length explains the observed increase of the red response and the shift of the IQE maximum.

5.2.3.3 Extraction of the carrier diffusion length

The photogenerated current from the base, the space charge region and the emitter, each contribute to the quantum efficiency. For the present devices, recombination in the base clearly dominates over rear surface recombination. Thus, the effective diffusion length L_{eff} within the base region equals the bulk diffusion length L_{bulk} which is small compared to the thickness W of the cell [189]. Moreover, if the absorption length $L_\alpha = 1/\alpha$ is also small compared to W, the contribution of the carriers collected from the base to the internal quantum efficiency is [184]

$$IQE_{\text{base}} = \frac{\mathrm{e}^{-(W_{\text{em}}+W_{\text{SCR}})/L_\alpha}}{1 + L_\alpha/L_{\text{bulk}}}, \tag{5.8}$$

where W_{em} and W_{SCR} denote the width of the emitter and the space charge region, respectively. In the one-side abrupt junction approximation [190], the high doping level $p = 8\times10^{18}\,\text{cm}^{-3}$ of the base limits the width of the space charge region to $W_{\text{SCR}} < 14\,\text{nm}$, which is small compared to W_{em}. Therefore, the contribution of carriers generated within the space charge region is neglected. Finally, a fraction $1 - \exp(-W_{\text{em}}/L_\alpha)$ of the photogeneration occurs within the emitter region. However, when restricting the evaluation to $L_\alpha \gg W_{\text{em}}$, the emitter absorbs only a few per cent of the light coupled into the device. Furthermore, the probability of collecting the carriers generated in the emitter is low, due to the unpassivated front surface. Thus, for $L_\alpha \gg W_{\text{em}}$, the contribution of the emitter is negligible and the numerator of Eq. (5.8) approaches unity yielding [185]

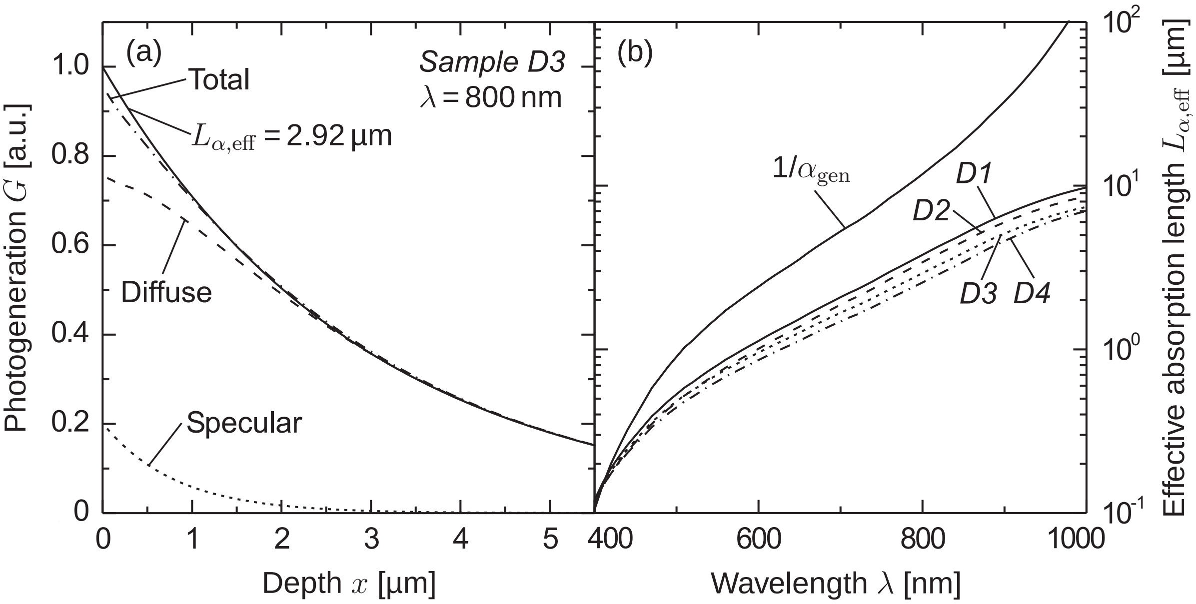

Figure 5.9. The left hand side presents specular and diffuse carrier generation profiles calculated for Sample D3 with the optical model from Chapter 4. The wavelength is $\lambda = 800\,\mathrm{nm}$. Fitting an exponential decay function (solid line) to the total generation profile yields an effective absorption length $L_{\alpha,\mathrm{eff}}$. The right hand side shows the effective absorption length $1/\alpha_{\mathrm{gen}}$ calculated for Sample D1 to D4. The absorption length for bulk silicon (free-carrier absorption neglected) is shown for comparison.

$$IQE \approx IQE_{\mathrm{base}} \approx \frac{1}{1 + L_\alpha / L_{\mathrm{bulk}}}. \tag{5.9}$$

Equation (5.9) enables a simple evaluation of the bulk diffusion length L_{bulk} by plotting the inverse IQE versus the absorption length L_α, although its validity is limited to $W_{\mathrm{em}} \ll L_\alpha \ll W$.

The above described evaluation requires the knowledge of the absorption length within the porous bulk of the devices. For an estimation of the effective absorption length $L_{\alpha,\mathrm{eff}}$, the optical model developed in the previous chapter is applied. Since the refractive index of the porous samples is not known, the performed simulations use the linear model from Eq. (4.13) for the complex effective refractive index $\tilde{n}_{\mathrm{eff}}$ thereby also accounting for parasitic free-carrier absorption. The scattering coefficient follows from Mie's theory using Eqs. (4.17) and (4.18). An SEM image analysis of each individual sample delivers the required pore size distribution $f(r)$. For the calculation of the scattering efficiency Q_{sca}, the approximated refractive index n_{eff} from the linear model is applied for both the size parameter $z = \pi d\, n_{\mathrm{eff}}/\lambda$ and the ratio $w = 1/n_{\mathrm{eff}}$. The simulated structure includes the non-porous substrate as well as a 20 nm thick pore-free layer at the front surface of the device, as described in Section 4.3. The depth resolution is 30 nm (see Section B.4.2).

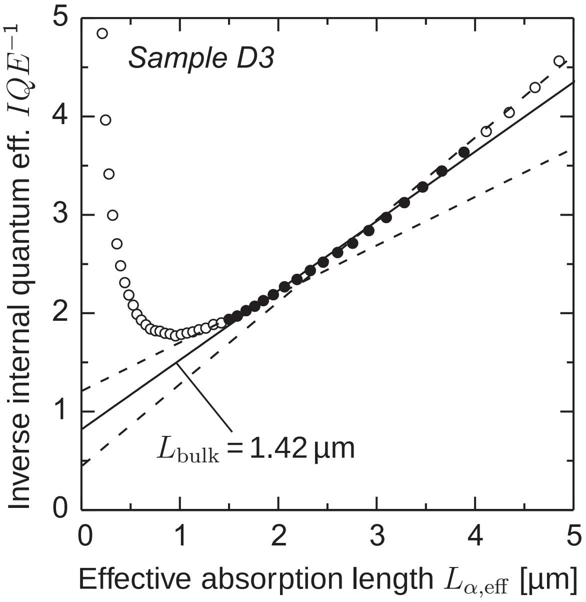

Figure 5.10. Inverse internal quantum efficiency (dots) of Sample D3 plotted versus the calculated effective absorption length. The IQE is corrected for free-carrier absorption. The solid lines are linear fits for the determination of the diffusion length L_{bulk} by means of Eq. (5.9).

Figure 5.9 (a) exemplifies the evaluation of the calculated absorption profile. The simulation provides both, the specular generation $G_{\text{spec}}(x)$ from Eq. (B.36) and the diffuse generation profile $G_{\text{diff}}(x)$ from Eq. (B.71). The effective absorption length $L_{\alpha,\text{eff}}$ follows from fitting an exponential decay function to the total generation profile $G(x) = G_{\text{spec}}(x) + G_{\text{diff}}(x)$. Figure 5.9 (b) shows the effective absorption lengths calculated for the four samples as well as the absorption length in bulk silicon. As explained above, the average pore size increases from Sample D1 to D4 resulting in an increased scattering coefficient, which, in turn, reduces the effective absorption length.

The calculated effective absorption length allows the determination of the carrier diffusion length L_{bulk} from the measured IQE by means of Eq. (5.9). However, the high doping level of the base requires the consideration of free-carrier absorption, not only for the determination of the absorption length, but also for the evaluation of the IQE. Multiplying the measured IQE values with $(\alpha_{\text{gen}} + \alpha_{\text{FC}})/\alpha_{\text{gen}}$ corrects for parasitic free-carrier absorption. Figure 5.10 presents the inverse IQE plotted versus the effective absorption length $L_{\alpha,\text{eff}}$. The slope of a linear fit (solid line) yields the diffusion length L_{bulk} after Eq. (5.9). The range for the fit is limited to $1.5\,\mu\text{m} < L_{\alpha,\text{eff}} < 4\,\mu\text{m}$ (filled dots in Fig. 5.10) to ensure the validity of Eq. (5.9). As expected from Eq. (5.9), the intercept of the fit with the y-axis is close to unity. A variation of the fitting range, as illustrated by the dashed lines in Fig. 5.10, gives an upper and lower limit for the diffusion length. These limits serve as an estimate for the uncertainty of the obtained values. Table 5.3 lists the diffusion lengths determined for the four SPS devices and for the non-porous reference.

Table 5.3. Sample properties and carrier diffusion length for the four SPS devices. The values are obtained from an analysis of the IQE that is measured after an initial degradation of the devices.

Sample	Porosity P [%]	Average pore diameter d_{avg} [nm]	Internal area A_{int} [m^2/cm^3]	Diffusion length L_{bulk} [µm]
D1	21.2 ± 0.4	41.2 ± 1.5	21.9 ± 0.7	0.39 ± 0.16
D2	25.9 ± 0.5	41.9 ± 1.9	24.8 ± 1.3	0.99 ± 0.38
D3	29.8 ± 0.5	51.3 ± 2.6	21.6 ± 1.2	1.42 ± 0.61
D4	32.8 ± 0.5	55.6 ± 4.6	18.8 ± 2.3	2.50 ± 0.96
Reference	-	-	-	4.94 ± 0.44

Another uncertainty results from approximating the refractive index of the porous layers by means of effective medium theory, as outlined above. The refractive index affects the scattering coefficient, which, in turn, determines the effective absorption length (see Section 4.3.4). For the samples analysed in the previous chapter, the difference in the Mie scattering coefficient that arises from either using the approximated refractive index n_{eff} or the actually measured values n_{meas} is less than a factor of two, as apparent from Fig. 4.14 on p. 63 (solid lines, $n_{\text{host}} = n_{\text{eff}}$ and $n_{\text{host}} = n_{\text{meas}}$). A sensitivity analysis shows that a variation of the scattering coefficient by a factor of two still yields results for the diffusion lengths that lie within the uncertainty range specified in Table 5.3. Thus, the inaccuracy that results from using an effective medium model for the unknown refractive index is of the same order as the specified uncertainties.

5.2.3.4 Effect of the internal surface area

The IQE analysis of the SPS diodes yields an effective bulk diffusion length that accounts for the increased path length of the carriers that have to travel around the pores. Hence, the actual diffusion length in the bulk of the porous matrix might be even higher. Table 5.3 shows that the effective bulk diffusion length increases from 0.39 µm for Sample D1 to 2.5 µm for Sample D4. In case of The latter is only a factor of two lower than the value of 4.94 µm, that is obtained for the non-porous reference cell. This number, in turn, complies with the value of $L_{\text{bulk}} = \sqrt{D\tau_{\text{bulk}}} = 4.6\,\mu\text{m}$ that follows from the literature for an Auger recombination limited lifetime of $\tau_{\text{bulk}} = 0.11\,\mu\text{s}$ [191] and a diffusion constant of $D = \mu_{\text{e}} k_{\text{B}} T/q = 1.9\,\text{cm}^2/\text{s}$ for an electron mobility of $\mu_{\text{e}} = 74.8\,\text{cm}^2/(\text{V s})$ [192].

Recombination at the large internal surface of the pore walls reduces the effective bulk diffusion length in the SPS devices compared to the reference. The known pore size distribution $f(r)$ allows the calculation of the internal surface to volume ratio

$$A_{\text{int}} = N_{\text{pore}} \int_0^\infty 4\pi r^2 f(r)\,\mathrm{d}r \tag{5.10}$$

assuming a spherical shape of the pores. Here, N_{pore} denotes the number of pores per unit volume as derived in Eq. (4.18). As apparent from Table 5.3, the pore size increases from Sample D1 to D4 resulting in a lower surface to volume ratio of the voids, which, in turn, reduces the internal surface A_{int}. Except for Sample D1, a higher diffusion length correlates with a reduced internal surface area of the SPS devices. These findings support the assumption that recombination via defects located at the internal surface reduce the carrier diffusion length in SPS. Therefore, an efficient collection of the photogenerated carriers requires a low internal surface area.

Sun et al. fabricated a photovoltaic cell from macroporous silicon that consisted of cylindrical pores with diameters in the µm range [193]. The internal surface of the macropores was $\sim 1\,\mathrm{m}^2/\mathrm{cm}^3$, thus much lower compared to SPS. Furthermore, the open structure of the macropores allowed the formation of an emitter at the pore walls by means of solid source diffusion. Both, the low internal area and the presence of the pn-junction at the pore surface enhanced the device performance. A device with ~70 % of the front surface shadowed by the metal contact still achieved an efficiency of 2.5 % [193].

5.3 Summary of Chapter 5

The electrical conductivity and the carrier diffusion length of SPS are investigated in this chapter. The resistivities measured for SPS films with porosities between 21 % and 33 % range from 21 mΩcm to 220 mΩcm, which is a factor of 2 to 21 higher than the substrate resistivity of 10 mΩcm. Higher porosities tend to result in an increased resistivity, although both, the porosity as well as the geometry of the microstructure, affect the resistivity of SPS. Compared to the resistivity of as-etched meso PS, which is of the order of $10^4\,\Omega$cm to $10^7\,\Omega$cm, the measured resistivities are only slightly above the bulk value, which is explained by the reduced internal surface and the increased thickness of the silicon bridges. Thus, the additional series resistance arising from the presence of the residual SPS layer at the rear side of a PSI solar cell (see Fig. 2.10 on p. 18) is negligible.

The minority carrier diffusion length follows from an analysis of the quantum efficiency of pn-diodes made of SPS. For the extraction of the diffusion length, the optical model developed in the previous chapter is applied. SPS devices with porosities between 21 % and 33 % and average pore diameters of 41 nm to 56 nm are analysed. The obtained diffusion lengths range from 0.39 µm to 2.5 µm, the latter being only a factor of two lower than the value of 4.94 µm that results for a non-porous reference cell made from the same starting material. Apparently, recombination via defects located at the pore walls limits the transport of photogenerated carriers in SPS, since with increasing internal area the devices exhibit a reduced minority carrier diffusion length.

6 Autodiffusion from porous silicon

The present chapter deals with the fabrication of PSI solar cells and introduces a novel concept for generating an emitter in these devices. “autodiffusion” denotes the formation of a highly doped region in the epitaxial layer by out-diffusion of dopant impurities from the growth substrate. This approach combines the epitaxial growth and the emitter diffusion into one single process and allows to completely omit a conventional emitter diffusion in the solar cell processing sequence.

6.1 Autodiffusion approach

Crystalline silicon thin-film technologies based on layer-transfer, such as the PSI process, utilise the epitaxial growth of a thin active layer on a silicon substrate exhibiting a porous surface layer. The growth process involves high temperatures leading to out-diffusion of dopant atoms from the silicon substrate. The re-introduction of these impurities into the epitaxial layer via the gas phase is denoted autodoping [194–196], while the transport directly through the solid, that is, from the substrate into the epitaxial layer, is referred to as solid-state diffusion [197, 198]. Both effects are usually unwanted, although they might also be used to produce a desired dopant distribution. For example Abdurakhmanov et al. suggested to use autodoping to create a dopant concentration gradient in the base of silicon solar cells [199].

For most monocrystalline silicon thin-film solar cells, emitter diffusion is performed in a tube furnace after the epitaxy [14, 84], as exemplified in Fig. 6.1 (a). However, the utilisation of dopant out-diffusion allows to avoid this high temperature processing step by forming an emitter already during epitaxy. Figure 6.1 (b) illustrates the basic idea of the autodiffusion approach. During the epitaxial growth of the active layer of the cell, dopant atoms diffuse from the highly doped growth substrate into the growing film to form a heavily doped region. This process might be used to form either an emitter or a high-low junction for back or front surface fields. The advantage of this concept is that the highly doped region automatically forms during the epitaxial growth of the bulk. The epitaxy and the diffusion are thus performed in one single processing step, which enables a simplified fabrication of PSI solar cells without the application of a conventional emitter diffusion process.

Another possible alternative for emitter formation is the epitaxial growth of the emitter. But in this case either two epitaxial reactors or a switching of the dopant type with long intermediate cleaning would be required. Autodiffusion avoids these difficulties. Furthermore, the autodiffusion concept allows the formation of an emitter at the rear side of the thin-film, that is the side facing the growth substrate. This side becomes accessible after

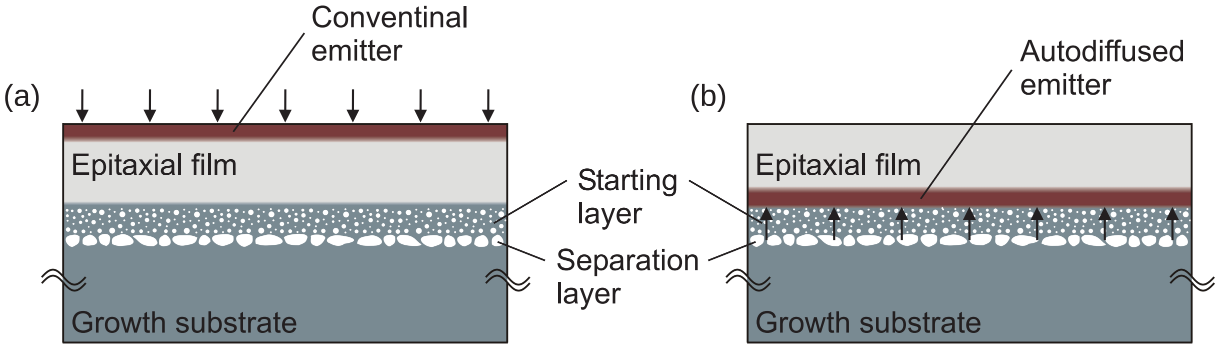

Figure 6.1. The left hand side illustrates the conventional diffusion of an emitter located on the front side of the epitaxial film (arrows). On the right hand side, the autodiffused emitter located on the rear side of the epitaxial film forms by out-diffusion of dopant impurities from the porous starting layer during epitaxy. If the growing film is n-type and the substrate is p^+-type, a p^+-emitter is formed.

the lift-off. But the glue that is used to attach the cell to the glass carrier limits the temperature for rear side processing to values below 300 °C. Thus, conventional diffusion processes with temperatures up to 1000 °C are not applicable. The option of generating an emitter or a high-low junction on the rear side of the thin-film by autodiffusion enhances the flexibility for the cell design.

6.2 Boron autodiffusion

As a first experimental approach to the realisation of autodiffusion, boron-doped substrates are used in this work, due to the available experience in the electrochemical etching of p^+-type material, which is also used for the conventional PSI process (see Section 2.3). The sheet resistance and the doping profile of the autodiffused layer are important parameters for solar cell applications. To estimate the expected sheet resistance, simulations using the commercially available software *Ssuprem3* [200] are carried out. This program simulates the solid-state diffusion of dopant atoms during the bake and the epitaxial growth of an n-type layer on a monocrystalline, non-porous, boron-doped substrate. Hence, these simulations do not account for the porous surface structure of the substrate. The results show that the substrate doping level has to be higher than $2\times10^{19}\,\mathrm{cm}^{-3}$ to achieve a sheet resistance in the range of $400\,\Omega/\square$ to $200\,\Omega/\square$. This means that for the realisation of autodiffusion within the PSI process, the boron doping level of the growth substrate must be increased from presently $8\times10^{18}\,\mathrm{cm}^{-3}$ to at least $2\times10^{19}\,\mathrm{cm}^{-3}$. Thus, the PSI process has to be transfered from $10\,\mathrm{m\Omega cm}$ substrates to substrates with a resistivity below $5\,\mathrm{m\Omega cm}$.

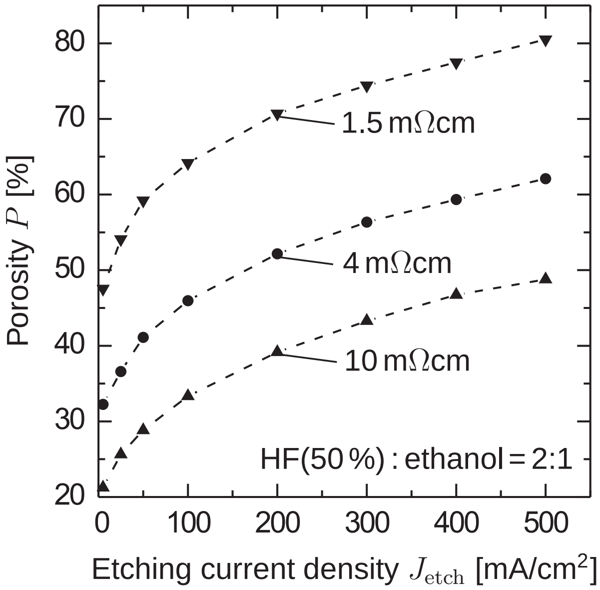

Figure 6.2. Dependence of the porosity P on the etching current density J_{etch} for the anodisation of (100)-oriented p^+-type silicon substrates. The etching solution is an HF(50 %) : ethanol = 2:1 (by volume) mixture. The dashed lines serve to guide the eye.

6.2.1 Layer-transfer using p^+-type substrates

The application of highly boron-doped substrates for the PSI process requires an adaptation of the porous layer formation, since the anodic etching process is sensitive to the substrate resistivity. For layer-transfer, a porous double layer on the substrate surface is needed (see Section 2.3). The double layer consists of a starting layer with a low porosity and a highly porous separation layer. The step in the porosity results from abruptly increasing the etching current density during the etching process.

In this section, the dependence of the porosity on the etching current density for (100)-oriented, p-type CZ substrates with a resistivity of 10 mΩcm, 4 mΩcm, and 1.5 mΩcm is investigated. The etching solution is an HF(50 %) : ethanol = 2:1 (by volume) mixture. The porosity of the etched layers is determined by gravimetrical measurements, as described in Section 2.1.6. Figure 6.2 shows the measured dependence of the porosity P on the etching current density J_{etch}. For all three analysed resistivities, P rises when increasing J_{etch}. In addition, the P-J_{etch} curve shifts to higher porosities when using substrates with a lower resistivity. As discussed in Section 2.1.4, a higher doping level causes a narrower depletion region which results in a reduced thickness of the remaining silicon bridges and, in turn, an increased porosity.

As mentioned above, the doping level of the substrate is an important parameter for the autodiffusion process. A high doping level gives a low sheet resistance of the autodiffused region. On the other hand, the porosity of the starting layer is a relevant factor, too. Closing of the porous surface during annealing of the porous silicon film was described for low porosities around 20 % [63]. The closed surface serves as a monocrystalline seed layer for the subsequent epitaxial growth of silicon layers with high electronic quality, that is, a carrier diffusion length that exceeds the layer thickness [14]. A higher porosity of the starting layer might inhibit a complete surface closure and introduce crystal defects that reduce the diffusion length of the photogenerated carriers in the grown silicon films and thereby the cell efficiency.

However, both parameters, the substrate doping level and the porosity of the starting layer, are interdependent, as apparent from Fig. 6.2. The resistivity of the substrate determines the minimum porosity that is achievable with the applied electrolyte. As a compromise between a low porosity and a high substrate doping level, substrates with a resistivity of 4 mΩcm are chosen for the boron autodiffusion process. Layer-transfer on these substrates is achieved by applying the etching parameters listed in Table A.5 in the Appendix. The formation of the separation layer requires a high etching current density of 480 mA/cm^2. To stabilise the etching process, the current density is first raised to half this value, that is 240 mA/cm^2, for 0.5 seconds before etching the separation layer at 480 mA/cm^2. The introduction of this intermediate etching step yields a more reproducible process. The applied etching parameters result in a starting layer with a thickness of 1 µm and a porosity of $P = (32 \pm 1)\,\%$, which is higher compared to $P = (21 \pm 1)\,\%$ for the previously used substrates with a resistivity of 10 mΩcm.

6.2.2 Modification of the epitaxial growth process

As described in Section 2.3, prior to the epitaxy a pre-annealing step is performed that removes the native oxide and enables the closing of the outer surface. However, it has to be taken into account that during high temperature annealing in an H_2 ambient, the dopant concentration at the substrate surface decreases due to out-diffusion of dopant atoms [195, 201]. These impurities diffuse into the gas phase and are thus lost for the subsequent autodiffusion.

Therefore the duration of the pre-annealing step is reduced to 5 minutes, which we find to be long enough for native oxide removal and reorganization of the porous silicon. The subsequent chemical vapour deposition (CVD) of the epitaxial film is performed under atmospheric pressure at 1100 °C with a growth rate of 0.8 µm/min and trichlorosilane as silicon source. Introducing a drive-in step after the CVD further lowers the sheet resistance of the autodiffused region. Therefore the samples are left in the reactor at 1100 °C for 60 minutes after epitaxy. This drive-in step could also be performed in a separate furnace, since only high temperatures and a clean environment are required, thereby allowing a higher throughput of the CVD reactor. Figure 6.3 shows a cross sectional SEM image of the reorganised porous starting layer with the epitaxial film on top. The image also reveals the dissolved separation layer and the p$^+$-type growth substrate.

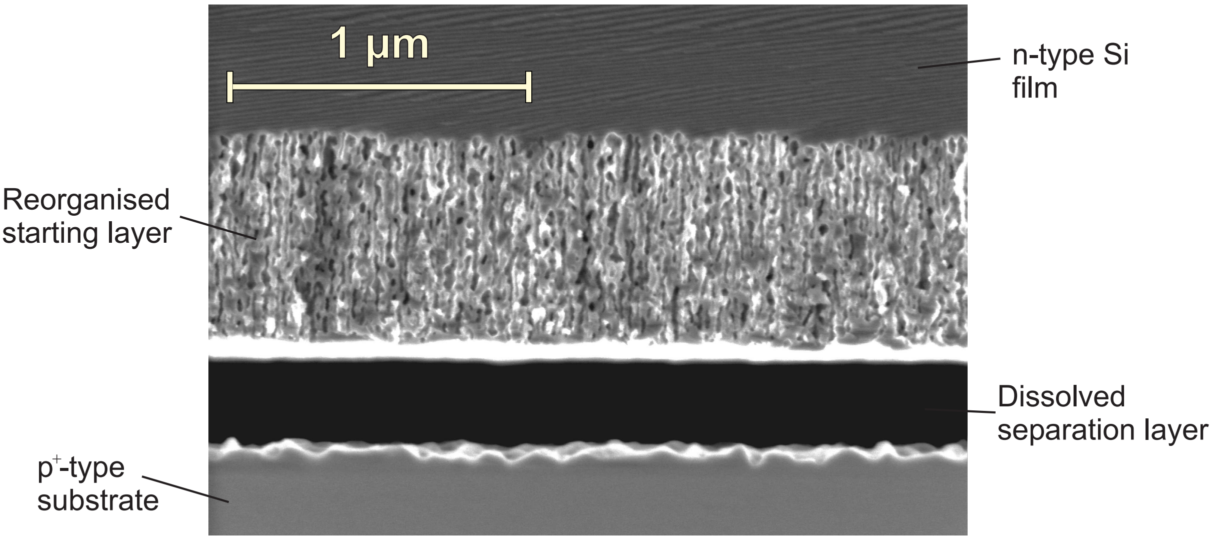

Figure 6.3. Cross sectional SEM image of the reorganised porous double layer formed on a p$^+$-type growth substrate and the epitaxial film. The separation layer between the starting layer and the growth substrate is completely dissolved.

6.2.3 Boron emitter characterisation

The dopant concentration profile that results from the above described process is of peculiar interest. For analysing this profile, samples from 4 mΩcm substrates with a porous double layer on the surface are prepared applying the etching parameters from Table A.5. n-type silicon thin-films with a phosphorus doping level of 2.7×10^{16} cm^{-3} and a thickness of (30 ± 2) µm are deposited on these substrates using the modified epitaxial growth process described above. After the epitaxy, the thin-film is glued to a glass carrier and lifted off by applying mechanical stress. An HF-dip followed by wet chemical etching in a 20 %(wt) KOH-bath at 30 °C selectively removes the sintered porous starting layer from the sample rear side. The etching process is highly selective and etches the reorganised starting layer with its sponge-like microstructure (see Fig. 6.3) with a much higher rate than the non-porous bulk. After the removal, a spreading resistance analysis [202] yields the depth profile of the dopant concentration within the autodiffused layer. For this measurement (performed by Solecon Laboratories in Reno, USA), the samples are beaveled at a small angle. Voltage probes oriented parallel to the bevel edge measure the spreading resistance at the beaveled surface. Literature values for the carrier mobility then allow the conversion of the resulting resistivity data into a carrier concentration depth profile. Finally, solving the Poisson equation permits the determination of the dopant concentration profile from the carrier concentration [203, 204].

Figure 6.4 shows the measured profile. The surface concentration is $N_\mathrm{surf} \approx 3\times10^{18}$ cm^{-3}, while the junction depth is $W_\mathrm{em} > 1$ µm. Additionally, the sheet resistance is measured by the four point probe technique, as described in Section 5.1.2.1. The measured sheet re-

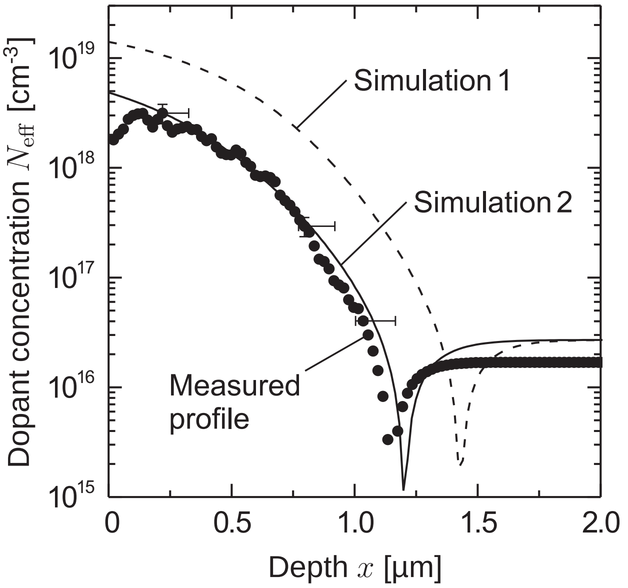

Figure 6.4. Measured doping profile (dots) of the autodiffused boron emitter after removal of the residual porous starting layer by selective etching. The lines show two process simulations using *Ssuprem3* [200]. The boron doping concentration of the substrate is $2.7\times10^{19}\,\mathrm{cm}^{-3}$ and $1\times10^{19}\,\mathrm{cm}^{-3}$ for Simulation 1 and Simulation 2, respectively.

sistance of $330\,\Omega/\square$ agrees well with the value of $340\,\Omega/\square$ calculated from the measured profile. The autodiffusion process thus generates an emitter that features a low surface concentration. This is important regarding surface passivation of the autodiffused emitter, since for passivated emitters a low surface concentration results in a low saturation current [205, 206].

Regarding the re-use of the highly doped substrate, the question arises if the substrate doping level significantly decreases due to the out-diffusion of dopant impurities. Integrating the profile of Fig. 6.4 shows that roughly $1.5\times10^{14}\,\mathrm{cm}^{-2}$ boron atoms diffuse from the porous silicon layer into the thin-film. This corresponds to only 10 % of the boron atoms initially present in the 1 µm thick porous silicon layer. Before the re-use, the substrate is cleaned which removes at least a few µm of the bulk material. Thus, the doping level at the surface of the substrate is restored to the initial level, allowing multiple re-use of the substrate.

6.2.4 Diffusion process simulations

For a more detailed understanding of the diffusion mechanism in the porous silicon layer, the experimental doping profiles are compared with *Ssuprem3* process simulations [200]. Two simulations are carried out with the applied process parameters as input data. Simulation 1 uses the actual substrate doping level of $2.7\times10^{19}\,\mathrm{cm}^{-3}$ (corresponding to 4 mΩcm) while Simulation 2 uses a lower doping level of $1\times10^{19}\,\mathrm{cm}^{-3}$. Both simulations do neither account for the porous structure of the growth substrate, nor for the re-incorporation of dopant atoms that evaporate from the substrate (autodoping). Instead, the out-diffusion of impurities during the bake and the solid-state diffusion during the epitaxial growth of the n-type layer on a 1 µm thick, non-porous starting layer is simulated. Apparent from Fig. 6.4, Simulation 1 overestimates both the peak concentration and the junction depth, while the agreement with Simulation 2 is satisfying. The profiles of Simulation 1 and Simulation 2 correspond to a sheet resistance of 141 Ω/□ and 338 Ω/□, respectively, whereas the measured sheet resistance is 330 Ω/□. Thus, the disagreement between Simulation 1 and the measured profile is large compared to the measurement uncertainty.

The selective etching of the porous silicon might also remove some of the bulk material leading to an additional uncertainty of the depth scale. However, the etching of the porous silicon takes approximately one minute and an estimation of the etching rate of the applied KOH solution [207] shows that at most 100 nm of bulk silicon are removed during etching, which is small compared to the junction depth of ∼1 µm. The error bars shown in Fig. 6.4 account for both, the measurement accuracy as well as the additional uncertainty due to the possible removal of bulk silicon during porous silicon etching.

The porous structure of the starting layer is likely to affect the out-diffusion process yielding a reduced boron concentration compared to the non-porous substrate assumed by Simulation 1. Firstly, about one third of the boron atoms are removed during the porous etching of the substrate. Secondly, the porous structure counteracts the out-diffusion of dopant impurities. The atoms have to diffuse around the pores in the solid phase or through the pores via the gas phase. The porous starting layer also exhibits a high concentration of defects present at its large internal surface leading to gettering of dopant atoms. Gettering of boron and other impurities by porous silicon was already reported by different authors [208–210]. However, assuming a reduced dopant concentration of $1{\times}10^{19}\,\mathrm{cm}^{-3}$ (Simulation 2) instead of $2.7{\times}10^{19}\,\mathrm{cm}^{-3}$ for the growth substrate, the simulated dopant profile complies well with the measured values.

6.2.5 Carrier lifetime analysis

The modification of the epitaxial growth process, as described in Section 6.2.2, and the higher porosity $P = 32\,\%$ of the starting layer compared to $P = 21\%$ for the conventional PSI-process, could possibly lead to a reduced electronic quality of the grown thin-films. Therefore, carrier lifetime investigations of n-type silicon thin-films, grown by the modified process, are carried out. Thin-film samples of different thicknesses are prepared in order to separate bulk and surface recombination.

6.2.5.1 Sample preparation

The porous etching of the substrate and the growth of the n-type silicon thin-film for the lifetime samples are performed as described in Section 6.2.3. Subsequently to the layer growth, a $POCl_3$-diffusion is performed for gettering metal impurities. After the removal of the diffused n^+-layer, the front side of the sample is passivated with an amorphous silicon nitride ($\mathrm{SiN_x}$) layer deposited using a plasma enhanced chemical vapor deposition (PECVD) system. In the next step, the thin-film is glued to a glass carrier and detached from the growth substrate. After the layer-transfer, a wet chemical etch removes the residual porous silicon layer and the autodiffused boron emitter from the rear side. The samples are etched for various durations yielding film thickness values ranging from 27 µm down to 10 µm. A layer of amorphous silicon (a-Si) is then deposited by PECVD at a temperature of 230 °C for passivating the bare n-type base. Finally the samples are annealed at 270 °C for 10 minutes to improve the surface passivation of the a-Si layer [211, 212].

6.2.5.2 Theory

For transient lifetime measurements the effective lifetime

$$\tau_{\mathrm{eff}} = \left(\frac{1}{\tau_{\mathrm{bulk}}} + \beta_0^2 D \right)^{-1} \tag{6.1}$$

depends on the bulk lifetime τ_{bulk}, the diffusion constant D, and the Fourier coefficient of the fundamental mode β_0 [186, 213]. The latter is given by the lowest non-zero root of [186, 213]

$$\tan(\beta_0 W) = \frac{(S_{\mathrm{f}} + S_{\mathrm{r}}) D\, \beta_0}{D^2 \beta_0^2 - S_{\mathrm{f}} S_{\mathrm{r}}}. \tag{6.2}$$

Here W denotes the thickness of the sample and S_{f} and S_{r} the front and rear surface recombination velocity, respectively. When the sum of the surface recombination velocities $S_{\mathrm{tot}} = S_{\mathrm{f}} + S_{\mathrm{r}} \ll D/W$ is small compared to D/W, the effective lifetime reduces to

$$\tau_{\mathrm{eff}} \approx \left(\frac{1}{\tau_{\mathrm{bulk}}} + \frac{S_{\mathrm{tot}}}{W} \right)^{-1}. \tag{6.3}$$

For the analysed samples $W \leq 30\,\mu\mathrm{m}$ is valid. With a phosphorus doping concentration of $2.7\times10^{16}\,\mathrm{cm^{-3}}$ and low injection conditions, a hole mobility of $\mu_{\mathrm{h}} = 385\,\mathrm{cm^2/(V\,s)}$ follows from literature values [192] giving a hole diffusion constant of $D = \mu_{\mathrm{h}} k_{\mathrm{B}} T/q = 9.9\,\mathrm{cm^2/s}$ at a temperature of 25 °C. Thus $D/W \geq 3000\,\mathrm{cm/s}$ is valid, which is much higher than S_{tot} values expected for passivated samples. In this case Eq. (6.3) is a good approximation of Eq. (6.1).

6.2.5.3 Effective lifetime of n-type silicon thin-films

The transient effective lifetime of the thin-film samples is measured using the microwave-detected photoconductance decay method (MW-PCD) [214, 215]. For this measurement, a laser pulse generates excess carriers in the bulk of the sample and the carrier concentration

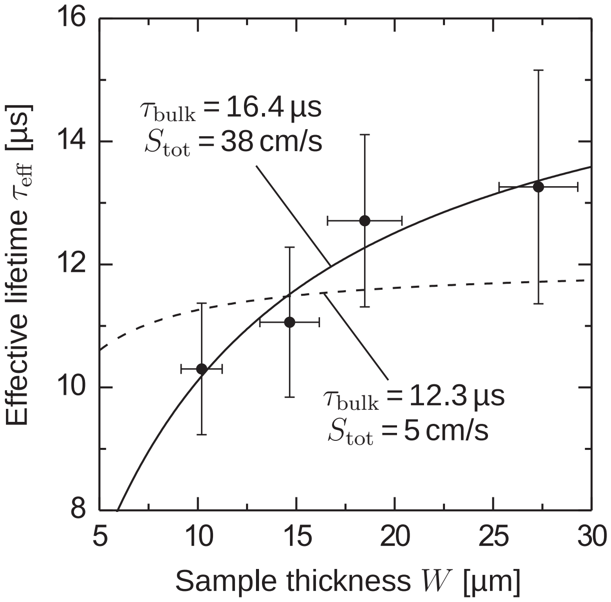

Figure 6.5. Measured effective lifetime (dots) of epitaxially grown n-type silicon thin-films for various film thickness values. The samples are passivated on both sides. The lines represent theoretical curves using Eq. (6.3) with parameter pairs $\tau_{\mathrm{bulk}} = 16.4\,\mu\mathrm{s}$ and $S_{\mathrm{tot}} = 38\,\mathrm{cm/s}$ (solid line) and $\tau_{\mathrm{bulk}} = 12.3\,\mu\mathrm{s}$ and $S_{\mathrm{tot}} = 5\,\mathrm{cm/s}$ (dashed line).

in the semiconductor is detected by measuring the microwave reflection. In the small-signal case, the change in the reflected microwave power is proportional to the excess carrier concentration and the decay time of the signal equals the effective lifetime of the generated carriers.

The measurements are performed at a bias light illumination of 0.3 suns. A mapping yields the spatial distribution of the transient effective lifetime $\tau_{\mathrm{eff}}(x, y)$ and the harmonic mean

$$\langle \tau_{\mathrm{eff}} \rangle = \left(\frac{1}{\mathrm{Area}} \int_{\mathrm{Area}} \tau_{\mathrm{eff}}(x, y)^{-1}\, \mathrm{d}x\mathrm{d}y \right)^{-1} \tag{6.4}$$

follows from averaging $\tau_{\mathrm{eff}}(x, y)^{-1}$ over the relevant sample area. The standard deviation of the $\tau_{\mathrm{eff}}(x, y)^{-1}$ distribution serves as an estimate for the relative error of $\langle \tau_{\mathrm{eff}} \rangle$.

Measuring the sheet resistance R_{sheet} of the thin-film samples by the four point probe technique (see Section 5.1.2.1), allows to determine the sample thickness $W = \rho / R_{\mathrm{sheet}}$ from the resistivity ρ. The resistivity $\rho = 0.23\,\Omega\mathrm{cm}$ for the n-type thin-films follows from measuring both, the layer thickness using an SEM and the sheet resistance of only one sample.

Figure 6.5 shows the measured effective harmonic mean lifetimes $\langle \tau_{\mathrm{eff}} \rangle$ of four samples with thicknesses between 10 µm and 27 µm. As expected from Eq. (6.3), the effective lifetime increases with the sample thickness. The solid line is a fit of Eq. (6.3) using τ_{bulk} and S_{tot} as free parameters. The best agreement with the experimental data is achieved for a bulk lifetime of $\tau_{\mathrm{bulk}} = 16.4\,\mu\mathrm{s}$ and a surface recombination velocity of $S_{\mathrm{tot}} = 38\,\mathrm{cm/s}$. This corresponds to a bulk diffusion length of $L_{\mathrm{bulk}} = \sqrt{\tau_{\mathrm{bulk}} D} = 127\,\mu\mathrm{m}$ for a diffusion constant of $D = 9.9\,\mathrm{cm}^2/\mathrm{s}$, as derived above. The average surface recombination velocity at the front and rear side is $S_{\mathrm{f}}, S_{\mathrm{r}} < 20\,\mathrm{cm/s}$.

In order to estimate the lower limit of the bulk lifetime $\tau_{\mathrm{bulk,min}}$ which is compatible with the experimental data, a second fit is performed assuming an extremely good surface passivation. In this second fit Eq. (6.3) is matched to the data, but this time the surface recombination is fixed to $S_{\mathrm{tot}} = 5\,\mathrm{cm/s}$ and only τ_{bulk} is varied. The least square fit (dashed line in Fig. 6.5) yields $\tau_{\mathrm{bulk,min}} = 12.3\,\mu\mathrm{s}$. The lower limit for the bulk diffusion length $L_{\mathrm{bulk,min}} = \sqrt{\tau_{\mathrm{bulk,min}} D} = 110\,\mu\mathrm{m}$ is thus still more than four times the layer thickness.

Thus, with a starting layer porosity of 32 % instead of 21 % and a pre-annealing step of 5 minutes instead of 30 minutes, a high electronic quality of the grown n-type silicon thin-films is achieved. This finding agrees with the results of Kraiem et al., who investigated the effect of the pre-annealing duration on the defect density of silicon thin-films grown on porous layers with a porosity of 23 % [216]. They even found a decrease of the defect density with shorter pre-annealing times. Moreover, the low rear surface recombination velocity $S_{\mathrm{r}} < S_{\mathrm{tot}} = 38\,\mathrm{cm/s}$ shows that low temperature PECVD of amorphous silicon effectively passivates the rear surface of the silicon thin-film, when it is already glued to the glass carrier, and thus handled in a not extremely clean environment.

6.2.6 n-type PSI solar cells with autodiffused boron-doped emitters

The previous sections describe the modifications of the PSI process carried out to meet the requirements of autodiffusion, that is, the adaptation of the etching process for the application of highly doped substrates, as well as the adjustment of the epitaxy for enhancing the out-diffusion of the dopant. Here, the developed autodiffusion process is applied to form boron emitters in n-type silicon thin-film solar cells.

6.2.6.1 Fabrication process

The electrochemical etching of the p^+-substrate and the subsequent growth of a $(30 \pm 2)\,\mu\mathrm{m}$ thick n-type layer are described in Section 6.2.3. After epitaxy, a $\mathrm{POCl_3}$-diffusion is performed to permit ohmic contact to the n-type base of the cell. Following the diffusion, the Ti/Pd/Ag front contact grid is formed by electron beam evaporation through a shadow mask. Then a KOH/isopropyl solution textures the front side with random pyramids and thereby removes the diffused n^+-layer between the grid fingers on the front side. However, the metal grid itself is not affected by the solution, so that the n^+-layer remains beneath the contact fingers and serves as a local front surface field (FSF) for ohmic contact to the base. In the next step, a $\mathrm{SiN_x}$ double layer is deposited by PECVD at 300 °C. The lower layer of this double layer structure is a thin passivation layer with a refractive index of 2.4 (measured at $\lambda = 633\,\mathrm{nm}$), while the upper layer serves as an anti-reflection coating (ARC) with a refractive index of 2.05 [217]. The cell is then glued to a $2.5 \times 2.5\,\mathrm{cm}^2$ glass carrier using transparent glue and the separation from the growth substrate is performed

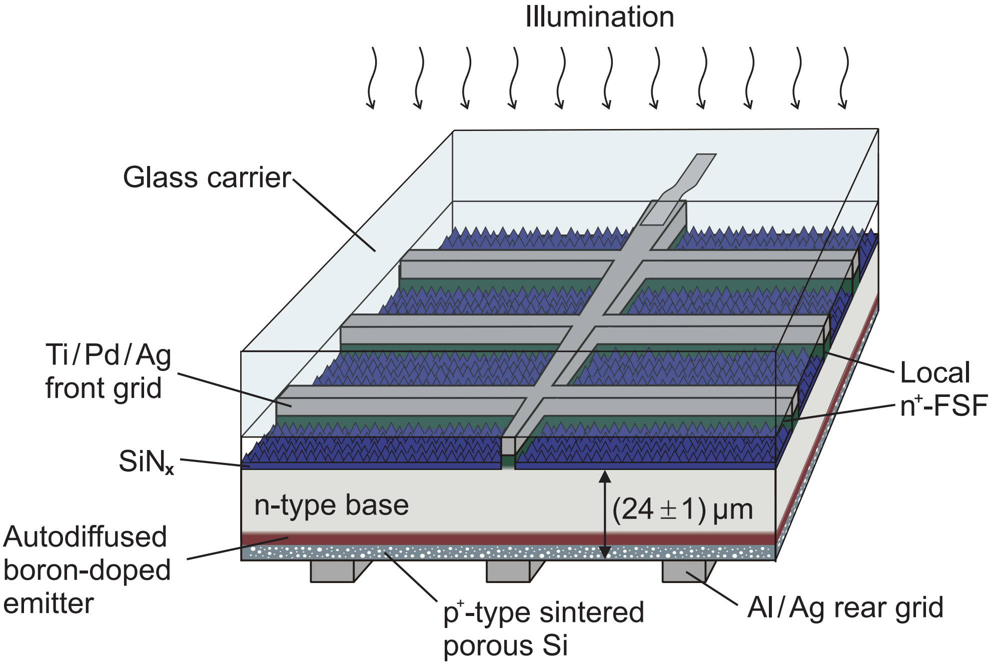

Figure 6.6. Schematics of the fabricated back-junction PSI solar cell with a n-type base and a boron-doped emitter formed by autodiffusion.

by applying mechanical stress. Finally, an Al/Ag back contact grid is deposited onto the SPS layer at the rear side, again by evaporating through shadow masks. In the described processing sequence, the residual SPS starting layer remains at the rear side of the cell, which allows a simplified fabrication of the devices. Thus, the cells do not feature any passivation on the rear junction emitter. Figure 6.6 schematically illustrates the resulting cell structure.

6.2.6.2 Cell Results and Discussion

Figure 6.7 shows the illuminated current-voltage curve of a solar cell fabricated by the above described process. The measurement is performed under standard testing conditions. An energy conversion efficiency of $\eta = (14.5 \pm 0.4)\,\%$ is achieved with a high short-circuit current density $J_{\mathrm{SC}} = (33.3 \pm 0.8)\,\mathrm{mA/cm^2}$. The cover glass does not feature an ARC. An ARC would further increase both, J_{SC} and η. Nevertheless, to the knowledge of the author, the short-circuit current density of $33.3\,\mathrm{mA/cm^2}$ is the highest so far published for a silicon thin-film solar cell based on layer-transfer. The open-circuit voltage of the cell is $V_{\mathrm{OC}} = (588 \pm 3)\,\mathrm{mV}$ and the fill factor $FF = (74.2 \pm 0.7)\,\%$. The cell area is $(4.02 \pm 0.01)\,\mathrm{cm^2}$, while the thickness of the cell is $(24 \pm 1)\,\mu\mathrm{m}$, measured with an SEM. This value includes the porous silicon layer on the back of the cell.

A low recombination velocity at the SiN$_x$-passivated front surface in combination with a bulk diffusion length of at least $111\,\mu\mathrm{m}$ allows the minority carriers generated close to the front surface to diffuse to the collecting emitter on the rear side. This results in a high

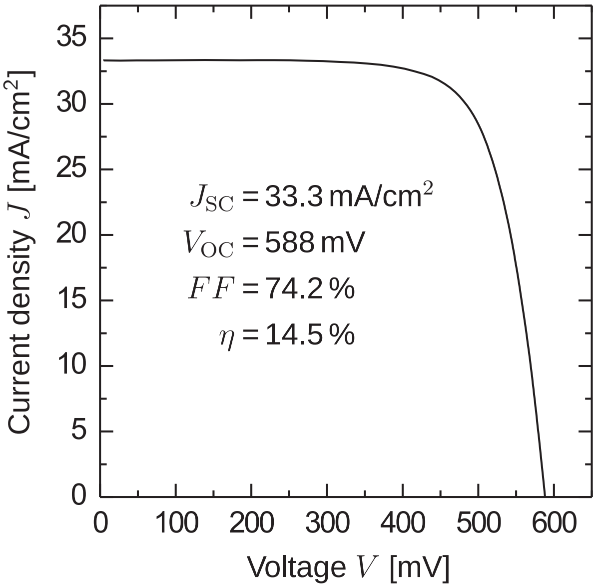

Figure 6.7. Illuminated current-voltage curve of a 2×2 cm^2 large n-type PSI solar cell with a boron emitter formed by autodiffusion. The structure of the cell is shown in Fig. 6.6. The measurement is performed at the calibration laboratory of FhG-ISE in Freiburg, Germany.

short-circuit current of the back-junction cell.

The high recombination at the non-passivated emitter rear surface is the dominant source of recombination. A lifetime measurement allows to estimate the recombination losses within the autodiffused boron emitter and the sintered porous silicon layer, as well as at the non-passivated rear surface. The analysed sample has a structure that is equivalent to the cell illustrated in Fig. 6.6, however it features no metallisation on the front and on the back and no local FSF. A lifetime mapping using MW-PCD, as described in Section 6.2.5.3, yields a transient effective lifetime of $\tau_{\mathrm{eff}} = (0.75 \pm 0.05)\,\mu\mathrm{s}$. For the calculation of the effective rear surface recombination velocity S_{r}, Eqs. (6.1) and (6.2) are solved using the parameters listed in Table 6.1. The result of $S_{\mathrm{r}} = (4050 \pm 500)\,\mathrm{cm/s}$ quantifies the recombination in the rear emitter as well as in the SPS layer and at the rear surface. This value corresponds to a saturation current of

$$J_{0,\mathrm{r}} = \frac{q n_{\mathrm{i}}^2 S_{\mathrm{r}}}{N_{\mathrm{D}}} = (2200 \pm 300)\,\mathrm{fA/cm^2}, \tag{6.5}$$

for a phosphorus doping level of $N_{\mathrm{D}} = 2.7\times10^{16}\,\mathrm{cm^{-3}}$ and an intrinsic carrier concentration of $n_{\mathrm{i}} = 9.6\times10^{9}\,\mathrm{cm^{-3}}$ at 25 °C [135–137][1]. This recombination current limits the open-

---

[1] Altermatt et al. calculated $n_{\mathrm{i,eff}} = 1.11\times10^{10}\,\mathrm{cm^{-3}}$ at 300 K for p-type silicon with $N_{\mathrm{A}} = 3\times10^{16}\,\mathrm{cm^{-3}}$ [135]. This effective intrinsic carrier density also accounts for band gap narrowing. Assuming a similar value for the n-type sample analysed in this work and using the temperature dependence of n_{i} found by Sproul and Green [136] yields $n_{\mathrm{i,eff}} = 9.6\times10^{9}\,\mathrm{cm^{-3}}$ at 25 °C.

Table 6.1. Parameters used to calculate the effective surface recombination velocity $S_{\mathrm{r}} = (4000 \pm 500)$ cm/s for the autodiffused emitter including the SPS layer and the non-passivated rear surface using Eqs. (6.1) and (6.2). Due to the textured surface on the front side of the analysed sample, an increased front surface recombination velocity S_{f} of 30 cm/s is assumed instead of the average of 20 cm/s measured for the planar lifetime samples.

Parameter	Value	Unit
W	24 ± 1	µm
τ_{eff}	0.75 ± 0.05	µs
τ_{bulk}	16.4	µs
D	9.9	cm^2/s
S_{f}	30	cm/s

circuit voltage of an ideal device to

$$V_{\mathrm{OC}} \leq \frac{k_{\mathrm{B}}T}{q} \ln\left(\frac{J_{\mathrm{SC}}}{J_{0,\mathrm{r}}}\right) = (602 \pm 4)\,\mathrm{mV}, \tag{6.6}$$

with the Boltzmann constant k_{B} and the temperature $T = 298.2$ K. This value is only slightly higher than the measured open-circuit voltage of (588 ± 3) mV. The difference is due to additional recombination in the bulk and on the front surface and a finite parallel resistance. The achieved results demonstrate the feasibility of autodiffusion for emitter generation in PSI solar cells. The efficiency of 14.5 % for the fabricated n-type cell is comparable to efficiencies of 15.4 % (on 4 cm^2 area) [14] and 14.1 % (on 95.5 cm^2) [83] that were achieved for p-type PSI cells using a conventional $\mathrm{POCl_3}$-diffusion for the emitter formation. All cell processes neither use photolithography nor high temperature oxidation steps.

Assuming that most of the recombination at the rear side occurs in the SPS region and at the non-passivated surface, the efficiency of the fabricated n-type cell could be improved by removing the porous silicon layer from the rear emitter using the selective etch described above and applying a dielectric coating for surface passivation. The glue that is used to fix the cell to the cover glass limits the temperature for rear side processing to values below 300 °C. Thus amorphous silicon [218, 219] or amorphous silicon carbide layers [220, 221] deposited by PECVD at low temperatures are promising candidates for rear side passivation, whereas amorphous silicon nitride layers showed no passivating effect on boron-diffused emitters [221, 222].

6.3 Phosphorus autodiffusion

Phosphorus autodiffusion from highly phosphorus-doped substrates has several advantages compared to boron autodiffusion. Firstly, the fabrication of p-type cells with an autodiffused phosphorous emitter does not require any additional diffusion process, whereas a $POCl_3$-diffusion is applied in Section 6.2.6.1 to permit ohmic contact to the n-type base of PSI cells that feature a boron emitter formed by autodiffusion. A p-type base does not necessarily require a high doping concentration beneath the base contact, since most metals form ohmic contacts with acceptable contact resistances to moderately doped p-type silicon [223]. Thus, the use of autodiffused phosphorus emitters instead of boron emitters allows to completely omit a conventional diffusion step in the solar cell fabrication process.

Secondly, thin film solar cells require a surface texturing to enhance the optical absorption. For layer-transfer cells the simplest approach is to texture the growth substrate, since for recycled substrates, the texture also provides a surface cleaning step and removes any residual PS from the foregoing cycle. Moreover, texturing the thin film bears the risk of etching holes in very thin films (thickness below 10 µm). Phosphorus doping would allow to texture the growth substrate prior to the porous layer formation, whereas the texturing of highly boron-doped substrates (doping level $>10^{19}\,\mathrm{cm}^{-3}$) using KOH-based solutions is hardly possible, due to a low etching rate of this material in KOH [207]. The rear surface of thin-films grown on textured substrates is structured with inverted random pyramids, since the grown films resemble the surface structure of the growth substrate. This surface structure reduces the reflection losses when illuminating the cell from the rear surface, where the autodiffused emitter is located.

The realisation of phosphorus autodiffusion within the PSI process requires the application of highly phosphorus-doped n^+-type growth substrates. But so far, the PSI process has been performed on p^+-type substrates (see Section 2.3). The challenge is therefore to adapt the PSI process so that layer-transfer on n^+-type substrates is achieved, resulting in silicon thin-films with a carrier diffusion length that is large compared to the layer thickness.

6.3.1 Layer-transfer using n^+-type substrates

With the objective of realising layer-transfer, the porous layer formation on n^+-type silicon substrates is analysed. The substrates are (100)-oriented, phosphorus-doped CZ wafers with a resistivity of 2.6 mΩcm. As for the p-type substrates from Sections 2.3.1 and 6.2.1, an HF(50 %) : ethanol = 2:1 (by volume) mixture serves as the etching solution. No illumination is applied during the etching process. Figure 6.8 presents the measured dependence of the porosity P on the etching current density J_etch. For comparison, the P-J_etch curves for the p^+-type substrates with 10 mΩcm and 4 mΩcm from Fig. 6.2 are also shown.

In two aspects the etching behaviour of the n^+-type substrates differs from the anodisation of p^+-type substrates. Firstly, at low current densities, the n^+-type substrates exhibit a high porosity of $(37 \pm 2)\,\%$ compared to $(21 \pm 1)\,\%$ and $(32 \pm 1)\,\%$ for the p^+-type substrates. Thus, the starting layer formed on n^+-substrates features a porosity that exceeds

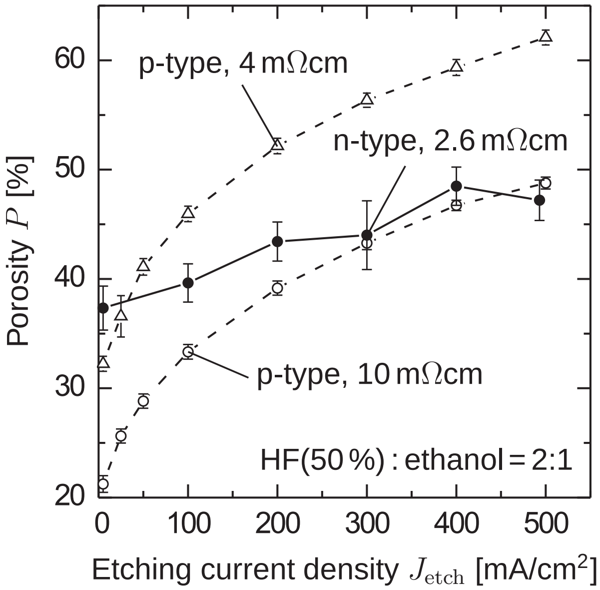

Figure 6.8. Dependence of the porosity P on the etching current density J_{etch} for the anodisation of (100)-oriented n$^+$-type and p$^+$-type silicon substrates using an HF(50 %) : ethanol = 2:1 (by volume) electrolyte. No illumination is applied during the etching process. The lines serve to guide the eye.

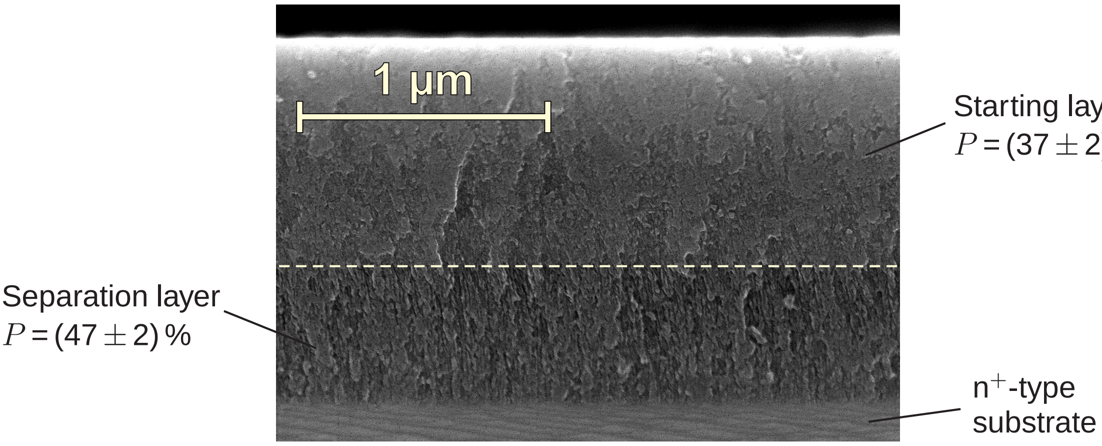

Figure 6.9. Cross sectional SEM image of a porous double layer formed on a n$^+$-type substrate applying the anodisation parameters from Table A.5. The step in the porosity between the starting and the separation layer is only (10 ± 4) %.

the porosity of the p^+-type starting layers and is almost a factor of two higher compared to the conventional process ($P = 21\,\%$, $10\,\mathrm{m\Omega cm}$ substrates). As explained in Section 6.2.1, the increased porosity could possibly lead to a reduced electronic quality of the grown thin-films.

Secondly, for the n^+-type substrates the porosity increases only moderately with the etching current density. However, the step in the porosity from the starting to the separation layer must be sufficiently high to enable the dissolving of the separation layer during annealing, which later permits the separation of the epitaxial film from the growth substrate. This means that a high current density is needed for the preparation of the separation layer on the n^+-type substrates.

Despite the flat shape of the P-J_{etch} curve, layer-transfer on $2.6\,\mathrm{m\Omega cm}$ n-type substrates is achieved by etching the starting layer with $5\,\mathrm{mA/cm^2}$ and the separation layer with $500\,\mathrm{mA/cm^2}$ resulting in porosities of $(37 \pm 2)\,\%$ and $(47 \pm 2)\,\%$, respectively. An SEM image of the as-etched double layer stack is shown in Fig. 6.9. Table A.5 in Appendix A lists the parameters in detail. The reproducible experiments show, that this step in porosity of only $(10 \pm 4)\,\%$ is sufficiently high to enable layer-transfer.

6.3.2 Epitaxial growth and solid-state diffusion

The epitaxy is performed as described in Section 6.2.2. The grown silicon layer has a thickness of $(32 \pm 2)\,\mu\mathrm{m}$ and is boron-doped with a concentration of $1.5 \times 10^{16}\,\mathrm{cm^{-3}}$. The only difference to the process described above is a reduced duration of 30 minutes for the drive-in compared to 60 minutes for the first experiments. The shorter drive-in allows a higher throughput and still results in a sufficiently low sheet resistance.

Figure 6.10 shows a cross sectional SEM image of the epitaxial film and the reorganised porous double layer. The microstructure of the reorganised starting layer formed on n^+-type substrates differs from the one formed on p^+-type substrates (see Fig. 6.3). The n^+-type SPS layer exhibits an inhomogeneous structure with small pores at the bottom and larger irregularly distributed pores in the top region. These pores exhibit diameters of several 100 nm, which is much larger compared to the pores observed in p^+-type SPS. The described inhomogeneity complicates the controlled removal of the SPS layer, since, in contrast to the SEM image from Fig. 6.3, there is no defined boundary between the SPS layer and the epitaxial film in the present case. Therefore, the SPS layer is not removed and the combined system that consists of the porous layer and the autodiffused region is analysed instead. The extraction of the dopant concentration profile from a spreading resistance analysis requires the knowledge of the carrier mobility [202]. However, the effective mobility within the SPS layer is unknown. Thus, only the sheet resistance is measured after the layer transfer. This measurement gives a sheet resistance of $R_{\mathrm{sheet}} = (160 \pm 16)\,\Omega/\square$. The corresponding sheet conductance $\sigma_{\mathrm{sheet}} = 1/R_{\mathrm{sheet}}$ applies for the sum of both the conductance of the autodiffused phosphorus emitter and that of the SPS starting layer, which is connected in parallel.

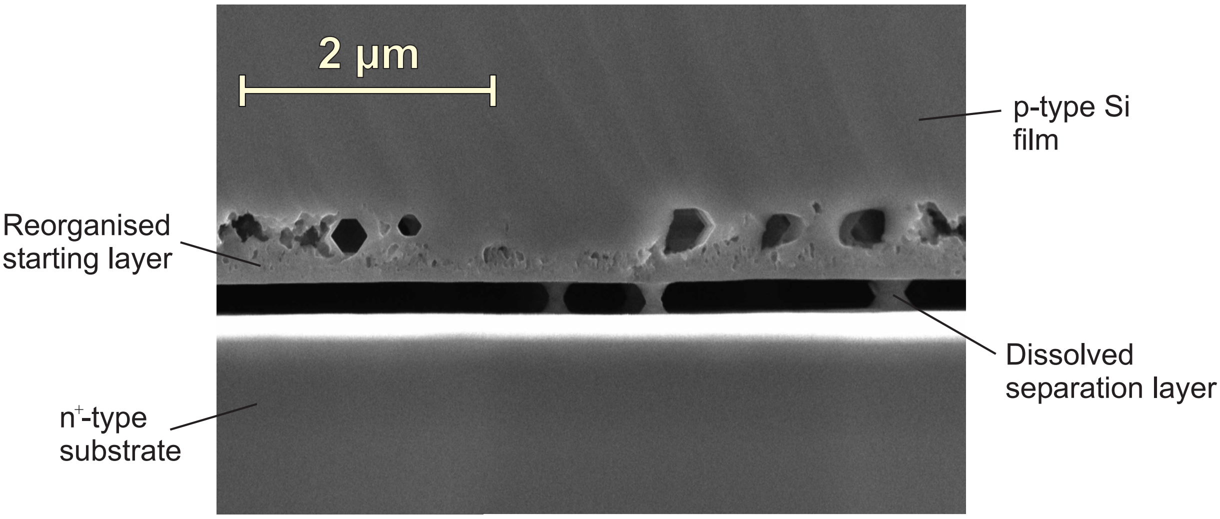

Figure 6.10. Cross sectional SEM image of the epitaxial p-type silicon film and the reorganised porous double layer. The film is still attached to the n^+-type growth substrate.

6.3.3 Carrier lifetime analysis

As described above, a high porosity of the starting layer could possibly reduce the bulk diffusion length of the grown silicon thin-films by introducing crystal defects. The porosity $P = (37 \pm 2)\,\%$ of the starting layer formed on n^+-type substrates even exceeds the value of $P = (32 \pm 1)\,\%$ for the $4\,\text{m}\Omega\text{cm}$ p^+-type substrates used for boron autodiffusion. Therefore the carrier diffusion length within the grown silicon layers is estimated from lifetime measurements.

6.3.3.1 Sample preparation

Lifetime samples are prepared from the grown p-type thin-films in the following way. A double layer stack of a-Si and SiN_x is used to passivate the front surface of the thin-film sample while it is still attached to the growth substrate. Both the a-Si and the SiN_x layer are deposited by PECVD at a temperature of 230 °C. In the next step the sample is glued to a glass carrier and detached from the substrate. After the transfer, a KOH solution removes the SPS layer and the autodiffused emitter from the rear side of the sample. Afterwards the sample is cleaned and the rear surface is passivated, again by depositing amorphous silicon with a PECVD system. Finally, an annealing step at 270 °C for ten minutes results in a distinct reduction of the surface recombination velocity at the a-Si-passivated surfaces [211, 212].

6.3.3.2 Effective lifetime of p-type silicon thin-films

The transient effective lifetime τ_eff of the thin-film sample is measured using the MW-PCD method, as outlined in Section 6.2.5.3 above. The measurement is performed at a

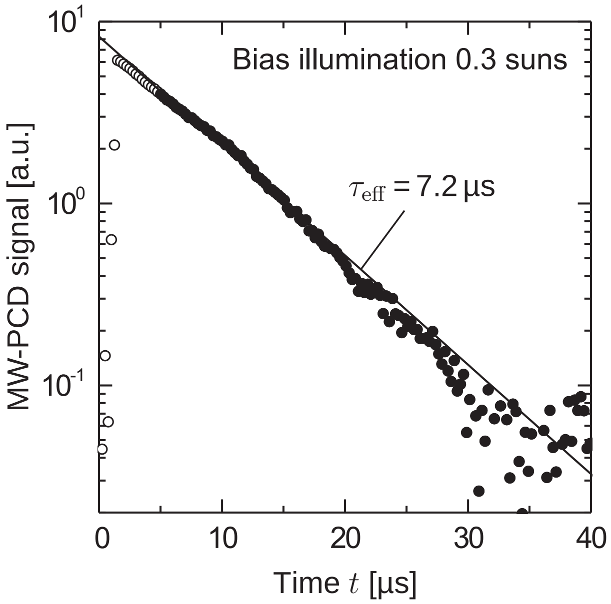

Figure 6.11. Locally measured MW-PCD transient signal (dots) of a passivated p-type silicon thin-film and fitted exponential decay function (solid line). During the measurement, white bias light corresponding to 0.3 suns illuminates the sample. Only the filled dots are used for the fit.

bias light illumination of 0.3 suns. Figure 6.11 presents a typically measured transient signal. Fitting an exponential decay function gives the local effective lifetime $\tau_{\mathrm{eff}}(x,y)$. A mapping yields the spatial lifetime distribution, and the effective lifetime for the sample follows from the harmonic mean using Eq. (6.4). This measurement (performed after the final annealing step) yields an effective lifetime of $\tau_{\mathrm{eff}} = (7.3 \pm 1)\,\mu\mathrm{s}$ for the passivated p-type silicon thin-films. Using an electron mobility of $\mu_{\mathrm{e}} = 1075\,\mathrm{cm}^2/(\mathrm{V\,s})$ [192], a diffusion constant of $D = \mu_{\mathrm{e}} k_{\mathrm{B}} T/q = 27.6\,\mathrm{cm}^2/\mathrm{s}$ follows. Thus, the measured lifetime corresponds to a diffusion length of $L_{\mathrm{bulk,min}} = \sqrt{\tau_{\mathrm{eff}} D} = (142 \pm 12)\,\mu\mathrm{m}$. This diffusion length represents a lower limit for the bulk diffusion length $L_{\mathrm{bulk}} > L_{\mathrm{bulk,min}}$, since for the bulk lifetime $\tau_{\mathrm{bulk}} > \tau_{\mathrm{eff}}$ is valid due to the remaining surface recombination. Assuming a surface recombination velocity of $S_{\mathrm{tot}} = 40\,\mathrm{cm/s}$, as measured for the passivated n-type films, and a thickness of $W = (23 \pm 2)\,\mu\mathrm{m}$, a bulk lifetime of $\tau_{\mathrm{bulk}} = (8.4 \pm 1.5)\,\mu\mathrm{s}$ corresponding to $L_{\mathrm{bulk}} = (151 \pm 13)\,\mu\mathrm{m}$ follows from Eq. (6.3). Thus, with a bulk diffusion length of at least four times the layer thickness, a sufficiently high electronic quality is achieved for p-type silicon thin-films grown on porous layers with a porosity of $(37 \pm 2)\,\%$.

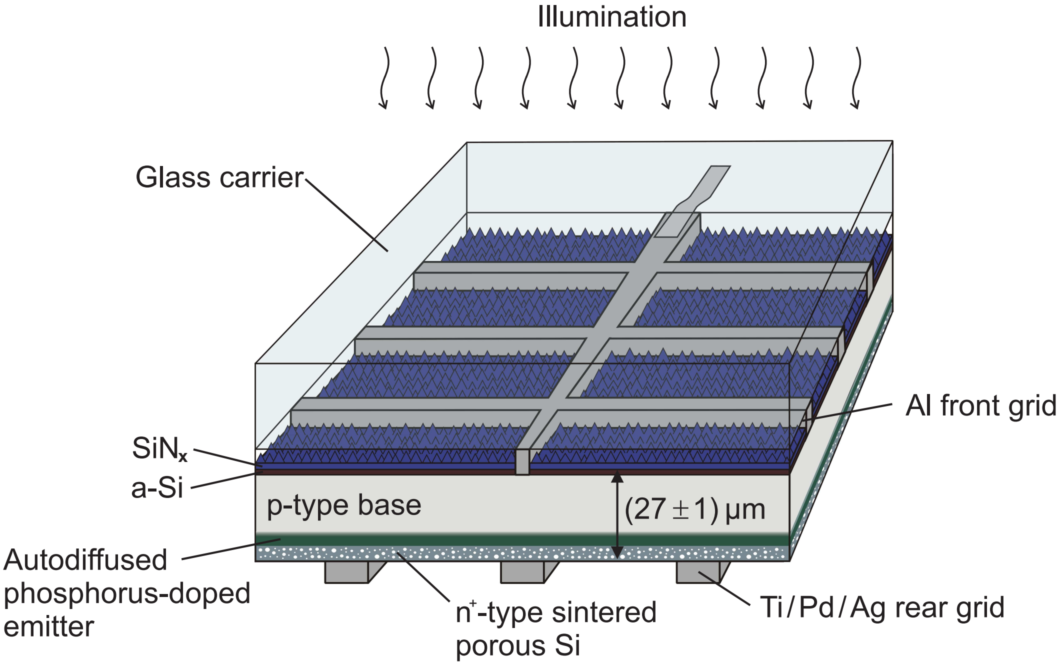

Figure 6.12. Schematics of the fabricated back-junction PSI solar cell with a p-type base and a phosphorus-doped emitter formed by autodiffusion.

6.3.4 p-type PSI solar cells with autodiffused phosphorus-doped emitters

PSI thin-film solar cells with a phosphorus emitter formed by autodiffusion are fabricated from the same run as the lifetime samples. The porous layer formation and the subsequent epitaxy are performed as described above. In contrast to the processing sequence described in Section 6.2.6, the present fabrication process does not contain any conventional diffusion process. Figure 6.12 shows the structure of the fabricated solar cells. The illuminated front of this rear junction cell is textured with random pyramids to reduce the reflection losses. A double layer stack of a-Si and SiN$_x$ [211, 224, 225] passivates the front surface of the cell. The front grid is formed by electron beam evaporation of aluminium through shadow masks. The grid is deposited onto the a-Si passivated front surface prior to the deposition of the SiN$_x$ ARC. By annealing at 300 °C during the SiN$_x$ deposition, the aluminium dissolves into the underlying a-Si layer and forms the front contact [226]. The autodiffused emitter located on the rear side of this cell remains non-passivated. The residual SPS layer is not removed, since the removal bears the risk of partly etching away the emitter, as explained above. The rear contact grid consists of a Ti/Pd/Ag stack, which is deposited onto the SPS layer.

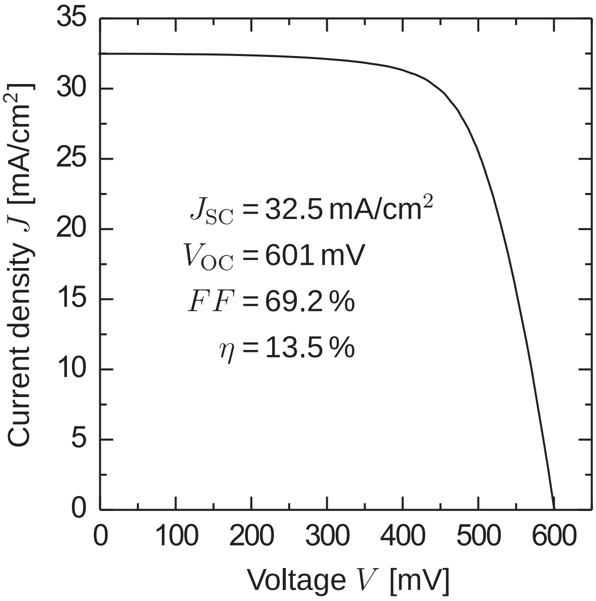

Figure 6.13. Illuminated current-voltage curve of a 2×2 cm^2 large p-type PSI solar cell with autodiffused phosphorus emitter. The structure of the cell is shown in Fig. 6.12. The measurement is performed in-house at ISFH.

6.3.4.1 Cell Results and Discussion

With this cell design an efficiency of 13.5 % (in-house measurement) is achieved. Figure 6.13 shows the illuminated current voltage curve, measured under standard testing conditions. The open-circuit voltage is 601 mV, the short-circuit current density 32.5 mA/cm^2 and the fill factor is only 69.2 %. The cell area is 4 cm^2 while the thickness of the cell is (27 ± 1) µm, measured with an SEM.

This result confirms that the autodiffusion concept also enables the formation of phosphorus-doped emitters, which allows the fabrication of silicon thin-film solar cells without the application of a conventional diffusion process, as demonstrated with the present device. The achieved efficiency is below the value of $\eta = 14.5\,\%$ for the n-type cell from the previous section. The main difference is the lower fill factor of $FF = 69.2\,\%$ compared to $FF = 74.2\,\%$ for the n-type cell. By increasing the fill factor, which is likely to be limited by a high series resistance, the efficiency of the p-type cell could be improved. Moreover, as for the n-type cell, the main source for recombination is the non-passivated rear emitter. Thus, as outlined above, another option to reach a higher efficiency is the passivation of the rear emitter by removing the residual porous silicon layer and depositing a dielectric coating for surface passivation. However, the selectivity of the KOH etching solution is much lower for the n$^+$-type SPS layers compared to p$^+$-type SPS layers from Section 6.2.3, due to large pores in n$^+$-type SPS layers (see Fig. 6.10), compared to the rather sponge-like configuration of the p$^+$-type SPS layer shown in Fig. 6.3 on p. 91. Thus, the removal of the n$^+$-type SPS layer shown in Fig. 6.10 bears the risk of partly etching away the autodiffused emitter.

6.4 Summary of Chapter 6

A novel approach is presented, which utilises the out-diffusion of dopant impurities from a highly doped growth substrate to form an emitter in the epitaxially grown active layer of a silicon thin-film solar cell. This "autodiffusion" process combines the epitaxial growth and the emitter diffusion into one single process and allows to completely omit the conventional emitter diffusion. The generation of both, boron- as well as phosphorus-doped emitters, is demonstrated. For the realisation of phosphorus autodiffusion, the PSI layer-transfer technique is successfully applied to n^+-type substrates for the first time.

A 24 µm thick n-type silicon thin-film solar cell with a boron-doped emitter formed by autodiffusion achieves an independently confirmed efficiency of 14.5 % and a high short-circuit current density of 33.3 mA/cm^2. The fabricated 27 µm thick p-type cells that feature an autodiffused phorphorus-doped emitter reach efficiencies of 13.5 % (in-house measurement). No conventional diffusion process is used for the fabrication of the p-type cells. The lower efficiency of the p-type cell results from a low fill factor of 69.2 % caused by an increased series resistance. For both cell types, the non-passivated emitter on the rear side is the main source of recombination. Thus, the removal of the residual SPS layer and a subsequent surface passivation of the rear emitter should result in an increased cell efficiency.

7 Solar cell device simulation

For very thin PSI cells with a thickness below 10 µm, light trapping becomes increasingly important, since 45 % of the photons from the solar spectrum (Air Mass 1.5 Global) exhibit a wavelength above 780 nm, where the absorption length in silicon exceeds 10 µm. As discussed in Chapter 4, light scattering by the pores in sintered porous silicon leads to an increased optical confinement and thus enhances the photogeneration within the PSI solar cell. On the other hand, the results from Chapter 5 show that the carrier diffusion length within the SPS layer is reduced due to recombination via defects located at the large internal surface of the pores. These two effects, light scattering and carrier recombination, are opposing and affect the performance of PSI solar cells.

In this chapter, simulations are performed to attain quantitative information on the impact of the two described phenomena on the solar cell efficiency. The thickness of the SPS layer is an important parameter, since both, the number of scattered photons and the amount of recombining carriers depend on the the layer thickness. The simulations allow the optimisation of the device geometry, as for example the determination of the optimum SPS layer thickness for a given thickness of the epitaxial layer. For this purpose, the optical model from Section 4.2.4 is applied to calculate the depth-resolved carrier generation profile within a planar PSI cell under solar illumination. The obtained generation profile is then passed to the device simulation program PC1D (version 5.5) [227], that delivers the current-voltage parameters and the energy conversion efficiency of the simulated device.

7.1 Simulated structures

Two different structures are analysed, a front and a back junction device. Figures 7.1 and 7.2 schematically illustrate the front and rear emitter cell, respectively. The design of the front junction cell is similar to that of the conventional PSI cells presented in Section 2.3.2, whereas the back junction cell resembles the configuration of the autodiffused emitter cells from Sections 6.2.6 and 6.3.4. In both cases, a planar geometry without any surface texture is assumed in order to exclusively analyse the light trapping effect due to scattering by the pores.

7.1.1 Front junction cell

The front side of this p-type cell features a n$^+$-type emitter with a surface concentration of of $1\times10^{20}\,\mathrm{cm}^{-3}$ and a junction depth of $W_{\mathrm{em}} = 0.3$ µm resulting in a sheet resistance of 81.8 Ω/□. These are typical numbers obtained from a POCl$_3$-diffusion performed at 800 °C to 900 °C [205]. For the passivated and partly metallised front surface, a recombination

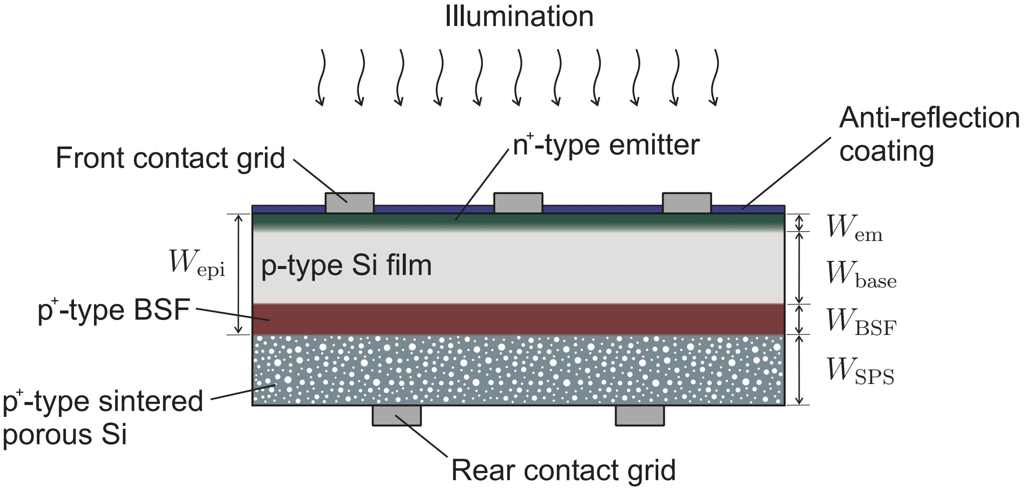

Figure 7.1. Schematics of the simulated PSI solar cell with a front emitter and a highly doped BSF layer between the base region and the residual SPS layer.

current density of $J_{0,\mathrm{f}} = 200\,\mathrm{fA/cm^2}$ is assumed, as expected for a metallisation fraction of $f_{\mathrm{met}} = 5\,\%$ [206].

The epitaxially grown layer consists of a base region with the thickness $W_{\mathrm{base}} + W_{\mathrm{em}}$ and a highly doped BSF region with the thickness W_{BSF}, as shown in Fig. 7.1. The presence of the highly doped BSF layer reduces the recombination at the rear side of the device [82]. The doping level of the p-type base is $3{\times}10^{16}\,\mathrm{cm^{-3}}$ and the bulk diffusion length $L_{\mathrm{base}} = 150\,\mathrm{\mu m}$, as experimentally determined in Section 6.3.3. The p$^+$-type BSF layer is simulated as a separate region with a doping density of $2{\times}10^{19}\,\mathrm{cm^{-3}}$ and an Auger recombination limited bulk lifetime of $\tau_{\mathrm{BSF}} = 0.024\,\mathrm{\mu s}$ [191]. The corresponding bulk diffusion length is $L_{\mathrm{BSF}} = 3.4\,\mathrm{\mu m}$ using the default parameters of the mobility model implemented in PC1D [227].

The SPS layer is of p$^+$-type with a doping level $8{\times}10^{18}\,\mathrm{cm^{-3}}$, which is the material predominantly investigated in this work. For SPS with a doping density of $N_{\mathrm{A}} = 6.5{\times}10^{17}\,\mathrm{cm^{-3}}$, a reduced hole mobility corresponding to 40 % of the bulk value was measured [171]. Thus for both, electrons and holes, the simulation applies mobility values that are reduced to 40 % of the values suggested by the mobility model of PC1D yielding $\mu_{\mathrm{e,SPS}} = 83.5\,\mathrm{cm^2/(V\,s)}$ for the electrons and $\mu_{\mathrm{h,SPS}} = 31.1\,\mathrm{cm^2/(V\,s)}$ for the holes. The carrier diffusion length within the SPS region is varied between 0.1 µm and 2 µm corresponding to the experimentally determined values from Table 5.3 on p. 85. A surface recombination current density of $J_{0,\mathrm{r}} = 1000\,\mathrm{fA/cm^2}$ is used for the non-passivated rear surface. This is about half of the experimentally determined value of $2200\,\mathrm{fA/cm^2}$ from Eq. (6.5), that accounts for both, recombination within the emitter and the 1 µm thick SPS layer, as well as at the non-passivated rear surface. The surface recombination velocity at internal interfaces, as for example between the epitaxial layer and the SPS region, is set to zero. Appendix C lists all applied parameters.

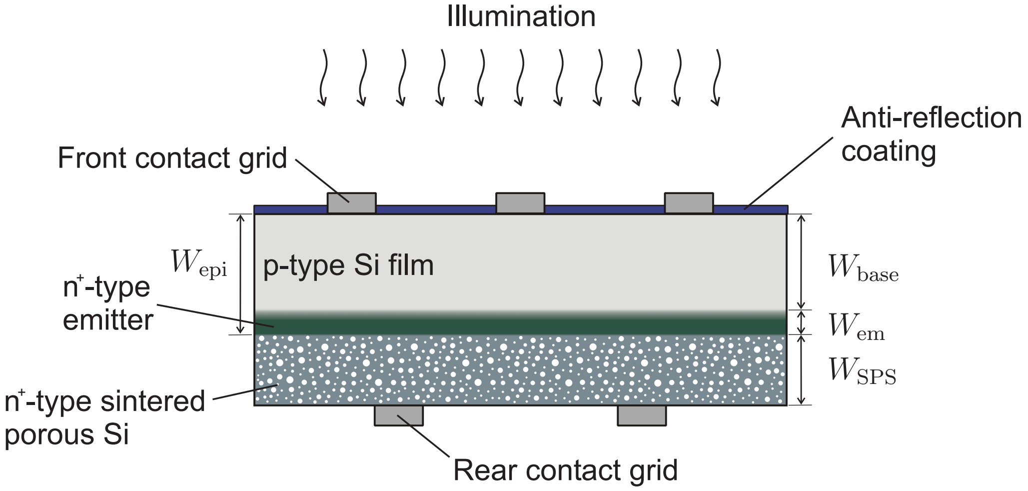

Figure 7.2. Schematics of the simulated PSI solar cell with a rear emitter formed by autodiffusion from the highly doped n^+-type SPS layer.

7.1.2 Back junction cell

In contrast to the above described cell, the device illustrated in Fig. 7.2 features an emitter that is located at the rear side of the epitaxial layer. This configuration results from forming the emitter by means of the autodiffusion process that is described in Chapter 6. Again, the base is of p-type with a doping concentration of $3{\times}10^{16}\,\mathrm{cm}^{-3}$ and a bulk diffusion length of 150 µm. The illuminated front surface is passivated and contacted by the front metal grid. For this surface, an effective recombination velocity of $S_\mathrm{f} = 315\,\mathrm{cm/s}$ is assumed, as experimentally determined for a-Si-passivated p-type PSI solar cells [219]. The equivalent recombination current density is $186\,\mathrm{fA/cm^2}$.

The rear emitter features a surface concentration of $1{\times}10^{19}\,\mathrm{cm}^{-3}$ and a junction depth of $W_\mathrm{em} = 1\,\mu\mathrm{m}$ corresponding to a sheet resistance of $113\,\Omega/\square$. These values resemble the experimentally obtained profile from Section 6.2.3. However, the simulation assumes a higher surface concentration, since a high doping level at the rear surface reduces the recombination losses similar to a BSF layer. Such a high surface concentration would result from using very highly doped n^+-type substrates with a resistivity below $2\,\mathrm{m}\Omega\mathrm{cm}$. As shown in Section 6.2.3, the doping level of the SPS layer must be sufficiently higher than the surface concentration of the autodiffused emitter. Therefore a dopant concentration of $4{\times}10^{19}\,\mathrm{cm}^{-3}$ is assumed for the n^+-type SPS layer. Again, the carrier mobilities are reduced to 40 % of the bulk values suggested by PC1D. The carrier diffusion length within the n^+-type SPS region is varied from 0.1 µm to 0.68 µm, where the latter corresponds to the Auger limit of 2.8 ns for the carrier lifetime in the bulk material. Appendix C summarises the simulation parameters for both structures.

7.1.3 Calculation of the carrier generation profile

The optical model from Section 4.2.4 enables the determination of the carrier generation profile that results from both, specular as well as diffuse absorption. The incident spectrum is the Air Mass 1.5 Global (AM1.5G) spectrum [228] normalised to $1000\,\mathrm{W/m^2}$. An anti-reflection coating with a refractive index of $n = 2$ (non-dispersive) and a thickness of 60 nm covers the front surface of both devices. Parasitic absorption within this coating is neglected. The optical model accounts for free-carrier absorption and uses the same dopant concentration profiles as the subsequent PC1D simulations.

The effective refractive index and the absorption coefficient of the SPS layer follow from the linear model of Eq. (4.13). The scattering coefficient is calculated by means of Mie's theory using Eqs. (4.17) and (4.18). As already described in Section 5.2.3.3, the effective refractive index n_{eff} from the linear model is also used for the calculation of both Mie scattering parameters, the size parameter z and the refractive index ratio w (see Eqs. (4.15) and (4.16)). In all cases, the porosity of the SPS layer is $P = 20\,\%$. Unless specified otherwise, a lognormal pore size distribution with a median of $d_{\mathrm{med}} = 35\,\mathrm{nm}$ and a width of $\sigma = 0.5$ is assumed, as determined for lowly porous SPS (see Section 2.2.3 and Table 4.1 on p. 42). The simulated structures exhibit a 20 nm thick pore-free layer at the rear surface of the SPS layer, as described in Section 4.3. The closed surface forms during the reorganisation of the porous layer. If not stated otherwise, the calculation assumes $\tilde{n} = 1$ for the medium behind the device. The spatial discretisation for the optical model is 10 nm within the SPS layer and ranges from 5 nm to 50 nm within the epitaxial layer.

The total carrier generation profile within the device

$$G(x) = (1 - f_{\mathrm{met}}) \int \left[A_{\mathrm{spec,gen}}(x,\lambda) + A_{\mathrm{diff,gen}}(x,\lambda)\right] \Phi_{\mathrm{AM1.5G}}(\lambda)\,\mathrm{d}\lambda \tag{7.1}$$

follows from the photon flux $\Phi_{\mathrm{AM1.5G}}(\lambda)$ of the AM1.5G spectrum [228] and the specular and diffuse generation profiles, $A_{\mathrm{spec,gen}}(x,\lambda)$ and $A_{\mathrm{diff,gen}}(x,\lambda)$, from Eqs. (B.36) and (B.71), respectively. Multiplying with $(1 - f_{\mathrm{met}})$ accounts for the shading by the front metal grid that covers a fraction of $f_{\mathrm{met}} = 5\%$ of the front surface.

Finally, PC1D [227] reads the cumulative generation profile, that follows from integrating the result from Eq. (7.1) with respect to x, and delivers the current-voltage parameters of the device, such as the short-circuit current J_{SC}, the open-circuit voltage V_{OC} and the energy conversion efficiency η.

7.2 Sintered porous silicon back reflector

The simulations allow to analyse the impact of a specific parameter, as for example the thickness of the SPS region, on the solar cell efficiency. The investigated parameters are the thickness W_{SPS} of the SPS layer, the carrier diffusion length L_{SPS} within this layer and the size of the pores.

The simulations consider values of 3 µm, 10 µm and 30 µm for the thickness W_{epi} of the epitaxial layer, which includes the emitter, the base region and, in case of the front junction cell, the BSF layer (see Figs. 7.1 and 7.2). These thickness values are maintained throughout all calculations, since the growth of an epitaxial layer with a certain thickness requires a certain technological effort. However, when keeping the epitaxial layer thickness constant while comparing the front and the back junction structure, it should be pointed out that the two devices do not feature the same thickness value for the base region. The difference becomes significant for thin cells. For example, the 3 µm thick epitaxial layer of a back junction cell consists of a base region with the thickness $W_{\text{base}} = 2\,\mu\text{m}$ and the rear emitter with the thickness $W_{\text{em}} = 1\,\mu\text{m}$. In case of the 3 µm thick front junction device, the thickness of the base region is $W_{\text{base}} = 2.6\,\mu\text{m}$ for $W_{\text{em}} = 0.3\,\mu\text{m}$ and a 0.1 µm thick BSF layer (see Figs. 7.2 and 7.1).

For the front junction cell, another important parameter is the thickness W_{BSF} of the BSF layer. On one hand the highly doped BSF prevents the minority carriers from recombining at the non-passivated rear surface yielding a higher open-circuit voltage [82]. On the other hand, free-carrier absorption and recombination within the BSF region reduce the efficiency. Thus, for each geometry and parameter set, there is an optimum thickness of the BSF layer. In this work, the thickness of the BSF region is optimised for each of the three considered cell thickness values using a set of standard parameters. These parameters are a diffusion length of $L_{\text{SPS}} = 0.5\,\mu\text{m}$, a lognormal pore size distribution with $d_{\text{med}} = 35\,\mu\text{m}$ and $\sigma = 0.5$, a constant thickness of the epitaxial layer and a variable thickness W_{SPS} of the SPS layer. The obtained optimum BSF thickness values are $W_{\text{BSF}} = 0.1\,\mu\text{m}$, 0.5 µm and 1.5 µm for a cell thickness of $W_{\text{epi}} = 3\,\mu\text{m}$, 10 µm and 30 µm, respectively. The thickness of the base region then follows as $W_{\text{base}} = W_{\text{epi}} - W_{\text{BSF}} - W_{\text{em}}$ with $W_{\text{em}} = 0.3\,\mu\text{m}$ in the present case (see Fig. 7.1).

7.2.1 Thickness of the SPS layer

Figure 7.3 presents the cumulated carrier generation G_{epi} within the epitaxial layer plotted as a function of the thickness W_{SPS} of the SPS layer. The generation rate is expressed in units of mA/cm^2, representing the short-circuit current density of an ideal device with an internal collection efficiency of unity. Due to the light scattering by the pores, the photogeneration G_{epi} within the epitaxial layer increases from 30.6 mA/cm^2 to 33.6 mA/cm^2 for a 30 µm thick front junction device and from 18.9 mA/cm^2 to 23.3 mA/cm^2 for a thickness of $W_{\text{epi}} = 3\,\mu\text{m}$. Thus, with decreasing cell thickness, the effect of the back reflector increases and thinner cells benefit stronger from the light trapping compared to thicker cells. The curves for the front and the back junction device are quite similar, however, the front junction device exhibits slightly higher numbers due to a lower doping level of the SPS region and thus less parasitic free-carrier absorption.

For an epitaxial layer thickness of 3 µm, the photogeneration of both structures reaches a maximum at $W_{\text{SPS}} = 2\,\mu\text{m}$. At this thickness value, a large fraction of the specular photons that reach the back of the cell are scattered within the SPS region, since the layer thickness W_{SPS} is comparable to the scattering length $L_\gamma = 1/\gamma$. For values $W_{\text{SPS}} > 2\,\mu\text{m}$, the photogeneration decreases again, since an increasing number of the scattered photons

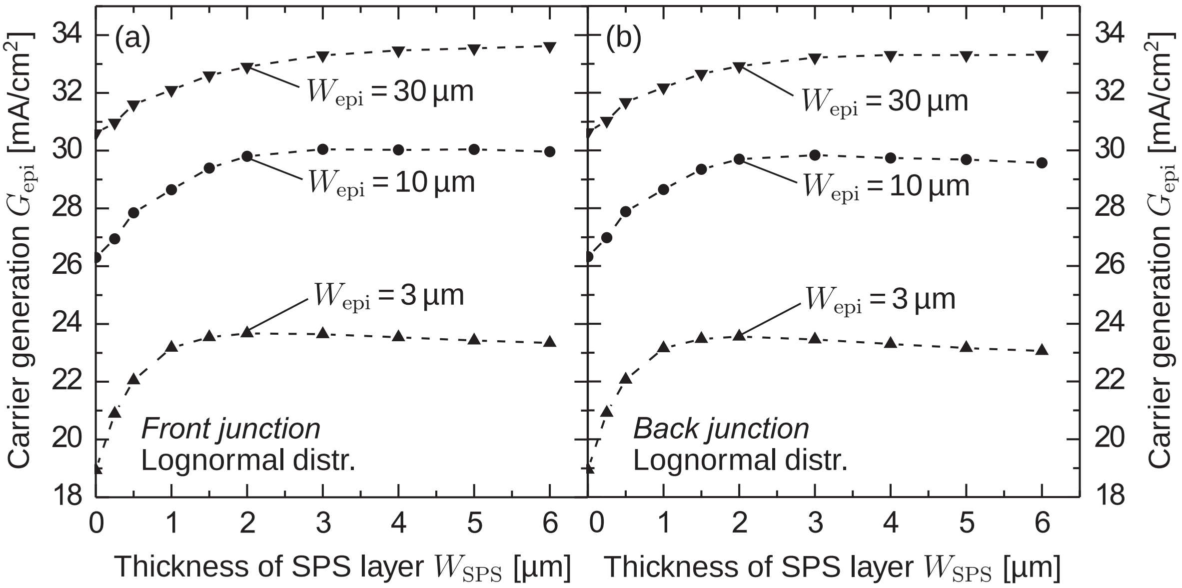

Figure 7.3. Cumulated carrier generation within the epitaxial layer for the two device structures and different thickness values of the SPS layer and the epitaxial layer. A lognormal pore size distribution with a median of $d_{\mathrm{med}} = 35$ nm and a width of $\sigma = 0.5$ is assumed. The lines serve to guide the eye.

is absorbed within the SPS region instead of being deflected by total reflection at the rear surface and scattered back into the epitaxial layer.

With increasing cell thickness, more of the incident specular radiation is absorbed within the epitaxial layer and only weakly absorbed photons at longer wavelength reach the SPS layer. In this case the photogeneration maximum is less pronounced. Moreover, these photons are less likely scattered within the SPS region, due to the lower scattering coefficient at longer wavelengths (see Fig. 4.6 on p. 51). Therefore the maximum moves to higher W_{SPS} values, where the thickness of the SPS layer approaches the scattering length L_γ.

Figure 7.4 shows the simulated conversion efficiencies that result from inserting the calculated generation profiles into PC1D. The efficiencies range from 9.2 % to 13 %, 13 % to 15.8 % and 14.9 % to 16.9 % for $W_{\mathrm{epi}} = 3$ µm, 10 µm and 30 µm, respectively. The curves resemble the characteristics of the photogeneration graphs from Fig. 7.3 above. Due to a small diffusion length of 0.5 µm, only a small fraction of the carriers generated within the SPS region are extracted. Therefore, the efficiency of the device scales with the amount of carriers generated within the epitaxial layer, explaining the similarity between Figs. 7.3 and 7.4.

For both device structures and all considered cell thickness values, a gain in the efficiency is achieved by using a SPS back reflector, compared to the case $W_{\mathrm{SPS}} = 0$. Thus, in the present case, the additional photogeneration due to light scattering by the pores clearly surpasses the recombination losses within the SPS layer.

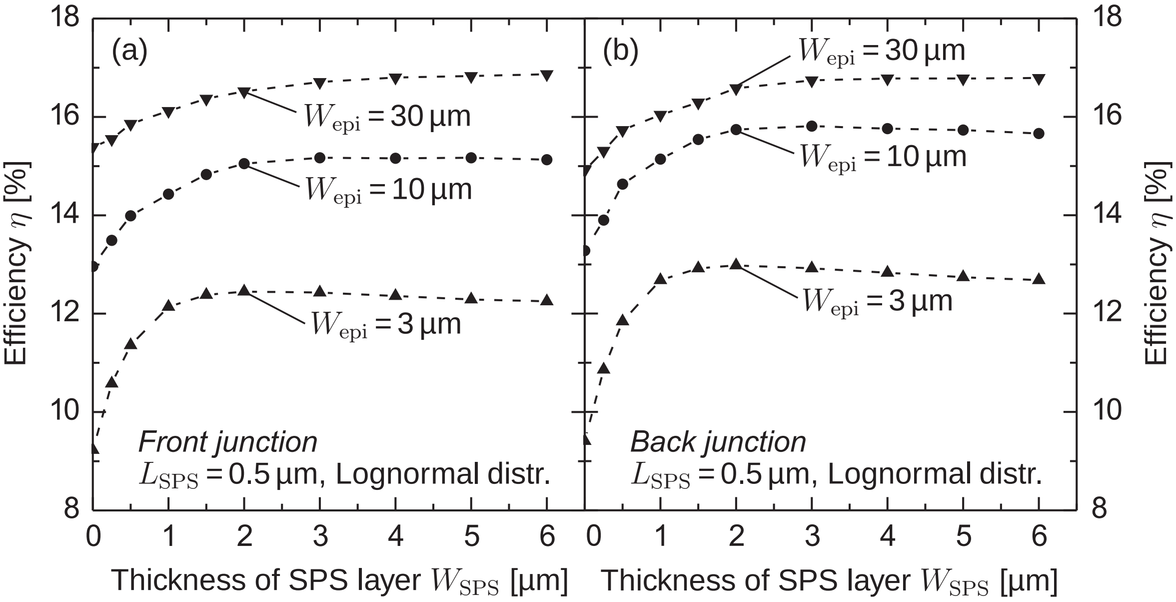

Figure 7.4. Simulated conversion efficiency of the two structures as a function of the thickness W_{SPS} of the SPS layer for different cell thickness values. The diffusion length within the SPS region is $L_{SPS} = 0.5\,\mu m$ and the parameters for the pore size distribution are $d_{med} = 35\,nm$ and $\sigma = 0.5$.

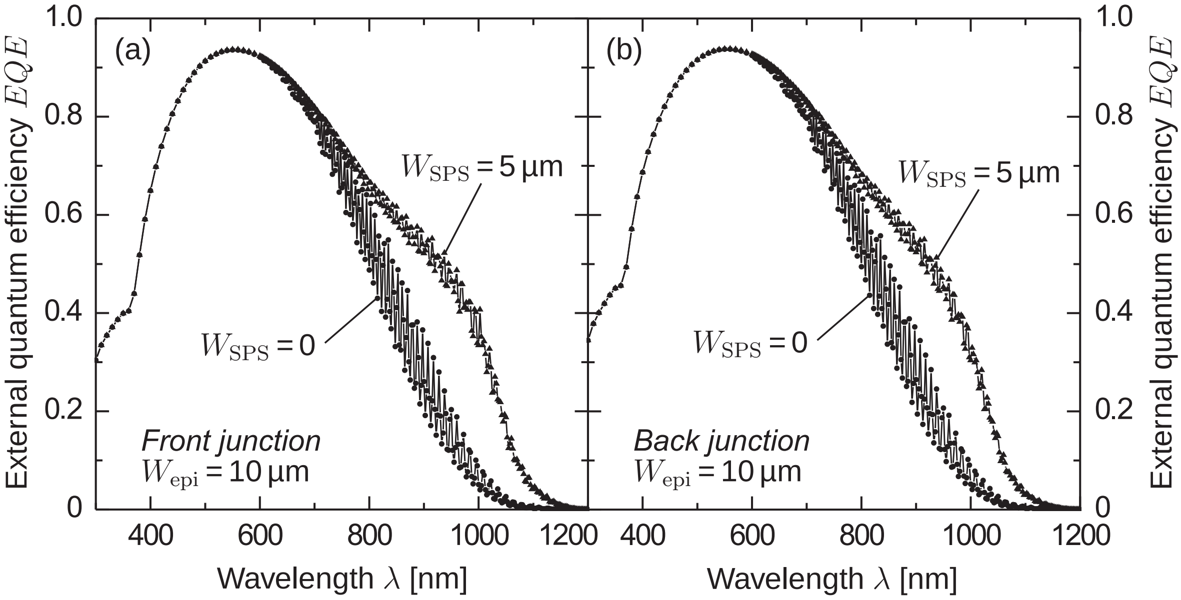

Figure 7.5. Calculated external quantum efficiency for the two structures and different thickness values of the SPS layer. The epitaxial film thickness is $W_{epi} = 10\,\mu m$ and the diffusion length within the SPS region $L_{SPS} = 0.5\,\mu m$. The pore size distribution parameters are $d_{med} = 35\,nm$ and $\sigma = 0.5$. The calculation accounts for a shading loss of 5 % by the front grid.

Figure 7.5 presents external quantum efficiencies calculated for devices with a 10 µm thick epitaxial layer. Again, the results for the front and the back junction structure are quite similar. The interferences reveal the coherent character of the optical model. In the wavelength range between 800 nm and 1000 nm, a 5 µm thick SPS back reflector enhances the *EQE* by a factor of 2.5 compared to $W_{\mathrm{SPS}} = 0$, corresponding to an increase of 3.7 mA/cm^2 (back junction) to 4.2 mA/cm^2 (front junction) in the short-circuit current.

7.2.2 Diffusion length within the SPS layer

Figure 7.6 illustrates the dependence of the cell efficiency on the diffusion length L_{SPS} within the SPS region. A 10 µm thick planar front junction cell achieves a maximum efficiency of 14.6 % for $L_{\mathrm{SPS}} = 0.1$ µm and 16.2 % for $L_{\mathrm{SPS}} = 2$ µm. Thus, the diffusion length within the SPS layer has a strong impact on the cell efficiency. This parameter not only determines the fraction of carriers collected from the SPS region, it also affects the excess carrier concentration within the device and thereby the open-circuit voltage.

However, light trapping due to scattering by the pores outbalances the recombination losses, even for a rather low diffusion length of only 0.1 µm. With this diffusion length, a 10 µm thick cell still gains about 1.5 % (absolute) in the efficiency by the SPS reflector.

The same holds for the back junction device. In this case the Auger lifetime of 2.8 ns limits the diffusion length within the n$^+$-type SPS region to values below 0.68 µm assuming a mobility of $\mu_{\mathrm{h}} = 62.6\,\mathrm{cm}^2/(\mathrm{V\,s})$ as mentioned in Section 7.1.2 above.

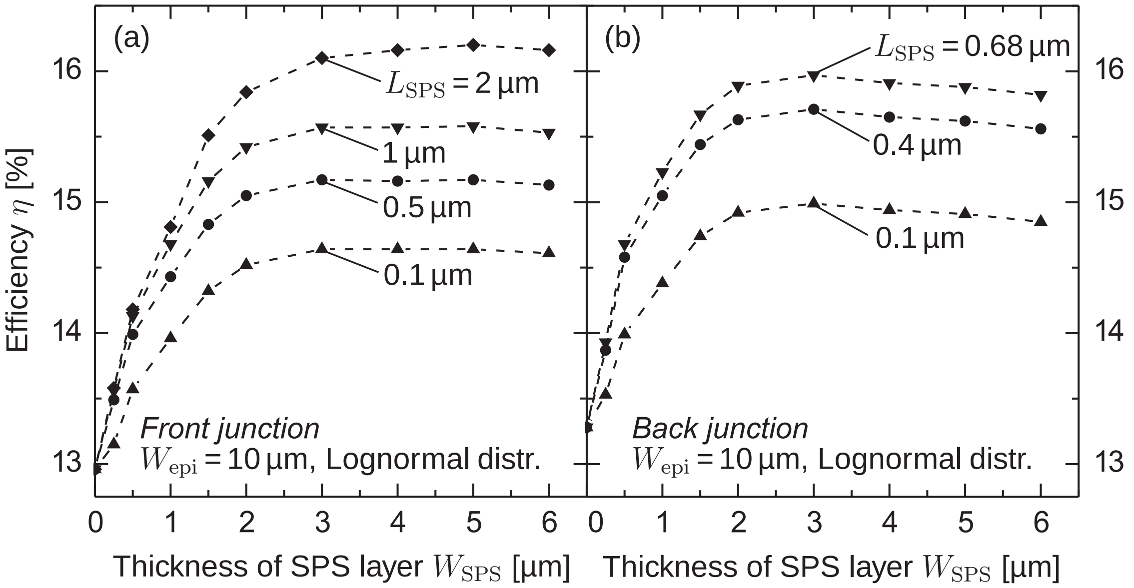

Figure 7.6. Impact of the diffusion length L_{SPS} within the SPS layer on the cell efficiency. The thickness of the epitaxial layer is $W_{\mathrm{epi}} = 10$ µm. Again, the pore size distribution is of lognormal type with $d_{\mathrm{med}} = 35$ nm and $\sigma = 0.5$.

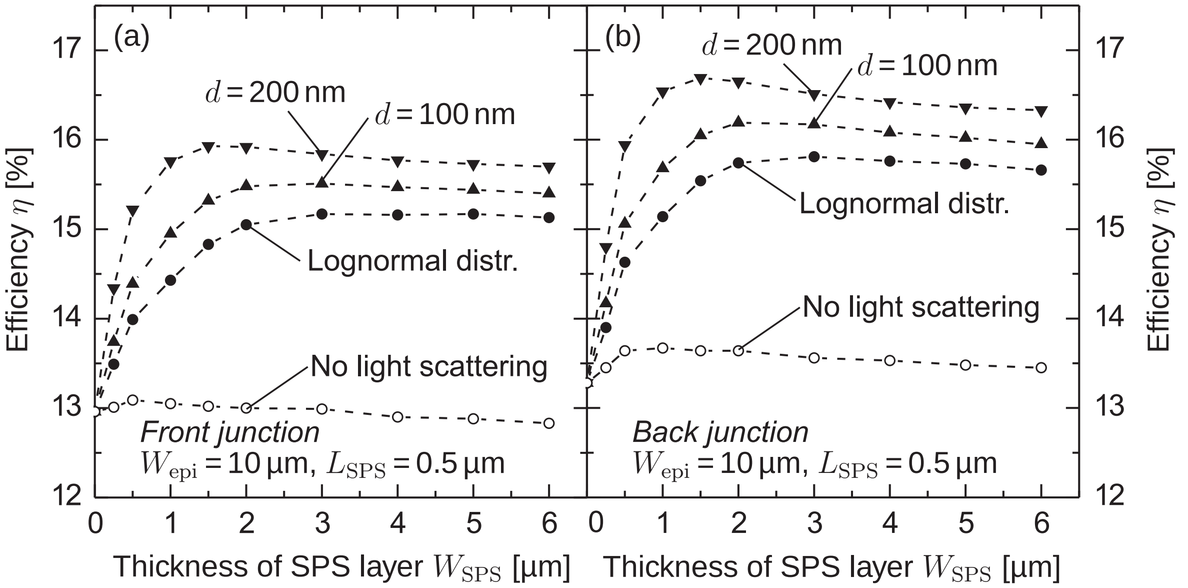

Figure 7.7. Effect of the pore size on the efficiency for 10 µm thick cells. Pore diameters of $d = 200\,\mathrm{nm}$, $d = 100\,\mathrm{nm}$ and a lognormal distribution with $d_{\mathrm{med}} = 35\,\mathrm{nm}$ and $\sigma = 0.5$ are compared. The open circles illustrate the case for a vanishing scattering coefficient (no light scattering). A diffusion length of $L_{\mathrm{SPS}} = 0.5\,\mu\mathrm{m}$ is used.

7.2.3 Size of the pores

Larger pores, as experimentally observed for n^+-type SPS in Section 6.3.2, lead to increased light scattering, since the scattering efficiency strongly increases with the pore diameter (see Fig. 4.5 on p. 50). Figure 7.7 exemplifies the impact of the pore size on the efficiency for a 10 µm thick cell. For solely analysing the light trapping effect of larger pores, a constant diffusion length of $L_{\mathrm{SPS}} = 0.5\,\mu\mathrm{m}$ is assumed for the SPS region. The maximum efficiency of the back junction device increases from 15.8 % to 16.7 % when changing the pore size from a lognormal distribution with a median of $d_{\mathrm{med}} = 35\,\mathrm{nm}$ and a width of $\sigma = 0.5$ to monodisperse spheres with $d = 200\,\mathrm{nm}$. When the scattering coefficient is set equal to zero, the maximum efficiency is only 13.7 %.

As explained above, for small diffusion lengths L_{SPS}, the efficiency scales with the photogeneration within the epitaxial layer. The larger pore size leads to an increased scattering coefficient, so that more photons are scattered back into the epitaxial layer yielding a higher photogeneration and thus higher efficiencies. Moreover, the increased scattering coefficient shifts the efficiency maximum to lower W_{SPS} values, since in this case a thinner SPS layer is sufficient for the randomisation of the specular light.

In the case of no light scattering, the efficiency of both structures first increases slightly with the thickness of the SPS layer and then starts to decrease again for $W_{\mathrm{SPS}} > 1\,\mu\mathrm{m}$. This increase does not originate from a higher photogeneration within the epitaxial layer.

Instead, for the back junction cell, the highly doped n^+-type SPS region prevents minority carriers from recombining at the rear surface, similar to the effect of a BSF layer. This shielding effect results in a higher open-circuit voltage compared to the case of $W_{\mathrm{SPS}} = 0$. For the front junction cell the present BSF region already reduces the rear surface recombination and the additional p^+-type SPS layer has only a weak effect. Therefore the efficiency increase is much weaker compared to the back junction cell. However, for the assumed diffusion length of $L_{\mathrm{SPS}} = 0.5\,\mu\mathrm{m}$ and $W_{\mathrm{SPS}} < 1\,\mu\mathrm{m}$, the described screening effect surpasses the recombination within the SPS layer in both cases, leading to an increased cell efficiency compared to $W_{\mathrm{SPS}} = 0$. For lower diffusion lengths of $L_{\mathrm{SPS}} < 0.3\,\mu\mathrm{m}$ for the front junction cell and $L_{\mathrm{SPS}} < 0.2\,\mu\mathrm{m}$ for the back collecting device, recombination within the SPS layer dominates. In this case, the efficiency decreases monotonically with the SPS layer thickness when light scattering is neglected.

7.3 Comparison with Lambertian back reflector

In a second step, simulations are performed to calculate the efficiency that would result from ideal optical and electrical conditions at the rear side of the device. These simulations allow a validation of the efficiency gain that results from light trapping due to the SPS layer. For this purpose, the carrier generation profile is calculated as described above, however, for both structures a Lambertian reflector replaces the SPS layer at the rear side of the epitaxial layer. This diffuse reflector deflects all incident photons back into the device and randomises their propagation direction. Such a rear reflector is implemented into the diffuse optical model by assuming a diffuse reflection of $R_{jk} = 1$ and, consequently, using $T_{jk} = 0$ for the matrix $\hat{M}_{jk}$ from Eq. (B.42) that describes the diffuse reflection at the rear surface. Since all incident photons are diffusely reflected, the specular reflection of the rear side is set to zero.

Moreover, for this optimum case-calculation, the front junction cell does not feature a highly doped BSF. Instead, an ideally passivated rear surface with a recombination velocity

Table 7.1. Current-voltage parameters of the two simulated structures assuming an ideal Lambertian rear reflector and zero recombination at the rear surface.

Structure	Thickness W_{epi} [μm]	Open-circuit voltage V_{OC} [mV]	Short-circuit current J_{SC} [mA/cm^2]	Fill factor FF [%]	Efficiency η [%]
Front junction	3	661	32.1	81.7	17.4
	10	660	34.4	81.6	18.5
	30	654	35.8	81.5	19.1
Back junction	3	672	32.7	81.5	17.9
	10	669	34.7	81.5	18.9
	30	660	34.9	81.5	18.7

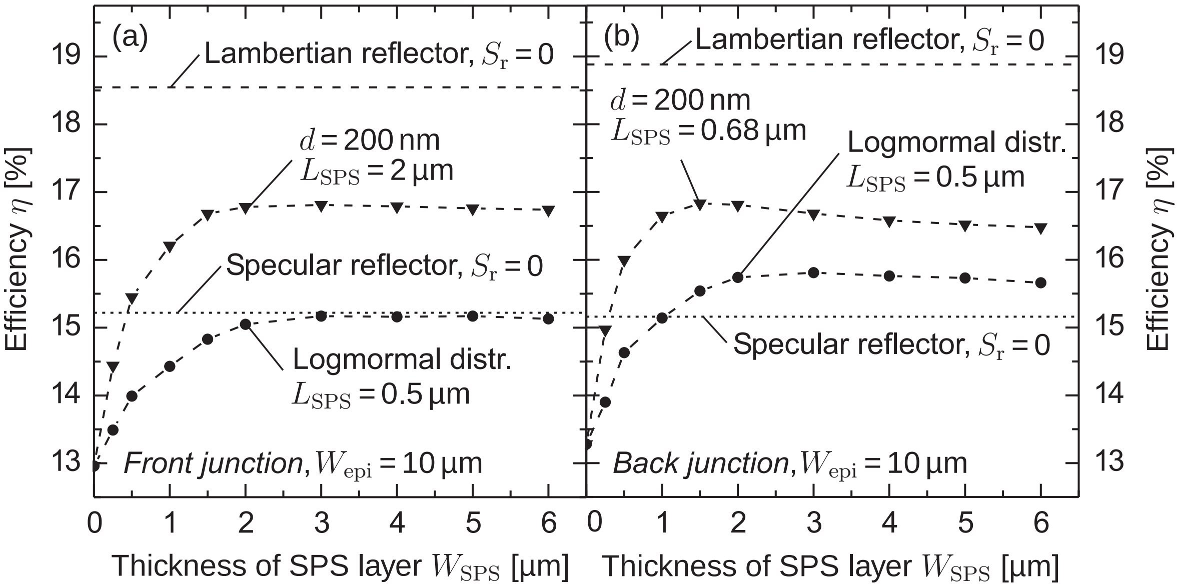

Figure 7.8. Efficiency potential of a 10 µm thick planar cell with a SPS back reflector (symbols) assuming different pore sizes and diffusion lengths L_{SPS} for the SPS region. For comparison, the efficiency resulting from no recombination at the rear surface and an ideal Lambertian reflector (dashed line) or a specular mirror (dotted line) are shown as well.

of $S_r = 0$ cm/s is assumed for both structures. All other electronic parameters are retained, as summarised in Appendix C.

Table 7.1 lists the current-voltage parameters that result from the optimum-case simulations. The efficiencies range from 17.4 % to 19.1 %. For both structures the open-circuit voltage V_{OC} decreases with increasing cell thickness due to a reduced excess carrier density, whereas the absorption and thus the short-circuit current density J_{SC} increase. In case of the front junction device, the rising of J_{SC} dominates and the efficiency increases with the cell thickness. For the back collecting cell, the two opposing trends are almost equally balanced yielding an efficiency maximum of $\eta = 19$ % at $W_{epi} \approx 17$ µm.

The values from Table 7.1 are comparable to the simulation results of Brendel [78], who calculated the efficiency potential of silicon thin-film solar cells assuming $L_{base} = 87$ µm, $S_r = 1000$ cm/s and 90 % of the photogeneration expected from a Lambertian light trapping scheme. These simulations predicted an efficiency of 18.6 % and 17.3 % for 25 µm and 2.5 µm thick cells, respectively.

Figure 7.8 shows the efficiency potential for 10 µm thick planar silicon solar cells with a SPS back reflector. For comparison, the dashed line marks the efficiency from Table 7.1, where an ideal Lambertian reflector and no recombination at rear surface is assumed. Compared to a cell with a non-passivated rear surface and no light trapping ($W_{SPS} = 0$), a SPS reflector with a lognormal pore size distribution ($d_{med} = 35$ nm, $\sigma = 0.5$) and a diffusion length of $L_{SPS} = 0.5$ µm achieves about 40 % of the the efficiency gain that would result from the ideal Lambertian reflector and $S_r = 0$. Assuming larger pores with a diameter of

200 nm, as observed for n^+-type SPS in Section 6.3.2, and a diffusion length of 2 µm for the p^+-type SPS region, as determined in Section 5.2.3, and the Auger limit of 0.68 µm for the n^+-type SPS layer, the efficiency increase due to the SPS reflector is more than 60 % of the benefit expected from a Lambertian reflector. Comparable results are obtained for a cell thickness of $W_{\mathrm{epi}} = 3$ µm and 30 µm.

Instead of using the SPS reflector, another option is the removal of the SPS layer and the application of a passivating dielectric mirror [229]. The dotted line in Fig. 7.8 marks the efficiency for the case for $S_{\mathrm{r}} = 0$ and an ideal specular rear reflector. This mirror reflects all incident photons back into the device, but without randomising their propagation direction. For both device configurations, such a rear reflector achieves an efficiency of 15.2 % (dotted line Fig. 7.8). Thus, for a 10 µm thick epitaxial layer, the efficiency level is comparable to that of the SPS reflector when using the lognormal pore size distribution and $L_{\mathrm{SPS}} = 0.5$ µm. However, for larger pores and $L_{\mathrm{SPS}} > 0.5$ µm the efficiencies achieved by means of a SPS reflector exceed those of the specular reflector. Similar results follow for the 3 µm and 30 µm thick devices.

7.4 Validity of the optical model

As described in Sections 4.2.4 and B.4, the optical model assumes that the propagation direction of a photon is completely randomised after reflection at or transmission through an internal interface between two adjacent layers. For layers with a thickness that exceeds the scattering length $L_\gamma = 1/\gamma$, the radiation is again randomised by subsequent scattering events which justifies this simplification, as discussed in Section 4.2.4. However, in contrast to the optically analysed samples from Chapter 4, the simulated devices feature an epitaxial layer with a vanishing scattering coefficient and thus an infinite scattering length. In this case, the change in the angular distribution of the diffuse radiation upon reflection or transmission at internal and external interfaces should be considered. In the present case, due to the higher refractive index of the epitaxial layer compared to the SPS layer, the angular distribution of the diffuse radiation that enters the epitaxial layer from the SPS layer narrows according to Snell's law and the Fresnel equations. Thus, the photons in the epitaxial layer propagate predominantly at smaller angles to the normal, resulting in a reduced effective path length and less total reflection at the front surface of the device. Consequently, in the present case, the simplifying assumptions of the optical model result in an overestimation of the diffuse absorption.

An exact calculation of the angular distribution throughout the simulation by means of the Snell and Fresnel equations would increase the complexity of the model and drastically extend calculation time. Therefore, the deviation that results from the simplification of the model is estimated for a few special cases. The results show that for illumination with the AM1.5G spectrum, the model overestimates the diffuse absorption within the epitaxial layer by 18 % to 16 % for epitaxial layers with a thickness between 3 µm and 30 µm, respectively. These deviations are acceptable in the present case, since most of the results of this chapter are interpreted in terms of a comparison between different structures.

7.5 Design considerations for thin PSI solar cells

The results of the performed simulations demonstrate that the efficiency of PSI thin-film cells strongly depends on the device geometry, in particular on the thickness of the SPS layer. For all analysed cases, the efficiency increases by using a SPS back reflector compared to no light trapping and, in order to fully utilise the light trapping effect, the SPS layer should be several µm thick.

For cells that feature textured surfaces, the surface texture already introduces light trapping and the effect of the additional light trapping by the SPS layer should be smaller compared to non-textured planar cells. The simulations performed in this work do not give an answer to the question whether such a textured device would benefit from a SPS reflector or if a dielectric mirror, that also passivates the rear surface, would be the better option [229]. The incorporation of the surface texture into the optical model would require a more advanced calculation for example by means of ray-tracing calculations [152, 230].

Another option to enhance the light trapping is the application of a multilayer stack consisting of several porous layers with different porosities and thus different optical constants. Several authors suggested to use porous multilayer systems as distributed Bragg reflectors [140, 141, 231].

Concerning the SPS microstructure, the substrate type and the etching and annealing conditions should be adjusted to produce larger pores with diameters of several 100 nm, as already experimentally observed in Section 6.3.2. Large pores give a twofold advantage: Firstly they significantly enhance the light scattering and secondly the reduced surface to volume ratio yields larger carrier diffusion lengths (see Section 5.2.3.4).

7.6 Summary of Chapter 7

In this chapter, simulations are performed for evaluating two opposing effects in PSI solar cells: Light scattering by the pores of the SPS layer on the one hand and the recombination within the SPS region on the other hand. The simulation results indicate that light trapping due to scattering by the pores surpasses the recombination losses for planar, non-textured PSI cells. Assuming a diffusion length of 0.5 µm within the SPS region and a lognormal pore size distribution with a median of $d_{\mathrm{med}} = 35\,\mathrm{nm}$ and a width of $\sigma = 0.5$, a 10 µm thick cell gains about 1.5 % (absolute) in efficiency by the SPS reflector compared to no light trapping and a non-passivated rear surface. The benefit is equivalent or slightly higher compared to using a 100 % reflecting specular mirror and an ideally passivated rear surface with $S_{\mathrm{r}} = 0$. The 1.5 % increase corresponds to 40 % of the efficiency gain that would result from an ideal Lambertian reflector and an ideally passivated rear surface. For larger pores and diffusion lengths above 0.5 µm, the numbers are even higher.

8 Summary

Porous silicon (PS) is a material used in various fields, such as sensors, optical components, chemical, biological and biomedical applications, as well as layer-transfer processes for silicon thin-film devices. In a number of applications, and for layer-transfer purposes in particular, PS is exposed to high temperatures, which causes a drastic change in the morphology of this material. Due to this structural alteration, the properties of annealed or sintered porous silicon (SPS) strongly differ from the as-prepared state. Whereas as-prepared PS has been intensely investigated, only a few publications report on the sintered state of PS.

Sintered porous silicon plays an important role for the development of solar cells from the Porous Silicon Process (PSI process). These devices are fabricated by epitaxially growing a thin silicon film on a monocrystalline silicon growth substrate that features a porous surface layer. When separating the device from the growth substrate, a layer of SPS remains at the rear side of the cell. Thus, for improving the efficiency of PSI solar cells, a comprehensive determination of the physical properties of SPS is essential.

This thesis focussed on the characterisation of sintered porous silicon and, in particular, its thermal, optical and electrical properties. In addition, an alternative technological approach for the formation of an emitter in PSI solar cells was developed and successfully implemented. Finally, device simulations that applied the determined optical and electronic parameters allowed to analyse the effect of the residual SPS layer on the efficiency of planar PSI thin-film solar cells.

The fragility of free standing SPS films required the development of a non-contact measurement method for the thermal characterisation of these samples. The approach developed in this work enabled the thermophysical analysis of free standing thin-films under ambient conditions, no vacuum system was required. The procedure applied an analysis based on lock-in thermography. An oscillating line-shaped laser source periodically heated the sample and an infrared camera imaged the exited thermal wave. The thermal properties were deduced from the amplitude and the phase of this wave. The analysis of both, the amplitude as well as the phase signal, permitted the measurement under ambient conditions, since the developed method accounted for thermal losses to the surrounding. The in-plane thermal diffusivity of the sample directly followed from the spatial temperature distribution, whereas for the determination of the in-plane thermal conductivity and the volumetric heat capacity, a temperature calibration of the system was required. An experimental verification of the procedure confirmed a measurement accuracy of 10 % for the developed measurement method.

The thermal analysis of free standing SPS films with porosities between 27 % and 66 % yielded values for the thermal conductivity ranging from 21 W/(m K) to 2.3 W/(m K) and a volumetric heat capacity between 1.46 J/(cm^3 K) and 0.45 J/(cm^3 K). The Looyenga model was successfully applied to describe the dependence of the thermal conductivity of SPS on the porosity. This analysis revealed that the thermal conductivity of the solid phase, that is, the silicon network arround the pores, was a factor of three lower than the thermal conductivity of bulk silicon. This reduction was assigned to a reduced mean free path of the phonons in the porous matrix due to scattering at the internal surfaces.

Measurements of the specular reflection and transmission of free standing SPS films allowed the determination of the refractive index and the scattering coefficient. The measured refractive index agreed with the predictions of effective medium models. The Looyenga model, the Bruggeman formula or a simple linear approach all comply with the measured values for wavelengths between 500 nm and 1000 nm. For wavelengths exceeding 1000 nm, the measured refractive index was closer to the Maxwell Garnett mixing rule representing a lower percolation strength and thus a reduced refractive index compared to the other models.

Mie's theory was applied to explain the observed light scattering by the spherical pores in SPS. A comparison between theory and experiment revealed that adjacent pores affect the scattering properties of the individual voids. Assuming a reduced refractive index for the host medium in Mie's theory accounted for the close spacing of the pores in SPS and resulted in an agreement between the measured and calculated scattering coefficients. The best match was achieved when applying the afore experimentally determined refractive index for the calculation of the Mie scattering efficiency of the individual pores.

A model for the propagation of the scattered diffuse light was developed and combined with a coherent calculation for the specular non-scattered radiation. The diffuse model applied a Lambertian absorption scheme for describing the spatial distribution of the diffuse radiation within the sample. The combined model was able to reproduce both, the specular as well as the diffuse component of the measured reflection and transmission of a free standing SPS sample.

The electrical conductivity of SPS showed a dependence on both the porosity and the microstructure of the samples. The measured resistivities for films fabricated from 10 mΩcm p-type substrates ranged from 21 mΩcm to 220 mΩcm for porosities between 21 % and 33 %. The resistivity tended to increase with the porosity, however, besides the porosity, a strong impact of the pore geometry on the resistivity was observed.

An analysis of the quantum efficiency of pn-diodes made from SPS enabled the determination of the minority carrier diffusion length within this material. The evaluation of the quantum efficiency required the application of the above mentioned optical model for the calculation of the effective absorption length in the porous bulk of the samples. For porosities between 21 % and 33 % and average pore diameters of 41 nm to 56 nm, the determined carrier diffusion length ranged from 0.39 µm to 2.5 µm, whereas an analysis of a non-porous reference device fabricated from the same 10 mΩcm material yielded a value of 4.94 µm. Recombination at defects located at the large internal area of the porous structure limited the transport of photogenerated carriers through the device, since samples with a low internal surface to volume ratio showed an increased carrier diffusion length.

Besides the characterisation of SPS, the present thesis dealt with the fabrication of silicon thin-film solar cells by means of the PSI layer-transfer process. Within the scope of this work, a novel process denoted “autodiffusion” was developed and experimentally implemented. This approach utilised the out-diffusion of dopant atoms from the highly doped growth substrate to generate an emitter or a high-low junction in the epitaxially grown film of a PSI solar cell. This concept enabled the simplified fabrication of PSI solar cells without the use of a conventional diffusion process, since the emitter automatically formed during the epitaxial growth of the silicon film. The generation of boron- as well as phosphorus-doped emitters by the autodiffusion process was demonstrated. The realisation of phosphorus autodiffusion required the transfer of the PSI technique from the commonly used p^+-type to n^+-type growth substrates. The performed experiments resulted in the first-time successful demonstration of layer-transfer from n^+-type substrates.

Both, n-type and p-type cells with boron- and phosphorus-doped emitters formed by out-diffusion from the growth substrate were prepared in order to demonstrate the feasibility of the autodiffusion approach. A $2\times2\,\mathrm{cm}^2$ large n-type cell with a thickness of 24 µm achieved an independently confirmed conversion efficiency of 14.5 % with a high short circuit current density of $33.3\,\mathrm{mA/cm}^2$. To the knowledge of the author, this was the highest short circuit current density so far published for a silicon thin-film solar cell. A 27 µm thick p-type cell with a phosphorus-doped emitter formed by autodiffusion achieved an efficiency of 13.5 % (in-house measurement). This p-type cell was fabricated without the application of a conventional diffusion process. The obtained results were comparable to the efficiency of 15.4 % reached by PSI solar cells with a similar film thickness and cell area but conventionally diffused emitters, which confirmed the feasibility of the autodiffusion approach.

Finally, one-dimensional solar cell device simulations were carried out for analysing the two opposing effects of light scattering by the pores on the one hand and recombination within the residual SPS layer on the other hand. These simulations revealed that, in the case of planar non-textured PSI cells, the increased absorption due to light scattering by the pores in the SPS layer tends to surpass the recombination losses within the same layer resulting in higher efficiencies for cells that feature a several µm thick layer of SPS at the rear side compared to a device without a residual SPS layer. The benefit due to the SPS back reflector typically corresponded to 40 % of the efficiency gain that would result from an ideal Lambertian reflector and an ideally passivated rear surface.

Appendix A

Sample preparation parameters

Table A.1. Parameters of anodic etching used for preparing the thermally analysed samples from Section 3.2.1. The etching solution is an HF(50%) : ethanol = 3:2 (by volume) mixture. Annealing is performed at 1000 °C for 30 minutes in a 1 bar hydrogen atmosphere.

Sample	Layer	Current J_{etch} [mA/cm^2]	Time t [s]
T1	Starting layer	5	500
	Separation layer	290	3
T2	Starting layer	30	450
	Separation layer	85	2
T3	Starting layer	60	290
	Separation layer	140	2
T4	Starting layer	90	250
	Separation layer	250	2
T5	Starting layer	120	220
	Interlayer	3	50
	Separation layer	265	2
T6	Starting layer	200	150
	Interlayer	3	50
	Separation layer	280	3
T7	Starting layer	350	100
	Interlayer	3	100
	Separation layer	320	3

Table A.2. Etching parameters for the fabrication of free-standing SPS films as given by Seel [130]. An HF(50%) : ethanol = 1:1 (by volume) electrolyte was applied and the samples were annealed for 20 minutes at 1000 °C.

Sample	Layer	Current J_{etch} [mA/cm^2]	Time t [s]
S1	Starting layer	5	125
	Separation layer	150	3
S2	Starting layer	5	250
	Separation layer	130	3
S3	Starting layer	5	480
	Separation layer	90	3

Table A.3. Etching parameters applied for the preparation of the resistivity samples from Section 5.1.1. The etching solution is an HF(50%) : ethanol = 2:1 (by volume) mixture. Sintering is performed for 60 minutes at 1100 °C.

Sample	Layer	Current J_{etch} [mA/cm^2]	Time t [s]
R1	Starting layer	5	500
	Separation layer	270	2.5
R2a	Starting layer	30	450
	Separation layer	240	2
R2b	Starting layer	30	450
	Separation layer	80	2
R3a	Starting layer	60	300
	Separation layer	90	2
R3b	Starting layer	60	300
	Separation layer	95	2
R4	Starting layer	90	250
	Separation layer	140	2

Table A.4. Parameters of anodic etching used for the preparation of the SPS pn-devices from Section 5.2.1. An HF(50%) : ethanol = 2:1 (by volume) mixture is applied. The samples are annealed for 60 minutes at 1100 °C.

Sample	Current J_{etch} [mA/cm^2]	Time t [s]	Layer thickness [µm]
D1	5	1800	14.5 ± 0.5
D2	30	320	13.5 ± 0.5
D3	60	180	12.7 ± 0.5
D4	90	130	12.8 ± 0.5

Table A.5. Parameters of anodic etching used to achieve layer-transfer on different (100)-oriented silicon substrates. The electrolyte is an HF(50 %) : ethanol = 2:1 (by volume) mixture. No illumination is applied during etching.

Doping	Resistivity [mΩcm]	Layer	Current J_{etch} [mA/cm^2]	Time t [s]
p-type	10	Starting layer	5	100
		Separation layer	150. . . 300	3
p-type	4	Starting layer	5	100
		Intermediate step	240	0.5
		Separation layer	480	1
n-type	2.6	Starting layer	5	100
		Separation layer	500	1

Appendix B

Optical models

B.1 Calculation of the Mie scattering efficiency and the asymmetry parameter

This section briefly reflects the calculation of the Mie scattering efficiency that is required for the determination of the scattering coefficient by Eq. (4.17) as well as the asymmetry parameter. For a detailed treatment of the Mie problem see Ref. 142.

The dimensionless scattering efficiency

$$Q_{\mathrm{sca}} = \frac{2}{z^2} \sum_{j=1}^{\infty} (2j+1) \left(|a_j|^2 + |b_j|^2 \right) \tag{B.1}$$

is a function of the size parameter

$$z = \frac{2\pi r \, n_{\mathrm{host}}}{\lambda}, \tag{B.2}$$

where λ is the vacuum wavelength, r the radius of the particle, n_{host} the real part of the refractive index of the non-absorbing host medium and

$$a_j = \frac{\psi_j'(wz)\psi_j(z) - w\psi_j(wz)\psi_j'(z)}{\psi_j'(wz)\xi_j(z) - w\psi_j(wz)\xi_j'(z)} \tag{B.3}$$

$$b_j = \frac{w\psi_j'(wz)\psi_j(z) - \psi_j(wz)\psi_j'(z)}{w\psi_j'(wz)\xi_j(z) - \psi_j(wz)\xi_j'(z)} \tag{B.4}$$

with $w = \tilde{n}_{\mathrm{emb}}/n_{\mathrm{host}}$ and $\tilde{n}_{\mathrm{emb}}$ the complex refractive index of the embedded spherical particle. The functions

$$\psi_j(z) = \sqrt{\frac{\pi z}{2}} J_{j+1/2}(z) \tag{B.5}$$

and

$$\xi_j(z) = \sqrt{\frac{\pi z}{2}} H^{(2)}_{j+1/2}(z) \tag{B.6}$$

follow from the Bessel functions of the first kind $J_{j+1/2}(z)$ and those of the third kind $H^{(2)}_{j+1/2}(z)$ (Hankel functions) and ψ'_j and ξ'_j denote the derivative of ψ_j and ξ_j with respect to z.

The asymmetry parameter g_{sca} quantifies the isotropy of the scattered radiation. It follows from the size parameter z, the scattering efficiency Q_{sca} and the coefficients a_j and b_j as

$$g_{\mathrm{sca}} = \frac{4}{z^2 Q_{\mathrm{sca}}} \sum_{j=1}^{\infty} \left[\frac{j(j+2)}{j+1} \Re\left(a_j a^*_{j+1} + b_j b^*_{j+1}\right) + \frac{2j+1}{j(j+1)} \Re\left(a_j b^*_j\right) \right] . \tag{B.7}$$

The calculation is implemented using the program *Matlab* [232]. The calculated scattering efficiencies agree to 10^{-4} with those obtained from the freeware program *MiePlot* [233]. The small difference might be caused by different calculation criteria for the series in Eq. (B.1).

B.2 Fresnel equations

The angle dependent amplitude reflection coefficients for a plane wave impinging from an angle θ to the normal of the planar interface between two adjacent media are [234]

$$\rho_{\mathrm{s}}(\theta) = \frac{-\sin(\theta - \theta')}{\sin(\theta + \theta')} \tag{B.8}$$

and

$$\rho_{\mathrm{p}}(\theta) = \frac{\tan(\theta - \theta')}{\tan(\theta + \theta')} \tag{B.9}$$

for s and p polarisation, respectively. The angle θ' follows from Snell's law

$$\tilde{n} \sin\theta = \tilde{n}' \sin\theta' \tag{B.10}$$

where $\tilde{n}$ and $\tilde{n}'$ denote the complex refractive indices of the two media. The reflection of non-polarised light

$$R_{\mathrm{F}}(\theta) = \frac{1}{2}\left(|\rho_{\mathrm{s}}(\theta)|^2 + |\rho_{\mathrm{p}}(\theta)|^2\right) . \tag{B.11}$$

follows from the absolute value of the coefficients ρ_s and ρ_p and the transmission is

$$T_\mathrm{F}\left(\theta\right) = 1 - R_\mathrm{F}\left(\theta\right). \tag{B.12}$$

For a wave impinging normally to the interface Eq. (B.11) reads

$$R_{\mathrm{F},\perp} = \left|\frac{\tilde{n} - \tilde{n}'}{\tilde{n} + \tilde{n}'}\right|^2, \tag{B.13}$$

which in the case of $\tilde{n} = 1$ further simplifies to

$$R_{\mathrm{F},\perp} = \frac{\left(1 - n'\right)^2 + \kappa'^2}{\left(1 + n'\right)^2 + \kappa'^2}, \tag{B.14}$$

where $\tilde{n}' = n' + \mathrm{i}\kappa'$.

B.3 Coherent transfer matrix technique

The algorithm applied in this work was described by Harbecke [153] and enables the calculation of the coherent specular reflection and transmission of planar multilayer structures. An expansion of this method, that is described below, also permits the determination of the depth-resolved absorption within the multilayer system.

When a plane electromagnetic wave passes the interface between a medium j and a medium k, the wave is partly transmitted and partly reflected. If the wave impinges normally to a planar interface, the transmission coefficient

$$\tau_{jk} = \frac{2\tilde{n}_j}{\tilde{n}_j + \tilde{n}_k} \tag{B.15}$$

and the reflection coefficient

$$\rho_{jk} = \frac{\tilde{n}_j - \tilde{n}_k}{\tilde{n}_j + \tilde{n}_k} \tag{B.16}$$

follow from the Fresnel equations [153,234] and depend on the complex refractive indices of the two media (see Section B.2). Here, $\tau_{jk} = 1 + \rho_{jk}$ is valid, because the Maxwell equations require that the component of the electric field tangent to the interface must be continuous across it. Figure B.1 illustrates the case for plane electromagnetic waves propagating from the left hand side to the right hand side $E^{\rightarrow}$ and vice versa $E^{\leftarrow}$. Here $E_{k\mathrm{b}}^{\rightarrow}$ denotes the field at $x_k = 0$ (left hand side of layer k), whereas $E_{k\mathrm{b}}^{\rightarrow}$ is the amplitude at $x_k = W_k$ (right hand side of the layer). At the interface between layer j and layer k, the sum of the reflected

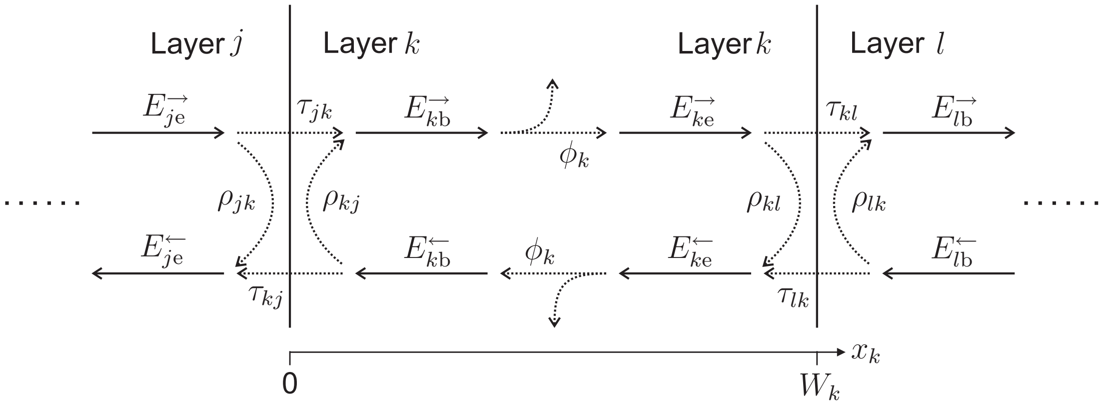

Figure B.1. Schematic for calculating the interface reflection and transmission as well as the bulk absorption for the amplitude of plane waves propagating through a multilayer stack.

and transmitted components of the incident waves are

$$E^{\rightarrow}_{k\mathrm{b}} = \tau_{jk} E^{\rightarrow}_{j\mathrm{e}} + \rho_{kj} E^{\leftarrow}_{k\mathrm{b}} \tag{B.17}$$

$$E^{\leftarrow}_{j\mathrm{e}} = \rho_{jk} E^{\rightarrow}_{j\mathrm{e}} + \tau_{kj} E^{\leftarrow}_{k\mathrm{b}}. \tag{B.18}$$

Solving for $E^{\rightarrow}_{je}$ and $E^{\leftarrow}_{je}$ and using the symmetry of the reflection coefficient $\rho_{jk} = -\rho_{kj}$ as well as $\tau_{jk}\tau_{kj} - \rho_{jk}\rho_{kj} = 1$ yields

$$E^{\rightarrow}_{j\mathrm{e}} = \frac{1}{\tau_{jk}} \left(E^{\rightarrow}_{k\mathrm{b}} + \rho_{jk} E^{\leftarrow}_{k\mathrm{b}} \right) \tag{B.19}$$

$$E^{\leftarrow}_{j\mathrm{e}} = \frac{1}{\tau_{jk}} \left(\rho_{jk} E^{\rightarrow}_{k\mathrm{b}} + E^{\leftarrow}_{k\mathrm{b}} \right), \tag{B.20}$$

or in matrix form

$$\begin{pmatrix} E^{\rightarrow}_{j\mathrm{e}} \\ E^{\leftarrow}_{j\mathrm{e}} \end{pmatrix} = \hat{T}_{jk} \cdot \begin{pmatrix} E^{\rightarrow}_{k\mathrm{b}} \\ E^{\leftarrow}_{k\mathrm{b}} \end{pmatrix}, \tag{B.21}$$

where

$$\hat{T}_{jk} = \frac{1}{\tau_{jk}} \begin{pmatrix} 1 & \rho_{jk} \\ \rho_{jk} & 1 \end{pmatrix} \tag{B.22}$$

is the transfer matrix describing the interface between medium j and medium k. If the wave passes trough a layer with the complex refractive index $\tilde{n}_k$, the field is modulated by the factor

$$\phi_k = \exp\left(\mathrm{i}\frac{2\pi}{\lambda}\tilde{n}_k W_k\right), \tag{B.23}$$

where W_k is the thickness of the layer. Thus the corresponding transfer matrix is

$$\hat{T}_k = \begin{pmatrix} 1/\phi_k & 0 \\ 0 & \phi_k \end{pmatrix}. \tag{B.24}$$

The transfer matrix $\hat{T}_{\text{stack}}$ for a multi layer stack that consists of N layers follows from multiplying the transfer matrices for the interfaces $\hat{T}_{jk}$ and those for the bulk of the layers $\hat{T}_k$, thus

$$\hat{T}_{\text{stack}} = \hat{T}_{01} \cdot \hat{T}_1 \cdot \hat{T}_{12} \cdot \hat{T}_2 \cdot \hat{T}_{23} \cdot \ldots \cdot \hat{T}_{(N-1)N} \cdot \hat{T}_N \cdot \hat{T}_{N0}. \tag{B.25}$$

Here the index $j = 0$ denotes the surrounding medium. For a wave impinging from the left hand side with an amplitude of unity, the reflected amplitude E_R and the transmitted amplitude E_T follow from

$$\begin{pmatrix} 1 \\ E_R \end{pmatrix} = \hat{T}_{\text{stack}} \cdot \begin{pmatrix} E_T \\ 0 \end{pmatrix}. \tag{B.26}$$

The specular reflection R_{spec} and transmission T_{spec} of the layer stack are thus given by

$$R_{\text{spec}} = |E_R|^2 = \left|\frac{T_{\text{stack}}^{(2,1)}}{T_{\text{stack}}^{(1,1)}}\right|^2 \tag{B.27}$$

and

$$T_{\text{spec}} = |E_T|^2 = \left|\frac{1}{T_{\text{stack}}^{(1,1)}}\right|^2, \tag{B.28}$$

respectively, where $T_{\text{stack}}^{(\text{j,k})}$ denotes the element from row j and column k of the matrix $\hat{T}_{\text{stack}}$. Once Eq. (B.26) is solved the method allows to calculate the amplitude

$$\begin{pmatrix} E_j^{\rightarrow}(x_j) \\ E_j^{\leftarrow}(x_j) \end{pmatrix} = \left(\hat{T}_{\text{stack}}(x_j)\right)^{-1} \cdot \begin{pmatrix} 1 \\ E_R \end{pmatrix} \tag{B.29}$$

of the wave at the depth x_j within layer j of the stack. Here

$$\hat{T}_{\text{stack}}(x_j) = \hat{T}_{01} \cdot \hat{T}_1 \cdot \hat{T}_{12} \cdot \hat{T}_2 \cdot \hat{T}_{23} \cdot \ldots \cdot \hat{T}_{(j-1)j} \cdot \hat{T}_j(x_j), \tag{B.30}$$

where $\hat{T}_j\left(x_j\right)$ follows from Eqs. (B.24) and (B.23) when x_j replaces W_j in Eq. (B.23). For calculating the fraction of the incident light absorbed within the layer, the result of Eq. (B.29) has to be transferred to the surrounding medium to account for the difference in the refractive indices, thus

$$\begin{pmatrix} E_{j0}^{\rightarrow}\left(x_j\right) \\ E_{j0}^{\leftarrow}\left(x_j\right) \end{pmatrix} = \hat{T}_{0j} \cdot \begin{pmatrix} E_{j}^{\rightarrow}\left(x_j\right) \\ E_{j}^{\leftarrow}\left(x_j\right) \end{pmatrix}, \tag{B.31}$$

where $\hat{T}_{0j}$ follows from Eqs. (B.15), (B.16) and (B.22) using the refractive index $\tilde{n}_j$ of layer j and that of the surrounding medium $\tilde{n}_0$. A slide with the thickness Δx_j extending from the depth x_j to $x_j + \Delta x_j$ within layer j absorbs the fraction

$$\begin{aligned} \Delta A_j\left(x_j, \Delta x_j\right) \;=\; & \left|E_{j0}^{\rightarrow}\left(x_j\right)\right|^2 - \left|E_{j0}^{\rightarrow}\left(x_j + \Delta x_j\right)\right|^2 \\ & + \left|E_{j0}^{\leftarrow}\left(x_j + \Delta x_j\right)\right|^2 - \left|E_{j0}^{\leftarrow}\left(x_j\right)\right|^2 \end{aligned} \tag{B.32}$$

of the incident intensity. The limit of Eq. (B.32) for small Δx_j enables the calculation of the absorption profile

$$A\left(x\right) = \lim_{\Delta x_j \rightarrow 0} \frac{\Delta A_j\left(x_j, \Delta x_j\right)}{\Delta x_j}, \tag{B.33}$$

where $x = x_j + \sum_{k=1}^{j-1} W_k$. This profile fulfils the condition

$$\int_0^W A\left(x\right) \mathrm{d}x = 1 - R_{\mathrm{spec}} - T_{\mathrm{spec}}, \tag{B.34}$$

where $W = \sum_j W_j$.

The absorption coefficient α includes all processes that attenuate the specular intensity, that is, absorption as well as scattering of photons. For example, in the case of SPS, the absorption coefficient is

$$\alpha = \alpha_{\mathrm{gen}} + \alpha_{\mathrm{FC}} + \gamma, \tag{B.35}$$

where γ is the scattering coefficient. For semiconducting materials such as silicon and SPS, the specular generation profile

$$A_{\mathrm{spec,gen}}\left(x\right) = f_{\mathrm{gen}}\left(x\right) A\left(x\right), \tag{B.36}$$

where $f_{\mathrm{gen}} = \alpha_{\mathrm{gen}}/\alpha$, is the fraction of A that is absorbed due to the generation of excess carriers, whereas for scattering media

$$I_{\mathrm{sca}}(x) = f_{\mathrm{sca}}(x)\, A(x)\,, \tag{B.37}$$

with $f_{\mathrm{sca}} = \gamma/\alpha$, is the initially scattered fraction. Consequently, the specular absorption profile, that accounts for all absorption processes apart from scattering, follows from

$$A_{\mathrm{spec}}(x) = (1 - f_{\mathrm{sca}}(x))\, A(x)\,. \tag{B.38}$$

Again, the program *Matlab* [232] is used for the implementation of the model. For testing the algorithm, the generation profile of an infinitely thick slab of silicon with different doping concentrations is calculated. The results agree with the absorption profiles obtained with the device simulation program PC1D (version 5.5) [227], that applies identical optical constants and the same parametrisation for the free-carrier absorption.

B.4 Modelling diffuse light propagation

B.4.1 Transfer matrix model for diffuse light

The problem of diffuse light propagation in multilayer systems, as for example described in Ref. 229, yields a system of coupled linear equations. In principle this approach permits the calculation of the diffuse light flux at every position of a multilayer stack which, in turn, enables the determination of the diffuse reflection and transmission, as well as the depth-resolved absorption of diffuse radiation. However, the number of equations increases with the number of layers, which complicates the handling of the equation system in the case of advanced multilayer structures.

In this section, a mathematical approach is used that gives identical results, but has the advantage of an easier implementation compared to solving a system of coupled linear equations. The calculation uses a transfer matrix technique similar to that presented in the previous section.

Figure B.2 illustrates the distribution of diffuse radiation within the multilayer stack. The denotation is identical to the one described in Section B.3 above. However, the present model addresses the diffuse intensity, not the wave amplitude. Therefore $T_{jk} + R_{jk} = 1$, where T_{jk} denotes the transmission from layer j to layer k and the fraction R_{jk} of the incident intensity is reflected back into layer j. Similar to the above described procedure, the sum of the reflected and transmitted components at the interface between layer j and layer k are

$$\begin{aligned} I_{k\mathrm{b}}^{\rightarrow} &= T_{jk} I_{j\mathrm{e}}^{\rightarrow} + (1 - T_{kj})\, I_{k\mathrm{b}}^{\leftarrow} && \text{(B.39)} \\ I_{j\mathrm{e}}^{\leftarrow} &= (1 - T_{jk})\, I_{j\mathrm{e}}^{\rightarrow} + T_{kj} I_{k\mathrm{b}}^{\leftarrow} && \text{(B.40)} \end{aligned}$$

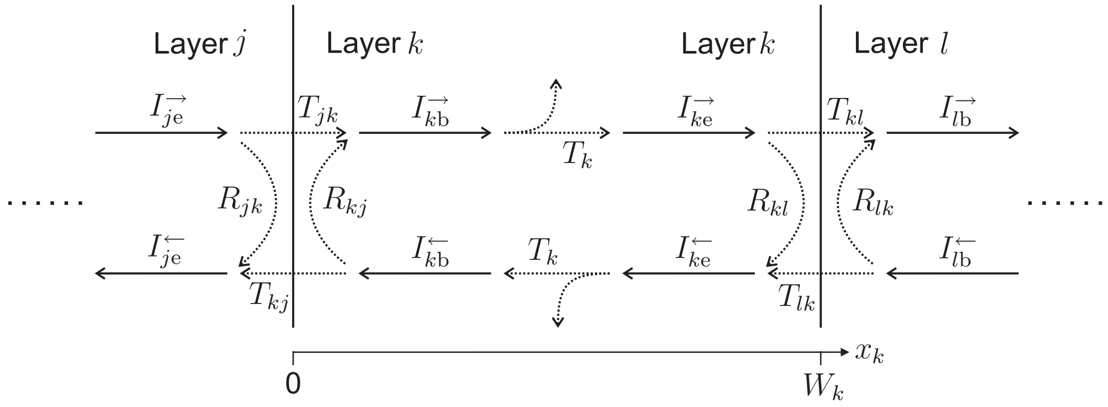

Figure B.2. Schematic for calculating the distribution of diffuse radiation propagating through a multilayer.

which corresponds to

$$\begin{pmatrix} I_{j\mathrm{e}}^{\rightarrow} \\ I_{j\mathrm{e}}^{\leftarrow} \end{pmatrix} = \hat{M}_{jk} \cdot \begin{pmatrix} I_{k\mathrm{b}}^{\rightarrow} \\ I_{k\mathrm{b}}^{\leftarrow} \end{pmatrix} \tag{B.41}$$

with

$$\hat{M}_{jk} = \frac{1}{T_{jk}} \begin{pmatrix} 1 & (T_{kj}-1) \\ (1-T_{jk}) & (T_{jk}+T_{kj}-1) \end{pmatrix} \tag{B.42}$$

being the transfer matrix that describes the reflection and transmission at the interface. Following the derivation of Section B.3, the transfer matrix for the bulk of layer j is

$$\hat{M}_j = \begin{pmatrix} 1/T_j & 0 \\ 0 & T_j \end{pmatrix}, \tag{B.43}$$

where T_j is the diffuse transmission through the layer. Again, the transfer matrix $\hat{M}_{\mathrm{stack}}$ describing a multilayer stack of N layers is

$$\hat{M}_{\mathrm{stack}} = \hat{M}_{01} \cdot \hat{M}_1 \cdot \hat{M}_{12} \cdot \hat{M}_2 \cdot \hat{M}_{23} \cdot \ldots \cdot \hat{M}_{(N-1)N} \cdot \hat{M}_N \cdot \hat{M}_{N0}. \tag{B.44}$$

If the diffuse light flux enters the stack from the front, the equation

$$\begin{pmatrix} 1 \\ R_{\mathrm{diff}} \end{pmatrix} = \hat{M}_{\mathrm{stack}} \cdot \begin{pmatrix} T_{\mathrm{diff}} \\ 0 \end{pmatrix} \tag{B.45}$$

has to be solved, whereas for diffuse illumination from the back

$$\begin{pmatrix} 0 \\ T_{\mathrm{diff}} \end{pmatrix} = \hat{M}_{\mathrm{stack}} \cdot \begin{pmatrix} R_{\mathrm{diff}} \\ 1 \end{pmatrix} \tag{B.46}$$

is valid. In the following, the latter case will be discussed. Solving Eq. (B.46) for R_{diff} and T_{diff} yields

$$R_{\text{diff}} = -\frac{M_{\text{stack}}^{(1,2)}}{M_{\text{stack}}^{(1,1)}} \tag{B.47}$$

and

$$T_{\text{diff}} = M_{\text{stack}}^{(2,2)} - \frac{M_{\text{stack}}^{(1,2)} M_{\text{stack}}^{(2,1)}}{M_{\text{stack}}^{(1,1)}}, \tag{B.48}$$

respectively. Again, $M_{\text{stack}}^{(\text{j,k})}$ denotes the element from row j and column k of the matrix $\hat{M}_{\text{stack}}$. The knowledge of R_{diff} and T_{diff} permits the calculation of the diffuse light flux intensities at the right hand side of layer j within stack

$$\begin{pmatrix} I_{j\text{e}}^{\rightarrow} \\ I_{j\text{e}}^{\leftarrow} \end{pmatrix} = \hat{M}_{j(j+1)} \cdot \ldots \cdot \hat{M}_{(N-1)N} \cdot \hat{M}_N \cdot \hat{M}_{N0} \cdot \begin{pmatrix} R_{\text{diff}} \\ 1 \end{pmatrix} \tag{B.49}$$

and those at the left hand side

$$\begin{pmatrix} I_{j\text{b}}^{\rightarrow} \\ I_{j\text{b}}^{\leftarrow} \end{pmatrix} = \hat{M}_j \cdot \begin{pmatrix} I_{j\text{e}}^{\rightarrow} \\ I_{j\text{e}}^{\leftarrow} \end{pmatrix}. \tag{B.50}$$

The diffuse intensities at the position x_j within layer j then follow from

$$I_j^{\rightarrow}(x_j) = I_{j\text{b}}^{\rightarrow} T_j(x_j) \tag{B.51}$$

and

$$I_j^{\leftarrow}(x_j) = I_{j\text{e}}^{\leftarrow} T_j(W_j - x_j), \tag{B.52}$$

where $T_j(x)$ is the diffuse transmission through a slab of medium j with the thickness x and fulfils the conditions $T_j(0) = 1$ and $T_j(W_j) = T_j$. This enables the determination of the spatially resolved diffuse absorption profile.

$$A_{\text{diff}}(x) = \lim_{\Delta x_j \to 0} \frac{\left[I_j^{\rightarrow}(x_j) - I_j^{\rightarrow}(x_j + \Delta x_j)\right] + \left[I_j^{\leftarrow}(x_j + \Delta x_j) - I_j^{\leftarrow}(x_j)\right]}{\Delta x_j}, \tag{B.53}$$

where $x = x_j + \sum_{k=1}^{j-1} W_k$. For the diffuse absorption profile

$$\int_0^W A_{\text{diff}}(x)\,\mathrm{d}x = 1 - R_{\text{diff}} - T_{\text{diff}} \tag{B.54}$$

is valid as well.

B.4.2 Distribution of the diffuse light intensity

Using the model for diffuse light propagation from the section above, the distribution of the scattered radiation within a multilayer system containing at least one scattering layer with $\gamma > 0$ is calculated as follows. The matrix for the complete layer stack

$$\hat{M}_{\text{stack}} = \hat{M}_{01} \cdot \hat{M}_1 \cdot \hat{M}_{12} \cdot \ldots \cdot \hat{M}_j \cdot \ldots \cdot \hat{M}_{(N-1)N} \cdot \hat{M}_N \cdot \hat{M}_{N0} \tag{B.55}$$

is separated into $\hat{M}_{\text{front}}(x)$ and $\hat{M}_{\text{back}}(x)$ at the distance x from the front surface. Here

$$\hat{M}_{\text{front}}(x) = \hat{M}_{01} \cdot \hat{M}_1 \cdot \hat{M}_{12} \cdot \ \ldots \cdot \hat{M}_j(x_j) \tag{B.56}$$

and

$$\hat{M}_{\text{back}}(x) = \hat{M}_j(W_j - x_j) \cdot \ldots \cdot \hat{M}_{(N-1)N} \cdot \hat{M}_N \cdot \hat{M}_{N0}, \tag{B.57}$$

where $x_j = x - \sum_{k=0}^{j-1} W_k$ is the distance from the front of layer j to the position x and

$$\hat{M}_j(x) = \begin{pmatrix} 1/T_j(x) & 0 \\ 0 & T_j(x) \end{pmatrix} \tag{B.58}$$

with the transmission $T_j(x)$ as defined in Section B.4.1 above. If photons are subject to scattering at the position x' and, after the scattering event, travel towards the front of the multilayer stack, the fraction of the scattered intensity $T_{\text{front}}(x')$ that escapes from the position x' through the front surface and the fraction $R_{\text{front}}(x')$ that is reflected within the front of the layer stack back to the same position follow from

$$\begin{pmatrix} 0 \\ T_{\text{front}}(x') \end{pmatrix} = \hat{M}_{\text{front}}(x') \cdot \begin{pmatrix} R_{\text{front}}(x') \\ 1 \end{pmatrix}. \tag{B.59}$$

Once $T_{\text{front}}(x')$ and $R_{\text{front}}(x')$ are determined, the algorithm described in Section B.4.1 allows the calculation of the absorption profile $A_{\text{front}}(x, x')$ for $x < x'$ within the front of the stack, by Eq. (B.53). Here, $A_{\text{front}}(x > x', x') = 0$. A similar calculation for photons that travel towards the rear side is

$$\begin{pmatrix} 1 \\ R_{\text{back}}(x') \end{pmatrix} = \hat{M}_{\text{back}}(x') \cdot \begin{pmatrix} T_{\text{back}}(x') \\ 0 \end{pmatrix} \tag{B.60}$$

and yields the absorption profile $A_{\text{back}}(x, x')$ for $x > x'$ within the rear of the multilayer stack. Equivalently, $A_{\text{back}}(x < x', x') = 0$. The sum $A(x, x') = A_{\text{front}}(x, x') + A_{\text{back}}(x, x')$ quantifies the probability for a photon initially scattered at the position x' to be absorbed at the position x. Since $A(x, x')$ includes both, absorption as well as scattering processes, the probability of being re-scattered at position x follows from multiplying $A(x, x')$ with the fraction $f_{\text{sca}}(x)$ of scattered photons. Thus, the re-scattering operator

$$\hat{S}(x, x') = \frac{f_{\text{sca}}(x)}{2} \begin{pmatrix} A_{\text{back}}(x, x') & A_{\text{front}}(x, x') \\ A_{\text{back}}(x, x') & A_{\text{front}}(x, x') \end{pmatrix}, \tag{B.61}$$

describes the probability for photons initially scattered at the position x' to be re-scattered at the position x. Here, the factor $1/2$ follows from the assumption that the scattering process is isotropic and the re-scattered radiation distributes equally among both propagation directions. Therefore the top and bottom row of $\hat{S}$ are identical. The matrix describing the internal reflections from x' back to the same position $x = x'$ is

$$\hat{R}_{\text{int}}(x, x') = \delta(x - x') \begin{pmatrix} 0 & R_{\text{front}}(x') \\ R_{\text{back}}(x') & 0 \end{pmatrix}. \tag{B.62}$$

Here, the structure of $\hat{R}_{\text{int}}$, with vanishing diagonal elements, reflects the fact that the photons change their propagation direction upon reflection.

If the distribution of the diffuse radiation after m scattering or internal reflection events is known, the distribution after $m+1$ events is

$$\begin{aligned} \begin{pmatrix} I^{\rightarrow}_{m+1}(x) \\ I^{\leftarrow}_{m+1}(x) \end{pmatrix} &= \int_0^W \left[\hat{S}(x, x') + \hat{R}_{\text{int}}(x, x')\right] \cdot \begin{pmatrix} I^{\rightarrow}_{m}(x') \\ I^{\leftarrow}_{m}(x') \end{pmatrix} \mathrm{d}x' \\ &= \hat{D} \cdot \begin{pmatrix} I^{\rightarrow}_{m}(x) \\ I^{\leftarrow}_{m}(x) \end{pmatrix}. \end{aligned} \tag{B.63}$$

Here, the re-distribution operator $\hat{D}$, that is defined as

$$\hat{D} \cdot \begin{pmatrix} f_1(x) \\ f_2(x) \end{pmatrix} := \int_0^W \left[\hat{S}(x, x') + \hat{R}_{\text{int}}(x, x')\right] \cdot \begin{pmatrix} f_1(x') \\ f_2(x') \end{pmatrix} \mathrm{d}x', \tag{B.64}$$

describes the re-distribution of the diffuse intensity after one scattering or internal reflection event. The initial distribution of the diffuse radiation

$$\begin{pmatrix} I^{\rightarrow}_{0}(x) \\ I^{\leftarrow}_{0}(x) \end{pmatrix} = f_{\text{sca}}(x)\, A(x) \begin{pmatrix} 1/2 \\ 1/2 \end{pmatrix} \tag{B.65}$$

follows from the the primary scattered fraction f_{sca} of the specular absorption profile $A(x)$ from Eqs. (B.37) and (B.33) when assuming that the scattered intensity distributes equally in both directions. Thus the cumulated diffuse radiation at the position x

$$\begin{pmatrix} I^{\rightarrow}(x) \\ I^{\leftarrow}(x) \end{pmatrix} = \sum_{m=0}^{\infty} \begin{pmatrix} I^{\rightarrow}_{m}(x) \\ I^{\leftarrow}_{m}(x) \end{pmatrix} = \sum_{m=0}^{\infty} \hat{D}^m \cdot \begin{pmatrix} I^{\rightarrow}_{0}(x) \\ I^{\leftarrow}_{0}(x) \end{pmatrix} \tag{B.66}$$

is given by the Neumann series of the operator $\hat{D}$ applied to the initial distribution. This series converges, since the norm $||\hat{D}||$ is smaller than unity. The limit of the Neumann series

$$\sum_{m=0}^{\infty} \hat{D}^m = \left(\mathtt{id} - \hat{D}\right)^{-1} \tag{B.67}$$

follows from the inverse of $(\mathtt{id} - \hat{D})$, where `id` denotes the identity. This is easily proven by multiplying Eq. (B.67) with $(\mathtt{id} - \hat{D})$. Once the cumulated intensities $I^{\rightarrow}(x)$ and $I^{\leftarrow}(x)$ are known, the diffuse reflection

$$R_{\text{diff}} = \int_0^W T_{\text{front}}(x')\, I^{\leftarrow}(x')\, \mathrm{d}x' \tag{B.68}$$

is given by summing up all radiation that escapes through the front. Similarly, the diffuse transmission is

$$T_{\text{diff}} = \int_0^W T_{\text{back}}(x')\, I^{\rightarrow}(x')\, \mathrm{d}x', \tag{B.69}$$

the diffuse absorption profile

$$A_{\text{diff}}(x) = (1 - f_{\text{sca}}(x)) \int_0^W \left[A_{\text{back}}(x,x')\, I^{\rightarrow}(x') + A_{\text{front}}(x,x')\, I^{\leftarrow}(x')\right] \mathrm{d}x' \tag{B.70}$$

and the diffuse photogeneration profile

$$A_{\text{diff,gen}}(x) = f_{\text{gen}}(x) \int_0^W \left[A_{\text{back}}(x,x')\, I^{\rightarrow}(x') + A_{\text{front}}(x,x')\, I^{\leftarrow}(x')\right] \mathrm{d}x'. \tag{B.71}$$

The sum of the diffuse reflection, transmission and absorption

$$R_{\text{diff}} + T_{\text{diff}} + \int_0^W A_{\text{diff}}(x)\, \mathrm{d}x = \int_0^W I_{\text{sca}}(x)\, \mathrm{d}x \tag{B.72}$$

equals the cumulated initial scattered intensity from Eq. (B.37).

A discretisation of the problem enables the implementation of the model using *Matlab* [232]. For this purpose the intensities and operators are evaluated at m discrete equidistant positions yielding vectors of m elements for the diffuse intensities $I^{\rightarrow}$ and $I^{\leftarrow}$ as well as a $2m$-by-$2m$ matrix for the operator $\hat{D}$. The limit of the Neumann series from Eq. (B.67) then follows from the inverse matrix of $(\mathbf{1} - \hat{D})$, where $\mathbf{1}$ denotes the identity matrix. The calculated spectra and absorption profiles converge for large m.

B.4.3 Lambertian light propagation

So far, for the diffuse model no assumption on the interface transmission T_{jk} from Eq. (B.42) and the bulk transmission T_j from Eqs. (B.43), (B.51) and (B.52) has been made. However, in the previous section, complete randomisation of the light after a scattering event is assumed. Consequently, a Lambertian absorption scheme should be applied. The Lambertian transmission of totally randomised light through a layer with the thickness W_j is [229, 235]

$$T_j = \int_0^{\frac{\pi}{2}} 2\sin\theta\cos\theta\exp\left\{-\frac{\alpha_j W_j}{\cos\theta}\right\}\mathrm{d}\theta, \tag{B.73}$$

where α_j is the absorption coefficient of the medium. Two partial integrations of Eq. (B.73) yield [154, 229]

$$T_j = \exp\left\{-\alpha_j W_j\right\}\left(1-\alpha_j W_j\right) + \left(\alpha_j W_j\right)^2 F\left(\alpha_j W_j\right). \tag{B.74}$$

Here $F(x) = \int_x^\infty z^{-1}\exp\{z\}\,\mathrm{d}z$ denotes the exponential integral function. The transmission $T_j(x_j)$ from the front of layer j to a depth x_j follows from replacing W_j in Eqs. (B.73) and (B.74) by x_j. Please note that for Lambertian transmission

$$T_j(x_1)\cdot T_j(x_2) \neq T_j(x_1+x_2). \tag{B.75}$$

If the randomised light first passes layer j and then the planar interface to the next adjacent layer k, the transmission through layer j and the interface between layer j and layer k follows from including the angle-dependent Fresnel transmission $T_\mathrm{F}\left(\tilde{n}_j, \tilde{n}_k, \theta\right)$ from Eq. (B.12) into the integral of Eq. (B.73) giving

$$T_j\cdot T_{jk} = \int_0^{\frac{\pi}{2}} 2\sin\theta\cos\theta\exp\left\{-\frac{\alpha_j W_j}{\cos\theta}\right\} T_\mathrm{F}\left(\tilde{n}_j, \tilde{n}_k, \theta\right)\mathrm{d}\theta. \tag{B.76}$$

Thus, the transmission through the interface is [154]

$$T_{jk} = \frac{\int_0^{\frac{\pi}{2}} 2\sin\theta\cos\theta\exp\left\{-\frac{\alpha_j W_j}{\cos\theta}\right\} T_\mathrm{F}\left(\tilde{n}_j, \tilde{n}_k, \theta\right)\mathrm{d}\theta}{\int_0^{\frac{\pi}{2}} 2\sin\theta\cos\theta\exp\left\{-\frac{\alpha_j W_j}{\cos\theta}\right\}\mathrm{d}\theta}. \tag{B.77}$$

This interface transmission depends on the complex refractive indices $\tilde{n}_j$ and $\tilde{n}_k$ of the two media, as well as on the absorbance $W_j \cdot \alpha_j$ of layer j.

Using the Lambertian transmissions from Eqs. (B.73) and (B.77) for the diffuse light propagation model described in the Sections B.4.1 and B.4.2 above, implies the assumption of a complete randomisation of the light after

- a scattering event

- reflection at an internal or external interface
- transmission through such an interface

These assumption are justified for weakly absorbing layers with a thickness in excess of the scattering length $L_\gamma = 1/\gamma$. In this case a subsequent scattering event randomises the reflected or transmitted photons before they are absorbed or reach the next interface.

Furthermore, when applying the Lambertian scheme, for the segmentation of the transfer matrix $\hat{M}$ from Eq. (B.55) into $\hat{M}_{\text{front}}$ and $\hat{M}_{\text{back}}$

$$\hat{M} \neq \hat{M}_{\text{front}} \cdot \hat{M}_{\text{back}} \tag{B.78}$$

follows, due to inequation (B.75). The splitting corresponds to the introduction of a completely randomising interface at the segmentation position. Thus, it is implicitly assumed that not only the photons that are subject to scattering at the segmentation position but also the diffuse radiation that passes through the interface at that position are completely randomised. Again, this fact is acceptable if the scattering length L_γ is small compared to both the absorption length $L_\alpha = 1/\alpha$ and the effective layer thickness $2W$.

Appendix C

Parameters for solar cell simulations

C.1 Front junction solar cell structure

General:

Device area	1 cm^2
Front contact resistance	0.25 Ω
Rear contact resistance	0.25 Ω
Internal conductor	1×10^{-4} S
Temperature	298.2 K

Emitter:

n$^+$-type, Gaussian function profile
$N_{\mathrm{surf}} = 1\times10^{20}\,\mathrm{cm}^{-3}$
$W_{\mathrm{em}} = 0.3\,\mu\mathrm{m}$
$R_{\mathrm{sheet}} = 81.8\,\Omega/\square$
$J_{0,\mathrm{f}} = 200\,\mathrm{fA/cm}^2$ corresponding to $S_{\mathrm{f}} = 35550\,\mathrm{cm/s}$

Base:

p-type
$N_{\mathrm{A}} = 3\times10^{16}\,\mathrm{cm}^{-3}$
$L_{\mathrm{bulk}} = 150\,\mu\mathrm{m}$

Back surface field:

p$^+$-type
$N_{\mathrm{A}} = 2\times10^{19}\,\mathrm{cm}^{-3}$
$L_{\mathrm{bulk}} = 3.4\,\mu\mathrm{m}$

Sintered porous silicon:

p$^+$-type
$N_{\mathrm{A}} = 8\times10^{18}\,\mathrm{cm}^{-3}$
$\mu_{\mathrm{e}} = 83.5\,\mathrm{cm}^2/(\mathrm{V\,s})$
$\mu_{\mathrm{h}} = 33.1\,\mathrm{cm}^2/(\mathrm{V\,s})$
$L_{\mathrm{bulk}} = 0.1\ldots2\,\mu\mathrm{m}$
$J_{0,\mathrm{r}} = 1000\,\mathrm{fA/cm}^2$ corresponding to $S_{\mathrm{r}} = 5.58\times10^4\,\mathrm{cm/s}$

C.2 Back junction solar cell structure

General:

Device area	$1\,\mathrm{cm}^2$
Front contact resistance	$0.25\,\Omega$
Rear contact resistance	$0.25\,\Omega$
Internal conductor	$1\times10^{-4}\,\mathrm{S}$
Temperature	$298.2\,\mathrm{K}$

Base:

p-type
$N_\mathrm{A} = 3\times10^{16}\,\mathrm{cm}^{-3}$
$L_\mathrm{bulk} = 150\,\mu\mathrm{m}$
$J_{0,\mathrm{f}} = 168\,\mathrm{fA/cm}^2$ corresponding to $S_\mathrm{f} = 315\,\mathrm{cm/s}$

Emitter:

n^+-type, Gaussian function profile
$N_\mathrm{surf} = 1\times10^{19}\,\mathrm{cm}^{-3}$
$W_\mathrm{em} = 1\ \mu\mathrm{m}$
$R_\mathrm{sheet} = 113.1\,\Omega/\square$

Sintered porous silicon:

n^+-type
$N_\mathrm{D} = 4\times10^{19}\,\mathrm{cm}^{-3}$
$\mu_\mathrm{e} = 33.7\,\mathrm{cm}^2/(\mathrm{V\,s})$
$\mu_\mathrm{h} = 62.6\,\mathrm{cm}^2/(\mathrm{V\,s})$
$L_\mathrm{bulk} = 0.1\ldots0.67\,\mu\mathrm{m}$
$J_{0,\mathrm{r}} = 1000\,\mathrm{fA/cm}^2$ corresponding to $S_\mathrm{r} = 1.17\times10^5\,\mathrm{cm/s}$

References

[1] A. Uhlir, Electrolytic shaping of germanium and silicon, *Bell Syst. Tech. J.* **35**, 333–347 (1956).

[2] D. R. Turner, Electropolishing silicon in hydrofluoric acid solutions, *J. Electroanal. Chem.* **105**, 402–408 (1958).

[3] D. R. Turner, On the mechanism of chemically etching germanium and silicon, *J. Electrochem. Soc.* **107**, 810–816 (1960).

[4] R. J. Archer, Stain films on silicon, *J. Phys. Chem. Solids* **14**, 104–110 (1960).

[5] Y. Watanabe, Y. Arita, T. Yokoyama and Y. Igarashi, Formation and properties of porous silicon and its application, *J. Electrochem. Soc.* **122**, 1351–1355 (1975).

[6] L. T. Canham, Silicon quantum wire array fabrication by electrochemical and chemical dissolution of wafers, *Appl. Phys. Lett.* **57**, 1046–1048 (1990).

[7] N. Koshida and H. Koyama, Visible electroluminescence from porous silicon, *Appl. Phys. Lett.* **60**, 347–349 (1992).

[8] A. G. Cullis, L. T. Canham and P. D. J. Calcott, The structural and luminescence properties of porous silicon, *J. Appl. Phys.* **82**, 909–965 (1997).

[9] T. Yonehara, K. Sakaguchi and N. Sato, Epitaxial layer transfer by bond and etch back of porous Si, *Appl. Phys. Lett.* **64**, 2108–2110 (1994).

[10] H. Tayanaka and T. Matsushita, in *Proceedings of the 6th Sony Research Forum*, p. 556 (1996). (in Japanese).

[11] R. Brendel, A novel process for ultrathin monocrystalline silicon solar cells on glass, in *Proceedings of the 14th European Photovoltaic Solar Energy Conference*, pp. 1354–1357 (1997).

[12] Y. H. Ogata, N. Yoshimi, R. Yasuda, T. Tsuboi, T. Sakka and A. Otsuki, Structural change in p-type porous silicon by thermal annealing, *J. Appl. Phys.* **90**, 6487–6492 (2001).

[13] G. Kuchler, D. Scholten, G. Müller, J. Krinke, R. Auer and R. Brendel, Fabrication of textured monocrystalline Si-films using the porous silicon (PSI)-process, in *Proceedings of the 16th European Photovoltaic Solar Energy Conference*, pp. 1695–1698 (2000).

[14] K. Feldrapp, R. Horbelt, R. Auer and R. Brendel, Thin-film (25.5 µm) solar cells from layer transfer using porous silicon with 32.7 mA/cm^2 short circuit current density, *Prog. Photovolt: Res. Appl.* **11**, 105–112 (2003).

[15] V. Lehmann, *Electrochemistry of Silicon, Instrumentation, Science, Materials and Applications*, Wiley-VCH, Weinheim (2002).

[16] H. Föll, Properties of silicon-electrolyte junctions and their application to silicon characterization, *Appl. Phys. A* **53**, 8–19 (1991).

[17] R. L. Smith and S. D. Collins, Porous silicon formation mechanisms, *J. Appl. Phys.* **71**, R1 (1992).

[18] F. Gaspard, A. Bsiesy, M. Ligeon, F. Muller and R. Herino, Charge exchange mechanism responsible for p-type silicon dissolution during porous silicon formation, *J. Electrochem. Soc.* **136**, 3043–3046 (1989).

[19] S. Ottow, G. S. Popkirov and H. Föll, Determination of flat-band potentials of silicon electrodes in HF by means of ac resistance measurements, *J. Electroanal. Chem.* **455**, 29–37 (1998).

[20] M. J. J. Theunissen, J. A. Appels and W. H. C. G. Verkuylen, Application of preferential electrochemical etching of silicon to semiconductor device technology, *J. Electrochem. Soc.* **117**, 959–965 (1970).

[21] M. J. J. Theunissen, Etch channel formation during anodic dissolution of n-type silicon in aqueous hydrofluoric acid, *J. Electrochem. Soc.* **119**, 351–360 (1972).

[22] V. Lehmann and H. Föll, Formation mechanism and properties of electrochemically etched trenches in n-type silicon, *J. Electrochem. Soc.* **137**, 653–659 (1990).

[23] V. Lehmann, The physics of macropore formation in low-doped n-type silicon, *J. Electrochem. Soc.* **140**, 2836–2843 (1993).

[24] V. Lehmann and U. Grüning, The limits of macropore array fabrication, *Thin Solid Films* **297**, 13–17 (1997).

[25] M. Itoh, N. Yamamoto, K. Takemoto and O. Nittono, Cathodoluminescence imaging of n-type porous silicon, *Jpn. J. Appl. Phys.* **35**, 4182–4186 (1996).

[26] M. Thönissen, S. Billat, M. Krüger, H. Lüth, M. G. Berger, U. Frotscher and U. Rossow, Depth inhomogeneity of porous silicon layers, *J. Appl. Phys.* **80**, 2990–2993 (1996).

[27] V. Lehmann, R. Stengl and A. Luigart, On the morphology and the electrochemical formation mechanism of mesoporous silicon, *Mater. Sci. Eng. B* **69-70**, 11–22 (2000).

[28] G. Lamedica, M. Balucani, V. Bondarenko, L. Franchina, L. Dolgyi, V. Yakovtseva and A. Ferrari, Investigation of morphology of porous silicon formed on n$^+$-type silicon, *J. Porous Mat.* **7**, 23–26 (2000).

[29] X. G. Zhang, S. D. Collins and R. L Smith, Porous silicon formation and electropolishing of silicon by anodic polarization in HF solution, *J. Electrochem. Soc.* **136**, 1561–1565 (1989).

[30] J. N. Chazalviel, M. Etman and F. Ozanam, A voltammetric study of the anodic dissolution of p-Si in fluoride electrolytes, *J. Electroanal. Chem.* **297**, 533–540 (1991).

[31] J. N. Chazalviel, C. da Fonseca and F. Ozanam, In situ infrared study of the oscillating anodic dissolution of silicon in fluoride electrolytes, *J. Electrochem. Soc.* **145**, 964–973 (1998).

[32] J. N. Chazalviel and F. Ozanam, A theory for the resonant response of an electrochemical system: Self-oscillating domains, hidden oscillation, and synchronization impedance, *J. Electrochem. Soc.* **139**, 2501–2508 (1992).

[33] J. N. Chazalviel, Ionic processes through the interfacial oxide in the anodic dissolution of silicon, *Electrochim. Acta* **37**, 865–875 (1992).

[34] C. Serre, S. Barret and R. Hérino, Characterization of the electropolishing layer during anodic etching of p-type silicon in aqueous HF solutions, *J. Electrochem. Soc.* **141**, 2049–2053 (1994).

[35] H. J. Lewerenz and M. Aggour, On the origin of photocurrent oscillation at Si electrodes, *J. Electroanal. Chem.* **351**, 159–168 (1993).

[36] V. Lehmann, On the origin of electrochemical oscillations at silicon electrodes, *J. Electrochem. Soc.* **143**, 1313–1318 (1996).

[37] M. I. J. Beale, J. D. Benjamin, M. J. Uren, N. G. Chew and A. G. Cullis, An experimental and theoretical study of the formation and microstructure of porous silicon, *J. Cryst. Growth* **73**, 622–636 (1985).

[38] M. I. J. Beale, N. G. Chew, M. J. Uren, A. G. Cullis and J. D. Benjamin, Microstructure and formation mechanism of porous silicon, *Appl. Phys. Lett.* **46**, 86–88 (1985).

[39] V. Lehmann and U. Gösele, Porous silicon formation: A quantum wire effect, *Appl. Phys. Lett.* **58**, 856–858 (1991).

[40] O. Bisi, S. Ossicini and L. Pavesi, Porous silicon: a quantum sponge structure for silicon based optoelectronics, *Surf. Sci. Rep.* **38**, 1–126 (2000).

[41] P. M. Hoffmann, I. E. Vermeir and P. C. Searson, Electrochemical etching of n-type silicon in fluoride solutions, *J. Electrochem. Soc.* **147**, 2999–3002 (2000).

[42] M. Niwano, T. Miura, Y. Kimura, R. Tajima and N. Miyamoto, Real-time, in situ infrared study of etching of Si (100) and (111) surfaces in dilute hydrofluoric acid solution, *J. Appl. Phys.* **79**, 3708–3713 (1996).

[43] B. Schwartz and H. Robbins, Chemical etching of silicon IV. Etching technology, *J. Electrochem. Soc.* **123**, 1903–1909 (1976).

[44] M. I. J. Beale, J. D. Benjamin, M. J. Uren, N. G. Chew and A. G. Cullis, The formation of porous silicon by chemical stain etches, *J. Cryst. Growth* **75**, 408–414 (1986).

[45] G.D. Stucky and J. E. Mac Dougall, Quantum confinement and host/guest chemistry: Probing a new dimension, *Science* **247**, 669–678 (1990).

[46] W.L. Wilson, P.F. Szajowski and L.E. Brus, Quantum confinement in size-selected, surface-oxidized silicon nanocrystals, *Science* **262**, 1242–1244 (1993).

[47] S. Schuppler, S. L. Friedman, M. A. Marcus, D. L. Adler, Y. H. Xie, F. M. Ross, Y. L. Chabal, T. D. Harris, L. E. Brus, W. L. Brown, E. E. Chaban, P. F. Szajowski, S. B. Christman and P. H. Citrin, Size, shape, and composition of luminescent species in oxidized Si nanocrystals and H-passivated porous Si, *Phys. Rev. B* **52**, 4910–4925 (1995).

[48] J. Von Behren, T. Van Buuren, M. Zacharias, E. H. Chimowitz and P. M. Fauchet, Quantum confinement in nanoscale silicon: The correlation of size with bandgap and luminescence, *Solid State Commun.* **105**, 317–322 (1998).

[49] V. Lehmann and R. Rönnebeck, The physics of macropore formation in low-doped p-type silicon, *J. Electrochem. Soc.* **146**, 2968–2975 (1999).

[50] X. G. Zhang, Mechanism of pore formation on n-type silicon, *J. Electrochem. Soc.* **138**, 3750–3756 (1991).

[51] H. Unno, K. Imai and S. Muramoto, Dissolution reaction effect on porous-silicon density, *J. Electrochem. Soc.* **134**, 645–648 (1987).

[52] M. G. Berger, *Poröses Silicium für die Mikrooptik: Herstellung, Mikrostruktur und optische Eigenschaften von Einzelschichten und Schichtsystemen*, PhD thesis, Institute of Thin Film and Ion Technology, Research Centre Jülich, RWTH Aachen University (1996).

[53] T. Nakagawa, H. Sugiyama and N. Koshida, Fabrication of periodic Si nanostructure by controlled anodization, *Jpn. J. Appl. Phys.* **37**, 7186–7189 (1998).

[54] G. Müller, *Restrukturierung von Porösem Silizium durch Temperaturbehandlung*, PhD thesis, Institute of Applied Physics, University of Erlangen-Nürnberg (2002).

[55] F. Ferrieu, A. Halimaoui and D. Bensahel, Optical characterisation of porous silicon layers by spectrometric ellipsometry in the 1.5-5 eV range, *Solid State Commun.* **84**, 293–296 (1992).

[56] C. Pickering, L. T. Canham and D. Brumhead, Spectroscopic ellipsometry characterisation of light-emitting porous silicon structures, *Appl. Surf. Sci.* **63**, 22–26 (1993).

[57] M. Fried, T. Lohner, O. Polgár, P. Petrik, É. Vázsonyi, I. Bársony, J. P. Piel and J. L. Stehle, Characterization of different porous silicon structures by spectroscopic ellipsometry, *Thin Solid Films* **276**, 223–227 (1996).

[58] L. A. A. Pettersson, L. Hultman and H. Arwin, Porosity depth profiling of thin porous silicon layers by use of variable-angle spectroscopic ellipsometry: A porosity graded-layer model, *Appl. Opt.* **37**, 4130–4136 (1998).

[59] D. R. Lide, *Handbook of Chemistry and Physics*, CRC Press, London, 82nd Edition (2001-2002). p. 12-97, p. 12-222, p. 12-218.

[60] V. Labunov, V. Bondarenko, I. Glinenko, A. Dorofeev and L. Tabulina, Heat treatment effect on porous silicon, *Thin Solid Films* **137**, 123–134 (1986).

[61] G. Müller, M. Nerding, N. Ott, H. P. Strunk and R. Brendel, Sintering of porous silicon, *phys. stat. sol. (a)* **197**, 83–87 (2003).

[62] N. Ott, M. Nerding, G. Müller, R. Brendel and H. P. Strunk, Structural changes in porous silicon during annealing, *phys. stat. sol. (a)* **197**, 93–97 (2003).

[63] N. Ott, M. Nerding, G. Müller, R. Brendel and H. P. Strunk, Evolution of the microstructure during annealing of porous silicon multilayers, *J. Appl. Phys.* **95**, 497–503 (2004).

[64] J. E. Geguzin, *Physik des Sinterns*, VEB Deutscher Verlag für Grundstoffindustrie, Leipzig (1973).

[65] D. J. Eaglesham, A. E. White, L. C. Feldman, N. Moriya and D. C. Jacobson, Equilibrium shape of Si, *Phys. Rev. Lett.* **70**, 1643–1646 (1993).

[66] N. Sato, K. Sakaguchi, K. Yamagata, Y. Fujiyama and T. Yonehara, Epitaxial growth on porous Si for a new bond and etchback silicon-on-insulator, *J. Electrochem. Soc.* **142**, 3116–3122 (1995).

[67] R. Herino, A. Perio, K. Barla and G. Bomchil, Microstructure of porous silicon and its evolution with temperature, *Mater. Lett.* **2**, 519–523 (1984).

[68] The University of Texas Health Science Center at San Antonio, *ImageTool v. 3.00*, `http://ddsdx.uthscsa.edu/dig/itdesc.html`.

[69] S. D. Wicksell, The corpuscle problem: A mathematical study of a biometric problem, *Biometrika* **17**, 84–99 (1925).

[70] G. Bach, Über die Größenverteilung von Kugelschnitten in durchsichtigen Schnitten endlicher Dicke, *Z. Angew. Math. Mech.* **38**, 256–258 (1958).

[71] G. Bach, Über die Bestimmung von charakteristischen Größen einer Kugelverteilung aus der Verteilung der Schnittkreise, *Z. Wiss. Mikrosk.* **65**, 285–291 (1963).

[72] P. L. Goldsmith, The calculation of true particle size distributions from the sizes observed in a thin slice, *Br. J. Appl. Phys.* **18**, 813–830 (1967).

[73] K. Fleischer, The tomato salad problem reconsidered, *Biometr. J.* **36**, 193–203 (1994).

[74] L. M. Cruz-Orive, Distribution-free estimation of sphere size distributions from slabs showing overprojection and truncation, with a review of previous methods, *J. microsc.* **131**, 265–290 (1983).

[75] G. K. Golubev and B. Y. Levit, Asymptotically efficient estimation in the Wicksell problem, *Ann. Statist.* **26**, 2407–2419 (1998).

[76] D. L. Sahagian and A. A. Proussevitch, 3D particle size distributions from 2D observations: stereology for natural applications, *J. Volcanol. Geotherm. Res.* **84**, 173–196 (1998).

[77] J. C. Russ and R. T. Dehoff, *Practical Stereology*, Plenum Press, New York, 2nd Edition (2000).

[78] R. Brendel, Thin-film crystalline silicon mini-modules using porous Si for layer transfer, *Solar Energy* **77**, 969–982 (2004).

[79] R. Horbelt, B. Terheiden, R. Auer and R. Brendel, Manifold use of growth substrate in the Porous Silicon - layer transfer - process, in *Proceedings of the 31st IEEE Photovoltaic Specialists Conference*, pp. 1193–1196 (2005).

[80] H. Tayanaka, K. Yamauchi and T. Matsushita, Thin-film crystalline silicon solar cells obtained by separation of a porous silicon sacrificial layer, in *Proceedings of the 2nd World Conference on Photovoltaic Solar Energy Conversion*, pp. 1272–1277 (1998).

[81] R. B. Bergmann, C. Berge, T. J. Rinke and J. H. Werner, Monocrystalline Si films from transfer processes for thin film devices, *Mater. Res. Soc. Symp. Proc.* **685E**, D2.1.1–D2.1.6 (2001).

[82] J. Mandelkorn and J. H. Lamneck, A new electric field effect in silicon solar cells, *J. Appl. Phys.* **44**, 4785–4787 (1973).

[83] B. Terheiden, R. Horbelt and R. Brendel, Thin-film solar cells and modules from the Porous Silicon process using 6" Si substrates, in *Proceedings of the 21st European Photovoltaic Solar Energy Conference*, pp. 742–745 (2006).

[84] C. Berge, R.B. Bergmann, T.J. Rinke and J.H. Werner, Monocrystalline silicon thin film solar cells by layer transfer, in *Proceedings of the 17th European Photovoltaic Solar Energy Conference*, pp. 1277–1281 (2001).

[85] D. G. Cahill, W. K. Ford, K. E. Goodson, G. D. Mahan, A. Majumdar, H. J. Maris, R. Merlin and S. R. Phillpot, Nanoscale thermal transport, *J. Appl. Phys.* **93**, 793–818 (2003).

[86] A. G. Nassiopoulou and G. Kaltsas, Porous silicon as an effective material for thermal isolation on bulk crystalline silicon, *phys. stat. sol. (a)* **182**, 307–311 (2000).

[87] C. Tsamis, A. G. Nassiopoulou and A. Tserepi, Thermal properties of suspended porous silicon micro-hotplates for sensor applications, *Sens. Actuators B* **95**, 78–82 (2003).

[88] A. Yamamoto, H. Takazawa and T. Ohta, Thermoelectric transport properties of porous silicon nanostructure, in *Proceedings of the 18th International Conference on Thermoelectrics*, pp. 428–431 (1999).

[89] R. G. Mathur, R. M. Mehra and P. C. Mathur, Thermoelectric power in porous silicon, *J. Appl. Phys.* **83**, 5855–5857 (1998).

[90] W. Lang, Thermal conductivity of porous silicon, in *Properties of Porous Silicon*, edited by L. Canham, Institution of Engineering and Technology, London (1997), pp. 138–141.

[91] Q. Shen and T. Toyoda, Dependence of thermal conductivity of porous silicon on porosity characterized by photoacoustic technique, *Rev. Sci. Instrum.* **74**, 601–603 (2003).

[92] V. Lysenko, S. Périchon, B. Remaki, D. Barbier and B. Champagnon, Thermal conductivity of thick meso-porous silicon layers by micro-Raman scattering, *J. Appl. Phys.* **86**, 6841–6846 (1999).

[93] G. Gesele, J. Linsmeier, V. Drach, J. Fricke and R. Arens-Fischer, Temperature-dependent thermal conductivity of porous silicon, *J. Phys. D: Appl. Phys.* **30**, 2911–2916 (1997).

[94] G. Benedetto, L. Boarino and R. Spagnolo, Evaluation of thermal conductivity of porous silicon layers by a photoacoustic method, *Appl. Phys. A* **64**, 155–159 (1997).

[95] D. Song and G. Chen, Thermal conductivity of periodic microporous silicon films, *Appl. Phys. Lett.* **84**, 687–689 (2004).

[96] D. Li, Y. Wu, P. Kim, L. Shi, P. Yang and A. Majumdar, Thermal conductivity of individual silicon nanowires, *Appl. Phys. Lett.* **83**, 2934–2936 (2003).

[97] J. D. Chung and M. Kaviany, Effects of phonon pore scattering and pore randomness on effective conductivity of porous silicon, *Int. J. Heat Mass Transfer* **43**, 521–538 (2000).

[98] W. J. Parker, R. J. Jenkins, C. P. Butler and G. L. Abbott, Flash method of determining thermal diffusivity, heat capacity and thermal conductivity, *J. Appl. Phys.* **32**, 1679–1684 (1961).

[99] J. C. Murphy and L. C. Aamodt, Photothermal spectroscopy using optical beam probing: Mirage effect, *J. Appl. Phys.* **51**, 4580–4588 (1980).

[100] P. K. Wong, P. C. W. Fung and H. L. Tam, Low thermal diffusivity measurements of thin films using mirage technique, *J. Appl. Phys.* **84**, 6623–6627 (1998).

[101] V. Drach, G. Harthausen, H.-P. Ebert and J. Fricke, Quantitative thermal characterisation of small samples via thermography, in *Proceedings of the Infrared Sensors and Systems International Conference*, pp. 191–196 (2002).

[102] V. Drach, H.-P. Ebert and J. Fricke, Noncontact determination of the thermal conductivity of fiberes, *High Temp. High Press.* **32**, 337–346 (2000).

[103] V. Drach, H.-P. Ebert and J. Fricke, A noncontact technique for the determination of the longitudinal thermal conductivity and diffusivity of foils, in *Proceedings of the 3rd European Thermal Science Conference*, pp. 637–643 (2000).

[104] O. Breitenstein and M. Langenkamp, *Lock-in Thermography, Basics and Use for Functional Diagnostics of Electronic Components*, Springer-Verlag, Berlin (2003). p. 13, Eq. (2.27) on p. 32, p. 181.

[105] M. A. J. Ångström, New method of determining the thermal conductibility of bodies, *Phil. Mag.* **25**, 130–142 (1863).

[106] H. S. Carslaw and J. C. Jaeger, *Conduction of Heat in Solids*, Oxford University Press, Oxford, 2nd Edition (1986). Eq. (3) on p. 137, Eq. (4) on p. 134.

[107] H. Altmann, *Bestimmung der Temperaturleitfähigkeit Dünner Schichten mit dem Ångström Verfahren*, PhD thesis, Department of Physics and Astronomy, University of Würzburg (1997). Eqs. (3.49) and (3.50) on p. 20.

[108] N. Horny and B. Lannoy, Lock-in thermography with a focal plane array, *Meas. Sci. Technol.* **14**, 439–443 (2003).

[109] D. Wu and G. Busse, Lock-in thermography for nondestructive evaluation of materials, *Rev. Gén. Therm.* **37**, 693–703 (1998).

[110] H. Schneider, C. Schönbein, M. Walther, K. Schwarz, J. Fleissner and P. Koidl, Photovoltaic quantum well infrared photodetectors: The four-zone scheme, *Appl. Phys. Lett.* **71**, 246–248 (1997).

[111] Wieland-Werke AG, *Datenblatt N29 Press/Ziehprodukte*, `http://www.wieland.de/internet/content/objectpiro.jsp?ID=1003269`.

[112] Goodfellow Corporation, *Technical data: Meaterial properties of Kapton MTB*, `http://www.goodfellow.com/csp/active/gfMaterialInfo.csp?MATID=IM30&result=7`.

[113] H. M. Relyea, F. Breidenich, J. V. Beck and J. J. McGrath, Measurement of thermal properties of thin films using infrared thermography, in *Proceedings of the 23rd International Thermal Conductivity Conference*, pp. 183–194 (1996). Eq. (7) on p. 191.

[114] H. Looyenga, Dielectric constants of heterogeneous mixtures, *Physica* **31**, 401–406 (1965).

[115] V. Lysenko, S. Périchon, B. Remaki and D. Barbier, Thermal isolation in microsystems with porous silicon, *Sens. Actuators A* **99**, 13–24 (2002). Section 3.1 on p. 16.

[116] G. Chen, Phonon heat conduction in nanostructures, *Int. J. Therm. Sci.* **39**, 471–480 (2000).

[117] G. Chen, Thermal conductivity and ballistic-phonon transport in the cross-plane direction of superlattices, *Phys. Rev. B* **57**, 14958–14973 (1998). Table I on p. 14967.

[118] G. Chen, Size and interface effects on thermal conductivity of superlattices and periodic thin-film structures, *J. Heat Transfer* **119**, 220–229 (1997).

[119] D. J. Bergman, The dielectric constant of a composite material - a problem in classical physics, *Phys. Rep.* **43**, 377–407 (1978).

[120] W. Theiss, The use of effective medium theories in optical spectroscopy, in *Festkörperprobleme; Advances in Solid State Physics*, edited by R. Helbig, volume 33, Vieweg, Braunschweig (1994), p. 149.

[121] A. E. Pap, K. Kordás, J. Vähäkangas, A. Uusimäki, S. Leppävuori, L. Pilon and S. Szatmári, Optical properties of porous silicon. Part III: Comparison of experimental and theoretical results, *Opt. Mater.* **28**, 506–513 (2006).

[122] P. A. Snow, E. K. Squire, P. St. J. Russell and L. T. Canham, Vapor sensing using the optical properties of porous silicon Bragg mirrors, *J. Appl. Phys.* **86**, 1781–1784 (1999).

[123] W. Theiss, S. Henkel and M. Arntzen, Connecting microscopic and macroscopic properties of porous media: choosing appropriate effective medium concepts, *Thin Solid Films* **255**, I77–180 (1995).

[124] W. Theiss and S. Hilbrich, Refractive index of porous silicon, in *Properties of Porous Silicon*, edited by L. Canham, Institution of Engineering and Technology, London (1997), pp. 223–228.

[125] W. Theiss, Optical properties of porous silicon, *Surf. Sci. Rep.* **29**, 91–192 (1997).

[126] G. Mie, Beiträge zur Optik trüber Medien, speziell kolloidaler Metallösungen, *Ann. Phys.* **25**, 377–445 (1908).

[127] M. Y. Ghannam, A. A. Abouelsaood and J. F. Nijs, A semiquantitative model of a porous silicon layer used as a light diffuser in a thin film solar cell, *Solar Energy Mat. and Solar Cells* **60**, 105–125 (2000).

[128] A. A. Abouelsaood, M. Y. Ghannam, L. Stalmans, J. Poortmans and J. F. Nijs, Experimental testing of a random medium optical model of porous silicon for photovoltaic applications, *Prog. Photovolt: Res. Appl.* **9**, 15–26 (2001).

[129] H. Seel and R. Brendel, Optical absorption in crystalline Si films containing spherical voids for internal light scattering, *Thin Solid Films* **451-452**, 608–611 (2004).

[130] H. Seel, Lichtstreuung in wärmebehandelten, porösen Si-Dünnschichten, Diploma thesis, Institute of Applied Physics, University of Erlangen-Nürnberg, (2002).

[131] M. A. Green and M. J. Keevers, Optical properties of intrinsic silicon at 300 K, *Prog. Photovolt: Res. Appl.* **3**, 189–193 (1995).

[132] M. A. Green, *Silicon Solar Cells: Advanced Principles and Practice*, Centre for Photovoltaic Devices and Systems, University of New South Wales, Sydney (1995). Appendix D, Eq. (4.8) on p. 48, pp. 51-54.

[133] D. A. Clugston and P. A. Basore, Modelling free carrier absorption in solar cells, *Prog. Photovolt: Res. Appl.* **5**, 229–236 (1997).

[134] P. K. Basu, *Theory of Optical Processes in Semiconductors, Bulk and Microstructures*, Clarendon Press, Oxford (1997). Section 9.2.4.

[135] P. P. Altermatt, A. Schenk, F. Goldhaar and G. Heiser, Reassessment of the intrinsic carrier density in crystalline silicon in view of band-gap narrowing, *J. Appl. Phys.* **93**, 1598–1604 (2003). Fig. 2 on p. 1599.

[136] A. B. Sproul and M. A. Green, Intrinsic carrier concentration and minority-carrier mobility of silicon from 77 to 300 K, *J. Appl. Phys.* **73**, 1214–1225 (1993). Eq. (7) on p. 1221.

[137] M. A. Green, Intrinsic concentration, effective density of states, and effective mass in silicon, *J. Appl. Phys.* **67**, 2944–2954 (1990).

[138] D. A. G. Bruggeman, The calculation of various physical constants of heterogeneous substances. I. The dielectric constants and conductivities of mixtures composed of isotropic substances, *Ann. Phys.* **24**, 636–664 (1935).

[139] J. C. Maxwell Garnett, Colours in metal glasses and in metallic films, *Phil. Trans. R. Soc. A* **203**, 385–420 (1904).

[140] J. Zettner, M. Thönissen, T. Hierl, R. Brendel and M. Schulz, Novel porous silicon backside light reflector for thin silicon solar cells, *Prog. Photovolt: Res. Appl.* **6**, 423–432 (1998).

[141] G. Müller, R. Brendel and M. Schulz, Light diffusing broad band Bragg reflectors for thin film silicon solar cells, in *Proceedings of the 16th European Photovoltaic Solar Energy Conference*, pp. 1699–1702 (2000).

[142] A. A. Kokhanovsky, *Optics of Light Scattering Media: Problems and Solutions*, Springer-Verlag, London, 2nd Edition (2001). Appendix 2 on p. 209.

[143] P. Chylek, Asymptotic limits of the Mie-scattering characteristics, *J. Opt. Soc. Am.* **65**, 1316–1318 (1975).

[144] A. Cohen, C. Acquista and J. A. Cooney, Extinction of light by large reflecting spheres, *Appl. Opt.* **19**, 2264–2265 (1980).

[145] C. Acquista, A. Cohen, J. A. Cooney and J. Wimp, Asymptotic behavior of the efficiencies in Mie scattering, *J. Opt. Soc. Am.* **70**, 1023–1025 (1980).

[146] T. B. A. Senior, Note on the extinction efficiency, *Appl. Opt.* **22**, 1796–1797 (1983).

[147] I. W. Sudiarta and P. Chýlek, Mie scattering efficiency of a large spherical particle embedded in an absorbing medium, *J. Quant. Spectrosc. Rad. Transf.* **70**, 709–714 (2001).

[148] M. Quinten and J. Rostalski, Lorenz-Mie theory for spheres immersed in an absorbing host medium, *Part. Part. Syst. Charact.* **13**, 89–96 (1996).

[149] Q. Fu and W. Sun, Mie theory for light scattering by a spherical particle in an absorbing medium, *Appl. Opt.* **40**, 1354–1361 (2001).

[150] I. W. Sudiarta and P. Chýlek, Mie-scattering formalism for spherical particles embedded in an absorbing medium, *J. Opt. Soc. Am.* **18**, 1275–1278 (2001).

[151] I. W. Sudiarta and P. Chýlek, Mie scattering by a spherical particle in an absorbing medium, *Appl. Opt.* **41**, 3545–3546 (2002).

[152] A. S. Glassner, *An Introduction to Ray Tracing*, Academic Press, London (1989).

[153] B. Harbecke, Coherent and incoherent reflection and transmission of multilayer structures, *Appl. Phys. B* **39**, 165–170 (1986).

[154] M. A. Green, Lambertian light trapping in textured solar cells and light-emitting diodes: Analytical solutions, *Prog. Photovolt: Res. Appl.* **10**, 235–241 (2002). Eq. (14) on p. 238, Eq. (9) on p. 238.

[155] J. C. Manifacier, J. Gasiot and J. P. Fillard, A simple method for the determination of the optical constants n, k and the thickness of a weakly absorbing thin film, *J. Phys. E: Sci. Instrum.* **9**, 1002–1004 (1976).

[156] T. Unagami, Formation mechanism of porous silicon layer by anodization in HF solution, *J. Electrochem. Soc.* **127**, 476–483 (1980).

[157] C. Peng, K. D. Hirschman and P. M. Fauchet, Carrier transport in porous silicon light-emitting devices, *J. Appl. Phys.* **80**, 295–300 (1996).

[158] M. Ben-Chorin, Resistivity of porous silicon, in *Properties of Porous Silicon*, edited by L. Canham, Institution of Engineering and Technology, London (1997), pp. 165–175.

[159] A. J. Read, R. J. Needs, K. J. Nash, L. T. Canham, P. D. J. Calcott and A. Qteish, First-principles calculations of the electronic properties of silicon quantum wires, *Phys. Rev. Lett.* **69**, 1232–1235 (1992).

[160] R. Tsu and D. Babic, Doping of a quantum dot, *Appl. Phys. Lett.* **64**, 1806–1808 (1994).

[161] V. Lehmann, F. Hofmann, F. Möller and U. Grüning, Resistivity of porous silicon: A surface effect, *Thin Solid Films* **255**, 20–22 (1995).

[162] M. Ben-Chorin, A. Kux and I. Schechter, Adsorbate effects on photoluminescence and electrical conductivity of porous silicon, *Appl. Phys. Lett.* **64**, 481–483 (1994).

[163] D. Stievenard and D. Deresmes, Are electrical properties of an aluminum-porous silicon junction governed by dangling bonds?, *Appl. Phys. Lett.* **67**, 1570–1572 (1995).

[164] L. Boarino, C. Baratto, F. Geobaldo, G. Amato, E. Comini, A. M. Rossi, G. Faglia, G. Lérondel and G. Sberveglieri, NO_2 monitoring at room temperature by a porous silicon gas sensor, *Mater. Sci. Eng. B* **69-70**, 210–214 (2000).

[165] L. Boarino, F. Geobaldo, S. Borini, A. M. Rossi, P. Rivolo, M. Rocchia, E. Garrone and G. Amato, Local environment of boron impurities in porous silicon and their interaction with NO_2 molecules, *Phys. Rev. B* **64**, 205308 (2001).

[166] E. Garrone, S. Borini, P. Rivolo, L. Boarino, F. Geobaldo and G. Amato, Porous silicon in NO_2: A chemisorption mechanism for enhanced electrical conductivity, *phys. stat. sol. (a)* **197**, 103–106 (2003).

[167] A. J. Simons, T. I. Cox, M. J. Uren and P. D. J. Calcott, The electrical properties of porous silicon produced from n^+ silicon substrates, *Thin Solid Films* **255**, 12–15 (1995).

[168] A. J. Simons, Carrier mobility in porous silicon, in *Properties of Porous Silicon*, edited by L. Canham, Institution of Engineering and Technology, London (1997), pp. 176–184.

[169] T. J. Rinke, R. B. Bergmann and J. H. Werner, Quasi-monocrystalline silicon for thin-film devices, *Appl. Phys. A* **68**, 705–707 (1999).

[170] T. J. Rinke, R. B. Bergmann, R. Brüggemann and J. H. Werner, Ultrathin quasi-monocrystalline silicon films for electronic devices, *Solid State Phenomena* **67-68**, 229–234 (1999).

[171] T. J. Rinke, R. B. Bergmann and J. H. Werner, Structure and properties of quasi-monocrystalline silicon thin-films, *Mater. Res. Soc. Symp. Proc.* **558**, 251–256 (2000).

[172] L. B. Valdes, Resistivity measurements on germanium for transistors, *Proceedings of the Institute of Radio Engineers* **42**, 420–427 (1954).

[173] D. K. Schroder, *Semiconductor Material and Device Characterization*, Wiley, New York (1990). Section 1.2, Section 8.4.1.

[174] F. Duerinckx, K. Van Nieuwenhuysen, H.J. Kim, I. Kuzma-Filipek, G. Beaucarne and J. Poortmans, Light trapping for epitaxial thin film crystalline silicon solar cells, in *Proceedings of the 20th European Photovoltaic Solar Energy Conference*, pp. 725–728 (2005).

[175] R. Schwarz, F. Wang, M. Ben-Chorin, S. Grebner, A. Nikolov and F. Koch, Photocarrier grating technique in mesoporous silicon, *Thin Solid Films* **255**, 23–26 (1995).

[176] Y. Lubianiker, I. Balberg, J. Partee and J. Shinar, Porous silicon as a near-ideal disordered semiconductor, *J. Non-Cryst. Solids* **198-200**, 949–952 (1996).

[177] T. Rinke, *Transfersolarzellen aus monokristallinem Dünnschichtsilicium*, PhD thesis, Institute of Physical Electronics, University of Stuttgart (2003). Section 4.4 on p. 64.

[178] M. A. Green, *Solar Cells: Operating Principles, Technology and System Applications*, Prentice-Hall Inc., Englewood Cliffs (1982). Section 5.4.4 on p. 96.

[179] G. F. J. Garlick and A. H. Kachare, Forward- and reverse-bias tunneling effects in n^+-p silicon solar cells, *Appl. Phys. Lett.* **36**, 911–913 (1980).

[180] G. I. Andersson and O. Engström, Forward-bias tunneling at defect clusters in silicon emitter junctions, *J. Appl. Phys.* **69**, 4418–4425 (1991).

[181] G.A.M. Hurkx, D.B.M. Klaassen and M.P.G. Knuvers, A new recombination model for device simulation including tunneling, *IEEE Trans. Electron Dev.* **39**, 331–338 (1992).

[182] U. Rau, Tunneling-enhanced recombination in Cu(In,Ga)Se_2 heterojunction solar cells, *Appl. Phys. Lett.* **74**, 111–113 (1999).

[183] C. Peters, *Optimierung von MIS-Inversionsschichtsolarzellen*, PhD thesis, Department of Physics, University of Hannover (2005).

[184] N. D. Arora, S. G. Chamberlain and D. J. Roulston, Diffusion length determination in p-n junction diodes and solar cell, *Appl. Phys. Lett.* **37**, 325–327 (1980).

[185] P. A. Basore, Extended spectral analysis of internal quantum efficiency, in *Proceedings of the 23rd IEEE Photovoltaic Specialists Conference*, pp. 147–152 (1993).

[186] B. Fischer, *Loss Analysis of Crystalline Silicon Solar Cells using Photoconductance and Quantum Efficiency Measurements*, PhD thesis, Department of Physics, University of Konstanz (2003). Eqs. (4-13) and (4-12) on p. 59.

[187] J. Metzdorf, Calibration of solar cells. 1: The differential spectral responsivity method, *Appl. Opt.* **26**, 1701–1708 (1987).

[188] R. Brendel, Note on the interpretation of injection-level-dependent surface recombination velocities, *Appl. Phys. A* **60**, 523–524 (1995).

[189] M. Hirsch, U. Rau and J. H. Werner, Analysis of internal quantum efficiency and a new graphical evaluation scheme, *Solid-State Electron.* **38**, 1009–1015 (1995). Fig. 2 (b).

[190] S. M. Sze, *Physics of Semiconductor Devices*, Wiley-Interscience, New York, 2nd Edition (1981). Eq. (15a) on p. 77.

[191] M. J. Kerr and A. Cuevas, General parameterization of Auger recombination in crystalline silicon, *J. Appl. Phys.* **91**, 2473–2480 (2002). Eq. (20) on p.2477.

[192] A. B. Sproul, M. A. Green and A. W. Stephens, Accurate determination of minority carrier- and lattice scattering-mobility in silicon from photoconductance decay, *J. Appl. Phys.* **72**, 4161–4171 (1992).

[193] W. Sun, N. P. Kherani, K. D. Hirschman, L. L. Gadeken and P. M. Fauchet, A three-dimensional porous silicon p-n diode for betavoltaics and photovoltaics, *Adv. Mater.* **17**, 1230–1233 (2005).

[194] W.C. O'Mara, R. B. Herring and L. P. Hunt, *Handbook of Semiconductor Silicon Technology*, William Andrew Publishing, Noyes (1990). Section 5.5.2.

[195] H.-R. Chang, Autodoping in silicon epitaxy, *J. Electrochem. Soc.* **132**, 219–224 (1985).

[196] M. W. M. Graef, B. J. H. Launissen and H. H. C. de Moor, Antimony, arsenic, phosphorus, and boron autodoping in silicon epitaxy, *J. Electrochem. Soc.* **132**, 1942–1953 (1985).

[197] A. S. Grove, A. Roder and C. T. Sah, Impurity distribution in epitaxial growth, *J. Appl. Phys.* **36**, 802–810 (1965).

[198] D. Widmann, H. Mader and H. Friedrich, *Technologie hochintegrierter Schaltungen*, Springer-Verlag, Berlin, 2nd Edition (1996). Section 3.3.2.

[199] B. M. Abdurakhmanov and R. R. Bilyalov, Use of autodoping to create extracting electric fields in the base of silicon solar cells, *Semicond. Sci. Technol.* **11**, 921–926 (1996).

[200] Silvaco Int., *Ssuprem3 1D Process Simulation*, `http://www.silvaco.com/products/vwf/athena/ss3/ss3_br.html`.

[201] K. Suzuki, H. Yamawaki and Y. Tada, Boron out diffusion from Si substrates in various ambients, *Solid-State Electron.* **41**, 1095–1097 (1997).

[202] R. G. Mazur and D. H. Dickey, A spreading resistance technique for resistivity measurements in Si, *J. Electrochem. Soc.* **113**, 255–259 (1966).

[203] W. Vandervorst and T. Clarysse, Recent developments in the interpretation of spreading resistance profiles for VLSI-technology, *J. Electrochem. Soc.* **137**, 679–683 (1990).

[204] D. H. Dickey, A poisson solver for spreading resistance analysis, *J. Vac. Sci. Technol. B* **10**, 438–441 (1992).

[205] A. Goetzberger, B. Voß and J. Knobloch, *Sonnenenergie: Photovoltaik*, Teubner, Stuttgart, 2nd Edition (1997). Fig. 6.9 on p. 112, Section 7.2.1.2.1 on p. 167.

[206] M. J. Kerr, J. Schmidt and A. Cuevas, Surface recombination velocity of phosphorus-diffused silicon solar cell emitters passivated with plasma enhanced chemical vapor deposited silicon nitride and thermal silicon oxide, *J. Appl. Phys.* **89**, 3821–3826 (2001).

[207] H. Seidel, L. Csepregi, A. Heuberger and H. Baumgärtel, Anisotropic etching of crystalline silicon in alkaline solutions, *J. Electrochem. Soc.* **137**, 3626–3632 (1990). Fig. 8 on p. 3630.

[208] N. Khedher, M. Hajji, M. Hassen, A. Ben-Jaballah, B. Ouertani, H. Ezzaouia, B. Bessais, A. Selmi and R. Bennaceur, Gettering impurities from crystalline silicon by phosphorus diffusion using a porous silicon layer, *Solar Energy Mat. and Solar Cells* **87**, 605–611 (2004).

[209] Y. S. Tsuo, P. Menna, J. R. Pitts, K. R. Jantzen, S. E. Asher, M. M. Al-Jassim and T. F. Ciszek, Porous silicon gettering, in *Proceedings of the 25th IEEE Photovoltaic Specialists Conference*, pp. 461–464 (1996).

[210] P. Menna, Y. S. Tsuo, M. M. Al-Jassim, S. E. Asher, R. Matson and T. F. Ciszek, Purification of metallurgical-grade silicon by porous-silicon etching, in *Proceedings of the 2nd World Conference on Photovoltaic Solar Energy Conversion*, pp. 1232–1235 (1998).

[211] H. Plagwitz, Y. Takahashi, B. Terheiden and R. Brendel, Amorphous Si/SiN double layers: A low temperature passivation method for diffused phosphorus as well as boron emitters, in *Proceedings of the 21st European Photovoltaic Solar Energy Conference*, pp. 688–691 (2006).

[212] S. Dauwe, *Low-Temperature Surface Passivation of Crystalline Silicon and its Application to the Rear Side of Solar Cells*, PhD thesis, Department of Physics, University of Hannover (2004). Section 5.2 on p. 101.

[213] M. Schöfthaler, *Transiente Mikrowellenreflexion zur kontaktlosen Trägerlebensdauermessung an Silizium für Solarzellen*, PhD thesis, Institute of Physical Electronics, University of Stuttgart (1995).

[214] J. M. Borrego, R. J. Gutmann, N. Jensen and O. Paz, Non-destructive lifetime measurement in silicon wafers by microwave reflection, *Solid-State Electron.* **30**, 195–203 (1987).

[215] P. A. Basore and B. R. Hansen, Microwave-detected photoconductance decay, in *Proceedings of the 21rd IEEE Photovoltaic Specialists Conference*, pp. 374–379 (1990).

[216] J. Kraiem, E. Tranvouez, S. Quoizola, A. Fave, A. Kaminski, J. P. Boyeaux, G. Brémond and M. Lemiti, Study of porous silicon layer for epitaxial thin film silicon solar cells, in *Proceedings of the 31st IEEE Photovoltaic Specialists Conference*, pp. 1107–1110 (2005).

[217] J. D. Moschner, J. Henze, J. Schmidt and R. Hezel, High-quality surface passivation of silicon solar cells in an industrial-type inline plasma silicon nitride deposition system, *Prog. Photovolt: Res. Appl.* **12**, 21–31 (2004).

[218] M. Schaper, J. Schmidt, H. Plagwitz and R. Brendel, 20.1%-efficient crystalline silicon solar cell with amorphous silicon rear-surface passivation, *Prog. Photovolt: Res. Appl.* **13**, 381–386 (2005).

[219] H. Plagwitz, A. Wolf, B. Terheiden and R. Brendel, a-Si:H passivation scheme for monocrystalline silicon thin-film solar cells applying the PSI process, in *Technical Digest of the 15th International Photovoltaic Science and Engineering Conference*, pp. 989–990 (2005).

[220] I. Martín, M. Vetter, M. Garín, A. Orpella, C. Voz, J. Puigdollers and R. Alcubilla, Crystalline silicon surface passivation with amorphous SiC_x:H films deposited by plasma-enhanced chemical-vapor deposition, *J. Appl. Phys.* **98**, 114912 (2005).

[221] R. Petres, J. Libal, R. Kopecek, M. Vetter, R. Ferre, I. Martín, D. Borchert, I. Röver, K. Wambach and P. Fath, Passivation of p^+-surfaces by PECVD silicon carbide films - A promising method for industrial silicon solar cell applications, in *Technical Digest of the 15th International Photovoltaic Science and Engineering Conference*, pp. 128–129 (2005).

[222] S. Dauwe, L. Mittelstädt, A. Metz and R. Hezel, Experimental evidence of parasitic shunting in silicon nitride rear surface passivated solar cells, *Prog. Photovolt: Res. Appl.* **10**, 271–278 (2002).

[223] D.K. Schroder and D. L. Meier, Solar cell contact resistance - A review, *IEEE Trans. Electron Dev.* **31**, 637– 647 (1984).

[224] H. Plagwitz, M. Schaper, A. Wolf, R. Meyer, J. Schmidt, B. Terheiden and R. Brendel, 20% efficient silicon solar cell with local contacts to the a-Si:H passivated rear side by means of annealing (COSIMA), in *Proceedings of the 20th European Photovoltaic Solar Energy Conference*, pp. 725–728 (2005).

[225] A. Bentzen, A. Ulyashin, A. Suphellen, E. Sauar, D. Grambole, D. N. Wright, E. S. Marstein, B. G. Svensson and A. Holt, Surface passivation of silicon solar cells by amorphous silicon/silicon nitride dual layers, in *Technical Digest of the 15th International Photovoltaic Science and Engineering Conference*, pp. 316–317 (2005).

[226] H. Plagwitz, M. Nerding, N. Ott and H. P. Strunkand R. Brendel, Low-temperature formation of local Al contacts to a-Si:H-passivated Si wafers, *Prog. Photovolt: Res. Appl.* **12**, 47–54 (2004).

[227] D. A. Clugston and P. A. Basore, PC1D version 5: 32-bit solar cell modelling on personal computers, in *Proceedings of the 26th IEEE Photovoltaic Specialists Conference*, pp. 207–210 (1997).

[228] Renewable Resource Data Center, *Reference Solar Spectral Irradiance: Air Mass 1.5*, `http://rredc.nrel.gov/solar/spectra/am1.5/`.

[229] R. Brendel, *Thin-Film Crystalline Silicon Solar Cells, Physics and Technology*, Wiley-VCH, Weinheim (2003). Appendix A on p. 181.

[230] R. Brendel, Sunrays: a versatile ray tracing program. for the photovoltaic community, in *Proceedings of the 12th European Photovoltaic Solar Energy Conference*, pp. 1339–1342 (1994).

[231] G. Beaucarne, F. Duerinckx, I. Kuzma, K. Van Nieuwenhuysen, H.J. Kim and J. Poortmans, Epitaxial thin-film Si solar cells, *Thin Solid Films* **511-512**, 533–542 (2006).

[232] MathWorks Inc., *Matlab v. 5.2*, `http://www.mathworks.com/products/matlab`.

[233] P. Laven, *MiePlot v. 3.4.16*, `http://www.philiplaven.com/mieplot.htm`.

[234] E. Hecht, *Optics*, Addison Wesley, San Francisco, 4th (international) Edition (2002). Eqs. (4.47) on p. 115 and (4.48) on p. 116 , Eqs. (4.42) and (4.43) on p. 115.

[235] A. Luque, *Physical Limitations to Photovoltaic Energy Conversion*, Adam Hilger, Bristol (1990). p. 28.

List of publications

Journal papers

1. A. Wolf, P. Pohl and R. Brendel, Thermophysical analysis of thin films by lock-in thermography, *J. Appl. Phys.* **96**, 6306–6312 (2004).
2. A. Wolf and R. Brendel, Thermal conductivity of sintered porous silicon films, *Thin Solid Films* **513**, 385–390 (2006).
3. A. Wolf, B. Terheiden and R. Brendel, Autodiffusion: A novel method for emitter formation in crystalline silicon thin-film solar cells, *Prog. Photovolt: Res. Appl.* **15**, 199–210 (2007).
4. A. Wolf, B. Terheiden and R. Brendel, Light scattering and diffuse light propagation in sintered porous silicon, submitted to *J. Appl. Phys.* (2007).

Conference papers

1. A. Wolf, P. Pohl and R. Brendel, Determination of thermophysical properties of thin films for photovoltaic applications, in *Proceedings of the 31st IEEE Photovoltaic Specialists Conference*, pp. 1749–1752 (2005).
2. H. Plagwitz, M. Schaper, A. Wolf, R. Meyer, J. Schmidt, B. Terheiden and R. Brendel, 20% efficient silicon solar cell with local contacts to the a-Si:H passivated rear side by means of annealing (COSIMA), in *Proceedings of the 20th European Photovoltaic Solar Energy Conference*, pp. 725–728 (2005).
3. H. Plagwitz, A. Wolf, B. Terheiden and R. Brendel, a-Si:H passivation scheme for monocrystalline silicon thin-film solar cells applying the PSI process, in *Technical Digest of the 15th International Photovoltaic Science and Engineering Conference*, pp. 989–990 (2005).
4. A. Wolf, B. Terheiden and R. Brendel, Autodiffused boron emitter for n-type monocrystalline si thin-film solar cells, in *Proceedings of the IEEE 4th World Conference on Photovoltaic Energy Conversion*, pp. 992–995 (2006).
5. A. Wolf, B. Terheiden and R. Brendel, Formation of phosphorus emitters in crystalline silicon thin-film solar cells by the novel autodiffusion process, in *Proceedings of the 21st European Photovoltaic Solar Energy Conference*, pp. 730–733 (2006).

Patent applications

1. A. Wolf, B. Terheiden and R. Brendel, Verfahren zur Herstellung eines Halbleiterbauelementes mit einem gezielt dotierten Oberflächenbereich unter Verwendung von Aus-Diffusion und entsprechendes Halbleiterbauelement, PCT patent application No. PCT/EP2007/002468 (20 March 2007).

Danksagung

Ein herzliches **Dankeschön** an all die Menschen, die zum Gelingen dieser Arbeit beigetragen haben:

Prof. Dr. Rolf Brendel für die ausgezeichnete Betreuung dieser Arbeit, speziell in der Anfangsphase am ZAE in Erlangen, für viele hilfreiche Anregungen sowie den Freiraum beim Ausgestalten dieser Arbeit;

Prof. Dr. Karina Morgenstern für die bereitwillige Übernahme des Korreferats;

Prof. Dr. Max Schulz für die Möglichkeit meine Doktorarbeit am ZAE Bayern zu beginnen;

Dr. Barbara Terheiden für die intensive und herzliche Betreuung am ISFH, die zahlreichen Anregungen und Diskussionen zu Physik und Technologie, sowie das geduldige Korrekturlesen meiner Manuskripte;

Jan Hensen für die Hilfestellung beim Porosizieren, sowie Lotte Ehlers, Renate Horbelt, Sabine Kirstein, Anja Lohse, Agnes Merkele und Marita Steinhof für Unterstützung bei der Solarzellen-Prozessierung;

den MitdoktorandInnen und WissenschaftlerInnen Dr. Pietro Altermatt, Robert Bock, Dr. Karsten Bothe, Dr. Peter Engelhardt, Dr. Bernhardt Fischer, Enrique Garralaga, Adnan Hammud, Dr. Nils-Peter Harder, Sonja Hermann, Dr. Mark Köntges, Mihael Manole, Dr. Rüdiger Meyer, Dr. Heiko Plagwitz, Dr. Peter Pohl, Klaus Ramspeck, Dr. Rolf Reinecke-Koch, PD Dr. Jan Schmidt und Christian Schmiga sowie allen weiteren Mitarbeitern für die hervorragende Zusammenarbeit und das positive, humorvolle Arbeitsklima am ISFH;

Stefan Beisse, Gerwin Gross, Andreas Treder und Michael Weiss vom Technik- und Werkstatt-Team des ISFH für die kompetente Instandhaltung der Anlagen und Messtechnik;

Astrid Kidzun, Richard Auer und Dr. Vladimir Gazuz für die angenehme und freundliche Arbeitsatmosphäre am ZAE in Erlangen;

Dr. Gunter Müller für die Einführung in die Technologie des elektrochemischen Ätzens am ZAE, sowie für die Unterstützung während meiner Arbeit;

Dr. Wolfgang Appel (IMS Stuttgart) für das geduldige beantworten meiner zahlreichen Fragen zur Silizium Epitaxie und PD Dr. Wolfgang Theiss (W. Theiss Hard- and Software) für anregende Diskussionen zur Optik von porösem Silizium.

und natürlich meinen Mitbewohnern der Solar-WG Barbara, Renate und Till für eine unvergessliche Zeit in Hameln!

Lebenslauf

Persönliche Daten

Name	Andreas Klaus Wolf
Anschrift	Zur Eichwiese 56, 64367 Mühltal
Geburtsdatum	19. März 1977
Nationalität	deutsch
Familienstand	verheiratet

Schulbildung

1983 - 1987	Carlo-Mierendorff-Schule (Grundschule) in Griesheim
1987 - 1989	Förderstufe und
1989 - 1993	Gymnasialzweig der Gerhart-Hauptmann-Schule (Gesamtschule) in Griesheim
1993 - 1996	Eleonorenschule (Gymnasium) in Darmstadt Abitur im Juni 1996

Zivildienst

Oktober 1996 - Oktober 1997	Johanniter-Unfall-Hilfe in Griesheim

Studium

Oktober 1997 - August 2003	**Technische Universität Darmstadt** Physik Studium, Vordiplom im Oktober 1999 Diplomprüfung im August 2003
August 2000 - Juni 2001	**Königlich Technische Hochschule (KTH)** **Stockholm, Schweden** Auslandsstudienjahr im Fachbereich Physik

Anstellung

September 2003 - September 2004	**Bayerische Zentrum für Angewandte Energieforschung (ZAE Bayern)** Wissenschaftlicher Mitarbeiter der Abteilung Thermosensorik und Photovoltaik in Erlangen
seit Oktober 2004	**Institut für Solarenergieforschung Hameln (ISFH)** Wissenschaftlicher Mitarbeiter im Bereich Photovoltaik, Gruppe Silizium-Dünnschicht Solarzellen